2015

Contributions to the development of microgrids: Aggregated modelling and operational aspects

Athmi Vidarshika Jayawardena
University of Wollongong, avj998@uowmail.edu.au

School of Electrical, Computer and Telecommunications Engineering

Contributions to the Development of Microgrids: Aggregated Modelling and Operational Aspects

Athmi Vidarshika Jayawardena, BSc(Eng)

Supervisors

Dr. Lasantha Meegahapola, Dr. Duane Robinson & Prof. Sarath Perera

This thesis is presented as part of the requirements for the

Award of the Degree of

Doctor of Philosophy

of the

University of Wollongong

March 2015

Dedicated to my parents...

Certification

I, Athmi Vidarshika Jayawardena, declare that this thesis, submitted in fulfilment of the requirements for the award of Doctor of Philosophy, in the School of Electrical, Computer and Telecommunications Engineering, University of Wollongong, is entirely my own work unless otherwise referenced or acknowledged. This manuscript has not been submitted for qualifications at any other academic institute.

Athmi Vidarshika Jayawardena

Date: 08 March 2015

Abstract

Increasing levels of penetration of distributed energy resources (DERs) have transformed distribution networks from passive to active networks and introduced the concept of microgrids. Dynamic characteristics of microgrids operating either in grid connected or islanded modes can be different from the traditional distribution networks due to the combination of different DERs. In order to make microgrid operation attractive, the issues associated with microgrids need to be properly analysed. This thesis examines the modelling of microgrids and investigates different aspects of their operation.

In the first phase of the work presented in this thesis, dynamic characteristics of microgrids comprising different distributed generators are investigated. The importance of understanding the dynamic behaviour of microgrids is highlighted through a comparative analysis carried out on a hybrid microgrid. A simulation model of a hybrid microgrid comprising a PV system, a doubly-fed induction generator (DFIG) based wind power plant, a mini hydro power plant, and loads is developed for the analysis. This study revealed that the dynamic characteristics of the microgrid are significantly influenced by the characteristics of individual DERs and their control systems. It has been noted that during grid connected mode, features of the external grid also have an impact on microgrid behaviour.

The second phase of this thesis is focused on aggregated modelling of grid connected microgrids comprising both inverter interfaced and non-inverter interfaced DERs. For stability analysis, the common practice is to separate the power system into a study area of interest and external areas. In general, the study area is represented in a detailed manner while external areas are represented by dynamic equivalents. This thesis investigates the applicability of modal analysis as a tool for dynamic model equivalencing of grid connected hybrid microgrids while introducing a new index to identify the dominant modes of the system. The grid connected microgrid is represented as a single dynamic device while retaining the important

dynamics. Linearised models of different DERs with control systems and loads are developed for this study. Several case studies are carried out to validate the reduced order dynamic model of the microgrid by testing under different operating conditions. Furthermore, the model equivalencing is applied on microgrids in a multi-microgrid environment to validate the methodology.

Similar to the large generators in conventional power systems, grid connected microgrids have the potential to participate in energy markets to achieve technical, financial and environmental benefits. In order to enable such operation, a systematic approach in developing a capability tool for a grid connected microgrid is presented in the next phase of this thesis. A grid connected microgrid can be viewed as a single generator or a load depending on power import or export at the grid supply point. However, unlike in a single generator with simple machine limitations, active and reactive power transfer limits of a grid connected microgrid depend on many factors, including different and multiple machine capability limits, local load demands, and distribution line capacities. A mathematical model is developed to establish the active and reactive power transfer capability at the point of common coupling, considering all aspects of grid connected microgrids. Capability diagrams for different microgrid scenarios are derived using the mathematical model, and the applicability of microgrid capability diagram as a tool in the energy market operation is also presented.

The low voltage ride through (LVRT) capability of grid connected microgrids and the potential to provide voltage support as an ancillary service for the main grid are investigated in the final phase of the thesis. Two approaches are followed to investigate the LVRT capability of a microgrid as a single entity. In the first approach, dynamic voltage support at the microgrid point of common coupling is improved by using a distribution static synchronous compensator (DSTATCOM) connected to the low voltage side of the distribution transformer of the microgrid. The collective effect of the LVRT capabilities of the distributed generators in the microgrid is used to provide voltage and reactive power support to the external grid in the second

approach. Furthermore, operation of the DSTATCOM in multi-microgrid environment and islanded mode are also investigated under different operating conditions. Impact of the DSTATCOM location in the microgrid is also analysed by installing it at the low voltage side of the microgrid distribution transformer, at distributed generator terminals and at the bus bar with lowest reactive power margin. Variations of the microgrid system parameters during the fault and after fault clearance are analysed to identify the most appropriate location for DSTATCOM operation. It was identified that having the DSTATCOM at the low voltage side of the microgrid distribution transformer is far more beneficial in situations of microgrid transition from grid connected to islanded mode of operation, which would improve the microgrid voltage profile. DSTATCOM operation would reduce the reactive power demand from the external grid which arises due to faults in microgrids containing mains connected induction motor loads.

Based on the studies presented in this thesis, it can be identified that integration of multiple microgrids into the utility grid will allow the microgrids to provide ancillary services to the main grid during grid connected mode, and provide emergency services to adjacent microgrids during a utility grid outage. The work presented in this thesis provides the groundwork which will enable microgrids to perform such ancillary services.

Acknowledgements

I wish to express my sincere appreciation to many people who have helped me throughout my PhD candidature at the University of Wollongong.

I wish to thank my supervising team Dr Lasantha Meegahapola, Dr Duane Robinson and Professor Sarath Perera for the valuable guidance and encouragement given throughout my studies. I wish to particularly thank Professor Sarath Perera for providing me the opportunity to pursue postgraduate studies at the University of Wollongong and the support given throughout the study period in many ways.

The personal and administrative support provided by Jacqueline Adriaanse, Sasha Nikolic, Roslyn Causer-Temby, and all the Technical Staff of School of Electrical, Computer and Telecommunications Engineering, University of Wollongong are acknowledged with gratitude.

I would like to thank Dr Upuli Jayatunga, and my colleagues Brian Perera, Malithi Gunawardana, Amila Wickramasinghe, Dothinka Ranamuka and Kanchana Amarasekara for their support given during my stay in Wollongong.

Special thanks go to my uncle, Ananda Jayawardana and aunt Champa Jayawardana for supporting me in numerous ways during my candidature.

Last but not least, my heartiest gratitude goes to my parents, Upali Jayawardena and Malathie Fernando, my husband, Devinda Perera, my sister, Savidya and brother-in-law, Hirulak for their unconditional love and continuous support. Thank you so much for your endless love, encouragement, guidance and all the sacrifices you made on behalf of me to come this far. I would not have been able to complete this thesis without you.

List of Principal Symbols and Abbreviations

ADNC	active distribution network cell
ANN	artificial neural network
AVR	automatic voltage regulator
CCT	critical clearing time
CHP	combined heat and power
DER	distributed energy resources
DFIG	doubly-fed induction generator
DG	distributed generator
DNSP	distribution network service provider
DSL	DIgSILENT simulation language
DSTATCOM	distribution static synchronous compensator
GHG	greenhouse gas
GSP	grid supply point
HV	high voltage
HVDC	high voltage direct current
IM	induction motor
LV	low voltage
LVRT	low voltage ride through
MC	microsource controller
MCC	microgrid central controller
MG	microgrid
MHPP	mini-hydro power plant
MPPT	maximum power point tracking
MV	medium voltage
ODE	ordinary differential equation
PCC	point of common coupling
p.f.	power factor
PHEV	plug-in hybrid electric vehicle
PLL	phase locked loop
PMS	power management strategies
pu	per unit
PV	photovoltaic

ROCOF	rate of change of frequency
SCC	short circuit capacity
SG	synchronous generator
SMA	selective modal analysis
SME	synchronic model equivalencing
V2G	vehicle-to-grid
VR	voltage regulation
VSI	voltage source inverter
WTG	wind turbine generator
A	system matrix
α	exponent of the static load active power
β	exponent of the static load reactive power
C_{dc}	storage capacitance
C_{ir}	center of the circle defining DFIG rotor current limitation
C_{is}	center of the circle defining DFIG stator current limitation
$C_{o/p}$	output coefficient matrix
$D-Q$	dq axis of the global reference frame
δ_i	angle between the d-axis of the global reference frame and the d-axis of the local reference frame corresponding to the i^{th} dynamic device
Δi_{DGi}	variation of output current of the i^{th} DG
ΔI_{di}, ΔI_{qi}	variation of the dq axes currents of the i^{th} dynamic device in the local reference frame
ΔI_{Di}, ΔI_{Qi}	variation of the dq axes currents of the i^{th} dynamic device in the global reference frame
ΔI_{pcc}	variation of the current vector through the microgrid pcc
$\Delta\omega_i$	variation of angular frequency of the i^{th} local dq reference frame
Δv_{DGi}	variation of the terminal voltage of the i^{th} DG
ΔV_{di}, ΔV_{qi}	variation of the dq axes voltages of the i^{th} dynamic device in the local reference frame
ΔV_{Di}, ΔV_{Qi}	variation of the dq axes voltages of the i^{th} dynamic device in the global reference frame
ΔV_{pcc}	variation of the voltage vector at the microgrid pcc
Δx	variation of the state variables
Δy_{pcc}	variation of the output vector at the microgrid pcc

Δz	variation of the transformed state variable vector
$d_i - q_i$	local dq axis of the i^{th} dynamic device
E_{fd}	excitation voltage of the SG
f_{dq}	state variables in the local reference frame
f_{DQ}	state variables in the global reference frame
f_{max}	maximum switching frequency achieved using a hysteresis current controller
γ_{nr}	modes to be eliminated from the original model
γ_r	modes to be retained in the reduced model
H	inertia constant
I_{di}, I_{qi}	dq axes currents of the i^{th} dynamic device in the local reference frame
i_{fd}	excitation current of the SG
J	combined moment of inertia of generator and turbine
K_e	exciter gain of the AVR
K_f	feedback loop gain of the AVR
K_i	gain of the integral controller
K_p	gain of the proportional controller
K_{pll}	gain of the PLL
L	coupling inductance
Λ	diagonal matrix with the eigenvalues of the system matrix
λ_i	i^{th} eigenvalue
M_1, M_2	systems coefficient matrices of the equivalent microgrid model
N_1, N_2	output coefficient matrices of the equivalent microgrid model
ω_i	angular frequency of the i^{th} local dq reference frame
$P_{ext.grid}$	active power contribution from the external grid
P_{GSP}	active power flow throughout the microgrid GSP
P_{gi}	active power output from the DG at the i^{th} node
ϕ_m	m^{th} left eigenvector of the system matrix
ϕ_{ml}	l^{th} element of the left eigenvector ϕ_m
P_i	active power flow through the i^{th} node
P_{li}	active power demand of the load at the i^{th} node
P_{out}	active power output from DG
P_{ref}	reference of the active power controller
P_{tr}	active power flow through the transformer

Q_{gi}	reactive power output from the DG at the i^{th} node
Q_i	reactive power flow through the i^{th} node
Q_{li}	reactive power demand of the load at the i^{th} node
Q_{out}	reactive power output from DG
Q_{ref}	reference of the reactive power controller
Q_{tr}	reactive power flow through the transformer
r_{ir}	radius of the circle defining DFIG rotor current limitation
r_{is}	radius of the circle defining DFIG stator current limitation
R_p	permanent droop of the hydro-turbine governor
R_T	temporary droop of the hydro-turbine governor
s	slip of the induction machine
σ_i	real part of the i^{th} eigenvalue
$\sigma_{i-normalised}$	eigenvalue index
σ_{max}	real part of the eigenvalue located furthest away from the origin
$S_{nominal}$	rated apparent power
$\sum DG\,cost$	total cost of DG operation per hour
$\sum P_{DG}$	total active power supplied from the DGs
$\sum P_{loss}$	total active power loss in the microgrid
T	time period
T_e	exciter time constant
T_f	feedback loop time constant of the AVR
T_G	main servo time constant
θ_{ik}	phase angle of the line admittance between node i and node k
T_i	transformation matrix
T_{io}	transformation matrix with initial conditions
T_m	mechanical torque of the SG
T_p	pilot valve and servomotor time constant
T_r	voltage transducer time constant
T_R	reset time of the hydro turbine governor
T_w	water starting time
u	input variables
φ_i	i^{th} right eigenvector of the system matrix
φ_{lm}	l^{th} element of the right eigenvector φ_m
V_{dc}	maximum allowed voltage across the capacitor
V_{dcref}	reference dc voltage across the capacitor

V_{di}, V_{qi}	dq axes voltages of the i^{th} dynamic device in the local reference frame
V_m	maximum phase voltage
V_{ref}	voltage reference of the reactive power controller
x	state variables
X	reactance
$x_{o/p}$	sub vector of Δx comprising the original states contributing to the system output
$x_{no/p}$	sub vector of Δx comprising the original states with no contribution to the system output
y	output variables
Y_{ik}	element in the i^{th} row and k^{th} column of the network admittance matrix
Z_{ik}	magnitude of the line impedance between node i and node k
Z_m	magnetic impedance of the DFIG
z_{nr}	transformed states assumed to reach the steady state instantly
z_r	transformed states to be retained in the reduced model
Z_s	stator impedance of DFIG

Publications Arising from the Thesis

1. A.V. Jayawardena, L. Meegahapola, S. Perera and D. Robinson, Dynamic Characteristics of a Hybrid Microgrid with Inverter and Non-Inverter Interfaced Renewable Energy Sources: A Case Study, In *Proc. Int. Conf. Power System Technology (POWERCON 2012)*, Oct. 2012.

2. A. V. Jayawardena, L. G. Meegahapola, D. A. Robinson, and S. Perera, Capability Chart: A New Tool for Grid-tied Microgrid Operation, In *Proc. IEEE PES Transmission & Distribution Conference and Exposition*, April, 2014.

3. A. V. Jayawardena, L. G. Meegahapola, D. A. Robinson, S. Perera, Microgrid capability diagram: A tool for optimal grid-tied operation, *Renewable Energy*, vol. 74, pp 497-504, Feb. 2015.

4. A. V. Jayawardena, L. G. Meegahapola, D. A. Robinson, and S. Perera, Representation of a Grid-tied Hybrid Microgrid as a Reduced Order Entity for Power System Studies, *International Journal of Electrical Power and Energy Systems*, vol. 73, pp 591-600, Dec. 2015.

Table of Contents

List of Figures

List of Tables

Chapter 1

Introduction

1.1 Statement of the Problem

Integration of distributed energy resources (DERs) into the electrical power distribution network has gathered momentum in the recent years due to policy directives on reduction in greenhouse gas emissions from electrical power generation. At the same time, increasing penetration of DERs has improved reliability and energy efficiency through localised generation, and has evaded the requirement for transmission network expansion [1, 2].

Modern and future electricity distribution networks will comprise of increasing penetration of distributed generators (DGs) (including wind turbines, photovoltaic (PV) systems, fuel cells, small scale hydro generators, micro-turbines and other cogeneration plants) and energy storage devices (batteries, super capacitors and flywheels) [3]. These technologies combined with associated loads have transformed distribution networks from passive to active networks with bidirectional power flows, thereby introducing the concept of microgrids. Microgrids are capable of operating in grid connected and islanded modes where decision making and control architecture are different from conventional interconnected distribution systems [3–7]. Considering the present status of knowledge and experience related to microgrids, there are several areas in which new knowledge needs to be developed to ensure their

successful integration and operation, which is the main focus of this thesis. These areas will be briefly introduced in the subsequent paragraphs.

Dynamic characteristics of microgrids can be different from conventional grids, which are typically based on centralised synchronous generators (SGs) [3]. With the expanding number and size of microgrids, associated technical challenges such as (a) dynamic stability issues, (b) protection coordination, and (c) power quality and reliability issues will increase [2]. Out of these, dynamic stability issues arising due to systems with simultaneously present inverter and non-inverter interfaced DERs have received very little attention. Different inherent characteristics of DERs, power dispatch levels, relative DER capacities, and external grid characteristics are some of the important features of significant interest in relation to microgrid dynamic behaviour. Furthermore, comprehensive transient and small-signal stability assessment is considered as a significant technical challenge associated with future microgrids.

Microgrids comprising multiple DERs are being increasingly considered for integration into electricity networks. Considering the potential multiplicity of DERs in a single location and distributed nature of such entities, it is impractical to represent them as detailed models in power system simulations. This has led to a need for new and accurate, but simplified models of grid connected microgrids. Such simplified models of microgrids will be useful to electricity utilities in performing dynamic studies by representing grid connected microgrids as simplified generators or load units depending on their power export and import nature at the grid supply point.

Similar to conventional generators, grid connected microgrids have the potential to be able to participate in the energy market in the future to achieve technical, financial and environmental benefits. Effective participation in the energy markets requires a comprehensive understanding of the full capability of the microgrid. Therefore, it is essential to develop a planning tool to establish individual and combined microgrid capability. Active and reactive power exchange capability of a grid

connected microgrid with the utility grid is one of the important features that needs to be known by either the microgrid controller or the distribution network service provider (DNSP) in order to successfully participate in the future energy market. Hence, the development of an active and reactive power capability diagram of a grid connected microgrid will further facilitate DNSPs and microgrid controllers in market operation.

Integration of multiple microgrids into the utility grid will allow microgrids to provide ancillary services to the utility during normal operation. Such microgrids can also provide emergency services to adjacent microgrids during a utility grid outage.

When DER penetration is large, disconnecting DERs during a low voltage event is no longer acceptable as DERs are expected to support the grid for stabilising the voltage. Keeping relevant DERs online will assist in avoiding sudden loss of active power, which can lead to power system collapse. The capability of microgrids to ride through low voltages due to disturbances in the utility grid has not been thoroughly investigated. Thus, it is important to analyse the overall low voltage ride through (LVRT) capability of a grid connected microgrid as a single entity. LVRT capability enables the microgrid to provide network support to the external grid during external faults by supplying reactive power and maintaining the voltage at the microgrid point of common coupling (PCC).

1.2 Research Objectives and Methodology

This thesis examines the modelling of microgrids and investigates the ability of microgrids to provide network support to the utility grid through various ancillary services, which would make microgrids a more attractive solution to the issues associated with the evolving power system comprising new distributed generation technologies.

The first objective of this thesis is to investigate the dynamic characteristics

of a hybrid microgrid with inverter and non-inverter interfaced DERs. This is accomplished by developing a microgrid model comprising different DER models, and the impact of different inherent characteristics of the DERs, power dispatch levels, relative DER capacities. External grid characteristics on the microgrid dynamic behaviour are studied in detail.

Distribution network dynamics will become imperative when investigating the stability of power systems. Hence, systems can no longer be represented merely by a static load at the PCC. In particular, the dynamics of microgrids during grid connected mode must be taken into account in order to accurately characterise the stability of the network. Unlike traditional SGs and their auxiliary components, effects of grid connected microgrid dynamics on large power systems have yet to be completely characterised. Thus, the second objective of this thesis is to develop an aggregated model of a grid connected microgrid which would represent the aggregated load and generation at the PCC while retaining the important dynamics. For this purpose, the thesis takes an approach by investigating the applicability of modal analysis as a tool for model equivalencing of grid connected microgrids with inverter and non-inverter interfaced DERs. Validity of the reduced order dynamic equivalent is tested under different operating conditions with different load types and fault conditions.

Similar to the large generators in traditional power systems, future microgrids could participate in electricity markets as single entities to supply energy and other ancillary services to the network. In order to enable such operation, it is essential to develop a systematic approach for deriving a capability diagram for a grid connected microgrid representing the active and reactive power exchange capability of the microgrid with the main grid, which is the third objective of this thesis. This tool can be used to assist in understanding the microgrid active and reactive power capability while allowing the optimum operation of DERs, and will provide coordinated support to the network through ancillary services as required. Various features such as different load modelling aspects, individual machine limitations,

and effects of plug-in hybrid electric vehicles (PHEVs) and other reactive power devices are considered in developing the capability diagram.

As the fourth objective, this thesis investigates the LVRT capability of grid connected microgrids as an ancillary service provider to the utility grid. At present, some national grid codes have enforced wind turbine generators to maintain LVRT capability when connected to the transmission and distribution networks. In the context of microgrids, maintaining the connection between the utility and the microgrid is highly desirable except when the fault is between the substation and the microgrid. In such a situation, the separation is required as fast as possible leading to islanded operation of the microgrid. Faults outside the microgrid can create voltage sags at the microgrid PCC which may also cause problems to the DERs and sensitive loads inside the microgrid. In such situations, DERs within the microgrid will operate according to their inbuilt LVRT capabilities. Hence, this thesis investigates the overall impact of the LVRT capabilities of DERs at the microgrid PCC, and the capability of a grid connected microgrid to support the utility grid through external faults.

1.3 Outline of the Thesis

A brief summary of the contents of the remaining chapters of this thesis is given below:

Chapter 2 is a literature review covering the background information required to carry out the work presented in this thesis. This chapter presents an overview of the past developments in research work related to microgrid dynamic studies, microgrid model equivalencing and microgrid ancillary services.

Chapter 3 describes a case study on the dynamic behaviour of a hybrid microgrid comprising inverter and non-inverter interfaced DERs. The study examines the influence of the variations in active power dispatch levels and generator sizing on the dynamic characteristics of the microgrid. In addition, dynamic responses of

microgrids in grid connected and islanded modes are analysed. Impact of external grid characteristics on microgrid operation is also examined in this chapter.

Chapter 4 presents the detailed procedure for developing a small signal dynamic model of a grid connected microgrid comprising both inverter and non-inverter interfaced DERs.

The mathematical model developed in Chapter 4 is used as a tool in Chapter 5 for describing the microgrid model equivalencing approach using modal analysis. Validity of the reduced order dynamic equivalents are examined under different operating conditions. Furthermore, model equivalencing is applied on microgrids in a multi-microgrid environment to validate the methodology.

Chapter 6 presents a systematic approach for developing a capability diagram for a grid connected microgrid which represents the active and reactive power exchange capability of the microgrid with the main grid. The impact of different modelling aspects and network conditions are analysed using several case studies. Furthermore, operating points of the capability diagram are verified using time domain simulations. Applicability of capability diagrams as a graphical tool in the energy market operation is presented as a pathway and a solution to design microgrid participation into future ancillary services.

Chapter 7 investigates the low voltage ride through capability of a grid connected microgrid as a single entity. A distribution static synchronous compensator (DSTATCOM) is installed at different locations of the microgrid, and the voltage and reactive power support to the external grid is analysed. A grid connected microgrid is subjected to different operating conditions and the impact of DSTATCOM is investigated. Furthermore, DSTATCOM operation in a multi-microgrid environment and in islanded mode of operation are also investigated in this chapter.

Finally, Chapter 8 summarises the major contributions of this thesis and provides suggestions for future research work.

Chapter 2

Literature Review

2.1 Overview

This chapter presents a summary of the reviewed literature related to microgrids and their controls, past developments in research work related to microgrid dynamic studies, microgrid model equivalencing and low voltage ride through (LVRT) capability of distributed energy resources. The major contributions made by other researchers to the subject of microgrid studies are critically examined in order to identify the research gaps for further research.

2.2 Microgrids and Their Controls

2.2.1 Distributed Energy Resources and Microgrids

According to the definition given in [8], distributed generation (DG) is an electric energy source directly connected to the distribution network or on the customer side of the meter. DG technologies typically include wind turbines, solar photovoltaic (PV) systems, fuel cells, small hydro, microturbines and other cogeneration plants. These DGs along with distributed storage systems such as batteries, super capacitors and flywheels [4, 5] have formed the concept of distributed energy resources (DERs) which are usually connected to the medium voltage (MV) or low voltage (LV) grid

within the distribution system. DERs are being increasingly integrated as a means of power supply into the distribution system as opposed to reliance on bulk supply points from traditional centralised power plants. Environmental factors such as limiting the greenhouse gas (GHG) emissions and avoiding the investments of new transmission networks and large generating plants have been the primary motives behind the growth of DERs.

DERs have begun to feature active characteristics in the distribution networks with bidirectional power flows, converting the passive networks into active distribution networks. This has led to the concept of a microgrid, which may comprise part of the MV/LV distribution system including local loads and single or multiple DERs [1, 3, 4, 6, 9–12]. A microgrid is connected to the utility grid through the point of common coupling (PCC), and must be capable of operating in grid connected mode and at least serve a portion of the local load after being disconnected (islanded) from the utility grid [3, 13, 14]. From the customer point of view, microgrids provide both electricity and thermal needs, and have also increased reliability and improved energy efficiency through localised generation and demand side management [1,2,6,12]. Microgrids are capable of providing network support to the utility grid by using local DERs. Some of the ancillary services that can be provided by the microgrids include: frequency and voltage control, congestion management, reduction of grid losses and distribution system service restoration.

The ownership of a microgrid heavily influences the ultimate configuration and operation of the microgrid, resulting in different operational objectives. Microgrids owned by private industrial and commercial organisations have primarily focused on economical and reliable power supply. Microgrids based on government organisations, such as military based microgrids, have a strong focus on energy reliability and safety. These microgrids try to improve the economic aspect by operating in parallel to the utility grid. Electric utility companies attempt to ensure service quality across the distribution system and microgrids [6, 9, 15].

2.2.2 Microgrid Controls

DERs can be divided into two groups in terms of their interfacing mechanism with the microgrid. One group includes rotating machines that are directly coupled to the microgrid, while others are coupled through power electronic interfaces. Therefore, the control concepts and power management strategies used in a microgrid comprising both inverter and non-inverter interfaced DERs are significantly different from those of a conventional power system. Different hierarchical control strategies are adopted at different network levels in order to achieve better coordination among the DERs and the local loads. The control strategies must allow the microgrids to operate in islanded mode due to faults or any other large disturbances in the external grid. In grid connected mode, microgrids may export/import active and reactive power to/from the utility grid depending on their primary objective.

According to [6], microgrids can be operated in either centralised or decentralised manner depending on the responsibilities assumed by the different control levels. In centralised control, the microgrid central controller (MCC), which is the main interface between the microgrid and the distribution network service provider (DNSP), has the main responsibility to optimise the microgrid operation [3, 16]. In a decentralised control approach, DERs are controlled and optimised locally by the microsource controllers (MCs) that are responsible for individual DERs [17, 18].

A hierarchical control of microgrids have been proposed recently to standardise microgrid operation [11, 19]. As illustrated in Fig. 2.1 [11], at the bottom level, a primary controller is responsible for protection functions, local voltage control and power sharing management among multiple DERs to ensure system reliability. At the next level, the secondary controller restores microgrid frequency and voltage either by communicating with the MCC in a centralised manner or by using multi-agent systems in a decentralised manner [18]. The tertiary controller at the top level carries out the economic optimisation based on the energy prices and market operation. Furthermore, the tertiary controller can communicate with the DNSP in order

to optimise microgrid operation with the utility grid. In order to carry out successful operation of microgrids, it is vital to have a proper communication methodology. Communication in microgrids is being carried out based on radio communication, through telephone lines, power-line carrier or using a wireless medium (internet and global system for mobile communication) [11].

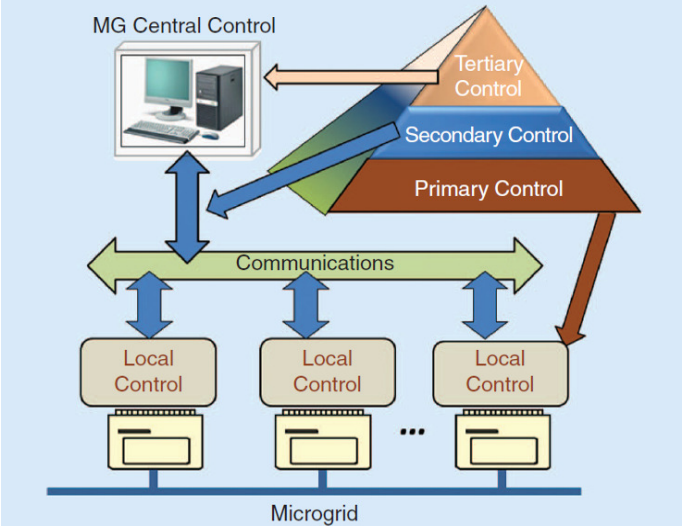

Figure 2.1: Microgrid control levels [11]

2.2.3 Microgrid Test Systems

In this section, a review of the major microgrid test facilities available in North America, Europe, and Asia are presented.

The Smart Grid R & D department of the U.S. Department of Energy (DOE) has carried out projects on dynamic optimisation of distribution grid operations through integration of advanced sensing, communication, and control technologies [20]. The two major R & D and demonstration programs currently active in the USA are: (a) The SPIDERS (Smart Power Infrastructure Demonstration for Energy Reliability and Security) demonstration program which is co-run by the DOE, Department of Defense and Department of Homeland Security, and (b) the Renewable and Distributed Systems Integration (RDSI) microgrid grants program run by the DOE [6]. The goal of the SPIDERS program is to address energy security and reliability

concerns while the RDSI program is primarily focused on increasing the use of distributed energy during peak demand periods to prove the value of microgrids for utility load shedding.

In summary, the key developments in European microgrid projects are: development of the MCC and other controllers to support frequency and voltage droops, development of demand side management functions, and investigation of suitability of power-line communication as an infrastructure component for microgrids [21]. The "More Microgrids" project has focused on standardisation of technical and commercial protocols, development of alternative microgrid control strategies and network topologies based on multiple microgrids [22]. Two large research projects led by the National Technical University of Athens (NTUA), Greece have investigated the technical feasibility of implementing large penetration of renewable generations as microgrids, developed new control methodologies, and evaluated microgrids as reliable and efficient means of electricity supply [4, 13].

The New Energy and Industrial Technology Development Organisation (NEDO) is the largest public R & D management organisation in Japan for promoting the development of advanced industrial, environmental, new energy and energy conservation technologies. One of the important objectives of projects under NEDO is to solve problems that arise due to the connection of distributed renewable resources with power grids [6].

Table 2.1 summarises some large scale microgrid facilities available in Europe, North America, and Asia. However, apart from these projects, there are many small scale pilot projects, field demonstrations and recently, many universities have initiated developing microgrids based on their campuses [6, 12].

Table 2.1: Major microgrid test facilities available in Europe, North America, and Asia

Test facility		Description
Europe	Bronsbergen holiday park, Netherlands	Comprises of 108 roof top PV systems with a peak power of 315 kW each and has two battery banks [23].
	Kythnos microgrid, Netherlands	A single phase network comprised of a 5 kW diesel generator, two PV systems (10 kW, 2 kW), and two battery banks [24, 25].
	CESI RICERCA DER microgrid, Italy	A dc microgrid connected to a 23 kV network. Microgrid consists of PV systems, CHP systems, wind turbines, battery banks, and fly wheels [24, 25].
	Am Steinweg estate, Germany	An LV network with a CHP plant of 28 kW, a 35 kW PV system and a lead acid battery bank. The system is operated using the power flow and power quality management system [24].
	Wallstadt district of Mannheim, Germany	The LV system is a typical residential area with an inter-meshed ring grid structure. The site includes several privately owned small photovoltaic systems and one private cogeneration unit [6]. The project has tested seamless transition between grid connected and islanded mode, and has installed software agents responsible for the management of loads and DERs.
Japan	Aomori microgrid, Hachinohe	PV systems and small wind turbines (total capacity of 100 kW), three 170 kW gas engines and 100 kW battery storage are connected to a sewage treatment plant, four schools, and three city offices. Research activities have been conducted on power quality, reduction in GHG emission and cost effectiveness [4, 26].
	Aichi microgrid, Central Japan airport	Demonstration project with a power supply comprising of various fuel cell systems (total of 1395 kW), PV systems (330 kW), and battery storage [4, 26].
	Kyoto microgrid, Kyotango	Virtual microgrid as each DER and corresponding demand site is connected through a control system. Gas engines with a total capacity of 400 kW, a 250 kW fuel cell system, a 60 kW PV system, a 50 kW wind turbine, and a battery storage unit are included. Supply and demand management is carried out using remote monitoring and control [4, 26].
	Sendai microgrid	Consists of gas generators (2 x 350 kW), a fuel cell system (250 kW), a PV system (50 kW), and battery storage with various compensating devices. Project targets are to achieve multiple power quality and reliability levels, and to compare the financial feasibility of those approaches with conventional uninterrupted power supply systems (UPS) [4, 27].

	Test facility	Description
USA	CERTS microgrid, Ohio	Three diesel generators of 60 kW and three storage devices, a static switch, three feeders with loads. Provides plug-and-play operation for DERs, uses waste heat, and enhance robustness and reliability of the electricity supply [7, 28].
	Santa Rita Jail-CERTS Microgrid Demonstration	The microgrid comprises of a 1 MW fuel cell, 1.2 MW PV system, two 1.2 MW diesel generators, a 2 MW / 4 MWh storage system, a fast static switch, and a power factor correcting capacitor bank [6, 29].
	Borrego Springs Microgrid, San Diego	The total installed capacity of 4 MW with two 1.8 MW diesel generators, a large 500 kW/1500 kWh battery, three smaller 50 kWh batteries, six 4 kW/8 kWh home energy storage units, about 700 kW of rooftop PV and 125 residential home area network systems [6].
	University of Wisconsin, Madison	The CERTS microgrid concept has been implemented here including two sources, five sets of 3-phase loads and a static switch to allow connection to the grid [5].
	The Fort Collins Microgrid, Colorado	Technologies in the project include PV systems, CHP, microturbines, fuel cells, plug-in hybrid electric vehicles, thermal storage, load shedding and demand-side management possibilities [6]. The main goals are to develop a coordinated system of mixed DERs for the city and reduce peak loads by 20-30%.
	Illinois Institute of Technology, Chicago	On campus DERs include roof-top PV panels, wind generation units, large scale battery systems, and charging station for electric vehicles. The peak load of the campus is around 10 MW and the full islanding capability had been tested [6].
	Allegheny Power, West Virginia	The microgrid includes 160 kW of natural gas internal combustion engine generators, 40 kW of PV system and an energy storage capable of providing about 24 kW for a two-hour period while loads include two commercial buildings with a demand around 200 kW [6].
	UCSD Project, San Diego	The microgrid consists of two 13.5 MW gas turbines, a 3 MW steam turbine and a 1.2 MW PV system which provides 85% of campus electricity needs, 95% of its heating and 95% of its cooling [6].
	Maxwell Air Force Base Alabama	This is a military microgrid project which includes two 600 kW diesel backup generator sets and a new CERTS-based 100 kW generator set [6].

Test facility		Description
USA	University of Nevada, Las Vegas	This project includes rooftop PV systems in 185 houses and the goal is to reduce the peak electricity demand by 65% [6].
	Mad River, Waitsfield, Vermont	Comprises of commercial, industrial and residential loads with PV systems and microturbines as DERs [25].
Canada	The BC Hydro Boston Bar system	A 69/25 kV substation connected to three radial feeders and two 4.32 MW run-of-river type hydro units. This has contributed to the development of microgrid islanding, resynchronisation and black start capability [4, 25].
	Hydro-Quebec (HQ)	Total load of 15 MW is connected to a 125 kV line and a 31 MW thermal power plant. This has improved power supply reliability on rural feeders [4].
	Ramea microgrid project	Comprises of a diesel power plant (3 x 925 kW units) and a wind power plant (390 kW), with a system peak load of 1.2 MW [4, 25].
	Fortis-Alberta microgrid	Consists of a 3.8 MW wind generation and a hydro generation of 3 MW in a 25 kV distribution network [4, 25].This is not allowed to operate in islanded mode.
China	Dongao Island, Zhuhai City	Comprises of a 1000 kW PV system, a 50 KW wind generation, a 1220 kW diesel generator and a 2000 kVAh battery bank. The microgrid has a control unit with a bidirectional inverter and a monitoring unit equipped with GPRS wireless communication devices [6].
	Nanji Island, Zhejiang	The stand-alone microgrid consists of 10, 100 kW wind generators, 545 kW of PV, 30 kW of marine power generation, 300 kW of storage batteries and a 1600 kW standby diesel generator. The project will also replace all internal combustion engine vehicles on the island with electric vehicles (EV) [6].
	Dongfushan Island Zhejiang, Eastern Fushan	The microgrid uses hybrid ac and dc bus bars, and comprises of seven 30 kW wind turbines, a 100 kW PV system, a set of seawater desalination system, and batteries. The operating strategy aims to maximise the use of renewable energy. At present, it is the largest off-grid operating microgrid system in China [6].

2.3 Dynamics of Microgrids

Unlike in traditional power systems with passive distribution networks, dynamics associated with active distribution networks comprising microgrids can be significantly different due to the combination of power electronic interfaced DERs and directly coupled rotating machines. Furthermore, stability problems initiated in every microgrid may be completely different to each other. The effectiveness of the stability improvement methods vary depending on the application and the system operating conditions [30].

Stability of microgrids during islanded mode is investigated in [31–38]. Impact of different loading conditions and constant power load modelling on the stability of islanded microgrids are addressed in [31] and [32]. In [33], an active damping control with a virtual resistance is proposed to eliminate power instability, while in [34], efficiency of frequency control with an internal oscillator and regulation of island voltage with voltage feedback signal in voltage source converters is demonstrated during islanded mode.

The importance of having properly controlled inverter interfaced DGs is illustrated by the system studies carried out in [35] based on one SG and an inverter interfaced DG during and subsequent to islanding of a microgrid. Such controllers can minimise the adverse impacts due to planned and un-planned islanding of a microgrid. Through various simulation scenarios, it is identified that without fast control actions of inverter interfaced DGs, network disturbances can result in frequency and power oscillations in the microgrid.

In [36], dynamic performance of a microgrid during islanded and grid connected modes is improved by using DFIGs with voltage and frequency regulation capabilities. Dynamic studies are carried out considering a DFIG and a SG while operating them in constant power factor mode (closer to unity). The study suggested that post transient power and frequency oscillations in a microgrid could be damped by implementing a primary frequency control strategy in the DFIG.

Stability of an islanded microgrid comprising a directly coupled diesel generator and inverter interfaced DERs, and their control interactions are analysed in [37]. An eigenvalue analysis and time domain analysis are performed on the islanded microgrid model. According to the study, power-frequency droop of the inverter interfaced DERs does not have a significant impact on the system stability compared to the diesel generators.

A strategy to reduce oscillations during synchronisation is presented in [38] with investigations on interactions between non-inverter interfaced (based on diesel generators) and inverter interfaced DGs in an islanded microgrid. According to the results, frequency and active power oscillations are less for the inverter interfaced DERs compared to non-inverter interfaced DERs. Voltage angle based droop control strategy is proposed for inverter interfaced DERs to reduce the frequency oscillations in the microgrid. The transient behaviour of DGs in the microgrid is investigated during the DG synchronisation and load changes. Power sharing strategies based on frequency and voltage droop are implemented in DGs to improve the smooth synchronisation and dynamic power sharing, resulting in less transient oscillations in the microgrid.

Small signal stability analysis on an islanded microgrid is carried out in [39–41]. A systematic approach for small signal modelling of inverter based islanded microgrid is presented in [39]. According to the study, grid connected microgrid dynamics are determined mainly by the utility grid due to the relatively insignificant capacity of the DERs. However, in islanded mode, local DERs mainly determine the dynamic behaviour of the microgrid. During sudden load transients, DERs located near the load respond quickly depending on the effective impedance seen by the PCC of the load. Due to the significant resistance present in the distribution network, considerable reactive power exchange between the inverters for an active power variation has been observed. This is compensated to some extent by increasing the droop in the voltage controllers. In [40], small signal stability studies are undertaken using time domain simulations on an islanded microgrid comprising wind turbine generators,

a PV system, a diesel generator, fuel cells, a battery storage system and a flywheel system. Simplified first order transfer models are used to represent the DERs while power losses and controllers are ignored in the case studies.

Investigations on power management strategies (PMS) for an islanded microgrid based on active and reactive power control methods are presented in [41]. Three reactive power control strategies are proposed based on: (a) voltage droop characteristics, (b) voltage regulation, and (c) load reactive power compensation. A real power control strategy is developed based on droop characteristics, and a complimentary frequency restoration method. A microgrid model with two inverter interfaced DERs and a single SG in a MV distribution network is developed to investigate small signal dynamics of a linearised microgrid model. Eigenvalue analysis is carried out on two scenarios based on the PMSs. The study has identified that the small signal stability margin increases when real power is mainly supplied by inverter interfaced DERs. However, analysis of system oscillatory modes has revealed that mechanical oscillatory modes of the conventional generator have a strong influence on the dynamic behaviour of the microgrid. Furthermore, these oscillatory modes do not depend on the PMS implemented in the microgrid. According to the study, voltage regulation or reactive power compensation is more suitable as the reactive power management strategy for DERs located closer to each other.

The studies indicate that microgrids can maintain the desired power quality, even for the sensitive loads during pre-planned islanding transitions [35]. Successful mode transfer requires islanding detection and subsequent change in control strategy of DERs units of the microgrid. Dynamic behaviour of a microgrid due to unplanned islanding mainly depends on the few factors: pre-planned operating conditions, type and location of the fault, islanding detection time, combination of DERs within the microgrid, and post fault switching actions of the system. Smooth islanding with state feedback control and islanding stability characteristic are discussed in [42]. A seamless transfer from grid connected mode to islanded mode is achieved by switching the control strategy of the DGs from state feedback to voltage control strategy.

In [30], different stability improvement methods for microgrids such as reactive power compensation with DSTATCOM, energy storage systems (flywheel), stabilisers with inverter interfaced DERs, and load shedding schemes are summarised.

Most of the studies have emphasised on the importance of including proper control strategies in DERs in order to achieve stable microgrid operation. Even though many studies have focused on islanded operation of microgrids, it is also important to investigate microgrid dynamic behaviour in grid connected mode with different DERs, and the effects of external grid on microgrid stability.

2.4 Model Equivalencing Techniques

In traditional power system dynamic studies, the distribution network has been represented by an equivalent load model [43]. However, with the increasing penetration of DERs, system dynamics introduced at both MV and LV levels have changed distribution networks from a passive form to an active form. Hence, such systems can no longer be represented merely by simple static loads. In particular, the dynamics of microgrids operating in grid connected mode must be taken into account in order to accurately characterise the dynamic and steady state stability of the network. As the microgrid paradigm is becoming popular, it is impractical to represent them as detailed models in power system simulations. It will be attractive for electricity utilities to employ equivalent models of microgrids in dynamic studies by representing grid connected microgrids as simplified units at the PCC.

It is necessary to assess the concepts behind the commonly used dynamic equivalencing techniques in order to identify their applicability in microgrids. For stability analysis, common practice is to separate the power system into a study area of interest and external areas. In general, the study area is represented in a detailed manner, while external areas are represented by dynamic equivalents [44–46]. These equivalent models can approximate the effects of the external systems on the study system. Three main approaches are reported in the literature on model equivalencing

techniques applied to power systems: (a) modal methods based on linearised models of the external systems, (b) coherency methods based on identifying coherent groups of generators, and (c) system identification methods based on measurement and simulation responses. These techniques will be elaborated in the next three subsections.

2.4.1 Modal Methods

For stability analysis, power systems can be modelled as a combination of differential and algebraic equations as given in (2.1).

$$\begin{aligned} \dot{x} &= f(x, u) \\ y &= g(x, u) \end{aligned} \tag{2.1}$$

where x, y and u are vectors of the state variables, outputs and inputs respectively. Linearisation of (2.1) around an equilibrium point will result in the form:

$$\begin{aligned} \Delta\dot{x} &= A\Delta x + B\Delta u \\ \Delta y &= C\Delta x + D\Delta u \end{aligned} \tag{2.2}$$

Modal methods are based on linearised systems which can be described by (2.2). Characteristics of the system stability are defined by the eigenvalues of the system matrix A. In model truncation method, reduction of a linearised system is carried out by removing the highly damped modes represented by eigenvalues far away from the origin and retaining less damped modes [45–49]. The relatively less damped modes will be present in the system response over a longer period which determines the overall response. In modal analysis, different model reduction techniques have been used to derive the equivalent external system.

In selective modal analysis (SMA), relevant dynamics of the model to be reduced are chosen through an iterative procedure without conducting a full eigenvalue analysis of the system [50, 51]. The iterative algorithm starts with an initial guess of an

eigenvalue and the corresponding right eigenvector, without conducting full eigen analysis of the system. SMA has been applied to systems with SGs where prior knowledge of state variables is available. If convergent, the algorithm converges to the retained eigenvalues and eigenvectors of the system matrix A. Convergence of the algorithm is verified using the participation matrix. This method has not been applied to systems with inverter interfaced generators, where a prior knowledge of the state variables giving rise to low frequency oscillations is not available. There will be some difficulty in deciding on the significant state variables in such systems.

Synchronic model equivalencing (SME) for developing structure preserving dynamic equivalents is presented in [52, 53]. A study area and external areas to be aggregated are identified using generalised slow coherency technique [54], which is applicable only to SGs. Each external area is represented by a detailed reference generator and less relevant generators are equivalenced similar to the SMA technique. The effect of each less relevant generator in the external area is represented by a dependent current source driven by the motion of the relevant generators.

In [55, 56], model reduction is carried out on a distribution system with integrated DERs, using Hankel-Norm approximation, focusing on the observability and controllability properties of the system. This methodology tries to achieve a compromise between a small worst case error and small energy error. The particular method cannot be applied to systems with very large dimensions and is not suitable for steady state applications [57]. Singular value perturbation theory is applied to a large wind park model in [58] to obtain a reduced order model. This technique decomposes the system into fast and slow dynamics. The system is reduced by first neglecting the fast dynamics and reinforcing their effects into the reduced model through boundary layer corrections calculated in different time scales [57].

Modal methods can be used in microgrids comprising inverter and non-inverter interfaced DERs in order to decouple the fast and slow dynamics. Due to the strong mathematical base, it is interesting to investigate the applicability of basic modal

analysis with further modifications or enhancements, as a tool for developing slow dynamics equivalent models for grid connected microgrids. However, care must be taken in applying modal methods for systems with inverter interfaced DERs, since their state variables are not well known as in the case of conventional SGs.

2.4.2 Coherency Methods

Coherency based methods are used to aggregate and reduce synchronous generators in an external system. The equivalencing process of coherency methods consists of three major steps: (a) coherency identification, (b) aggregation of coherent generators, and (c) reduction of generator bus bars and loads [59]. According to [60], a group of generating units is defined as a coherent group, if the particular group of generators oscillates with the same angular speed, and with generator terminal voltages in a constant complex ratio, for a given disturbance. Thus, generators in a coherent group can be attached to a common bus bar, if required through an ideal, complex ratio transformer. Reduced order models derived from coherency based methods have physical correspondence with the components of the power system. Coherency of generators is independent on the magnitude of the disturbance.

Most of the coherency identification techniques consider a linearised system model in state space form:

$$\dot{x} = Ax \tag{2.3}$$

In [61], the time domain response of (2.3) is solved for a specified fault in the power system, and the rotor angles of generators are compared. The generators with rotor angles swinging together are identified as coherent. In [62], coherency is determined by analysing the coupling of generators in the state matrix A. A group of generators is identified as coherent, if the coupling coefficients among them are high. A method based on the concept of slow oscillations originated by two groups of strongly coherent generators interconnected through weak ties is presented in [63] (Fig. 2.2). The work illustrates how two groups of oscillating generators are identified

using the eigenvectors associated with the mode of oscillation.

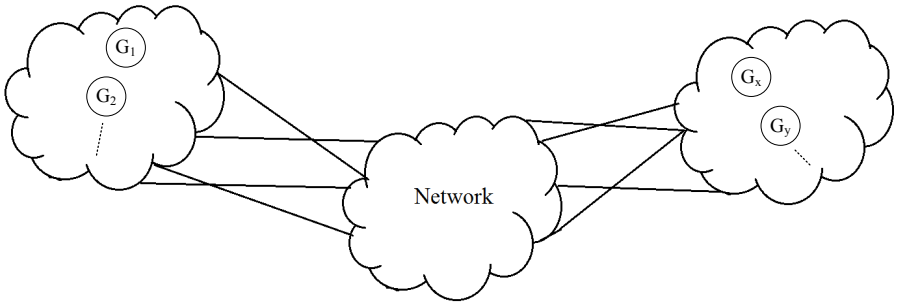

Figure 2.2: Coherency grouping of generators

In [64], a method which involves the calculation of distant measures to draw boundaries, and pattern recognition technique to identify coherent generators is suggested. Inertial and slow coherency based generator identification is presented in [54]. Many other coherency identification methods have been proposed using artificial neural networks [65], fuzzy sets [66], and Taylor series expansion [67]. Coherency identification techniques incorporating voltage dynamics as well as rotor dynamics in order to improve the accuracy of dynamic equivalents are proposed in [59].

Generators identified to be in a coherent group are aggregated in order to derive an equivalent generator model. In classical aggregation, the coherent generators are represented by an equivalent classical generator model. The equivalent inertia is taken as the sum of the inertia of all generators in the group, and the equivalent transient reactance is obtained by paralleling the transient reactances of all generators in the group [68]. A detailed aggregation is carried out if some or all the generators in a coherent group have similar control systems. The parameters of the equivalent models are obtained using two approaches: a least square fit of the frequency responses to determine the linear characteristics, and an evaluation of the time-domain constraints to set the nonlinear characteristics [68]. In [60], linear and non-linear parameters are considered separately for the aggregation. The parameters of the equivalent transfer function are tuned to match the aggregated transfer functions with a minimal error. Aggregation methods based on the preservation

of the structure of the coefficient matrices in the time domain representations are presented in [69–71]. The stability equivalents are developed based on the power invariance condition at the tie bus bars and at the generator internal bus bars of the coherent generators in [72], whereas, both modal analysis and coherency method are used in [73] for deriving dynamic equivalents of power systems.

Equivalencing of generators need to be followed by network reduction, which can be carried out by either eliminating or aggregating the remaining nodes and the transmission lines of the external system [74, 75]. In load elimination, loads are modelled as constant admittances and are eliminated using a Ward equivalent. Node elimination is carried out by making the injected currents at the boundary nodes equal to the currents on tie lines according to the equivalent Norton model.

In coherency recognition of synchronous generators, the electromechanical behaviour is analysed based on the generator rotor angle and speed, which makes these methods inapplicable to microgrids, as most of the DERs are electronically interfaced to the grid and are not characterised by rotor angle and speed (e.g. wind, PV systems, fuel cells, and battery banks).

2.4.3 System Identification and Simulation Based Methods

System identification techniques for model equivalencing are based on observations and measurements of the system to be modelled. The system identification process consists of four main steps: (a) generation of data, (b) selection of the model structure, (c) selection of identification method, and (d) model validation. However, the non-linear system identification based techniques are application dependent. After selecting a suitable model structure, the recorded data from especially designed system experiment is used to fit model parameters of the system with acceptable accuracy. The model parameters are adjusted with proper training algorithms. Depending on the prior knowledge of the system to be reduced, three different approaches are available: (a) black-box model [76–78], (b) white-box model, and (c)

grey-box model [79–82]. In a black-box model, the structure of the model is not known prior, and the input data is mapped to the output data so as to obtain the exact output from the equivalenced model. In white-box modelling, model parameters are identified from a known structure, and mathematical model of each physical component of the system is determined [80]. For systems with known structure but with unknown parameters, the grey-box model is used where the parameters are estimated in a similar way to those in the black-box model. Grey-box modelling is a combination of black-box modelling and white-box modelling. However, if the available prior knowledge is insufficient to build a model structure with well defined physical properties, standard models have to be used to fit in the available data. Care must be taken when the collected data set is divided between the training and validation data sets.

A black-box dynamic model of a MV microgrid is developed in [78] based on prony analysis and non-linear least-square optimisation. The proposed model is suitable only for a microgrid subjected to internal disturbances. The black-box approach is used in [76, 77], in deriving the dynamic equivalent of the distribution network, where the model is developed in the form of state space auto-regressive model with exogenous input. The equivalent model is highly dependent on the type and location of the disturbance. In [79,82], equivalent model of an active distribution network cell (ADNC) comprising an inverter interfaced generator and a composite load model connected in parallel is derived using a grey-box model. A grey-box technique is combined with an evolutionary particle swarm optimisation algorithm for parameter estimation of a microgrid in [80]. The microgrid model used in this study has focused on representing the microgrid slow dynamics, similar to the active power control found in diesel generators.

Artificial neural networks (ANN) are also used as a technique for deriving dynamic equivalents of distribution networks [83]. Parameters of the neural network dynamic equivalent model are selected using an appropriate training process. The complex voltages, power transfer, and injected currents during fault simulation are

used to prepare suitable patterns for ANN training. This work only considered fuel cells and microturbines as distributed generators in the network. In [84, 85], ANN has been used to develop measurement based dynamic equivalents for power systems.

Genetic algorithms which minimise the error index between measured output and the calculated output are used to estimate the parameters of the dynamic equivalent model in [86–88]. A dynamic equivalent model of a distribution network cell is developed based on prony analysis and non-linear least square optimisation in [89]. In [90], an equivalent model of the external system is estimated where the estimation algorithm uses an error function which is repeated until all equivalent parameters are identified.

Recently, studies have been conducted on aggregating wind farms into equivalent wind turbine generators (WTG) for dynamic studies [91, 92]. In the aggregation process, it has been assumed that all WTGs have the same wind incident or the average wind incident on an individual WTG. In another approach, wind turbines with similar wind speeds are aggregated separately and represented by an equivalent WTG [93, 94].

In system identification and simulation based model equivalencing methods, the model parameters need to be adjusted with proper training algorithms with a large amount of data sets, which is time consuming. Furthermore, these methods lack strong mathematical background compared to modal methods, and the estimated parameters do not properly interpret the physical relevance to the dynamic equivalent of power systems.

2.5 Capability Diagrams of Microgrids

2.5.1 Markt Operation of Microgrids

The microgrid paradigm has gained much interest in the electricity industry due to the increased penetration of DERs. A grid connected microgrid can be viewed as a single generator or a load depending on power export and import at the PCC. Many studies have been conducted focusing on optimising the power availability, optimising the generator utilisation and minimising operation costs within the distribution network while minimising power flow through the PCC [18, 95–101].

Currently, Demand Response (DR) is widely being used in distribution systems, which is considered as a demand management strategy to encourage end-user customers to use their appliances in response to changes in the price of electricity over time, or to give incentive payments designed to induce lower electricity use at times of high market prices or when grid reliability is threatened. This will allow customers to manage their power usage preferences in a way that will benefit not only themselves, but also the power grid [102–105].

Generally, it is challenging for a microgrid to match supply and demand due to several reasons. First, the power demand depends on external factors and varies dramatically, second, each energy user can have its own utility preference of energy usage at different time slots; third, due to the various types of power generation technologies the power generation cost will also vary as a function of time and weather factors, as an example, for a solar energy center, the power generation cost will be much cheaper in the day time than during the night time. Under a certain resource constraint, it is necessary to decide the amount of energy generation and consumption at each time so that the social welfare of the microgrid can be maximised.

An inter-connected network enables the surplus generation from one microgrid to be used to meet the local demand of its neighbourhood. According to traditional

power system economics, energy trade is always beneficial to both sides and thus should be encouraged. By trading with each other, each microgrid can make use of its comparative advantage and achieve an increase of social welfare [102–105].

A DR srategy can be deployed for several retail electricity meters, and some of the connected loads can be controlled for purposes of providing services to a bulk power system service. It is desirable to require fast, continuous monitoring of each large generator that is providing a large amount of an ancillary service so that its response is immediately visible to the system operator [106–109].

Demand Side Management requires utilities and customers to work cooperatively to reduce peak load, improve utilisation at off-peak hours, and hence it will improve system efficiency and reduce generation costs. From the utilities perspective, electricity market and system operation have to deal with the variability and uncertainty of large-scale wind and solar power generation in their generation scheduling. DR aims to reduce peak demand to reduce the risk of potential disturbances, avoiding additional capital investment for additional plants as well as avoiding the use of more expensive and less efficient generating plants. Another less common use of DR is to increase demand during periods of high supply and/or low demand to maintain the grid stability [110].

Although ancillary services have always been part of the electric industry, their relevance has been recognised after the introduction of competition in the electric industry, and have been considered as services that can be traded on a market. Authors in [111] provide a comparative analysis of different ancillary services markets, revising their technical and economic aspects, in order to offer a guide for their implementation.

In [112], the problems of market monitoring and control of ancillary services of future energy systems are presented. It is highlighted that the grid operators need to acquire ancillary services through competitive markets for control of the system operation. With the implementation of emerging smart metering technology, the spot price of energy can be send to the customer. For the provision of voltage

control, generators, synchronous condensers, capacitors and inductors, static VAR compensators and distributed generators can be utilised. An overview of markets for ancillary services, which are regulated and traded differently within and across borders in the Nordic countries is presented in [113]. However, distribution level was not considered in this study.

According to [114], in a deregulated electricity market, two types of services are provided; energy service and ancillary service. Energy service purchase electricity from generators while ancillary services have two types of payments: reserve and energy payments. In this study, an economic analysis is presented on the profitability of the battery storage operator taking part in both energy and ancillary markets.

The sustainability and reliability of microgrids in a regional power market in terms of multiple indices for the regional grid considering the North-western European electricity market is discussed in [115]. A model-based approach for estimating commercial building frequency regulation capability is presented in [116]. A model predictive control framework is proposed to determine optimal operating strategies in consideration of energy use, energy expense, peak demand, economic demand response revenue, and frequency regulation revenue. The methodology is demonstrated through simulation for medium office and large office building applications, highlighting its ability to merge revenue generating opportunities with traditional demand and cost reducing objectives.

In [117], two optimisation models are described to allocate three ancillary services among microgrid agents, namely, reactive power/voltage control, active power balancing and demand interruption. These models assume that microgrid agents participate in the day-ahead market sending their bids to the MCC that acts as an interface with the market operator. Once the market operator returns the economic dispatch of the microgrid agents, the MCC checks its technical feasibility and activates an adjustment market to change the initial schedule and to allocate these three ancillary services. In this method, the MCC will run an ac power flow to check for the technical feasibility once the economic generation dispatch schedule is received

from the market operator.

In [118], a proposal for an ancillary services market framework addressing voltage control in a multi-microgrid systems is presented. A reactive power market for MV distribution system is proposed involving DGs. In this methodology, each participant is given the opportunity to submit its bid to the reactive power market and the market settlement is performed using an Optimal Power Flow (OPF) solution in order to minimise the price of reactive power purchased by the Distribution System Operator (DSO). The proposed market is based on reactive power and runs daily after the scheduling of the generation units for a period of operation of one day.

Both [119] and [120] discuss about participation of DERs in ancillary markets such as reserve service and voltage control, and the regulatory issues such as electricity trading between a microgrid and the utility. Due to increased penetration of DERs, the bidirectional interaction between wholesale markets/transmission operation and retail markets/distribution operations has become a new paradigm. The expected generation surplus due to demand response strategy and DERs installed at distribution level has direct implications on the operation of the transmission system and the wholesale energy markets.

In [18], optimal resource allocation for minimising the operational costs within the microgrid is carried out by a MCC, and it is assumed that there is no limit to the power exchanged with the utility grid. Participation of microgrids in the open market is considered in [95], which enables microgrids to trade power with the utility grid. Along with demand side bidding, two market policies are considered for the participation of the microgrid in the energy market. In the first market policy, MCC aims to cater to the local load demand by harnessing the maximum power from local DERs while minimising the power export to the external grid. This allows the local consumers to gain benefits of the reduced operational costs. However, in the second market policy, the microgrid is allowed to exchange power with the external grid to maximise the revenue either by exporting excess power from DERs or by importing power from external sources. Furthermore, in demand

side bidding, consumers are given two options to bid for load shifting and load shedding. The total expenses include the compensations paid to the consumers for load shedding and for DERs for power curtailment. However, network security issues such as voltage limitations, thermal limitations and overloading of the connection with the external grid have not been considered in these studies. Furthermore, the DNSP or the distribution management system is unable to obtain the overall active and reactive power capabilities of the microgrid within the technical constraints for the considered time interval.

In [96], load demand of interconnected microgrids is managed by minimising the overall grid operational costs. In this concept, an MCC is responsible for the internal microgrid operational commands, while a global controller is introduced to coordinate multiple MCCs and the distribution network. This study is performed assuming that the demand of each microgrid is met by the internal DERs, and if required by the external resources including other microgrids and the main grid. From numerical analysis, it is suggested that the grid connected mode yields financial benefits compared to the islanded mode of operation in systems with interconnected microgrids.

2.5.2 Capability Diagrams of Microgrids

Allowing grid connected microgrids to participate in the energy and ancillary service markets while fulfilling the local energy demand will provide opportunities for additional revenue. However, considerable planning and understanding of the technical capabilities of a microgrid as an energy resource is required. In order to enable this operation and to make decisions in the market, MCCs and DNSPs must not only find the optimum operating conditions, but they must also be aware of the full active and reactive power exchange capability of the microgrid at the PCC. Furthermore, in a multi-microgrid environment where microgrids trade between themselves, capability diagrams of individual microgrids can be used as a tool for deciding the

maximum or optimal amount of power exchange.

Capability diagrams are considered essential system planning tools, and are widely used in power system operation. As illustrated in Fig. 2.3, the concept of a capability diagram is traditionally related to synchronous machines, and represents the area of permissible operation in terms of active and reactive power availability at the machine terminal [121, 122]. Recent research has been carried out on developing capability diagrams for DFIG based wind turbines [123, 124], grid connected PV units [125], generator-transformer units [126], combined cycle power plants [127], and for HVDC links [128]. A graphical method to determine the network limits of a wind farm is presented in [129]. The maximum allowable wind capacity which can be connected to a particular node without violating any network constraints is determined from the capability charts, where each operating constraint is represented as a loci in the complex power plane. For a multiple node system, the capability diagram is obtained by reducing the network into a two node system, and using Thevenin's equivalent for the system at the particular node of interest. However, practicability of this method reduces with the increasing size of the network.

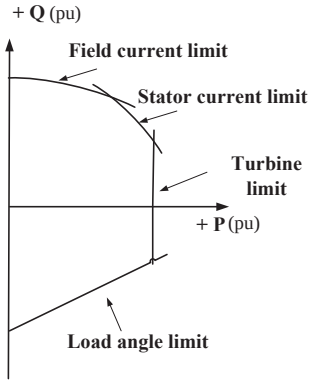

Figure 2.3: Active and reactive power capability diagram of a synchronous generator

The total load supply capability of a power system is modelled and represented as a capability diagram in [130] using an optimisation approach subjected to technical and operating constraints. The optimisation model is solved point by point for different total load angles in order to obtain the boundary of the capability diagram. However, in contrast to [130], for grid connected microgrids, it is necessary

to derive the capability diagram at the PCC. In [131], reactive power support from networks comprising only voltage controlling wind generators is analysed, where a P-Q capability diagram is derived without taking the local loads into account.

Deriving a diagram for the maximum power transfer capability of a grid connected microgrid is significantly different from individual DERs or wind farms, due to the complexity of the microgrid that arises as a result of the network configuration, network constraints and the combination of different DERs and loads.

2.6 Low Voltage Ride Through Capability of Microgrids

According to [132], voltage sags are short duration reductions in rms voltage, caused by network faults, sudden overloads and starting of large motors. The magnitude of voltage sag is determined mainly by factors such as: the distance to the fault, the cross section of the lines and cables, connection type of transformers between the location of fault and the recording point, type of the network (radial or meshed), and short-circuit impedance of the network.

When the penetration level of DERs in the system is high, and if DERs are set to be disconnected during relatively small voltage sags, disturbances or faults on the system could lead to a considerable generation deficit. However, such a scenario could be avoided if the DERs are kept online and allowed to ride through such events. Faults outside a microgrid can lead to voltage sags at the microgrid PCC which may cause problems to the DERs and sensitive loads inside the microgrid [133, 134]. In such situations, DERs within the microgrid will operate according to their inbuilt low voltage ride through (LVRT) capabilities [135–137] while providing active and reactive power support to the rest of the microgrid. The collective effect of LVRT capability of DERs will allow a microgrid to ride through low voltage events which arise due to disturbances at the utility grid as a single entity.

With the changing nature of generation mix at the distribution and sub transmission levels, many countries have adapted existing grid codes to ensure security of

power supply, reliability and power quality [138]. Fig. 2.4 illustrates a comparison of the LVRT requirements enforced by different national grid codes [139]. Fig. 2.5 (a) and Fig. 2.5 (b) illustrate the LVRT requirement enforced by the German grid code on synchronous and asynchronous type generating units respectively. Generators shall remain connected to the system (i.e. without tripping) when the system voltage measured at the high voltage (HV) terminal of the network transformer remains above the corresponding curve.

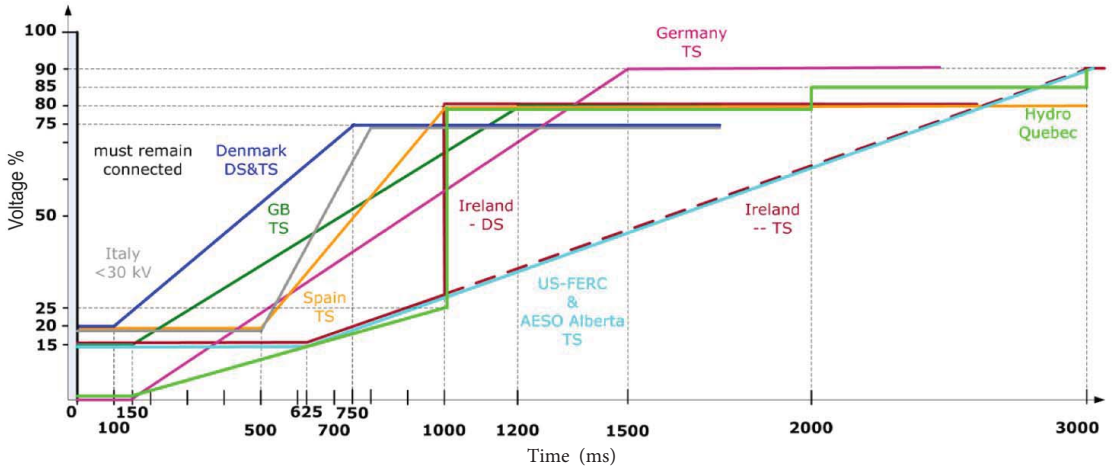

Figure 2.4: Low voltage ride through capability of WTGs in different national grid codes [120]

Initially, the LVRT capability was mainly aimed at wind turbines connected to high voltage network [140–143], and a considerable amount of research has been carried out on developing different control strategies for LVRT of wind farms [140–147]. According to some of the grid codes (e.g. German, Spanish, Great Britain and Irish grid codes), wind farms should provide reactive power to the network during and after faults in order to recover the network voltage in a similar way to the conventional synchronous generators [148]. Fig. 2.6 illustrates the voltage support required from the DERs during a grid fault [139]. However, due to the large penetration of WTGs at the distribution levels, grid codes are being modified so as to enforce LVRT capability from DERs connected to the medium and low voltage networks [144, 149–151].

Until recently, PV systems were not allowed to actively participate in grid sup-

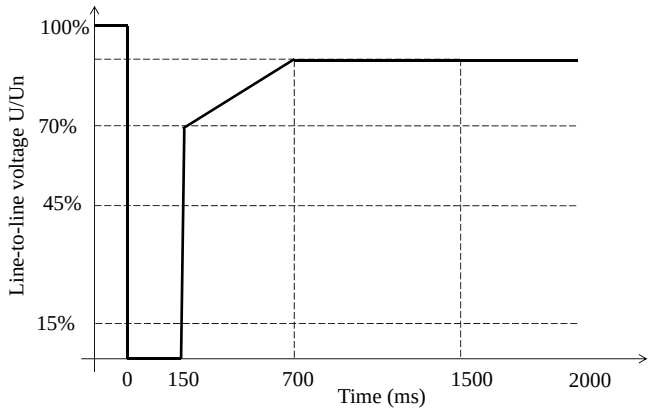

(a)

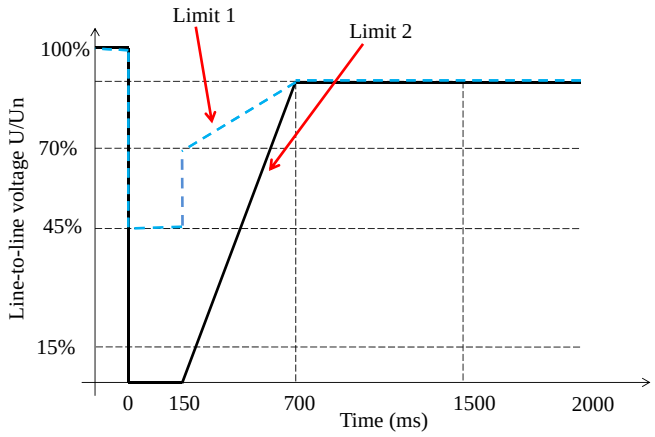

(b)

Figure 2.5: Voltage ride through requirement in Germany for (a) a synchronous generating plant and (b) an asynchronous generating plant during a fault occurrence in the grid [120]

port during systems faults and thus had to be disconnected from the grid. However, new grid codes (e.g. German and Spanish grid codes) are starting to enforce active network support regulations on large grid connected PV systems. Furthermore, recent research has also focused on LVRT capability of grid connected large scale PV systems [152–154]. With the increasing connection of small scale PV systems into the medium and low voltage systems, it is important that the PV systems adhere to the grid codes to improve system stability and power supply quality, similar to WTGs. Research work has been carried out in different parts of the world on various modelling and controlling strategies of grid connected PV systems capable of riding through low voltage levels [153–156]. Reactive power from the PV system should be injected depending on the voltage sag depth and the inverter current rating. At

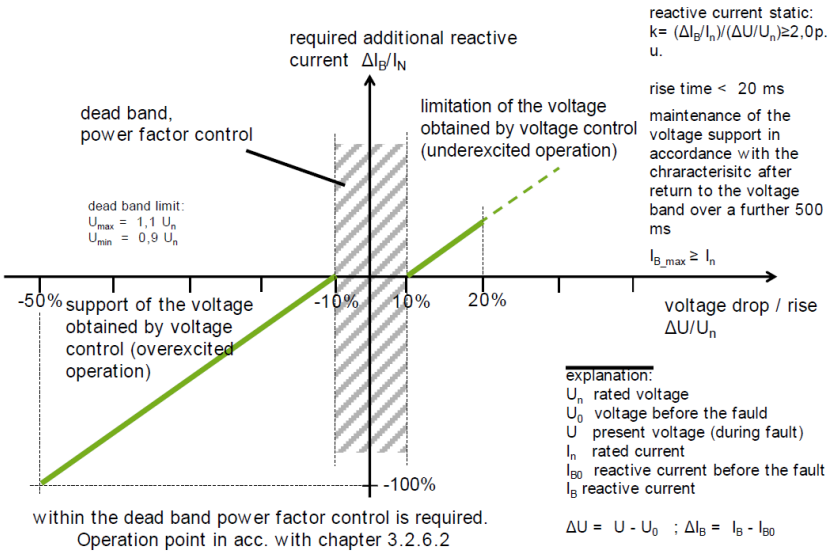

Figure 2.6: Voltage support in an event of grid fault [120]

the same time, the PV panels should switch to non-maximum power point tracking (MPPT) operation mode and be regulated according to the fault severity level in order to avoid tripping the inverter over-current protection.

Apart from WTGs and PV systems, research has been conducted on investigating the LVRT capability with regard to fuel cell generating systems (FCGS) while adhering to the new grid code requirements [151, 157, 158]. Backup energy storage devices such as battery banks, flywheels and capacitor banks can be installed in microgrids to provide ride through capabilities during system disturbances [10].

It is interesting to analyse the LVRT capability of a grid connected microgrid as a single entity. This will enable the microgrid to provide network support during external faults by providing reactive power and to maintain the voltage at the microgrid PCC. However, conflicts can be seen between the feeder protection and utility requirements for LVRT which are included in the grid codes of many countries with a large penetration levels of DERs [138]. The under-voltage protection is generally not coordinated with the LVRT requirement, resulting in tripping the under-voltage trip before the LVRT requirement is fulfilled. Table 2.2 presents typical voltage protection settings used at the distribution level in many countries [138].

Fig. 2.7 (a) and Fig. 2.7 (b) illustrate the overlapping of the under-voltage (dotted line) and LVRT characteristics in Finland and Germany respectively [138].

Table 2.2: Typical voltage protection settings used in many countries at distribution level (Un is the nominal voltage) [119]

Relay function	Threshold range	Time (s)
Under-voltage	<50%Un	<0.5
	50-80%Un	0.5-2
Over-voltage	>115%Un	0.1-1
	105-115%Un	1-30

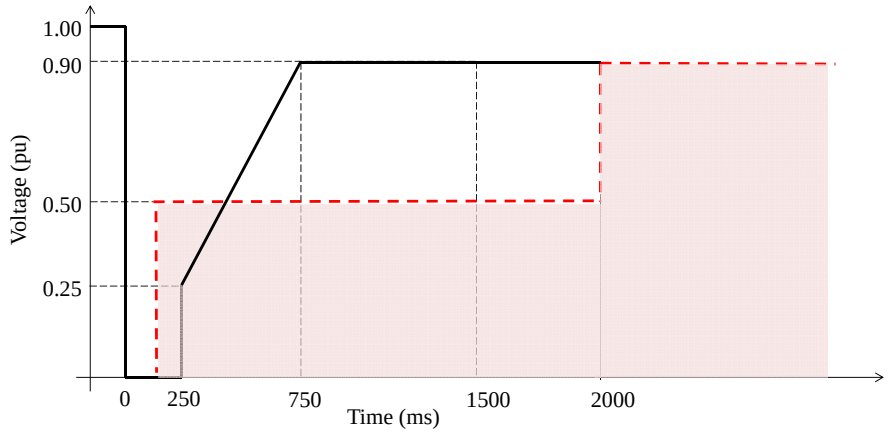

(a)

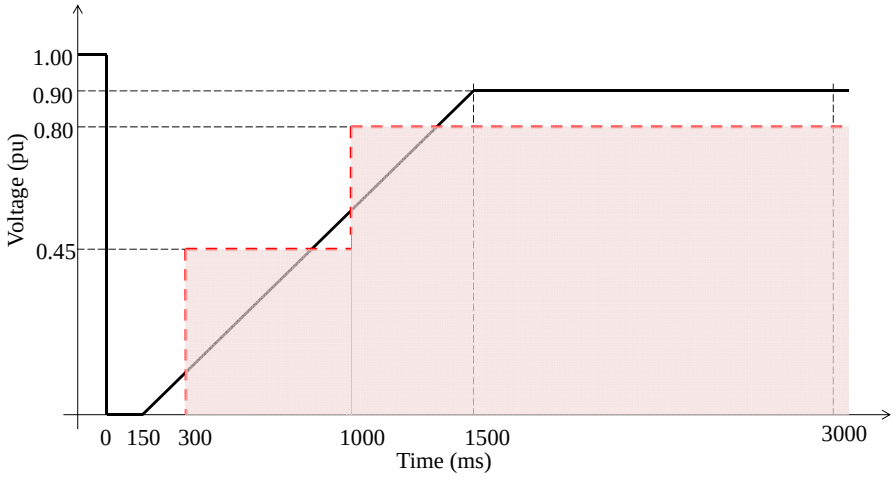

(b)

Figure 2.7: Under-voltage and LVRT coordination in (a) Finland and (b) Germany [119]

Furthermore, the capability to ride through faults must not affect the sensitivity of the microgrid islanding detection. Thus, there should be a coordination between the under-voltage protection relays, LVRT capability and other microgrid islanding

detection methods, such that these protection schemes are not activated before the LVRT requirement [159–161]. Hence, it is necessary to have a compromise between microgrid islanding and LVRT capability at the microgrid PCC.

2.7 Summary

This chapter summarised the existing knowledge in relation to microgrids and their controls, microgrid dynamic studies, microgrid model equivalencing and low voltage ride through capability of microgrids.

Main features of microgrid control strategies and the major microgrids test facilities operating around the world were summarised. In centralised control, the MCC has the main responsibility to optimise the microgrid operation which is the main interface between the microgrid and the distribution DNSP. In a decentralised control approach, DERs are controlled and optimised locally by the microsource controllers that are responsible for individual DERs. Most of the studies have emphasised on the importance of including proper control strategies in DERs in order to achieve stable microgrid operation. Even though many studies have focused on islanded operation of microgrids, it is also important to investigate microgrid dynamic behaviour in grid connected mode with different DERs, and to analyse the effects of external grid on microgrid stability.

Main model equivalencing techniques applied to power systems were outlined and their applicability to grid connected microgrids were discussed highlighting the merits and demerits of the different techniques. In coherency recognition of SGs, the electromechanical behaviour is analysed based on the generator rotor angle and speed, which make these methods infeasible for deriving dynamic equivalents to microgrids, as most of the DERs are electronically interfaced to the grid, and are not characterised by rotor angle and speed. System identification techniques for model equivalencing are based on observations and measurements of the system to be modelled. In system identification and simulation based model equivalencing

methods, the model parameters need to be adjusted with proper training algorithms with a large amount of data sets, which is time consuming. Furthermore, these methods lack strong mathematical background compared to modal methods, and the estimated parameters do not properly interpret the physical relevance to the dynamic equivalent of power systems.

The basic modal method has not been applied to grid connected hybrid microgrids as a means for deriving dynamic equivalent models. Thus, it is important to further develop an approach for investigating the applicability of modal analysis as a tool for dynamic model equivalencing of grid connected microgrids with inverter and non-inverter interfaced DERs.

The concept of capability diagram for grid connected microgrids was introduced while discussing the capability diagrams of individual DERs and other available approaches to determine the load supply capability of power systems. Similar to the large generators in traditional power systems, the future microgrids will be able to participate in electricity markets as single entities to supply energy and other ancillary services to the network. In order to enable such operation, it is essential to develop a systematic approach for deriving a capability diagram for a grid connected microgrid representing the active and reactive power exchange capability of the microgrid with the main grid. This tool can be used to assist in understanding the microgrid active and reactive power capability while allowing the optimum operation of DERs, and will provide coordinated support to the network through ancillary services as required.

A brief introduction to LVRT capability of different DERs was provided in this chapter. The LVRT requirements of different grid codes were discussed and the importance of the LVRT capability of grid connected microgrids was highlighted. As an ancillary service provider to the utility grid, it is important to analyse the overall capability of grid connected microgrid to support voltage and provide reactive power during and after disturbances.

Chapter 3

Preliminary Investigations on Dynamic Characteristics of a Hybrid Microgrid using Time Domain Simulations

3.1 Introduction

Comprehensive transient stability assessment is vital in understanding the behaviour of microgrids during grid disturbances. As emphasised in Chapter 2, a range of aspects such as different inherent characteristics of DERs, different power dispatch levels, generator capacities, and external grid characteristics will play prominent roles in successful design and operation of microgrids.

In this chapter, the importance of understanding the dynamic behaviour of microgrids is highlighted through a comparative analysis carried out on a hybrid microgrid containing a photovoltaic (PV) system, a doubly-fed induction generator (DFIG), and a synchronous generator (SG) based mini-hydro power plant (MHPP) developed in DIgSILENT PowerFactory.

On many occasions, generalised models of inverter interfaced DERs have been

used in dynamic stability studies [35, 37, 39, 41]. However, due to unique dynamic characteristics associated with DERs, it is important to represent DERs using detailed models for dynamic simulation. With the increasing penetration of different generation technologies in electricity networks as stated in Chapter 2, it is essential to consider different combinations of DERs in dynamic studies. In the literature, much interest has been given to islanded microgrids. Thus, this chapter mainly focuses on the importance of investigating microgrid dynamic behaviour in grid connected mode with different DERs, and analyses the influence of the external grid characteristics on microgrid stability. Understanding the dynamic characteristics of grid connected microgrids will be beneficial in developing aggregated models for microgrids. Furthermore, these studies will assist in understanding the capability of grid connected microgrids to provide ancillary services to the utility in the future.

Section 3.2 of the chapter presents the microgrid test model and the DER models developed in DIgSILENT PowerFactory. Analysis of microgrid dynamics due to different disturbances in the microgrid is presented in Section 3.3. Section 3.4 presents the influence of external grid characteristics on the grid connected microgrid followed by a summary in Section 3.5.

3.2 Modelling of Microgrid Test System

In order to characterise the dynamics of grid connected microgrids with different types of DERs, time domain simulations were carried out using a microgrid model developed in DIgSILENT PowerFactory. This section presents the modelling description of the microgrid test system and the DERs used for the study. The DERs were modelled using the DIgSILENT simulation language (DSL).

3.2.1 The Microgrid Test System

The IEEE-13 node test feeder [162] was used to analyse the dynamic behaviour of a microgrid with inverter and non-inverter based DERs. Fig. 3.1 illustrates the

single line diagram of the 4.16 kV microgrid model implemented in DIgSILENT PowerFactory for this dynamic study. Necessary modifications were made to the IEEE-13 node test feeder in order to establish a electrically balanced microgrid system. The total active and reactive power demands of the microgrid were 3.8 MW and 2.6 MVAr respectively. Two switched shunt capacitor banks were installed at Bus bar 611 and Bus bar 675 to provide the reactive power support to the microgrid. The microgrid voltage was maintained between 0.95 pu-1.05 pu at steady state, and the microgrid was connected to the external grid through a 115 kV/4.16 kV, 10 MVA transformer. Basic parameters of the microgrid are given in Table 3.1. Line lengths of the microgrid system are given in Appendix A. Three types of DERs namely: MHPP, DFIG and PV systems were considered in the study.

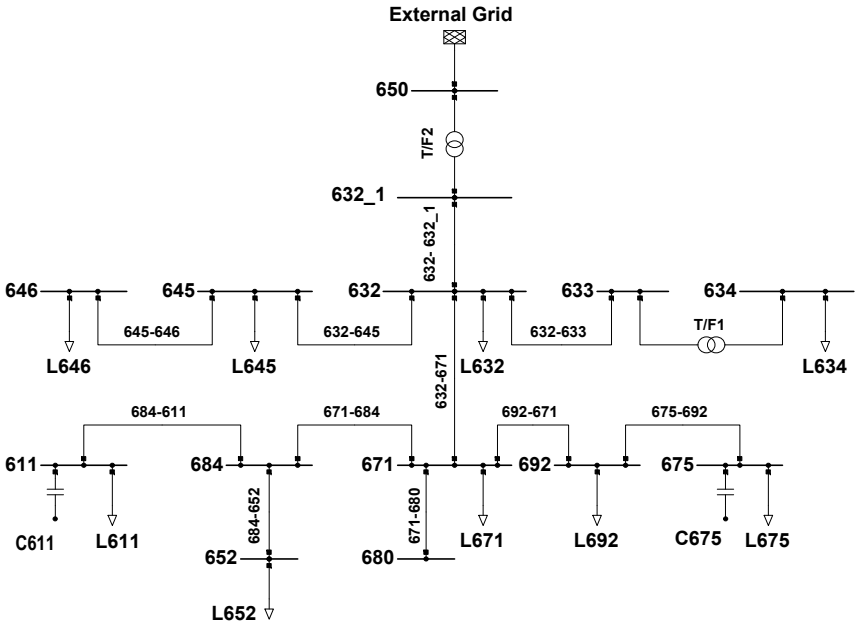

Figure 3.1: Single line diagram of the microgrid test system

Table 3.1: Microgrid parameters (50 Hz)

O/H Line parameters	(0.3+j0.3) Ω/km
Transformer 1 (T/F 1)	1 MVA, 4.16 kV/0.48 kV
Transformer 2 (T/F 2)	10 MVA, 115 kV/4.16 kV
Capacitor bank C 611	0.9 MVAr
Capacitor bank C 675	0.6 MVAr
External grid short circuit capacity	1000 MVA

3.2.2 Dynamic Models of the Distributed Energy Resources

Mini-hydro power plant

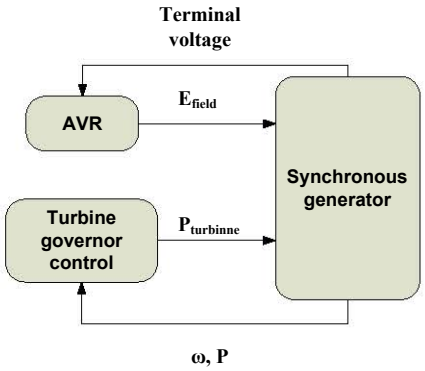

Figure 3.2: Simulation model of the MHPP

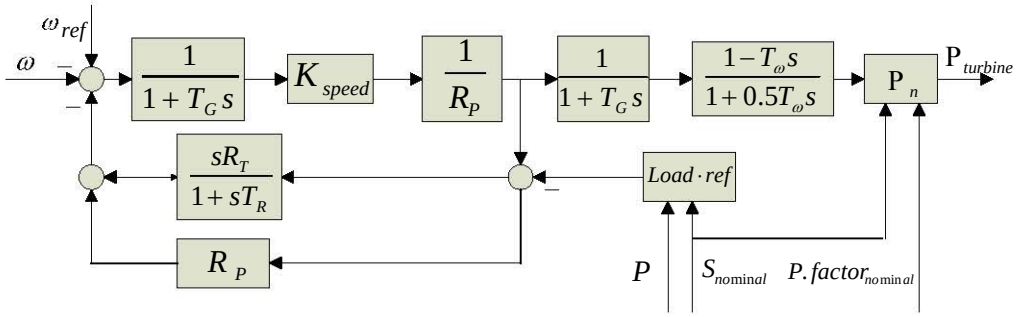

(a)

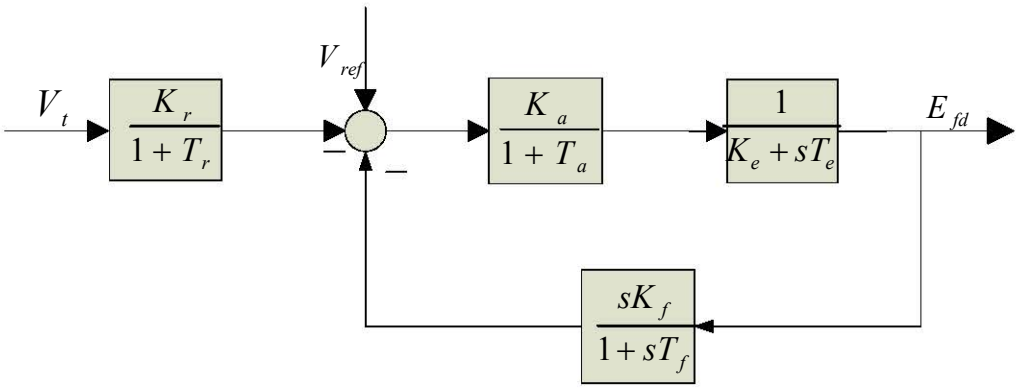

(b)

Figure 3.3: (a) Hydro turbine governor model and (b) AVR system

The plant model of the SG represents an MHPP as illuatrated in Fig. 3.2. The hydro turbine governor model [163] illustrated in Fig. 3.3 (a) was implemented, and included the characteristics of the permanent and transient droops, governor servo

motor, and hydro turbine. The IEEE type-AC1A excitation system [164] implemented in the MHPP is illustrated in Fig. 3.3 (b).

Doubly-fed induction generator (DFIG)

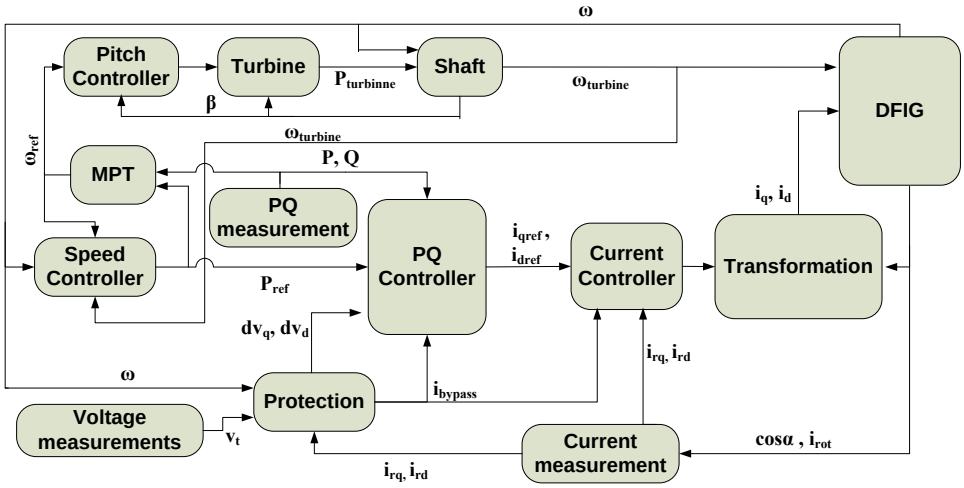

Figure 3.4: Simulation model of the DFIG

Fig. 3.4 illustrates the functional block diagram of DFIG simulation model developed in DIgSILENT PowerFactory [165]. The DFIG drive-train was represented as a two-mass model (i.e. turbine and generator inertia), and power dispatch of the DFIG was controlled by a P-Q (active and reactive) controller and a fast current controller. The current controller was comprised of a damping controller which could quickly dampen the power oscillations. The crowbar protection was employed to protect the rotor-side converter from large rotor current transients during faults. Wind speed was assumed to be constant during the time frame considered in the dynamic studies.

PV system

Fig. 3.5 illustrates the PV model developed in DIgSILENT PowerFactory. The PV system was operated at the constant power factor control mode, while the irradiance level and temperature were assumed to be constant during the time frame considered

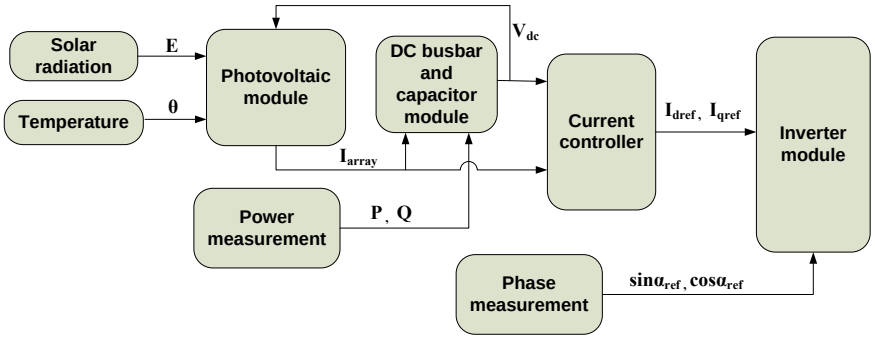

Figure 3.5: Simulation model of the PV system

in the dynamic studies. Current output from the PV module and from the dc link are fed into the current controller, which in turn generates the reference currents to the inverter module.

3.3 Microgrid Dynamics due to Disturbances

3.3.1 Microgrid Dynamics During Unplanned Islanding

Simulation scenarios were formulated to investigate the dynamics associated with unplanned islanding, and the influence of DER power rating, SG inertia constant (H) and combination of DERs on the transients of the microgrid. During grid connected mode, the microgrid generated 4 MW of active power while the two capacitor banks, the MHPP and the external grid provided the required reactive power support in order to cater for the load demand, and to maintain an acceptable voltage profile of the microgrid.

Different active power combinations between inverter interfaced (DFIG and PV) and non-inverter based (MHPP) DERs were analysed by adopting different apparent power ratings for the individual types. Generators were operated at their rated active power output levels, and the total active power generation of the microgrid was maintained at 4 MW to cater for the local power demand. Following four scenarios (1-4) were analysed while altering the active power contribution from each generator. In the first two scenarios, inertia constant of the SG was kept constant

for different generator ratings according to (3.1), where the stored kinetic energy varied with the SG rating. In the last two scenarios, the SG inertia constant was varied with the machine capacity in order to maintain the same stored kinetic energy in accordance with (3.1).

$$H = \frac{1/2J\omega^2}{S} \tag{3.1}$$

where, S is the generator rated apparent power, J is the machine inertia, and ω is the machine speed.

Both the DFIG and PV system were operated in unity power factor mode. During grid connected mode, frequency reference was taken from the external grid, while in islanded mode, the microgrid frequency was controlled by the MHPP. The MHPP operated in voltage control mode and 100% SG corresponds to the scenario where the MHPP operated at rated power output (4 MW). The DFIG and PV system were operated at unity power factor.

Scenario 1:

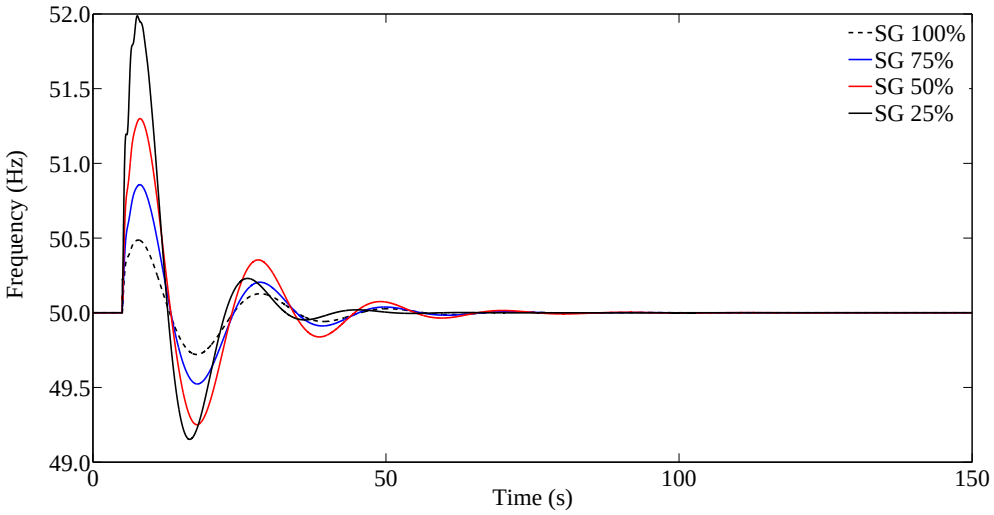

Figure 3.6: Power frequency variations of the microgrid due to unplanned islanding with different combinations of DFIG and MHPP

In this scenario, a MHPP and a DFIG were connected to Bus bars 646 and 680

respectively to supply the active power demand of the microgrid. Inertia constant of the SGs were kept constant and the microgrid system was isolated from the bulk supply point at $t = 5\,s$ to simulate a sudden unplanned islanding.

Scenario 2:

In order to observe the impact of DER type, the DFIG connected to the microgrid in Scenario 1 was replaced with a PV system having the same power rating. The microgrid system was isolated from the bulk supply point at $t = 5\,s$ to simulate a sudden unplanned islanding.

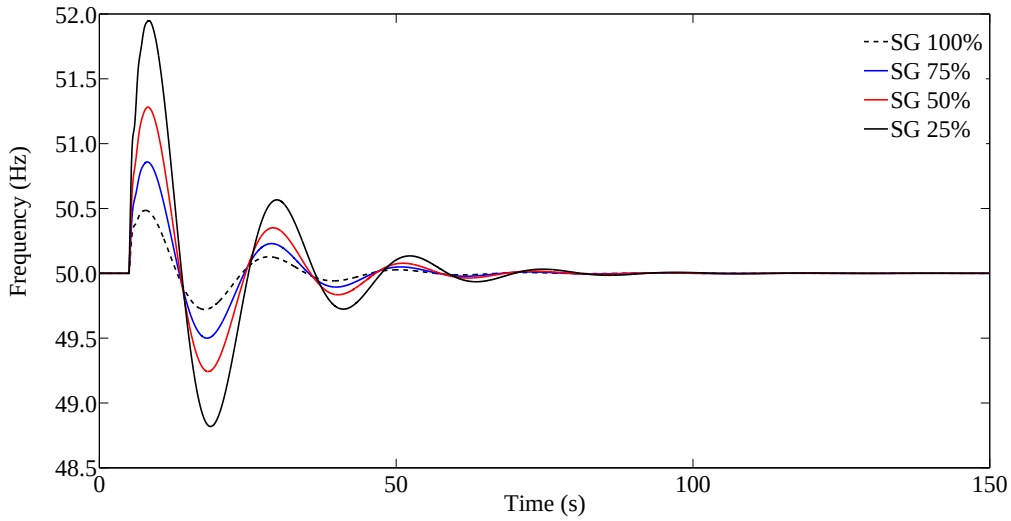

Figure 3.7: Power frequency variations of the microgrid due to unplanned islanding with different combinations of PV and MHPP

Scenario 3:

In this scenario, a MHPP (with varying inertia constant) and a DFIG were connected to Bus bars 646 and 680 respectively to supply the active power demand of the microgrid. Ratings of the DERs were changed such that the total stored energy of the SG was maintained at a constant level. The microgrid system was isolated from the bulk supply point at $t = 5\,s$ to simulate a sudden unplanned islanding.

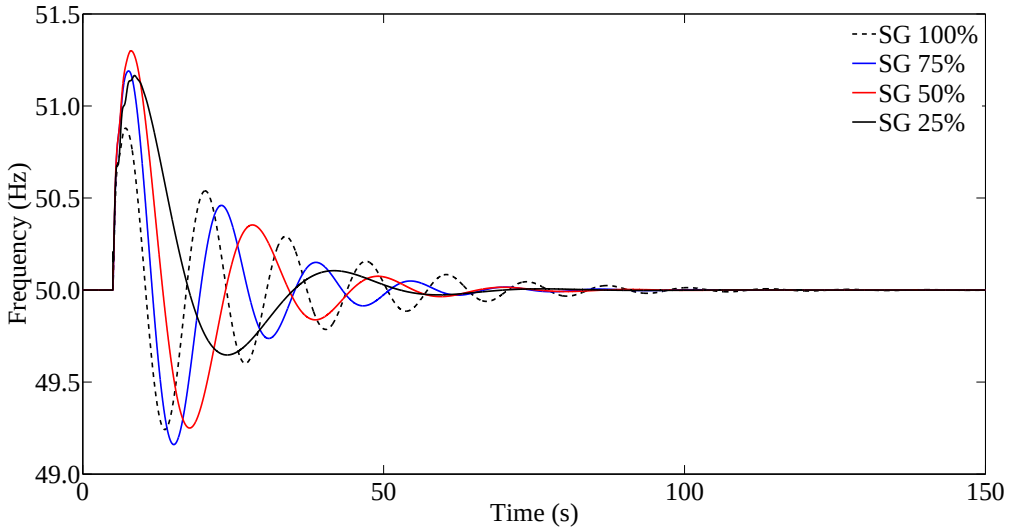

Figure 3.8: Power frequency variations of the microgrid due to unplanned islanding with different combinations of DFIG and MHPP (for different H values)

Scenario 4:

In order to observe the impact of DER type, the DFIG connected to the microgrid in Scenario 3 was replaced with a PV system having the same power rating. The microgrid system was isolated from the bulk supply point at $t = 5\,s$ to simulate a sudden unplanned islanding.

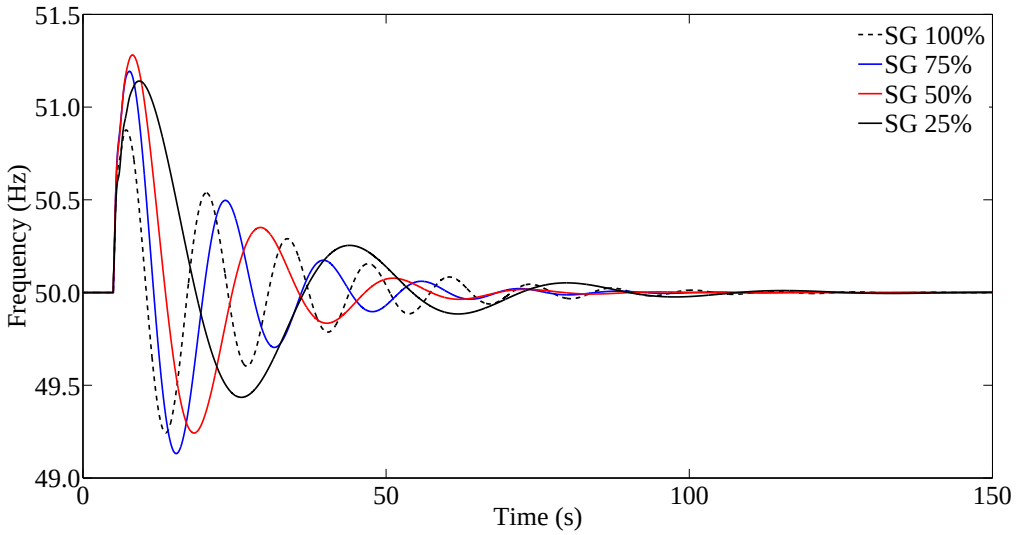

Figure 3.9: Power frequency variations of the microgrid due to unplanned islanding with different combinations of PV and MHPP (for different H values)

Both Fig. 3.6 and Fig. 3.7 related to Scenario 1 and 2 exhibit similar responses to unplanned islanding of the microgrid, irrespective of the combination of the DERs.

It can be observed that the magnitude of the maximum deviation of microgrid frequency increases as the non-inverter interfaced DER (MHPP) capacity is reduced. This occurs as the stored kinetic energy is increased in the SG with the reduction of machine rating for the same inertia constant.

In Scenario 3 and 4, the SG inertia was varied according to the machine capacity in order to maintain a constant stored energy. Both Fig. 3.8 and Fig. 3.9 exhibit similar responses in relation to unplanned islanding of the microgrid, irrespective of the combinations of the DERs. Before islanding, the surplus active power generated in the microgrid was exported to the external grid. After islanding, active power generation from the MHPP was reduced by the turbine governor controller in order to maintain the microgrid frequency at 50 Hz. In this scenario, it can be observed that the higher contribution of active power from the inverter interfaced DERs leads to reduced oscillations in the power frequency of the islanded microgrid. According to (3.1), this is due to the inertia constant of the SG which was increased with the reduction of machine rating, as both DFIG and PV were operated in constant power factor mode and did not contribute to the total inertia of the system. In all four scenarios, the power frequency oscillations due to the unplanned islanding of the microgrid were mainly determined by the inertial characteristics of the SG of the MHPP.

The maximum rate of change of frequency (ROCOF) of the microgrid for all four scenarios are summarised in Table 3.2 and Table 3.3. Due to lack of available inertial response from DFIG and PV systems, inertial response was provided only by the MHPP in the microgrid. Hence, effective angular acceleration of the SG would increase, resulting in an increase in the maximum ROCOF. This can be clearly observed from Table 3.2 and Table 3.3, where the maximum ROCOF occurred with 25% active power contribution from the MHPP in the microgrid. Therefore, design of islanding protection schemes for microgrids consisting of both inverter and non-inverter based DERs need to be carried out giving special attention to the proportion of each type of DER.

Table 3.2: Maximum ROCOF for Scenario 1 and Scenario 2

Active power contribution from the MHPP	Maximum ROCOF (Hz/s)	
	DFIG and MHPP	PV and MHPP
25%	16.71	12.48
50%	13.54	7.71
75%	5.38	3.36
100%	1.00	0.96

Table 3.3: Maximum ROCOF for Scenario 3 and Scenario 4

Active power contribution from the MHPP	Maximum ROCOF (Hz/s)	
	DFIG and MHPP	PV and MHPP
25%	16.64	11.89
50%	13.54	7.71
75%	6.11	3.69
100%	1.44	1.41

Table 3.4 presents the minimum voltage at the grid connection point as a percentage of steady state voltage during unplanned islanding of the microgrid corresponding to Scenario 3. It can be observed that with the increased penetration of MHPP, voltage sag level has improved due to the reactive power support provided by the SG.

Table 3.4: Minimum voltage magnitude as a percentage of the steady state voltage during islanding for Scenario 3

Active power contribution from the MHPP	Minimum voltage/ Steady state voltage (%)
25%	91.05
50%	92.60
75%	92.90
100%	93.20

3.3.2 Dynamic Characteristics in Grid Connected and Islanded Modes due to Large Disturbances

In this section, four different scenarios were analysed in order to investigate dynamic characteristics due to large disturbances of a microgrid in grid connected and

islanded modes. In the first scenario, impact of the type of DER on fault recovery of a grid connected microgrid was analysed. In the second scenario, a comparison was carried out on post fault behaviour in grid connected and islanded modes. Effects of the type of the DER control mode on the fault recovery was analysed in the third scenario. In the fourth scenario, the microgrid was subjected to a sudden increase in load and the post disturbance behaviour was analysed for grid connected and islanded modes.

Scenario 1:

In this scenario, the post fault behaviour of individual DERs in a grid connected microgrid and the dynamic response of the external grid were analysed. During the steady state, the total active power demand of the microgrid was met by an individual DER. The MHPP was operated at the terminal voltage control mode and 100% MHPP corresponds to the scenario where the MHPP generated the entire 4 MW of active power. Both DFIG and the PV system were operated at unity power factor. A three-phase short-circuit fault was applied to Bus bar 634 at $t = 120$ s and cleared after 150 ms.

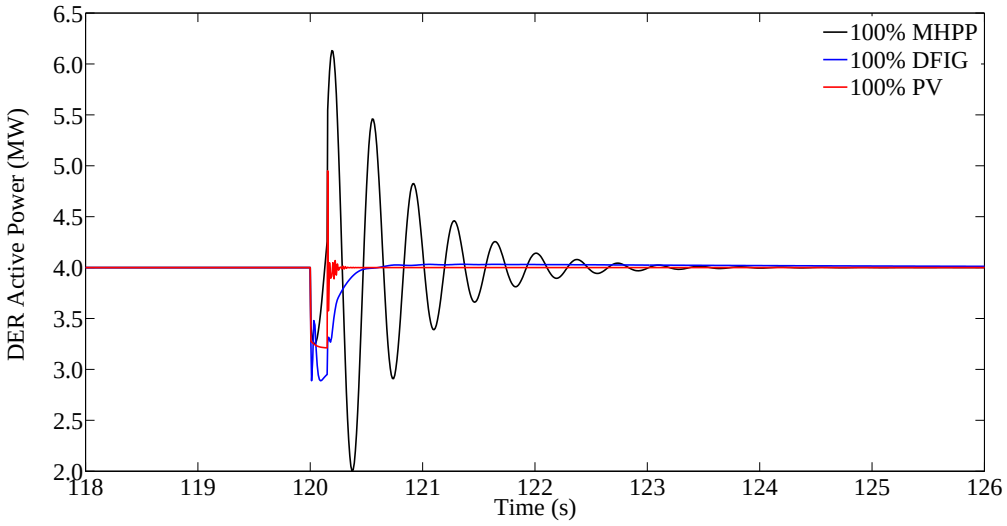

Figure 3.10: Active power output from the DERs in grid connected mode

It can be observed from Fig. 3.10 and Fig. 3.11 that only the MHPP contributes to the post fault oscillations of the microgrid system that arises as a result of its inertia,

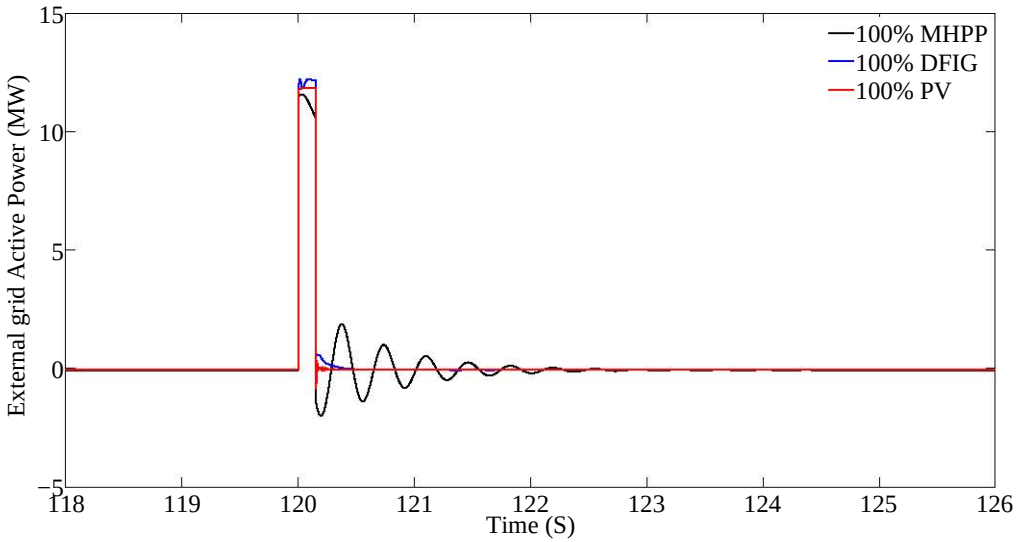

Figure 3.11: Active power supply from the external grid in grid connected mode

whereas both DFIG and the PV system respond to the fault fast and stabilises the DER output through fast PQ controllers.

Scenario 2:

In order to analyse the post fault behaviour of the microgrid, the same three-phase short-circuit fault was applied to Bus bar 634 at $t = 120\,\text{s}$ and cleared after 150 ms during grid connected and islanded modes. In this scenario, the total active power for the microgrid was supplied by an MHPP and a PV system. The MHPP was operated at the terminal voltage control mode and 100% SG corresponds to the scenario where the MHPP operated at rated power output (i.e. 4 MW), while the PV system was operated at unity power factor.

Compared to the islanded mode, post fault frequency of the microgrid in grid connected mode recovers quickly resulting from the support from the external grid (refer Fig. 3.12 and Fig. 3.13). According to Fig. 3.12, less power contribution from the MHPP of the microgrid in grid connected mode is favourable for damping the post fault oscillations. As expected, Fig. 3.13 and Fig. 3.14 demonstrate that an increase in the power contribution from the PV system negatively affects damping of post fault transients of the hybrid microgrid in islanded mode.

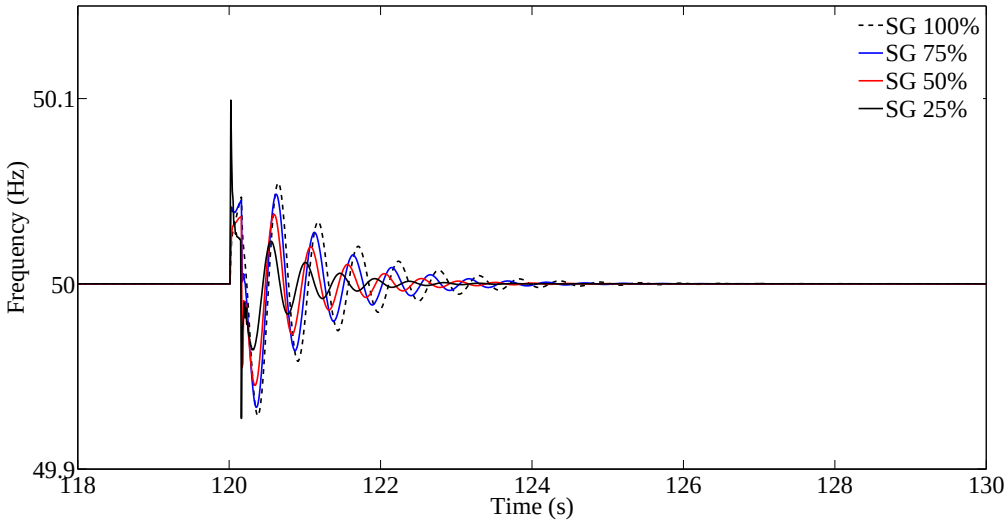

Figure 3.12: Microgrid frequency variations due to a three-phase short-circuit fault in grid connected mode

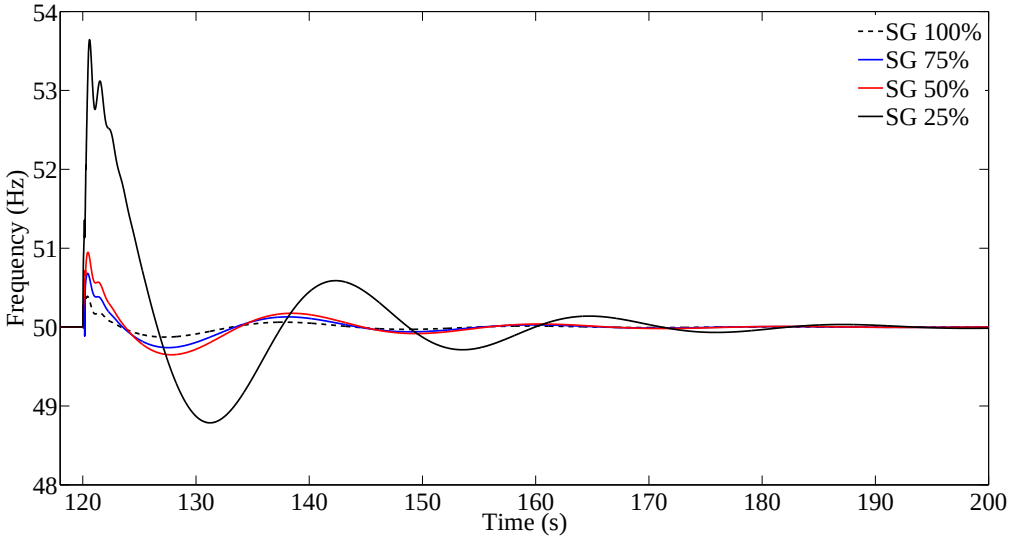

Figure 3.13: Microgrid frequency variations due to a three-phase short-circuit fault in islanded mode

Scenario 3:

Similar to the previous scenario, a three-phase short-circuit fault was applied to Bus bar 634 at $t = 120\,\mathrm{s}$ and cleared after 150 ms during grid connected mode. In this scenario, the total active power for the microgrid was supplied by the combination of the MHPP with both DFIG and PV systems separately. The MHPP was operated at the terminal voltage control mode and 100% MHPP corresponds to the scenario where the MHPP generated the entire 4 MW of active power. Both DFIG and the

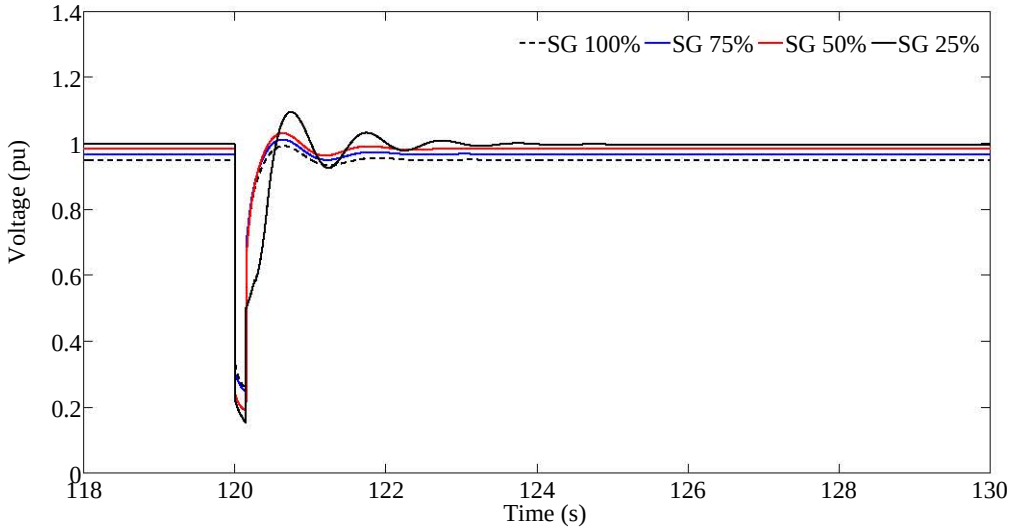

Figure 3.14: Voltage variations at Bus bar 652 due to the three-phase short-circuit fault in islanded mode

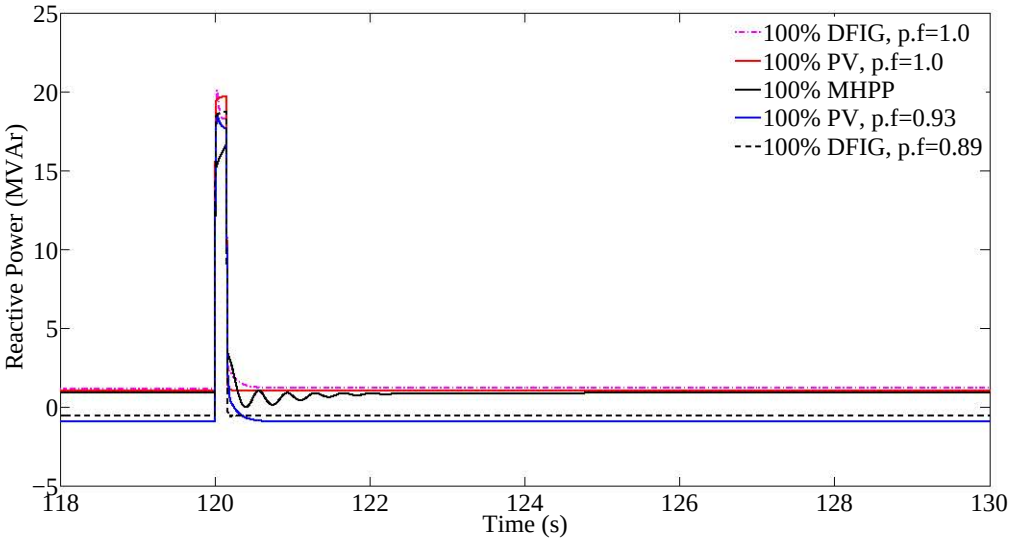

Figure 3.15: Reactive power supply from the external grid for DERs operating at different power factors

PV systems were operated at different power factors.

Fig. 3.15 illustrates the reactive power variations of the external grid while Fig. 3.16 illustrates the corresponding voltage variations at the microgrid PCC. A positive value indicates the reactive power flow from external grid to the microgrid (power import) and vice versa. A microgrid comprising only a DFIG which is operating at unity power factor has the highest reactive power demand during the fault due to the activation of crowbar protection. Least reactive power demand is from the MHPP,

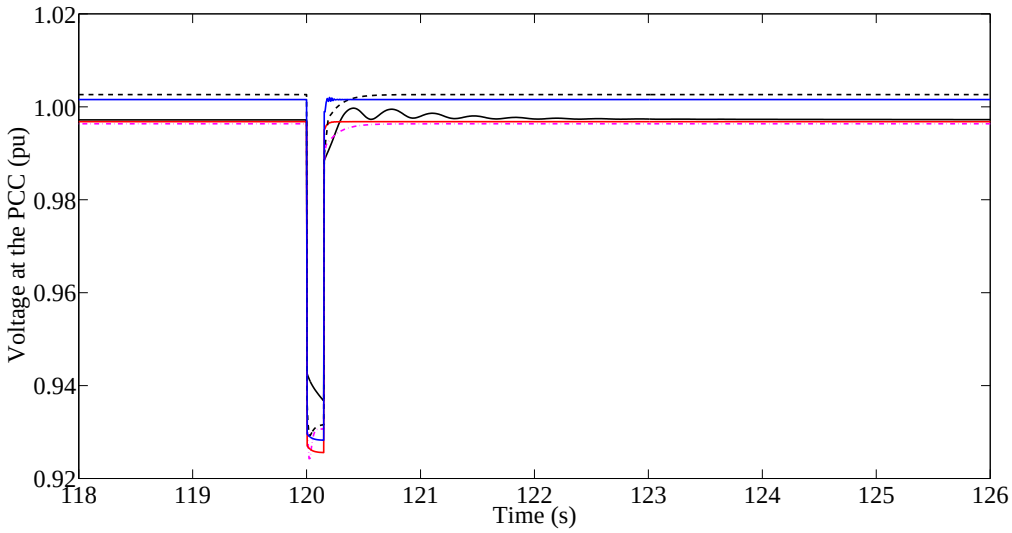

Figure 3.16: Voltages at the microgrid PCC for DERs operating at different power factors

which provides dynamic reactive power support during the fault. However, when the DFIG and the PV system operate below unity power factor, the microgrid is able to export reactive power to the external grid during the steady state. Furthermore, post fault oscillations can only be seen when the microgrid comprises of a MHPP which has a SG directly coupled to the network. In the absence of inertial response, the DFIG and the PV system do not contribute to the post fault oscillations.

Scenario 4:

In this scenario, the microgrid was subjected to a 30% increase in both active and reactive power demand by the load at Bus bar 652 during grid connected and islanded modes. The total active power for the microgrid was supplied by an MHPP (2.5 MVA) and DFIG system (2.5 MVA). The MHPP was operated in the terminal voltage control mode and the DFIG system was operated in constant power factor mode with a 0.89 lagging power factor.

During the grid connected mode, increase in load demand was catered by the external grid. However, in the islanded mode, additional active and reactive power demand from the load was provided by the MHPP as the DFIG was operating in power factor control mode, dispatching predefined power levels as illustrated

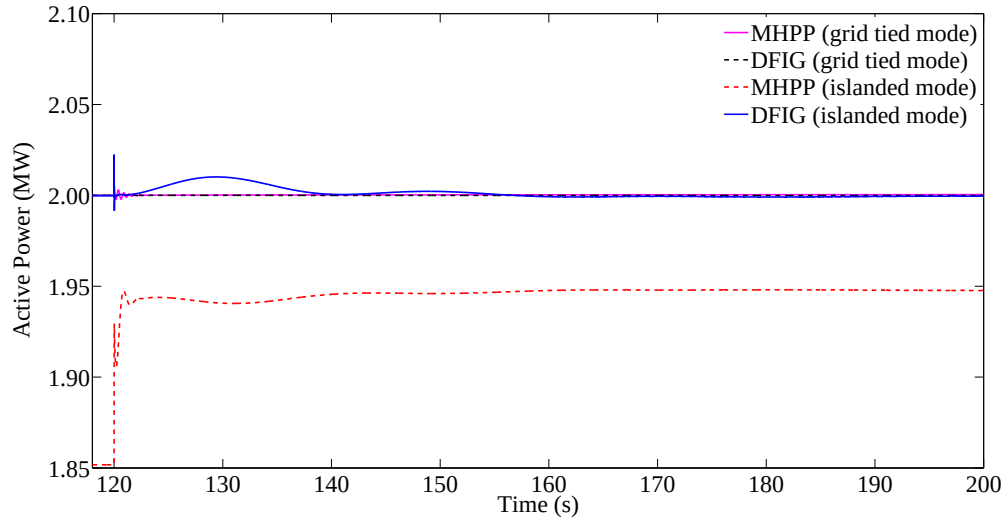

Figure 3.17: Active power output of the MHPP and the DFIG due to a load increase in grid connected and islanded modes

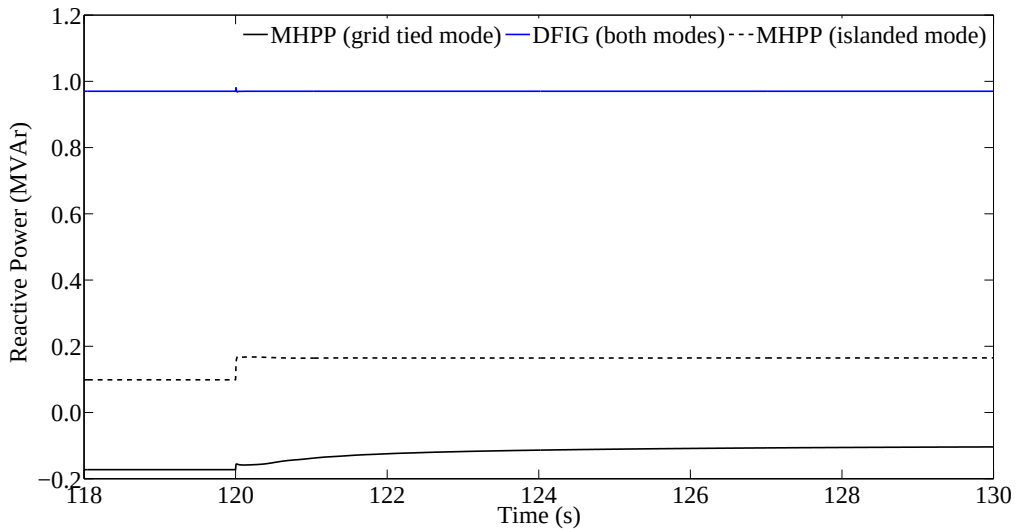

Figure 3.18: Reactive power output of the MHPP and the DFIG due to a load increase in grid connected and islanded modes

in Fig. 3.17 and Fig. 3.18. As expected, Fig. 3.19 and Fig. 3.20 illustrate that the particular load increase has a negligible impact on the microgrid frequency and voltage during grid connected mode.

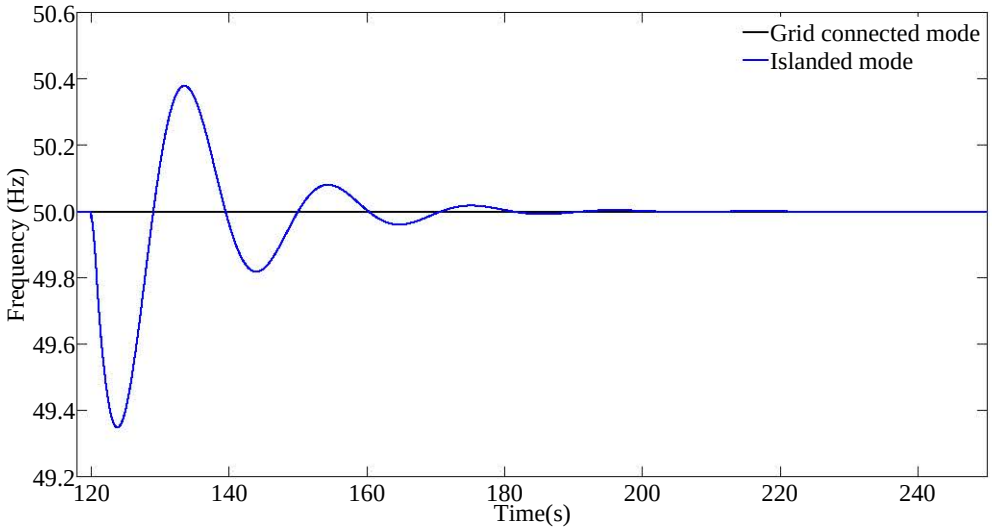

Figure 3.19: Variations of the microgrid frequency due to a load increase in grid connected and islanded modes

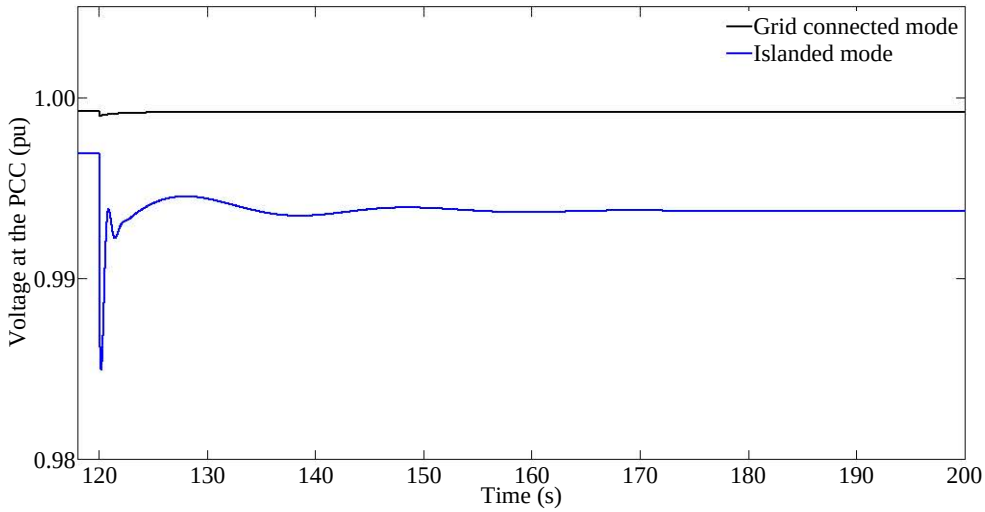

Figure 3.20: Variations of the microgrid PCC voltage due to a load increase in grid connected and islanded modes

3.4 Influence of External Grid Characteristics on the Grid Connected Microgrid

3.4.1 Effect of External Grid Short-Circuit Capacity on Microgrid Voltage

Impact of the short circuit capacity (SCC) of the external grid on the microgrid was analysed by applying a three-phase short circuit fault to Bus bar 634 at $t = 1$s for 150 ms. Active power demand of the microgrid was catered for by an MHPP

connected at Bus bar 646 and a DFIG at Bus bar 680 each having a capacity of 2.5 MVA. Similarly, DFIG was replaced with a PV system, and the same fault was applied to the microgrid. The magnitude of the maximum voltage sag at the microgrid PCC for different SCC levels of the external grid are illustrated in Fig. 3.21.

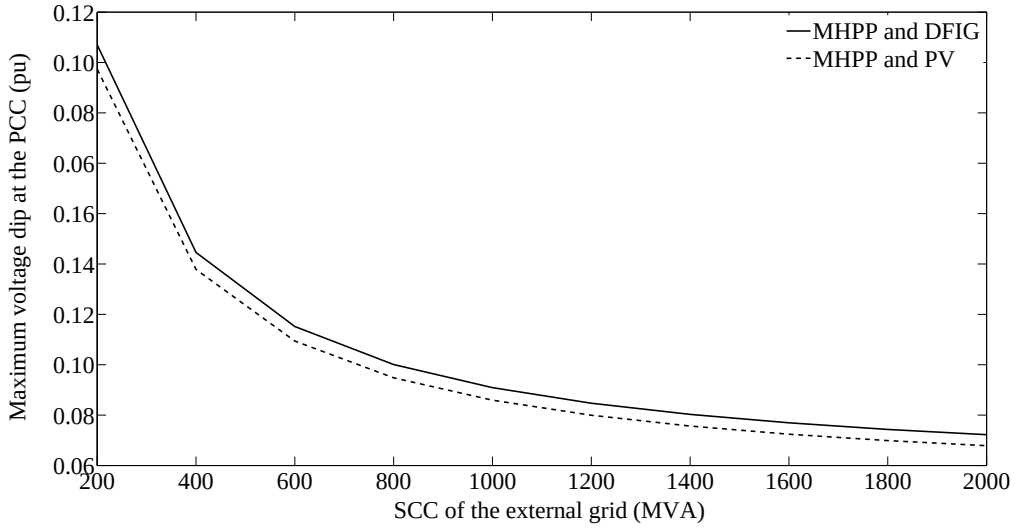

Figure 3.21: Variation of the maximum voltage dip at the PCC with the external grid SCC

As expected, the external grid with higher SCC levels provides better voltage support to the grid connected microgrid. The microgrid with DFIG and MHPP demonstrates a slightly larger voltage dip compared to the combination of PV and MHPP as illustrated in Fig. 3.21. During the fault, voltage drop in the DFIG stator windings produces sudden changes in the machine stator flux resulting a rapid increase in the stator current. Due to the magnetic coupling between the stator and the rotor, a high current will flow in the rotor and the converter. In order to protect from high currents, crowbar resistors are used to bypass the converters. Activation of these crowbar resistors converts the DFIG into a squirrel cage induction generator which consumes increased reactive power during voltage dips. Consequently, high reactive power absorption results in larger voltage drop within the microgrid. However, PV systems do not have such reactive power requirement: hence provide better performance during voltage dips.

3.4.2 Effect of External Grid Inertia on Microgrid

Similar to the previous scenario, the same fault was applied in the microgrid and the maximum ROCOF was observed for different external grid inertia levels. According to Table 3.5, external grid inertia does not have a significant impact on the maximum ROCOF for a particular combination of DERs. However, the microgrid with DFIG and MHPP has indicated higher ROCOF values compared to microgrids with PV and MHPP. As per Section 3.4.1, this is due to the larger power variation in the DFIG compared to PV system during the fault.

Table 3.5: Maximum ROCOF for different external grid inertia constants

External grid inertia constant (s)	Maximum ROCOF (Hz/s)	
	With DFIG & MHPP	With PV & MHPP
4	0.02486	0.00843
6	0.02490	0.00865
10	0.02496	0.00901
14	0.02500	0.00928
18	0.02503	0.00947

3.5 Summary

In this chapter, preliminary investigations of the dynamic characteristics of microgrids under different operating conditions were carried out using time domain simulations. Simulations were undertaken using DIgSILENT PowerFactory by developing a microgrid network comprising a PV system, a DFIG and an MHPP as DERs and local loads. Dynamic impact of a range of aspects such as different inherent characteristics of DERs, different power dispatch levels, generator capacities, and external grid characteristics on microgrid operation were analysed under different scenarios.

It was clearly evident that the DERs with a directly coupled rotor to the network have a significant influence on the post fault oscillations in the microgrid as the inertial response of inverter interfaced DER is either unavailable (e.g. PV system) or decoupled from the network (e.g. DFIG). Microgrids with smaller system rotational

inertia have a larger frequency deviation for a given mismatch between load and the power generation. However, depending on the speed, accuracy and artificial damping provided by the controllers, the inverter interfaced DERs would also have a substantial impact on the microgrid stability. The fast controllers will allow the inverter interfaced DERs to respond to disturbances quickly and reach the steady state after a fault clearance.

When different DER types are operating simultaneously in a microgrid, special care must be taken in designing the protection schemes such as microgrid islanding detection. Special attention is also required when a microgrid is transferring from grid connected mode to islanded mode, as the operation of mixed DER types exhibit different responses with and without the external grid. In addition, dynamic reactive power compensation and emulated frequency response schemes must be implemented in microgrids to preserve voltage and frequency stability when operating in islanded mode.

Microgrids operating in parallel with the external grid have a higher power supply reliability. It was highlighted that the external grid SCC plays an important role in maintaining an acceptable microgrid voltage profile. The study has shown that the dynamic characteristics of the microgrid are significantly influenced by the individual characteristics of DERs and their control systems. Furthermore, studies have also shown that different power dispatch levels, generator MVA capacities, and external grid characteristics also influence the dynamic behaviour of the microgrid, thus these factors should be considered when planning microgrids, and in particular designing protection systems for the microgrid.

In the future, when microgrids become more commonplace with higher penetration of DERs, the stability and security of the utility grid will be influenced significantly. Thus, microgrids need to be designed properly to take care of their dynamic impact on the utility grid such that overall stability and reliability of the whole system is significantly improved.

Chapter 4

Dynamic Equivalent of a Grid Connected Microgrid - Methodology and Modelling

4.1 Introduction

In many engineering applications, complex mathematical models can be derived to represent the dynamic behaviour of individual components and systems. Although a complicated higher order mathematical model will generally more accurately represent system dynamics, sometimes it is often desirable to have a simplified reduced order model which will retain the important features of the system, but limit requirements of computational and data storage capabilities.

In traditional power system analysis, dynamics of distribution networks were not required to be considered in stability studies as networks were generally passive. However, with the increasing penetration of DERs and grid connected microgrids, distribution networks have begun to feature active characteristics with bidirectional power flows. Hence, such systems can no longer be represented merely by using static load models. It is impractical for utilities to represent individual and combined DERs as detailed models in power system simulations, and this has led to

a need for new and accurate simplified models of grid connected microgrids. Such simplified models of microgrids will be useful to electric utilities in performing dynamic studies by representing grid connected microgrids as simplified generators or loads depending on the power export and import status at the microgrid PCC.

This chapter is focused on a model equivalencing methodology applicable to grid connected microgrids comprising both inverter and non-inverter interfaced DERs. The objective is to present a novel application of modal analysis for representing grid connected hybrid microgrids as reduced order single entities suitable for power system studies by preserving the important dynamics. The model reduction approach is presented in this chapter outlining the dynamic models of individual dynamic components. Validation of the model equivalencing approach is carried out using various case studies in Chapter 5.

A discussion on the selection of a suitable dynamic model equivalencing methodology for grid connected microgrids is presented in Section 4.2. Section 4.3 covers the theory behind the model equivalencing methodology selected for the work presented in this thesis. Section 4.4 presents modelling details of an inverter interfaced DER, a conventional DER, loads and the network of a grid connected microgrid suitable to be used in model equivalencing methodology, followed by the chapter summary in Section 4.5.

4.2 Selection of the Dynamic Model Equivalencing Methodology for Grid Connected Microgrids

As explained in Section 4.1, model equivalencing or reduction is to replace a given complex mathematical model of a system with a less complex model which would still capture all the important dynamics associated with the original system. Model equivalencing involves a trade off between model order and the degree to which the characteristics of the original system are reflected in the reduced model.

For stability analysis, the common practice is to separate the power system into a study area of interest and external areas. In general, the study area is represented in a detailed manner while external areas are represented by dynamic equivalents [45,46]. These equivalent models will approximate the effects of the external systems on the study system, as parts of the system electrically far away from a disturbance will have little effect on the study system dynamics, hence, it is unnecessary to model them with greater accuracy.

As empahsised in Chapter 2, coherency based methods which identify coherent groups of generators governed by generator rotor behaviour following a disturbance, cannot be applied to modern inverter interfaced DERs due to decoupling of rotor dynamics from the network (e.g. DFIGs and microturbines) or due to the absence of such rotor dynamics (e.g. PV and battery storage systems). Out of the three main methods stated in Chapter 2, only system identification methods use measured data to select model parameters of the dynamic equivalent model. The model parameters need to be adjusted with proper training algorithms using a large amount of data sets, which is time consuming. Furthermore, these methods lack strong mathematical background compared to modal methods, and the estimated parameters do not properly interpret the physical relevance to the dynamic equivalent of power systems.

Generally, in modal methods, reduction of the linearised system is carried out by removing the eigenvalues located furthest from the origin, and retaining the eigenvalues with small negative real parts and the less damped eigenvalues. The relevant variables with respect to that principle are kept and the remaining variables are expressed in terms of the dominant variables. Thus, overall dynamic characteristics of the reduced system will be similar to the original system. Unlike system identification methods which depend on parameter estimation, traditional model equivalencing methodologies are firmly based on mathematical concepts and have significant physical relevance to the system dynamics. However, care must be taken in applying modal methods for systems with inverter interfaced DERs, as their state

variables are not well known as in the case of conventional SGs.

As mentioned in Chapter 2, the basic modal method has not been applied to grid connected hybrid microgrids as a means for deriving dynamic equivalent models. Thus, this chapter takes an approach in investigating the applicability of modal analysis as a tool for dynamic model equivalencing of grid connected microgrids containing inverter and non-inverter interfaced DERs.

4.3 Dynamic Model Equivalencing Methodology

The dynamic model reduction process covered in this section is illustrated in Fig. 4.1. As explained in Chapter 2, while appropriate for conventional systems based on SGs, selective modal analysis [50, 51] was considered not suitable for hybrid microgrids. This is due to the difficulty in determining the significant states of inverter-interfaced DERs at the initial stages of the method without carrying out a full eigenvalue analysis. From various modal methods available in the literature, the matrix transformation technique in [46] was selected and adapted for this work, as it allowed full eigenvalue analysis of the hybrid microgrid model. In this approach, an additional step is introduced to identify and group the dominant system modes which are to be retained in the dynamic equivalent microgrid model. Furthermore, the grid connected microgrid is represented in a similar way to any other grid connected dynamic device suitable for power system stability studies. The steps (Blocks A, B, C and D in Fig. 4.1) associated with the enhanced model equivalencing process are described in the following subsections.

4.3.1 Linearised Microgrid Model

For the purpose of stability analysis of large power systems, microgrids connected outside the study area of interest can be represented as linear systems [45, 46]. Influence of the control systems and inherent dynamic characteristics of DERs and loads are captured by modelling these elements using ordinary differential equations,

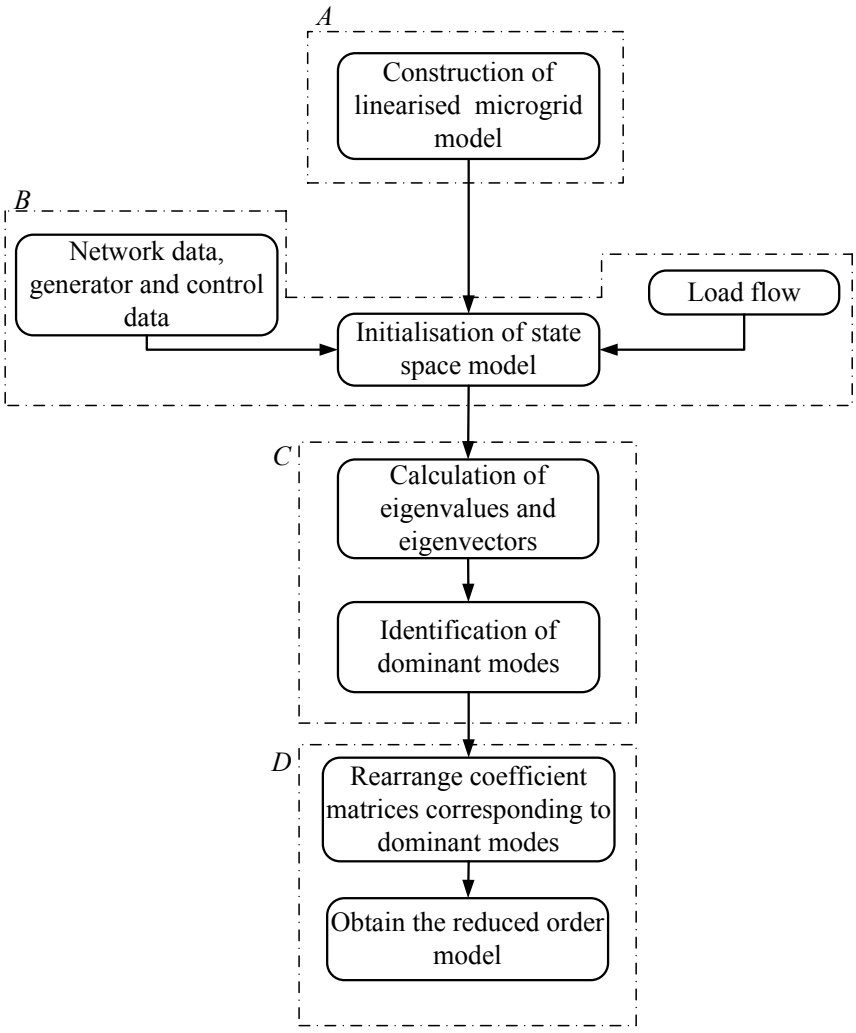

Figure 4.1: Model reduction approach applied to grid connected microgrids based on the enhanced modal method

which in turn used to develop the state space model of the microgrid. From the study system point of view, a microgrid can be seen as a single generator or load in a linearised state-space form as follows:

$$\Delta\dot{x} = A_{MG}\Delta x + B_{MG}\Delta v_{pcc} \tag{4.1}$$

$$\Delta y_{pcc} = C_{MG}\Delta x + D_{MG}\Delta v_{pcc} \tag{4.2}$$

$$[\Delta y_{pcc}] = \begin{bmatrix} \Delta i_{pcc} \\ \Delta\omega_{ref} \end{bmatrix} \tag{4.3}$$

where, $A_{MG}\,(n \times n)$, $B_{MG}\,(n \times 1)$, $C_{MG}\,(m \times n)$, and $D_{MG}\,(m \times 1)$ are coefficient matrices of the system.

Vector Δx contains states of the dynamic devices in the microgrid while vector Δv_{pcc} represents the voltage at the microgrid PCC as an input to the system. Current through the microgrid PCC, Δi_{pcc}, and speed deviation of the microgrid reference d-q frame $\Delta\omega_{ref}$ are taken as the microgrid outputs in the vector Δy_{pcc}. Derivation of (4.1) and (4.2) are explained in detail using a microgrid model in Section 4.4. A block diagram of a grid connected microgrid expressed by (4.1) and (4.2) is illustrated in Fig. 4.2. Time domain solutions to the state space equation given in (4.1) and (4.2) are obtained from the following equations:

$$x(t) = e^{A_{MG}t}x(t_0) + \int_{t_0}^{t} e^{A_{MG}(t-\tau)}B_{MG}v_{pcc}(\tau)d\tau \tag{4.4}$$

$$y(t) = C_{MG}e^{A_{MG}t}x(t_0) + C_{MG}\int_{t_0}^{t} e^{A_{MG}(t-\tau)}B_{MG}v_{pcc}(\tau)d\tau + D_{MG}v_{pcc}(t)$$

4.3.2 Initialisation of the State-Space Model

Once the linearised microgrid model is constructed, the network, DERs and control data are incorporated into the model, and the load flow results are used to initialise the state-space model.

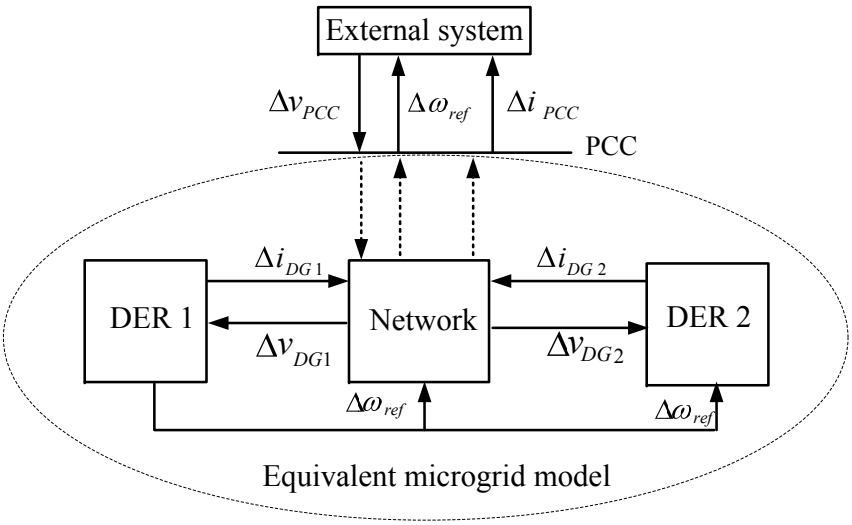

Figure 4.2: Block diagram of the linearised state-space model of a grid connected microgrid system comprising two DERs

4.3.3 Identification of Dominant Modes

Let the state space model of the system to be reduced be,

$$\Delta \dot{x} = A_{MG}\Delta x + B_{MG}\Delta v_{pcc} \tag{4.5}$$

As the first step in identifying the dominant modes, a coordinate transformation is carried out where it is possible to find a matrix P such that A_{MG} is transformed into a diagonal form as follows:

$$\Delta x \;=\; P\Delta z \tag{4.6}$$

Matrix P contains the eigen vectors of matrix A_{MG} as the columns.

$$P = \begin{bmatrix} \varphi_{11} & \varphi_{12} & \cdots & \varphi_{1n} \\ \varphi_{21} & \varphi_{22} & \cdots & \varphi_{2n} \\ \vdots & \vdots & & \vdots \\ \varphi_{n1} & \varphi_{n1} & \cdots & \varphi_{nn} \end{bmatrix} \tag{4.7}$$

$$p_i = \begin{bmatrix} \varphi_{1i} \\ \varphi_{2i} \\ \vdots \\ \varphi_{ni} \end{bmatrix} \tag{4.8}$$

$$P = [p_1,\, p_2,\, \cdots\cdots\cdots\, p_n] \tag{4.9}$$

where, φ_i is the i^{th} right eigenvector of A_{MG} corresponding to the i^{th} eigenvalue λ_i. Considering (4.5) - (4.9) [166],

$$\begin{aligned} \Delta\dot{z}(t) &= P^{-1}A_{MG}P\Delta z(t) + P^{-1}B_{MG}\Delta v_{pcc} \\ &= \Lambda\Delta z(t) + P^{-1}B_{MG}\Delta v_{pcc} \\ &= \Lambda\Delta z(t) + B^{'}\Delta v_{pcc} \end{aligned} \tag{4.10}$$

$$\Lambda = \begin{bmatrix} \lambda_1 & 0 & \cdots & 0 \\ 0 & \lambda_2 & & \vdots \\ \vdots & & \ddots & \vdots \\ 0 & \cdots & \cdots & \lambda_n \end{bmatrix} \tag{4.11}$$

where, $P^{-1}A_{MG}P = \Lambda$, and Λ is a diagonal matrix with the eigenvalues of matrix A_{MG}. Hence, the original state-space model of the grid connected microgrid represented in (4.5) is transformed into (4.10).

Modes corresponding to the eigenvalues with large negative real numbers are considered as non-dominant modes which are assumed to reach the steady state instantaneously following a step disturbance, compared to other modes. Hence, non-dominant modes that have less impact on the study system when observed from

the microgrid PCC can be eliminated from the transformed system model (4.10). It is important to retain the poorly damped oscillatory modes in the reduced order equivalent model.

In this section, a new index is defined for identifying the dominant modes which need to be retained in the reduced order equivalent microgrid model. The real part of the eigenvalues (σ_i) normalised as a percentage of the real part of the eigenvalue located furthest away from the origin (σ_{max}) is used as an index for the selection of dominant modes as expressed in (4.12).

$$\sigma_{i-normalised} = \frac{\sigma_i}{\sigma_{max}} \times 100\,\% \tag{4.12}$$

4.3.4 Rearrangement of Matrices and Model Reduction

After identifying the dominant modes, let Λ be rearranged as in (4.13) such that γ_r and γ_{nr} represent the modes to be retained in the reduced model and the modes to be eliminated from the original model respectively. The relevant state variables corresponding to the dominant modes are retained, and the remaining state variables are expressed in terms of retained state variables. Rows of matrix $B^{'}$ in (4.10) also need to be rearranged accordingly.

$$\begin{bmatrix} \Delta\dot{z}_r \\ \Delta\dot{z}_{nr} \end{bmatrix} = \begin{bmatrix} \gamma_r & 0 \\ 0 & \gamma_{nr} \end{bmatrix} \begin{bmatrix} \Delta z_r \\ \Delta z_{nr} \end{bmatrix} + \begin{bmatrix} B_r^{'} \\ B_{nr}^{'} \end{bmatrix} \Delta v_{pcc} \tag{4.13}$$

Reduced order system equation of (4.10) is given by,

$$\Delta\dot{z}_r = \gamma_r \Delta z_r + B_r^{'} \Delta v_{pcc} \tag{4.14}$$

where, z_r- transformed states to be retained in the reduced model, z_{nr}- transformed states assumed to reach the steady state instantly.

Contributions of state variables on the system modes are calculated using the participation factors [163]. Participating factors indicate the relative participation

of the respective states in the corresponding modes. Participation factor of an l^{th} state variable on the m^{th} mode is given by

$$p_{lm} = \varphi_{lm}\phi_{ml} \tag{4.15}$$

where, φ_{lm}- l^{th} element of the right eigenvector φ_m and ϕ_{ml}- l^{th} element of the left eigenvector ϕ_m.

Next, (4.2) can be rearranged such that,

$$\Delta y_{pcc} = C_{o/p}\Delta x_{o/p} + D_{MG}\Delta v_{pcc} \tag{4.16}$$

where, $x_{o/p}$- sub vector of Δx comprising the original states contributing to the system output, and $C_{o/p}$ is the sub matrix of C_{MG} comprising the columns corresponding to $x_{o/p}$.

In order to obtain the reduced order system output equation corresponding to (4.2), transformation matrix P in (4.6) is rearranged as follows:

$$\begin{bmatrix} \Delta x_{o/p} \\ \Delta x_{no/p} \end{bmatrix} = \begin{bmatrix} \alpha_r & \alpha_{nr} \\ \beta_r & \beta_{rn} \end{bmatrix} \begin{bmatrix} \Delta z_r \\ \Delta z_{nr} \end{bmatrix} \tag{4.17}$$

where, $x_{no/p}$- sub vector of Δx comprising the original states with no contribution to the system output. The r rows corresponding to the states $x_{o/p}$ are placed in the first r rows of matrix P while the first r columns are rearranged corresponding to the retained r eigenvalues.

For a step input $\dot{z}_{nr} = 0$, hence, using (4.13),

$$\Delta z_{nr} = -\gamma_{nr}^{-1} B_{nr}^{'} \Delta v_{pcc} \tag{4.18}$$

Using (4.17) and (4.18) in (4.16),

$$\Delta y_{pcc} = C_{o/p}\alpha_r \Delta z_r - C_{o/p}\alpha_{nr}\gamma_{nr}^{-1} B_{nr}^{'} \Delta v_{pcc} + D_{MG}\Delta v_{pcc}$$
$$\Delta y_{pcc} = C^{'}\Delta z_r + D^{'}\Delta v_{pcc} \tag{4.19}$$

where, $C^{'} = C_{o/p}\alpha_r$ and $D^{'} = D_{MG} - C_{o/p}\alpha_{nr}\gamma_{nr}^{-1}B_{nr}^{'}$. Hence, the reduced order dynamic equivalent of the microgrid model corresponding to (4.1) and (4.2) is given by (4.14) and (4.19).

This section described in detail all steps involved in modal reduction approach selected to be applied to grid connected microgrids based on enhanced modal method. This method is applied to a microgrid modelled as explained in the following section.

4.4 Modelling of the Microgrid for Model Equivalencing

This section presents the detailed modelling of an inverter interfaced DER, a non-inverter interfaced DER, loads and the network of a grid connected microgrid suitable for implementation of the selected model equivalencing methodology. All dynamic devices in the microgrid are represented by state-space models.

4.4.1 Global Reference Frame

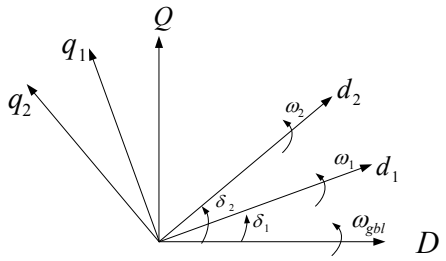

Figure 4.3: Global and local reference frames of the microgrid

In any microgrid system, it is necessary to define a global reference frame which would allow all dynamic devices and other network components rotating on local

reference frames to be represented in a common reference frame. Transformation from the local reference frames $(d_i - q_i)$ to the global reference frame $(D - Q)$ is carried out using (4.20).

$$[f_{QD}] = \begin{bmatrix} \cos\delta_i & \sin\delta_i \\ -\sin\delta_i & \cos\delta_i \end{bmatrix} [f_{qd}]$$

$$[f_{QD}] = [T_i][f_{qd}] \tag{4.20}$$

where, $[f_{QD}]$ - state variables in the global reference frame, $[f_{qd}]$ - state variables in the local reference frame, and δ_i - angle between the d-axis of the global reference frame and the d-axis of the local reference frame corresponding to the i^{th} dynamic device.

As illustrated in Fig. 4.2, when modelling the dynamic devices in a microgrid, current injected to the microgrid from each device is taken as the output signal of the device, and the respective terminal voltage of the device and the global reference frame frequency deviation are taken as the input signals. As the model equivalencing method is applied to linearised systems, (4.20) is linearised around an operating point.

In order to connect a dynamic device into the microgrid, output signals (currents) need to be expressed in the global reference frame as in (4.21) (it is assumed that $\cos(\Delta\delta) \simeq 1$ and $\sin(\Delta\delta) \simeq \Delta\delta$).

$$\begin{bmatrix} \Delta I_Q \\ \Delta I_D \end{bmatrix} = [T_{io}] \begin{bmatrix} \Delta I_q \\ \Delta I_d \end{bmatrix} + \begin{bmatrix} -I_{qo}\sin\delta_{io} + I_{do}\cos\delta_{io} \\ -I_{qo}\cos\delta_{io} - I_{do}\sin\delta_{io} \end{bmatrix} \Delta\delta \tag{4.21}$$

Similarly, the input voltage needs to be transformed from the global reference frame to the respective local reference frame as follows:

$$\begin{bmatrix} \Delta V_q \\ \Delta V_d \end{bmatrix} = [T_{io}]^{-1} \begin{bmatrix} \Delta V_Q \\ \Delta V_D \end{bmatrix} + \begin{bmatrix} -V_{qo} \sin \delta_{io} - V_{do} \cos \delta_{io} \\ V_{qo} \cos \delta_{io} + V_{do} \sin \delta_{io} \end{bmatrix} \Delta\delta \tag{4.22}$$

where, "$\circ$" represents the steady state operating point around which the equations are linearised.

4.4.2 Inverter Interfaced DER Model

For an inverter interfaced DER, it is be assumed that the output power of the dc voltage source connected to the inverter is constant during the time frame of the analysis. This will allow the dc side dynamics to be neglected in the converter model and to represent inverter interfaced DER based on any power source. Thus, a generic model is used to represent inverter interfaced DER units consisting of a constant dc voltage source, a converter power circuit and converter controls. As illustrated in Fig. 4.4, ac side of the converter is connected to the microgrid through a lumped impedance having a reactance of X and a resistance of R. The ordinary differential equations (ODE) describing the ac side of the converter can be expressed as follows:

$$E_{abc} = RI_{abc} + L\frac{dI_{abc}}{dt} + V_{abc} \tag{4.23}$$

Equation (4.23) is transformed into the local d-q reference frame defined at the DER terminal, where d-axis is always coincident with the instantaneous voltage vector, and the q-axis is in quadrature with it.

$$\begin{aligned} E_q &= RI_q + L\frac{dI_q}{dt} + \omega_{inv} L I_d \\ E_d &= V_d + RI_d + L\frac{dI_d}{dt} - \omega_{inv} L I_q \end{aligned} \tag{4.24}$$

where, $\omega_{inv} = d\delta_{inv}/dt$ and δ_{inv} is the angle between the d-axis of the global reference

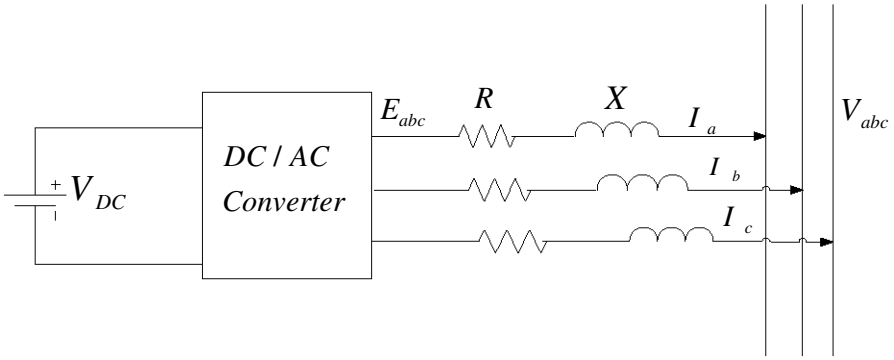

Figure 4.4: Inverter interfaced DER

frame and d-axis of the local reference frame of the corresponding inverter interfaced DER. In order to decouple the I_d and I_q components, a new variable is introduced as follows [167]:

$$V_{qnew} = E_q - \omega_{inv} L I_d \tag{4.25}$$
$$V_{dnew} = E_d - V_d + \omega_{inv} L I_q$$

Equations (4.24) and (4.25) are linearised around an operating point and combined to obtain the state-space format of the inverter as follows:

$$\Delta \dot{X}_{inv} = A_{inv} \Delta X_{inv} + \frac{1}{L} \Delta V_{qdnew} \tag{4.26}$$

where, $\Delta X_{inv} = [\Delta I_{q2}, \Delta I_{d2}]$ and $\Delta V_{qdnew} = [\Delta V_{qnew}, \Delta V_{dnew}]$.

The mathematical model of the linearised phase locked loop (PLL) circuit illustrated in Fig. 4.5 is expressed by (4.27) [168].

$$\omega_{inv} = K_{pll}(K_p + \frac{K_i}{s})(\delta_{ref} - \delta_{inv}) \tag{4.27}$$
$$\Delta \dot{\omega}_{inv} = -K_{pll} K_{p\omega} \Delta \omega_{inv} - K_{pll} K_i \Delta \delta_{inv}$$

where, K_{pll} is the gain of the input signal to the main PLL block, K_p and K_i are

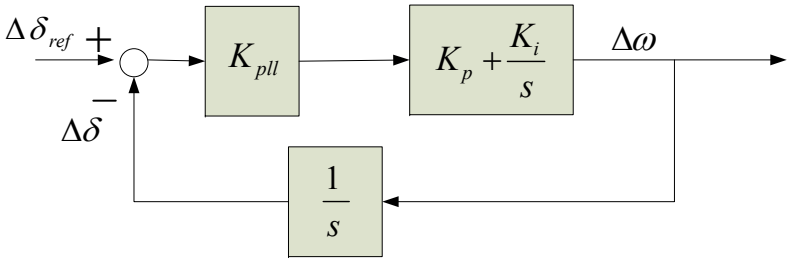

Figure 4.5: Linearised PLL circuit

the proportional and integral gains of the PI controller respectively.

In this chapter, the inverter interfaced DER is considered to be operated in the constant power factor mode. The d-axis current component accounts for the instantaneous active power, and the reference current for the d-axis current controller loop is provided by the active power control loop as illustrated in Fig. 4.6. Linearised equations describing the active power output of the DER are as follows:

$$\begin{aligned} P_{out} &= V_d^{'} I_d^{'} + V_q^{'} I_q^{'} \\ \Delta P_{out} &= V_{do}\Delta I_d^{'} + I_{do}\Delta V_d^{'} + V_{qo}\Delta I_q^{'} + I_{qo}\Delta V_q^{'} \end{aligned} \tag{4.28}$$

Instantaneous power output of the DER is calculated using filtered instantaneous voltage and current which are explained in (4.29).

$$\begin{aligned} \Delta\dot{I}_{qd}^{'} &= -\frac{1}{T_i}\Delta I_{qd}^{'} + \frac{1}{T_i}\Delta I_{qd} \\ \Delta\dot{V}_{qd}^{'} &= -\frac{1}{T_v}\Delta V_{qd}^{'} + \frac{1}{T_v}\Delta V_{qd} \end{aligned} \tag{4.29}$$

where, T_i and T_v are the time constants of the low pass filters of current and voltage signals.

Linearised active power controller and d-axis current controller dynamics are expressed in (4.30)-(4.33).

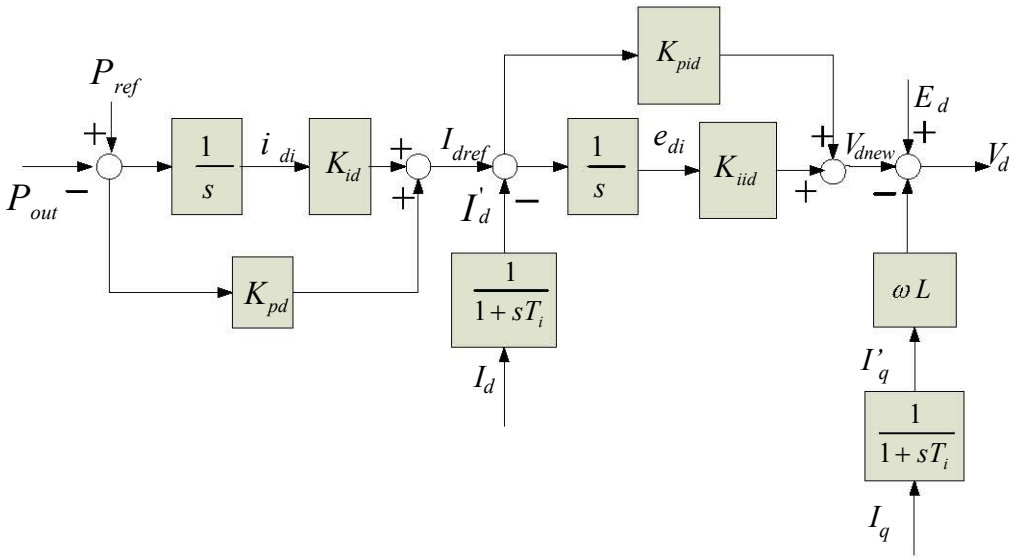

Figure 4.6: Active power controller and the d-axis current controller

$$\Delta\dot{i}_{di} = \Delta P_{ref} - \Delta P_{out} \tag{4.30}$$

$$\Delta\dot{e}_{di} = \Delta I_{dref} - \Delta I_d^{'} \tag{4.31}$$

$$\Delta I_{dref} = K_{id}\Delta i_{di} + K_{pd}(\Delta P_{ref} - \Delta P_{out}) \tag{4.32}$$

$$\Delta V_{dnew} = K_{iid}\Delta e_{di} + K_{pid}(\Delta I_{dref} - \Delta I_d^{'}) \tag{4.33}$$

where, K_{pd}, K_{pid} and K_{id}, K_{iid} are the proportional and integral gains of the PI controllers respectively.

Similarly, the reference for the q-axis current controller is generated using the reactive power control loop as illustrated in Fig. 4.7. Corresponding linearised equations for the reactive power output of the DER, reactive power controller and the q-axis controller can be described using (4.34) - (4.38).

$$\begin{aligned} Q_{out} &= V_d^{'}I_q^{'} - V_q^{'}I_d^{'} \\ \Delta Q_{out} &= V_{do}\Delta I_q^{'} + I_{qo}\Delta V_d^{'} - V_{qo}\Delta I_d^{'} - I_{do}\Delta V_q^{'} \end{aligned} \tag{4.34}$$

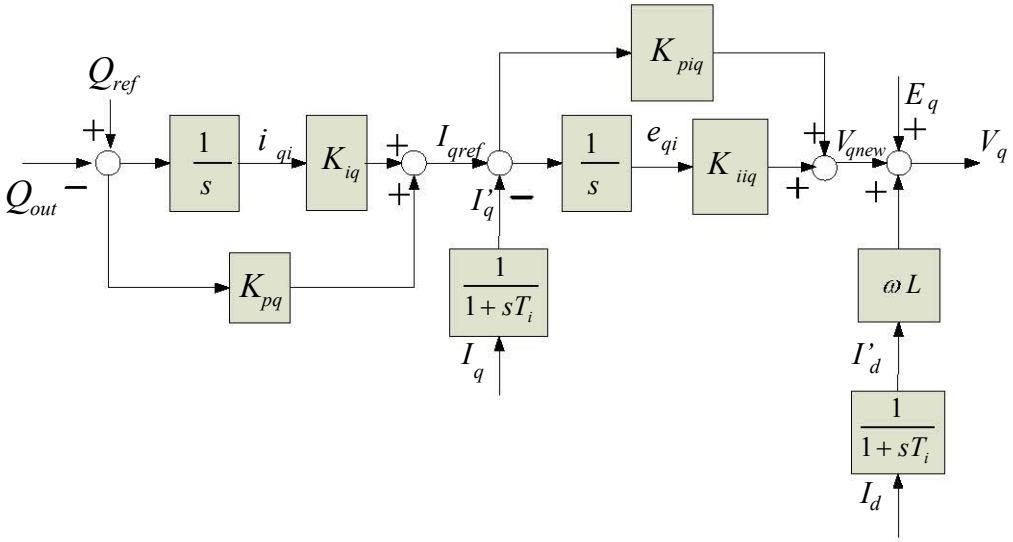

Figure 4.7: Reactive power controller and the q-axis controller

$$\Delta\dot{i}_{qi} = \Delta Q_{ref} - \Delta Q_{out} \tag{4.35}$$

$$\Delta\dot{e}_{qi} = \Delta I_{qref} - \Delta I_q^{'} \tag{4.36}$$

$$\Delta I_{qref} = K_{iq}\Delta I_{qi} + K_{pq}(\Delta Q_{ref} - \Delta Q_{out}) \tag{4.37}$$

$$\Delta V_{qnew} = K_{iiq}\Delta e_{qi} + K_{piq}(\Delta I_{qref} - \Delta I_q^{'}) \tag{4.38}$$

where, K_{pq}, K_{piq} and $K_{iq,}\, K_{iiq}$ are the proportional and integral gains of the PI controllers respectively.

Let the state variables and the disturbance inputs of the controllers be
$\Delta X_{con} = [\Delta V_q^{'}, \Delta V_d^{'}, \Delta I_q^{'}, \Delta I_d^{'}, \Delta i_{qi}, \Delta i_{di}, \Delta e_{qi}, \Delta e_{di}, \Delta\omega_{inv}]$ and
$\Delta U_{inv} = [\Delta Q_{ref}, \Delta P_{ref}]$ respectively. Then, (4.33) and (4.38) can be written in terms of ΔX_{con} and ΔU_{inv}.

$$\Delta V_{qdnew} = E_1\Delta X_{con} + E_2\Delta U_{inv} \tag{4.39}$$

Hence, state-space model of the converter (4.26) can be expressed in terms of controller state variables as in (4.40).

$$\Delta\dot{X}_{inv} = A_{inv}\Delta X_{inv} + \frac{1}{L}(E_1\Delta X_{con} + E_2\Delta U_{inv}) \tag{4.40}$$

Combining (4.27), (4.29)-(4.31), (4.35) and (4.36) will give the linearised state-space model of the active and reactive power controllers of the inverter interfaced DER.

$$\begin{aligned} \Delta\dot{X}_{con} &= A_{con}\Delta X_{con} + B_{con1}\Delta X_{inv} + B_{con2}\Delta V_{qd} + B_{con3}\Delta U_{inv} \\ \Delta y_{inv} &= C_{inv}\Delta X_{inv} + D_{inv}\Delta V_{qd} \end{aligned} \tag{4.41}$$

Inverter interfaced DER in the local reference frame is established using (4.40) and (4.41).

$$\begin{aligned} \begin{bmatrix} \Delta\dot{X}_{inv} \\ \Delta\dot{X}_{con} \end{bmatrix} &= \begin{bmatrix} A_{inv} & E_1/L \\ B_{con1} & A_{con} \end{bmatrix} \begin{bmatrix} \Delta X_{inv} \\ \Delta X_{con} \end{bmatrix} + \begin{bmatrix} 0 \\ B_{con2} \end{bmatrix} \Delta V_{qd} \\ &\quad + \begin{bmatrix} E_2/L \\ B_{con3} \end{bmatrix} \Delta U_{inv} \end{aligned} \tag{4.42}$$

Prior to connecting the inverter interfaced DER to the network, output signals (currents) are transferred to the global reference frame, and input signals (terminal voltages) are transferred to the local reference frame. Substitution of (4.21) and (4.22) in (4.42) describes the total inverter interfaced DER system as follows:

$$\begin{aligned} \Delta\dot{X}_{IIDER} &= A_{IIDER}\Delta X_{IIDER} + B_{IIDER}\Delta V_{QD-IIDER} \\ &\quad + \beta_{IIDER}\Delta U_{IIDER} \\ \Delta I_{IIDER} &= C_{IIDER}\Delta X_{IIDER} + D_{IIDER}\Delta V_{QD-IIDER} \end{aligned} \tag{4.43}$$

4.4.3 Non-Inverter Interfaced DER Model

In this section, a directly coupled SG is considered with a mini-hydro power plant (MHPP) as the plant model comprising an exciter and a hydro turbine-governor systems. The linearised ODEs of a salient-pole SG with damper windings on both d-q axes and field winding on the d-axis together with the mechanical system are expressed as follows [163]:

$$\begin{aligned} T_{do}^{'}\Delta\dot{E}_{q}^{'} &= \Delta E_{fd} - \Delta E_{q}^{'} - (X_d - X_d^{'})\Delta I_d \\ T_{do}^{''}\Delta\dot{E}_{q}^{''} &= -\Delta E_{q}^{''} + \Delta E_{q}^{'} - (X_d^{'} - X_d^{''})\Delta I_d \\ T_{qo}^{''}\Delta\dot{E}_{d}^{''} &= -\Delta E_{d}^{''} + (X_q - X_q^{''})\Delta I_q \end{aligned} \tag{4.44}$$

In per unit domain,

$$\begin{aligned} \Delta\dot{\delta} &= \omega_b \Delta\omega_{rpu} \\ \Delta\dot{\omega}_{rpu} &= \frac{1}{2H}(\Delta T_m - \Delta T_e) \\ T_e &= E_q^{"} I_q + E_d^{"} I_d - (X_d^{"} - X_q^{"}) I_d I_q \end{aligned} \tag{4.45}$$

Algebraic equations describing the voltage current relationship are as follows:

$$\begin{aligned} \Delta V_q &= \Delta E_{q}^{''} - R\Delta I_q - X_d^{''}\Delta I_d \\ \Delta V_d &= \Delta E_{d}^{''} - R\Delta I_d + X_q^{''}\Delta I_q \end{aligned} \tag{4.46}$$

where, V_q and V_d are the axial components of the DER terminal voltage.

Fig. 4.8 illustrates the excitation model [163] which is described by the set of equations in (4.47).

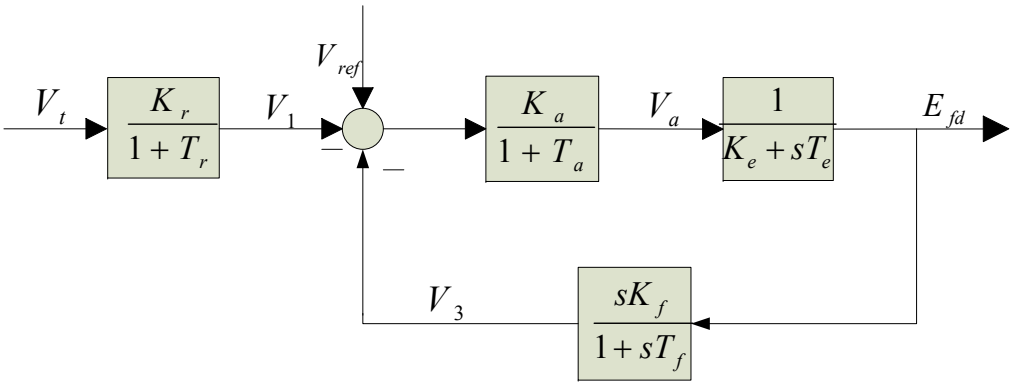

Figure 4.8: IEEE type-AC1A excitation system

$$
\begin{aligned}
\Delta\dot{V}_1 &= -\frac{1}{T_r}\Delta V_1 + \frac{K_r}{T_r}\Delta V_t \\
\Delta\dot{V}_a &= -\frac{K_a}{T_a}\Delta V_a - \frac{K_a}{T_a}\Delta V_3 - \frac{1}{T_a}\Delta V_{ref} + \frac{K_a}{T_a}\Delta V_{ref} \\
\Delta\dot{V}_3 &= \frac{K_f}{T_f T_e}\Delta V_a - \frac{1}{T_f}\Delta V_3 - \frac{K_e K_f}{T_e T_f}\Delta E_{fd} \\
\Delta\dot{E}_{fd} &= \frac{1}{T_e}\Delta V_a - \frac{K_e}{T_e}\Delta E_{fd}
\end{aligned}
\tag{4.47}
$$

Fig. 4.9 illustrates a linear approximation of the turbine governor model [163] and the corresponding ODEs are as follows:

$$
\begin{aligned}
\Delta X_1 &= \frac{1}{R_p}\Delta\omega \\
\Delta\dot{X}_2 &= \frac{1}{R_T}\Delta\dot{X}_1 + \frac{1}{R_T T_R}\Delta X_1 - \frac{R_p}{R_T T_R}\Delta X_2 \\
\Delta\dot{X}_3 &= -\frac{1}{T_G}\Delta X_3 + \frac{1}{T_G}\Delta X_2 \\
\Delta X_4 &= \Delta T_m \\
\Delta\dot{X}_4 &= -\frac{2}{T_\omega}\Delta X_4 + \frac{2}{T_\omega}\Delta X_3 - 2\Delta\dot{X}_3
\end{aligned}
\tag{4.48}
$$

Equations (4.44) to (4.48) are combined to obtained the complete linearised MHPP model as described in (4.49).

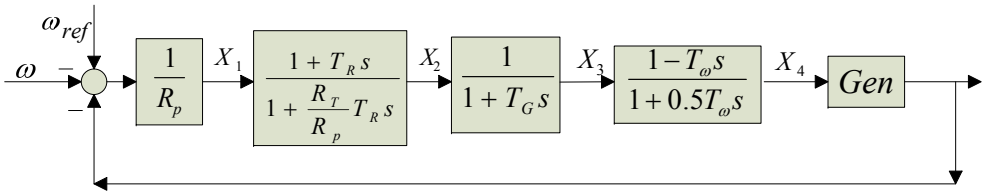

Figure 4.9: Linearised hydro turbine-governor model

$$\Delta\dot{X}_{MHPP} = A_1\Delta X_{MHPP} + B_1\Delta V_{qd} + \beta_1\Delta U_{MHPP} \tag{4.49}$$
$$\Delta y_{MHPP} = C_1\Delta X_{MHPP} + D_1\Delta V_{qd}$$

where, $\Delta X_{MHPP} = [\Delta\dot{E}_q^{"}, \Delta\dot{E}_d^{"}, \Delta\dot{E}_q^{'}, \Delta\omega, \Delta\delta_{rpu}, \Delta V_1, \Delta V_a, \Delta V_3, \Delta E_{fd},$
$\Delta T_m, \Delta X_2, \Delta X_3]$ and $\Delta U_{MHPP} = [\Delta V_{ref}]$.

Prior to connecting the MHPP to the network, output signals (currents) are transferred to the global reference frame and input signals (terminal voltages) are transferred to the local reference frame by substituting (4.21) and (4.22) in (4.49), and the complete MHPP model is given as follows:

$$\Delta\dot{X}_{MHPP} = A_{MHPP}\Delta X_{MHPP} + B_{SG}\Delta V_{QD-MHPP} + \beta_{MHPP}\Delta U_{MHPP} \tag{4.50}$$
$$\Delta I_{QD-MHPP} = C_{MHPP}\Delta X_{MHPP} + D_{SG}\Delta V_{QD-MHPP}$$

4.4.4 Network and Load Models

In this section, network transients are neglected as they are typically in the high frequency range with high damping ratios [169]. The static load is represented by a constant impedance while a 3^{rd} order induction motor (IM) model [163] is considered as a dynamic load, and the ODEs are as follows:

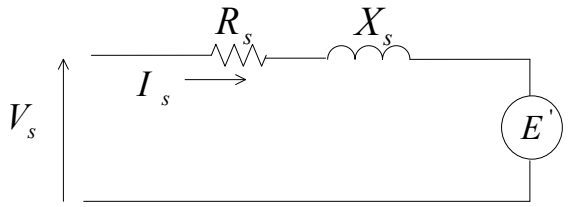

Figure 4.10: Induction machine equivalent circuit

$$
\begin{aligned}
\dot{E}_q^{'} &= -\omega_s s E_d^{'} - \frac{1}{T_\circ^{'}}(E_q^{'} - (X_s - X_s^{'})I_{ds}) \\
\dot{E}_d^{'} &= \omega_s s E_q^{'} - \frac{1}{T_\circ^{'}}(E_d^{'} + (X_s - X_s^{'})I_{qs}) \\
\omega_r &= \frac{1}{2H}(T_e - T_m) \\
s &= \frac{\omega_s - \omega_r}{\omega_s} \\
T_e &= E_d^{'} I_{ds} + E_q^{'} I_{qs}
\end{aligned}
\tag{4.51}
$$

where, s is the slip of the IM.

$$
\begin{aligned}
\Delta \dot{X}_{IM} &= A_{IM}\Delta X_{IM} + B_{IM}\Delta V_{QD-IM} + \beta_{IM}\Delta U_{IM} \\
\Delta I_{QD-IM} &= C_{IM}\Delta X_{IM} + D_{IM}\Delta V_{QD-IM}
\end{aligned}
\tag{4.52}
$$

where, $\Delta X_{IM} = [\Delta E_q^{'}, \Delta E_d^{'}, \Delta\omega_r]$ and $\Delta U_{IM} = [\Delta T_m]$.

The relationship between network voltages and currents referred to the global reference frame is described by the node admittance matrix in (4.53), including the constant impedance loads.

$$\Delta I_{QD} = Y \Delta V_{QD}$$

$$\begin{bmatrix} \Delta I_{Q1} \\ \Delta I_{D1} \\ \vdots \\ \Delta I_{Qm} \\ \Delta I_{Dm} \end{bmatrix} = \begin{bmatrix} G_{11} & B_{11} & \cdots & G_{1m} & B_{1m} \\ -B_{11} & G_{11} & \cdots & -B_{1m} & G_{1m} \\ \vdots & \vdots & & \vdots & \vdots \\ \vdots & \vdots & \cdots & G_{mm} & B_{mm} \\ \vdots & \vdots & \cdots & -B_{mm} & G_{mm} \end{bmatrix} \begin{bmatrix} \Delta V_{Q1} \\ \Delta V_{D1} \\ \vdots \\ \Delta V_{Qm} \\ \Delta V_{Dm} \end{bmatrix} \tag{4.53}$$

4.4.5 Overall Grid Connected Microgrid Model

Node matrix in (4.53) is rearranged as in (4.54).

$$\begin{bmatrix} \Delta I_{dyn} \\ \Delta I_{stat} \\ \Delta I_{pcc} \end{bmatrix} = \begin{bmatrix} Y_{d-d} & Y_{d-s} & Y_{d-pcc} \\ Y_{s-d} & Y_{s-s} & Y_{s-pcc} \\ Y_{pcc-d} & Y_{pcc-s} & Y_{pcc-pcc} \end{bmatrix} \begin{bmatrix} \Delta V_{dyn} \\ \Delta V_{stat} \\ \Delta V_{pcc} \end{bmatrix} \tag{4.54}$$

where, I_{dyn}- current injected into the network by the dynamic devices, I_{stat}- current injected to the network by the nodes without dynamic devices, and I_{pcc}- current injected into the network through the microgrid PCC.

As the currents injected into the microgrid by the nodes without dynamic loads are taken as zero, (4.54) can be further modified as in (4.55).

$$\begin{bmatrix} \Delta I_{dyn} \\ \Delta I_{pcc} \end{bmatrix} = \begin{bmatrix} Y_{11} & Y_{12} \\ Y_{21} & Y_{22} \end{bmatrix} \begin{bmatrix} \Delta V_{dyn} \\ \Delta V_{pcc} \end{bmatrix} \tag{4.55}$$

An expression for the current injected into the network by all the dynamic devices in the microgrid is derived by combining the outputs of the state-space models as follows:

$$\begin{bmatrix} \Delta I_{DER1} \\ \Delta I_{DER2} \\ \vdots \\ \Delta I_{IM1} \\ \Delta I_{IM2} \\ \vdots \end{bmatrix} = \begin{bmatrix} C_{DER1} & 0 & \cdots & 0 & 0 & \cdots \\ 0 & C_{DER2} & \cdots & 0 & 0 & \cdots \\ \cdots & \cdots & \cdots & \cdots & \cdots & \cdots \\ 0 & 0 & \cdots & C_{IM1} & 0 & \cdots \\ 0 & 0 & \cdots & 0 & C_{IM2} & \cdots \\ \cdots & \cdots & \cdots & \cdots & \cdots & \cdots \end{bmatrix} \begin{bmatrix} \Delta X_{DER1} \\ \Delta X_{DER2} \\ \vdots \\ \Delta X_{IM1} \\ \Delta X_{IM2} \\ \vdots \end{bmatrix} + \begin{bmatrix} D_{DER1} & 0 & \cdots & 0 & 0 & \cdots \\ 0 & D_{DER2} & \cdots & 0 & 0 & \cdots \\ \cdots & \cdots & \cdots & \cdots & \cdots & \cdots \\ 0 & 0 & \cdots & D_{IM1} & 0 & \cdots \\ 0 & 0 & \cdots & 0 & D_{IM2} & \cdots \\ \cdots & \cdots & \cdots & \cdots & \cdots & \cdots \end{bmatrix} \begin{bmatrix} \Delta V_{DER1} \\ \Delta V_{DER2} \\ \vdots \\ \Delta V_{IM1} \\ \Delta V_{IM2} \\ \vdots \end{bmatrix}$$

$$\Delta I_{dyn} = C_{dyn}\Delta X_{dyn} + D_{dyn}\Delta V_{dyn} \tag{4.56}$$

An expression for the generator terminal voltages is obtained from (4.55) and (4.56) as follows:

$$\begin{aligned} Y_{11}\Delta V_{dyn} + Y_{12}\Delta V_{pcc} &= C_{dyn}\Delta X_{dyn} + D_{dyn}\Delta V_{dyn} \\ \Delta V_{dyn} &= (Y_{11} - D_{dyn})^{-1}C_{dyn}\Delta X_{dyn} - (Y_{11} - D_{dyn})^{-1}Y_{21}\Delta V_{pcc} \end{aligned} \tag{4.57}$$

Similar to (4.56), state-space forms of individual dynamic devices are combined to obtain the overall system model.

$$\begin{bmatrix} \Delta\dot{X}_{DER1} \\ \Delta\dot{X}_{DER2} \\ \vdots \\ \Delta\dot{X}_{IM1} \\ \Delta\dot{X}_{IM2} \\ \vdots \end{bmatrix} = \begin{bmatrix} A_{DER1} & 0 & \cdots & 0 & 0 & \cdots \\ 0 & A_{DER2} & \cdots & 0 & 0 & \cdots \\ \cdots & \cdots & \cdots & \cdots & \cdots & \cdots \\ 0 & 0 & \cdots & A_{IM1} & 0 & \cdots \\ 0 & 0 & \cdots & 0 & A_{IM2} & \cdots \\ \cdots & \cdots & \cdots & \cdots & \cdots & \cdots \end{bmatrix} \begin{bmatrix} \Delta X_{SG} \\ \Delta X_{DG2} \\ \vdots \\ \Delta X_{IM1} \\ \Delta X_{IM2} \\ \vdots \end{bmatrix} +$$

$$\begin{bmatrix} B_{DER1} & 0 & \cdots & 0 & 0 & \cdots \\ 0 & B_{DER2} & \cdots & 0 & 0 & \cdots \\ \cdots & \cdots & \cdots & \cdots & \cdots & \cdots \\ 0 & 0 & \cdots & B_{IM1} & 0 & \cdots \\ 0 & 0 & \cdots & 0 & B_{IM2} & \cdots \\ \cdots & \cdots & \cdots & \cdots & \cdots & \cdots \end{bmatrix} \begin{bmatrix} \Delta V_{DER1} \\ \Delta V_{DER2} \\ \vdots \\ \Delta V_{IM1} \\ \Delta V_{IM2} \\ \vdots \end{bmatrix} +$$

$$\begin{bmatrix} \beta_{DER1} & 0 & \cdots & 0 & 0 & \cdots \\ 0 & \beta_{DER2} & \cdots & 0 & 0 & \cdots \\ \cdots & \cdots & \cdots & \cdots & \cdots & \cdots \\ 0 & 0 & \cdots & \beta_{IM1} & 0 & \cdots \\ 0 & 0 & \cdots & 0 & \beta_{IM2} & \cdots \\ \cdots & \cdots & \cdots & \cdots & \cdots & \cdots \end{bmatrix} \begin{bmatrix} \Delta U_{DER1} \\ \Delta U_{DER2} \\ \vdots \\ \Delta U_{IM1} \\ \Delta U_{IM2} \\ \vdots \end{bmatrix}$$

$$\Delta\dot{X}_{dyn} = A_{dyn}\Delta X_{dyn} + B_{dyn}\Delta V_{dyn} + \beta_{dyn}\Delta U_{dyn} \tag{4.58}$$

Substituting (4.57) into (4.58) yields:

$$\Delta\dot{X}_{dyn} = A_{dyn}\Delta X_{dyn} + B_{dyn}(Y_{11} - D_{dyn})^{-1}C_{dyn}\Delta X_{dyn} - B_{dyn}(Y_{11} - D_{dyn})^{-1}Y_{21}\Delta V_{pcc} + \beta_{dyn}\Delta U_{dyn}$$

$$\Delta\dot{X}_{dyn} = M_1\Delta X_{dyn} + M_2\Delta V_{pcc} + \beta_{dyn}\Delta U_{dyn} \tag{4.59}$$

where, $M_1 = [A_{dyn} + B_{dyn}(Y_{11} - D_{dyn})^{-1}C_{dyn}]$ and $M_2 = [-B_{dyn}(Y_{11} - D_{dyn})^{-1}Y_{21}]$.

From (4.55) an expression for the current through the microgrid PCC can be obtained as follows:

$$\Delta I_{pcc} = Y_{21}\Delta V_{dyn} + Y_{22}\Delta V_{pcc}$$

$$\Delta I_{pcc} = Y_{21}(Y_{11} - D_{dyn})^{-1}C_{dyn}\Delta X_{dyn} - Y_{21}(Y_{11} - D_{dyn})^{-1}Y_{21}\Delta V_{pcc} + Y_{22}\Delta V_{pcc}$$

$$\Delta I_{pcc} = N_1\Delta X_{dyn} + N_2\Delta V_{pcc} \tag{4.60}$$

$$\Delta\omega_{ref} = R\Delta X_{dyn} \tag{4.61}$$

where, $N_1 = [Y_{21}(Y_{11} - D_{dyn})^{-1}C_{dyn}]$ and $N_2 = [-Y_{21}(Y_{11} - D_{dyn})^{-1}Y_{21} + Y_{22}]$. $\Delta\omega_{ref}$ corresponding to the global reference frame in the microgrid is taken as an output from the microgrid model.

Equations (4.59) and (4.60) describe the microgrid in the form of (4.1) and (4.2). Thus, the node matrix is rearranged and combined with the equations of the dynamic devices in the microgrid such that the grid connected microgrid could be represented in a form analogous to the standard model of a dynamic device connected to the external grid.

4.5 Summary

The main objective of this chapter was to present a novel approach in representing grid connected microgrids as reduced order dynamic equivalents suitable for power system studies.

It was identified that the basic modal method had not been previously applied to grid connected microgrids comprising both inverter and non-inverter interfaced DERs as a model equivalencing methodology. This chapter presented the formulation behind the model equivalencing methodology based on modal method while introducing a new index to identify the dominant modes of the system. Representa-

tion of a microgrid as a single dynamic device connected to the external system was also introduced in this chapter, which can be employed to derive the dynamic equivalent of a grid connected microgrid. Furthermore, detailed modelling of an inverter interfaced DER with power controllers, non-inverter interfaced DER with governor and excitation controllers, induction motor load and network were presented as a base for the studies covered in the next chapter.

Chapter 5

Dynamic Equivalent of a Grid Connected Microgrid - Model Validation

5.1 Introduction

This chapter is focused on the application of the dynamic equivalent methodology explained in Chapter 4.

Mathematical models are developed in this chapter for different grid connected microgrids following the modelling procedures presented in Chapter 4. Validity of the dynamic model equivalencing approach is examined under different microgrid operating conditions. Furthermore, the dynamic model equivalencing is applied on microgrids in a multi-microgrid environment in order to show the feasibility of the methodology.

Section 5.2 presents several case studies carried out on a five-bus microgrid system comprising two DERs and two types of loads under different system operating conditions. Scalability of the proposed microgrid model equivalencing approach is demonstrated in Section 5.3 with a larger microgrid model based on the IEEE-13 node test feeder [162]. In Section 5.4, the dynamic equivalencing approach is

applied to a multi-microgrid system. Section 5.5 presents a discussion on the implementation of the proposed methodology in simulation platforms, performance of the proposed approach, and other practical aspects. A chapter summary is presented in Section 5.6.

5.2 Case Study 1 - Five Bus System

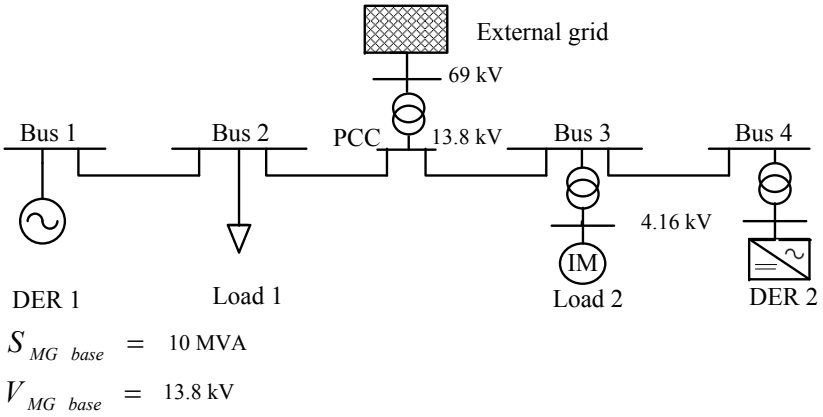

Figure 5.1: Single line diagram of the Microgrid System - 1

In this section, the dynamic equivalent model was derived for a five-bus microgrid model comprising two DERs and two loads. Different operating conditions such as power export mode, power import mode, and load variations were considered in order to validate the equivalent model. Steady state operating conditions of the microgrid system were obtained from a load flow analysis conducted on a non-linear microgrid model developed in DIgSILENT PowerFactory. As explained in Chapter 4, linearised model of the microgrid system was developed and a full eigenvalue analysis was carried out in MATLAB. In the microgrid system, the local reference frame of DER 1 was locked to the rotor of DER 1, and the global d-q reference frame was defined at the terminal of DER 1 (Bus 1). At the DER 2, local d-axis was assumed to be in the direction of the voltage vector at Bus 4.

5.2.1 Power Import from the External Grid

The single line diagram of the Microgrid System - 1 consisting of a 13.8 kV radial distribution feeder connected to the external grid (fault level = 1200 MVA, X/R=10) through a 69 kV/13.8 kV, 10 MVA transformer is illustrated in Fig. 5.1. The study system comprises a 5 MVA MHPP (DER 1) operating at terminal voltage control mode (Bus 1), a 1.5 MW, unity p.f. inverter interfaced DER (DER 2) operating at constant power factor control mode (Bus 4), a static load of 4.2 MW/1.2 MVAr at Bus 2, and an induction motor load of 1.42 MW, 0.85 p.f. connected through a 13.8 kV/4.16 kV, 2 MVA transformer (Bus 3). Details of the parameters of the SG, IM and the network are presented in the Appendix A, while the steady state operating conditions are presented in Table 5.1. It can be observed that the external grid was supplying active and reactive power to cater for the local demand of the microgrid.

Table 5.1: Steady state operating conditions of the microgrid components in power import mode

Microgrid component	Steady state operating condition
DER 1	4.00 MW/1.23 MVAr
DER 2	1.50 MW/0.00 MVAr
Load 1	4.20 MW/1.20 MVAr
Load 2	1.40 MW/0.84 MVAr
External grid	0.13 MW/0.88 MVAr

In order to validate the linearised MATLAB model, the microgrid was modelled in DIgSILENT PowerFactory, and the same small disturbance was applied to both models. Fig. 5.2 illustrates the responses of the current and voltage of DER 2 of the microgrid system obtained from the linearisd DIgSILENT PowerFactory model and MATLAB model for a 2 % step decrease in the real power output of DER 2 (P_{out}) at $t = 5$ s respectively. Comparison of the results in Fig. 5.2 (a) and Fig. 5.2 (b) from the DIgSILENT and MATLAB models indicates similar behaviour of the observed signals. The slight differences between the results from DIgSILENT PowerFactory model and the MATLAB model are due to the differences in the method of im-

plementation and the time delays associated with the measurement and calculation blocks.

As described in Section 4.4.3 of Chapter 4, the dominant modes to be retained in the equivalent model were calculated using the new index $\sigma_{i-normalised}$. Fig. 5.3 illustrates the indices corresponding to all eigenvalues. For this particular case study, modes corresponding to eigenvalues with normalised real parts less than 10.0 %, including two low frequency oscillatory modes were selected as the dominant modes. Eigenvalues and the dominant states corresponding to the modes retained in the equivalent microgrid model are given in Table 5.2. Corresponding matrices γ_r, $B_r^{'}$, $C^{'}$, and $D^{'}$ in (4.14) and (4.19) were calculated in MATLAB according to the description given in Section 4.3 of Chapter 4, which reduced the 29^{th} order model to an 18^{th} order equivalent model.

Responses of the full order model and reduced order model of the microgrid system for a 2 % step decrease in active power output P_{out} of DER 2 at $t = 5$ s are shown in Fig. 5.4. It can be observed from the figures that responses obtained from the full order model and reduced order equivalent model are in good agreement.

Table 5.2: Dominant modes for the power import mode

Mode	Eigenvalue	Dominant states
5	-110	Exciter of the SG (ΔV_1)
6	-74.4	Exciter of the SG (ΔE_{fd})
7	-37.3	Turbine-governor control of the SG (ΔX_1)
8,9	-2.05$\pm$12.95i	Rotor angle and speed deviation of the SG ($\Delta\omega, \Delta\delta_{rpu}$)
10	-3.08	Turbine-governor control of the SG (ΔX_2)
11	-0.61	Exciter of the SG (ΔV_3)
12	-1.09	Turbine-governor control of the SG (ΔT_m)
19	-149.0	Inverter state on DER 2 (ΔI_{q2})
20	-148.8	Inverter state on DER 2 (ΔI_{d2})
21,22	-10.98$\pm$11.41i	Induction motor load ($\Delta E_q^{'}, \Delta\omega_{IM}$)
23	-4.87	d-axis current controller of DER 2 (Δe_{di})
24	-4.85	q-axis current controller of DER 2 (Δe_{qi})
25	-21.9	Induction motor load ($\Delta E_d^{'}$)
26	-26.0	Active power controller of DER 2 (Δi_{di})
27	-25.0	Reactive power controller of DER 2 (Δi_{qi})
30	-129	Exciter of the SG (ΔV_a)

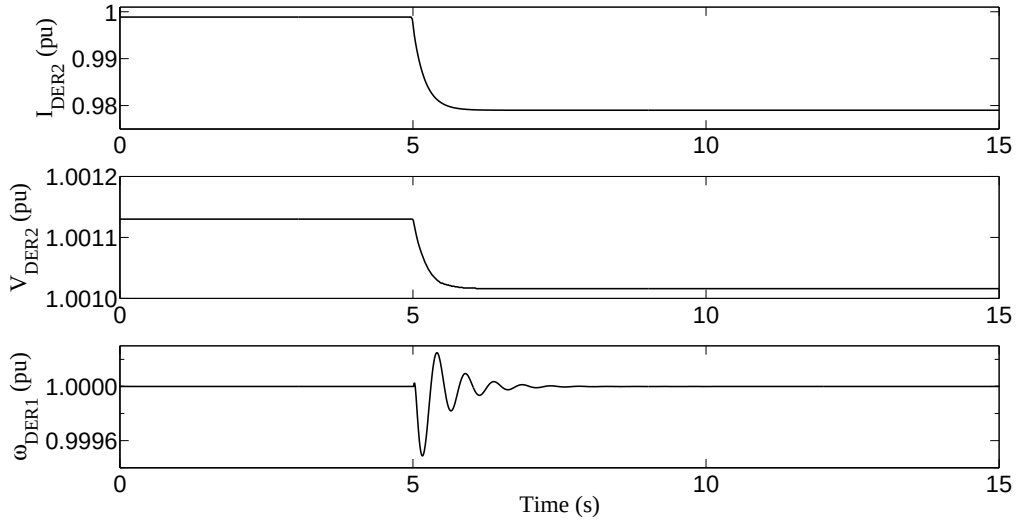

(a)

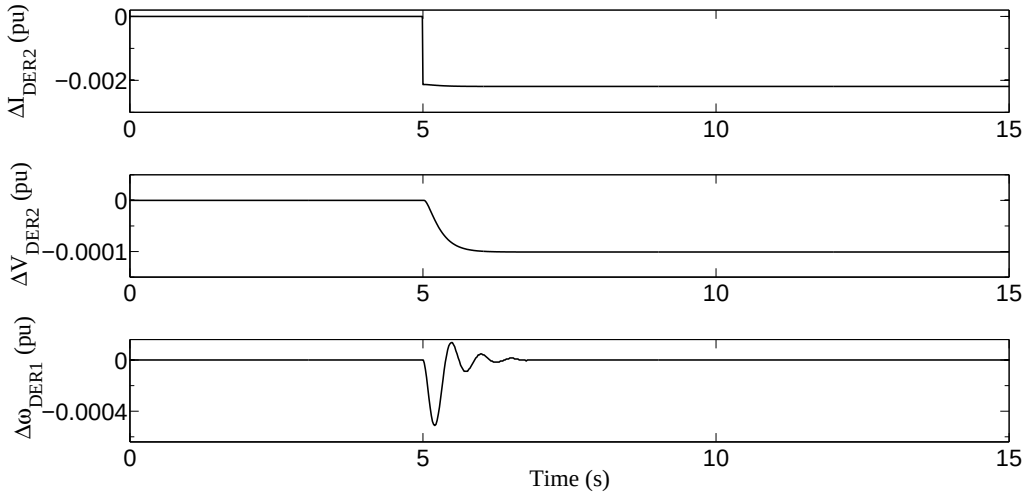

(b)

Figure 5.2: System responses from (a) DIgSILENT model and (b) the MATLAB model due to a 2 % step decrease in P_{out} of DER 2

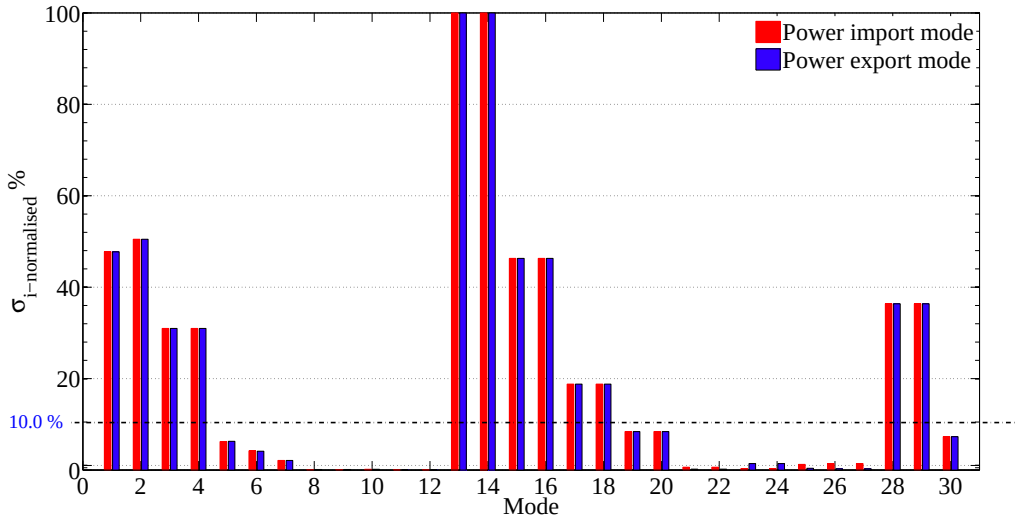

Figure 5.3: Normalised real parts of the eigenvalues for power import and export modes of the Microgrid System - 1

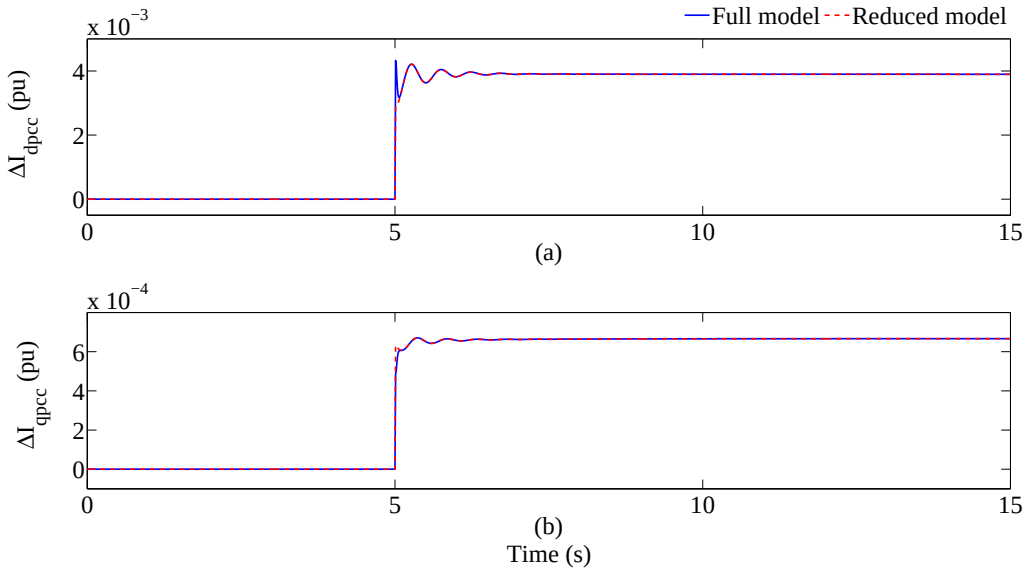

Figure 5.4: Deviations of the d-axis and q-axis currents through the microgrid PCC due to a 2 % step decrease in P_{out} of DER 2 in power import mode

5.2.2 Power Export to the External Grid

In this scenario, total load of the microgrid and the DER 1 (MHPP) rating were unchanged relative to the previous scenario (power import mode) in Section 5.2.1, while the rating of DER 2 was altered to 5 MVA operating at unity p.f. The corresponding steady state operating conditions are presented in Table 5.3, where the negative values indicate power import into the microgrid. It can be observed that

the additional active power generated in the microgrid was fed to the external grid while reactive power was supplied by the external grid to cater the local demand of the microgrid. Similar to the previous scenario, modes corresponding to eigenvalues with normalised real parts less than 10.0 %, including two low frequency oscillatory modes were selected as the dominant modes as illustrated in Fig. 5.3. Eigenvalues and the dominant states corresponding to the retained modes are given in Table 5.4, reducing the 29^{th} order model to a 18^{th} order model. It is to be noted that the eigenvalues have changed due to the change in the operating mode of the microgrid.

Table 5.3: Steady state operating conditions of the microgrid components in power export mode

Microgrid component	Steady state operating condition
DER 1	4.00 MW/1.11 MVAr
DER 2	5.00 MW/0.00 MVAr
Load 1	4.20 MW/1.20 MVAr
Load 2	1.40 MW/0.84 MVAr
External grid	-3.30 MW/1.15 MVAr

Table 5.4: Dominant modes for power export modes

Power export mode		
Mode	Eigenvalue	Dominant states
5	-111	Exciter of the SG (ΔV_1)
6	-72.9	Exciter of the SG (ΔE_{fd})
7	-37.3	Turbine-governor control of the SG (ΔX_1)
8,9	-2.26$\pm$12.63i	Rotor angle and speed deviation of the SG ($\Delta\omega, \Delta\delta_{rpu}$)
10	-2.97	Turbine-governor control of the SG (ΔX_2)
11	-0.61	Exciter of the SG (ΔV_3)
12	-1.09	Turbine-governor control of the SG (ΔT_m)
19	-149.0	Inverter state on DER 2 (ΔI_{q2})
20	-148.8	Inverter state on DER 2 (ΔI_{d2})
21,22	-3.38$\pm$5.95i	Induction motor load ($\Delta E_q^{'}, \Delta\omega_{IM}$)
23	-25.1	Active power controller of DER 2 (Δi_{di})
24	-25.0	Reactive power controller of DER 2 (Δi_{qi})
25	-6.76	Induction motor load ($\Delta E_d^{'}$)
26	-4.93	d-axis current controller (Δe_{di})
27	-4.90	q-axis current controller (Δe_{qi})
30	-129	Exciter of the SG (ΔV_a)

Responses of the full order model and reduced order equivalent model of the

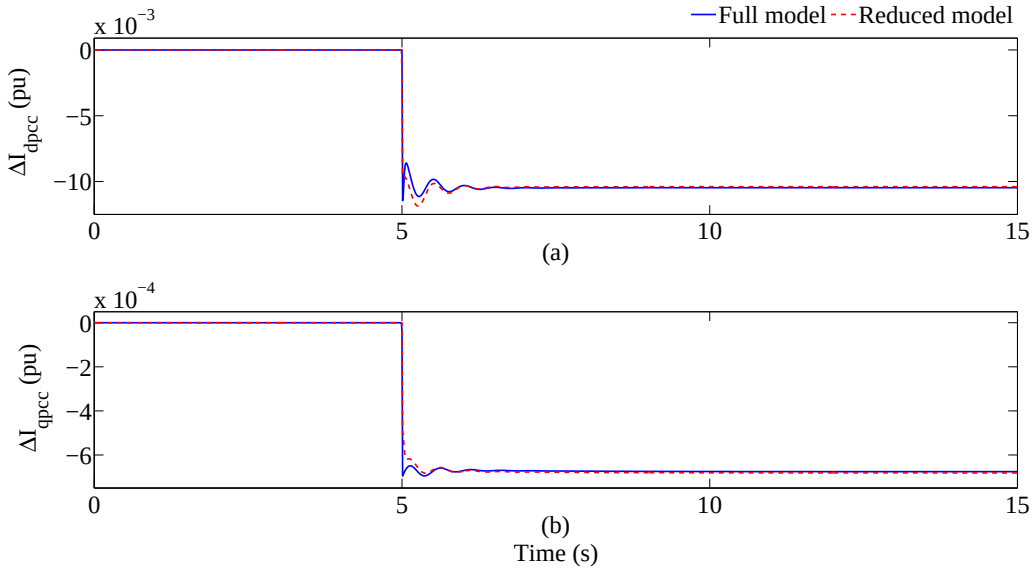

Figure 5.5: Deviations of the d-axis and q-axis currents through the microgrid PCC due to a 2 % step decrease in P_{out} of DER 2 in power export mode

microgrid system for a 2 % step decrease in active power output P_{out} of DER 2 at $t = 5$ s are shown in Fig. 5.5. It can be observed from the figures that the disturbance responses of the retained states and microgrid currents obtained from the equivalent model are in good agreement with those of the full model.

5.2.3 Variation of Loading Conditions

In order to study the system mode variation under different loading conditions, two different loading conditions were considered: (i) light load conditions with 50 % of nominal load, and (ii) heavy loading conditions with 110 % of nominal load. Fig. 5.6 illustrates the effects of the loading conditions on eigenvalues corresponding to the dominant modes of the microgrid system for both power import and export modes. It is to be noted that the dynamic equivalent of the microgrid system changes with system loading conditions. In Fig. 5.6, it can be observed that for the particular study system, load variation has an insignificant effect on non-oscillatory modes. As expected, with over loading conditions, oscillatory modes tend to move towards the unstable region. However, for this particular system, oscillatory modes varied within a very small region. Therefore, as the control strategies and controller param-

eters of DER units remained unchanged during grid connected operation, operating conditions with nominal load were considered for obtaining the equivalent model. Fig. 5.7 illustrates the deviations of the d-axis and q-axis currents through the microgrid PCC due to a 50 % load decrease in power import mode, obtained from the full model and the equivalent model of the Microgrid System - 1. It is to be noted that the dynamic equivalent of the microgrid system changes with system loading conditions.

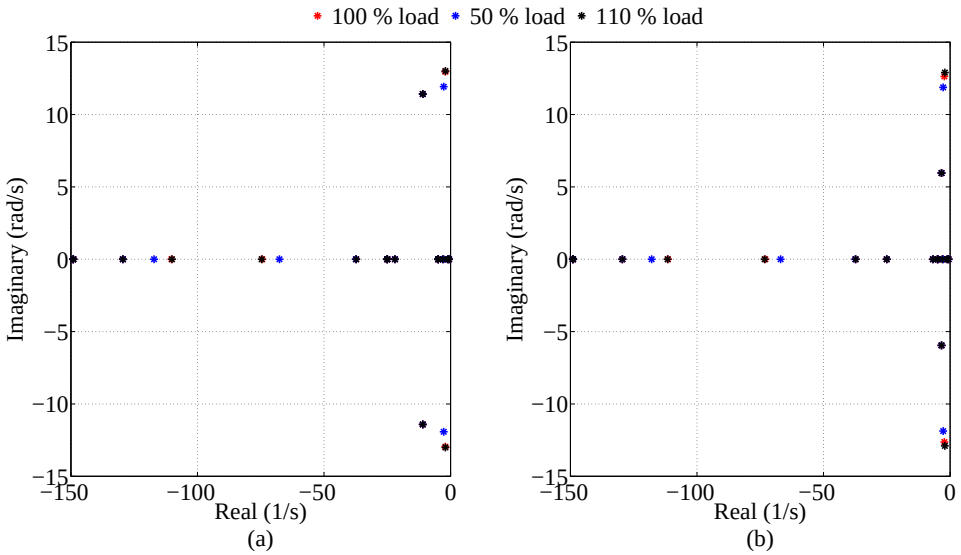

Figure 5.6: Dominant modes under different loading conditions for (a) power import, and (b) power export modes in Microgrid System - 1

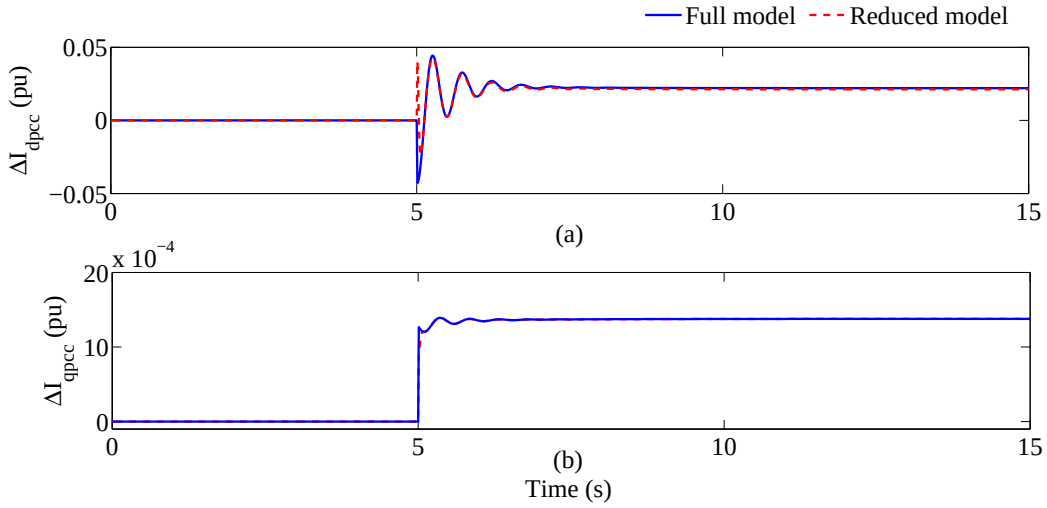

Figure 5.7: Deviations of the d-axis and q-axis currents through the microgrid PCC due to a 50 % load decrease in power import mode

5.2.4 Response to Short-Circuit Faults

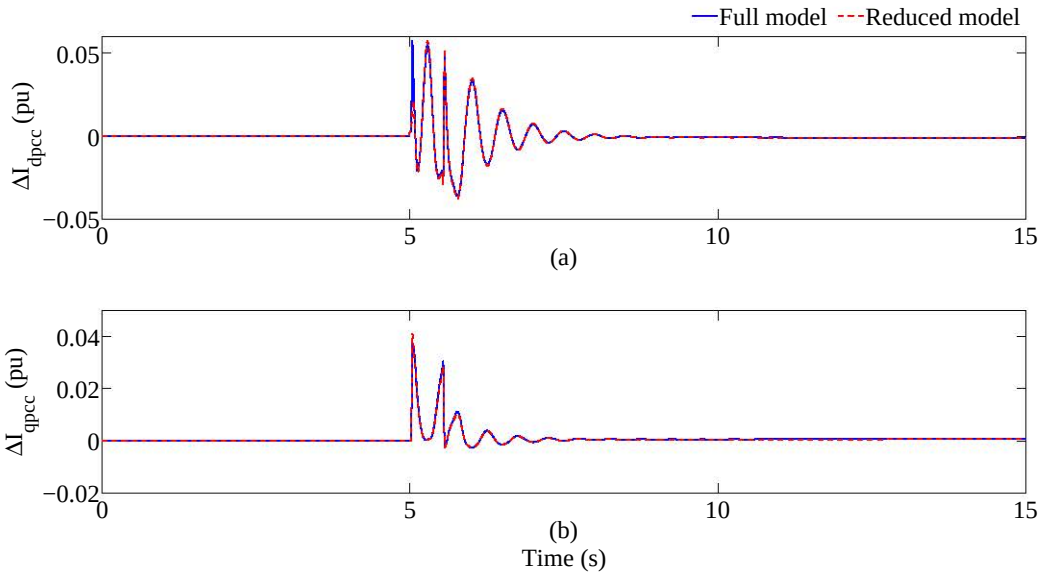

Figure 5.8: Deviations of the d-axis and q-axis currents through the microgrid PCC due to a distant fault in power import mode

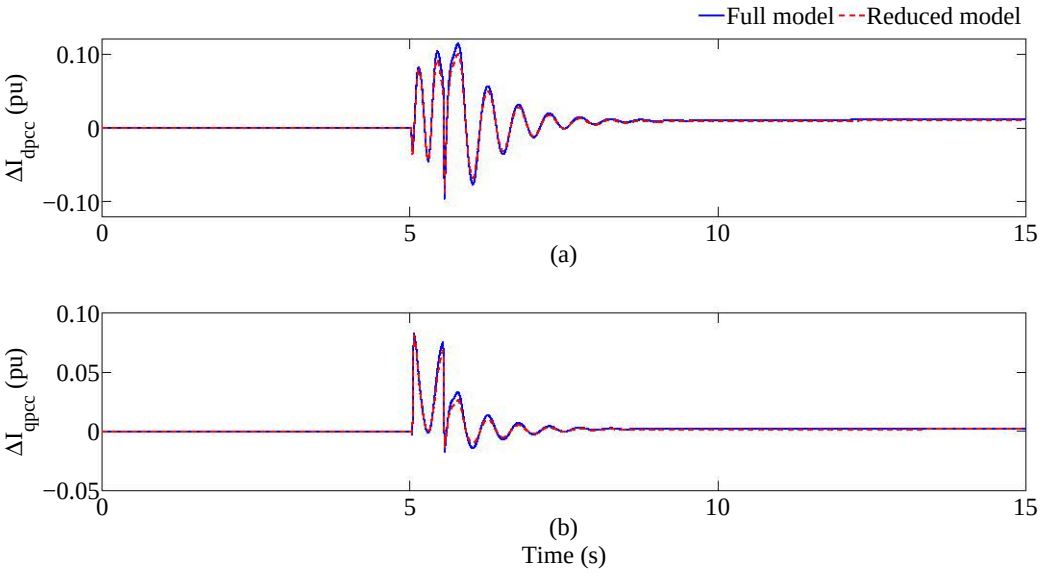

Figure 5.9: Deviations of the d-axis and q-axis currents through the microgrid PCC due to a distant fault in power export mode

In this section, the impact of a reflection of a distant three-phase short-circuit fault in the external grid on the microgrid PCC was analysed. A fault was created in the external grid at $t = 5\,\mathrm{s}$ and cleared after $0.5\,\mathrm{s}$. It can be observed from Fig. 5.8 and Fig. 5.9 that the reduced order equivalent model of the microgrid has

sufficiently captured the dynamic characteristics of the full order model during both power import and export modes.

5.3 Case Study 2 - IEEE-13 Node Distribution Network

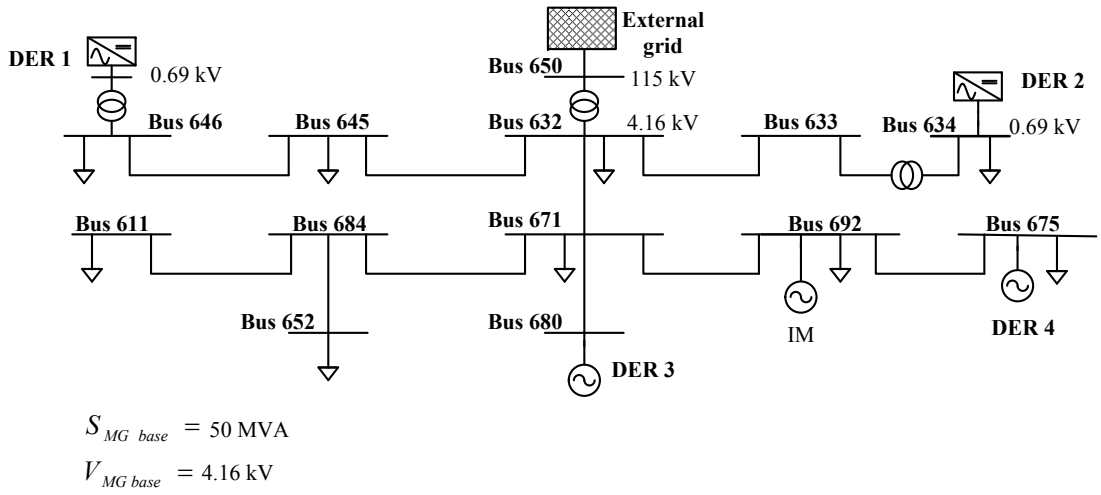

Figure 5.10: Single line diagram of the microgrid system based on the IEEE-13 node distribution test feeder

In order to demonstrate the scalability of the proposed microgrid model equivalencing approach, a large microgrid system was developed based on the IEEE-13 node distribution test feeder [162]. As illustrated in Fig. 5.10, necessary modifications were made to the IEEE-13 node distribution test feeder in order to obtain a three-phase balanced microgrid system. The microgrid system was connected to the external grid through a 115 kV/4.16 kV, 10 MVA transformer. Two inverter interfaced DERs (each rated at 0.5 MVA) operating at power factor mode were connected to Bus bar 646 and Bus bar 634. Two SG based DERs of 1.5 MVA and 5 MVA with exciter and governor controls were connected to Bus bar 680 and Bus bar 675 respectively. In addition to a static load, an induction motor load of 1.42 MW, 0.85 p.f. was connected to Bus bar 692. Load and network data of the 13 node microgrid system are presented in Appendix A. The grid connected microgrid exported active power to the external grid and imported reactive power to cater for the local

demand.

In the microgrid system, the local reference frames of DER 3 and DER 4 were locked to the rotors, and the global d-q reference frame was defined at the terminal of DER 4. In DER 1 and DER 2, local d-axes were assumed to be in the direction of the voltage vectors at Bus bar 646 and Bus bar 634 respectively.

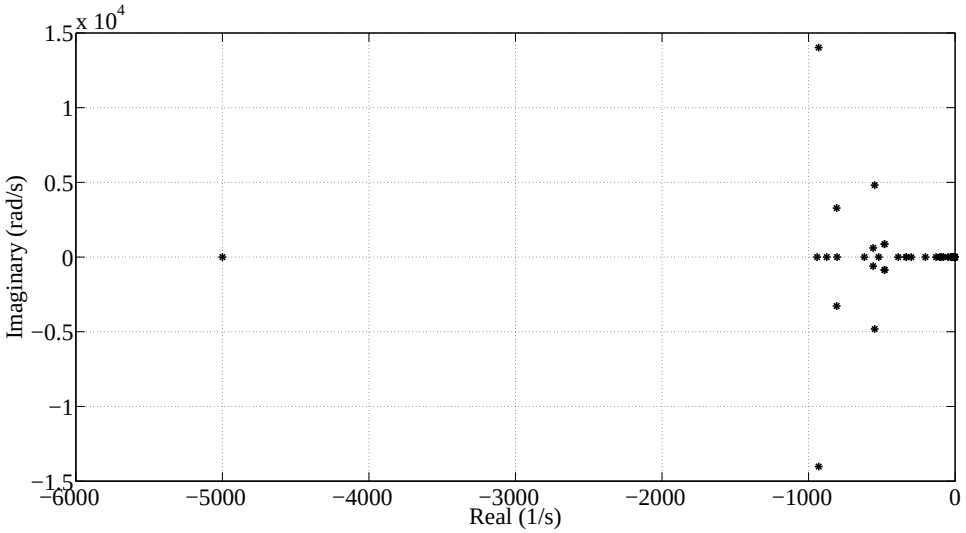

Figure 5.11: Eigenvalues of the 13 node microgrid system

Fig. 5.11 illustrates the eigenvalues of the microgrid system. From the eigenvalue analysis, three oscillatory modes were identified and selected to be retained in the reduced order equivalent model. The remainder of the dominant modes were identified using the normalised real part of eigenvalues as described in Section 4.3.3. For this particular microgrid system, modes corresponding to the eigenvalues with normalised real parts less than 5.0 % were selected as the non-oscillatory dominant modes. Using the model equivalencing approach described in Section 4.3, the 54^{th} full order model was reduced to a 35^{th} order equivalent model, and the retained modes are presented in Table 5.5.

The reduced order microgrid model was subjected to several disturbances in order to find the suitability of the proposed approach. Fig. 5.12 illustrates the system responses of the microgrid due to a 0.1 pu step decrease in the output active power (P_{out}) of DER 1 and DER 2 at $t = 5$ s and $t = 10$ s respectively. Furthermore,

Table 5.5: Dominant modes of the 13 node microgrid system

Mode	Eigenvalue	$\sigma_{i-normalised}\%$	Mode	Eigenvalue	$\sigma_{i-normalised}\%$
5	-92.35	1.85	37	-49.46	0.98
6	-94.04	1.88	38,39	-1.98±17.13i	0.04
7	-27.82	0.56	40	-16.11	0.32
8	-27.23	0.55	41,42	-1.91±10.27i	0.04
9	-3.83	0.07	43,44	-1.96±7.20i	0.04
10	-2.89	0.05	45	-6.08	0.12
19	-6.73	0.13	46	-3.75	0.07
20	-4.83	0.09	47	-2.78	0.05
21	-31.19	0.62	48	-2.01	0.04
22	-31.09	0.62	49	-0.64	0.01
34	-202.4	4.04	50	-1.12	0.02
35	-105.5	2.11	51	-0.83	0.01
36	-79.47	1.58	54	-129.4	2.58

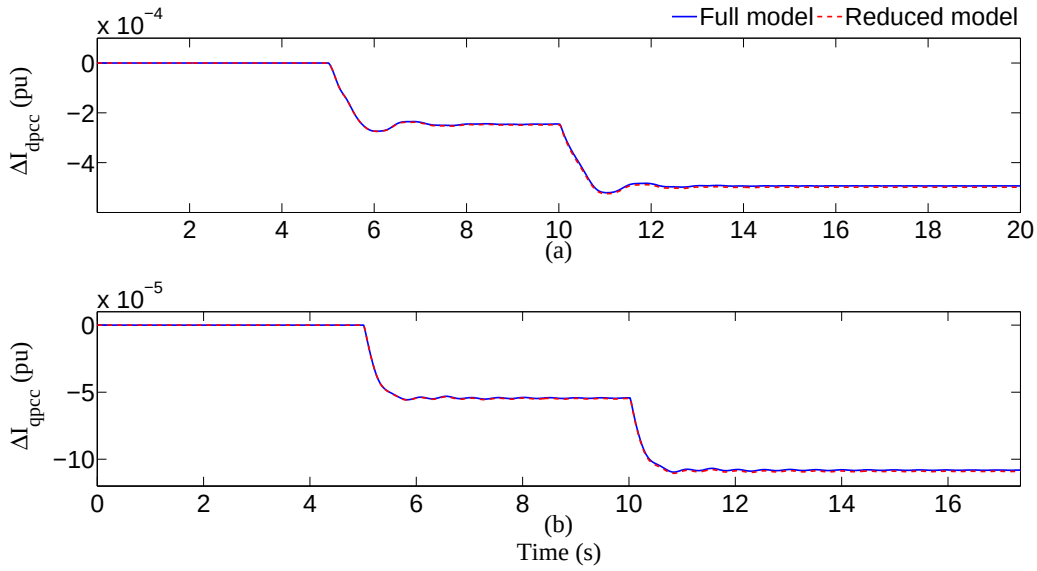

Figure 5.12: Deviations of the d-axis and q-axis currents through the microgrid PCC due to a decrease in P_{out} of DER 1 and DER 2

deviations of the d-axis and q-axis currents through the microgrid PCC, and the responses of the rotor speed of DER 3 and DER 4 due to a 50 % increase in the load at Bus bar 646 at $t = 5$ s are illustrated in Fig. 5.13 and Fig. 5.14 respectively.

In addition, a three-phase short-circuit fault was created within the external grid at $t = 5$ s and cleared after 0.5 s. The corresponding deviations of the currents through the microgrid PCC are presented in Fig. 5.15.

It can be observed from Fig. 5.12 to Fig. 5.15, that responses obtained from

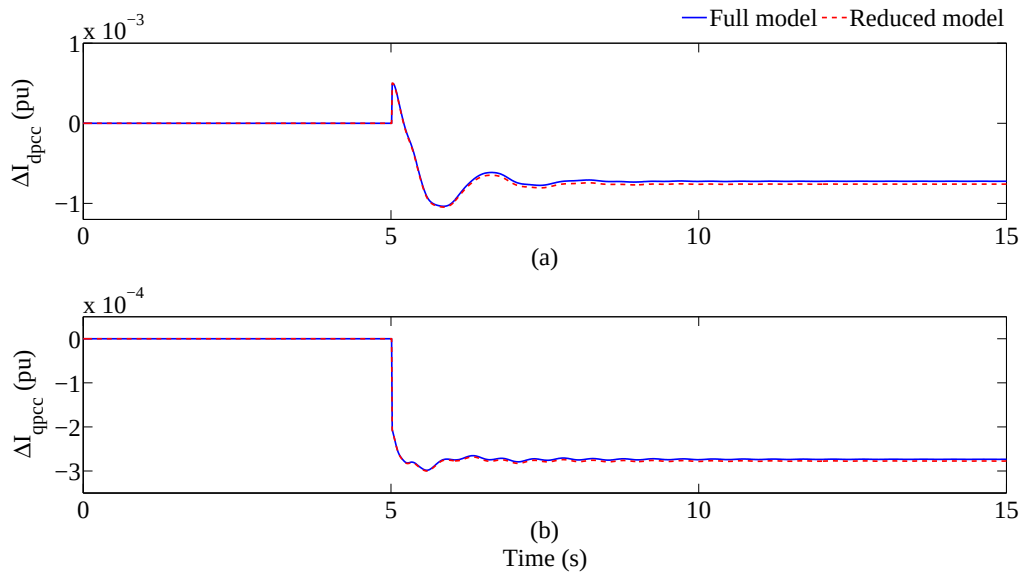

Figure 5.13: Deviations of the d-axis and q-axis currents through the microgrid PCC due to an increase in load at Bus bar 646

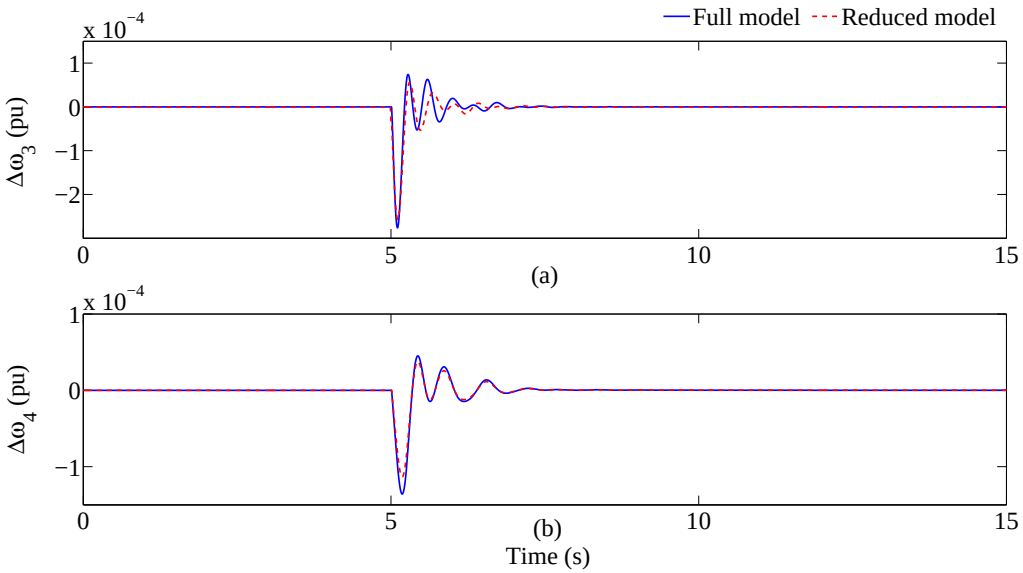

Figure 5.14: Deviations of rotor speed of the DER 3 and DER 4 due to an increase in load at Bus bar 646

the full model and reduced order equivalent model are in close agreement. The selected modes have retained the important dynamics of the microgrid model, which confirms the suitability of the proposed dynamic model equivalencing approach in representing grid connected large microgrids for power system studies.

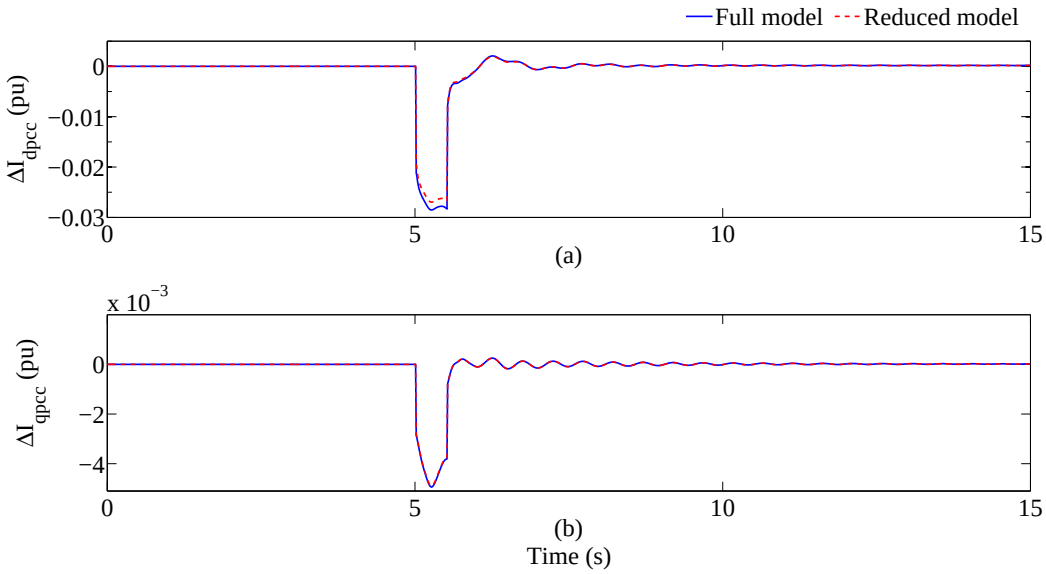

Figure 5.15: Deviations of the d-axis and q-axis currents through the microgrid PCC due to a fault in the external grid

5.4 Case Study 3 - Multi-Microgrid System

In order to validate the model equivalencing approach on grid connected microgrids, a multi-microgrid system illustrated in Fig. 5.16 is considered in this section. The system comprises of three separate microgrids and a 5 MVA, 0.8 p.f. SG connected to the 69 kV network through three 10 MVA, 69 kV/13.8 kV transformers and a 7.5 MVA, 69 kV/13.8 kV transformer respectively. The 69 kV network is connected to the external grid through a 50 MVA, 115 kV/69 kV transformer. Network parameters and load flow data of the multi-microgrid system are presented in Table 5.6 and Table 5.7 respectively. The mode of operation of the five bus system described in Section 5.2.1 were included in MG 1 and MG 2, whereas MG 3 is in the mode of operation of the five bus system considered in Section 5.2.2.

Table 5.6: Network parameters of the multi-microgrid system

R (Ω/km)	0.1
X (Ω/km)	0.3
Bus 3-Bus 1 (km)	2
Bus 1-Bus 5 (km)	2
Bus 2-Bus 5 (km)	2
Bus 4-Bus 2 (km)	2

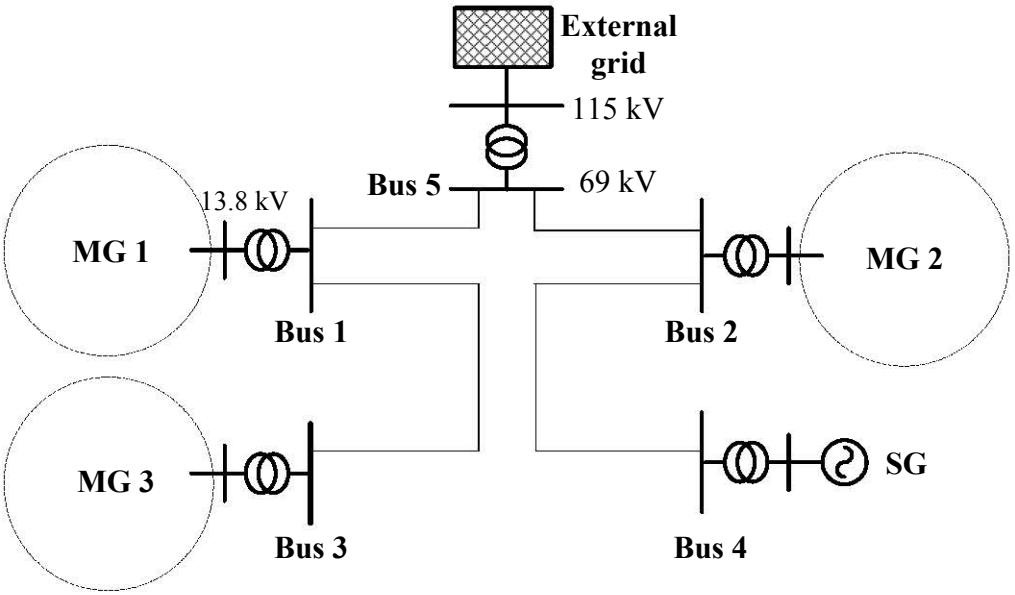

Figure 5.16: Single line diagram of the multi-microgrid system

Table 5.7: Calculated load flow data of the multi-microgrid system

	P (MW)	Q (MVAr)
MG 1	-0.13	-0.49
MG 2	-0.13	-0.49
MG 3	3.31	-0.66
SG	4.00	0.06
External grid	-7.02	1.81

In this case study, the dynamic equivalent model of each microgrid system was derived separately and connected to the 69 kV network along with a reduced order SG model. Use of dynamic equivalent models for microgrid systems resulted in a reduction of total system states from 103 to 59. Fig. 5.17 illustrates the selected eigenvalues of the full order system and the eigenvalues from the system with reduced order models. It can be observed that the system including the equivalent microgrid modes have preserved the dominant eigenvalues of the full order multi-microgrid system.

Fig. 5.18 to Fig. 5.21 illustrate the responses of currents through the PCC of the three microgrids and SG rotor speed deviation caused by a three-phase short-circuit

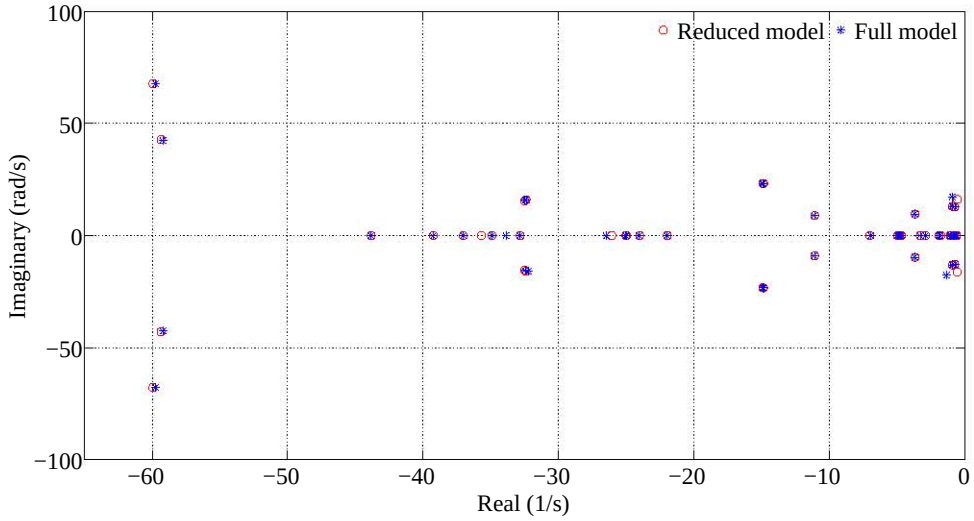

Figure 5.17: Dominant modes of the full order model and the dynamic equivalent model of the multi-microgrid system

fault within the external grid at $t = 5\,\mathrm{s}$. The fault was cleared after $0.5\,\mathrm{s}$, and it can be observed from the figures that reduced order microgrid models have captured the dominant dynamics of the detailed microgrid models.

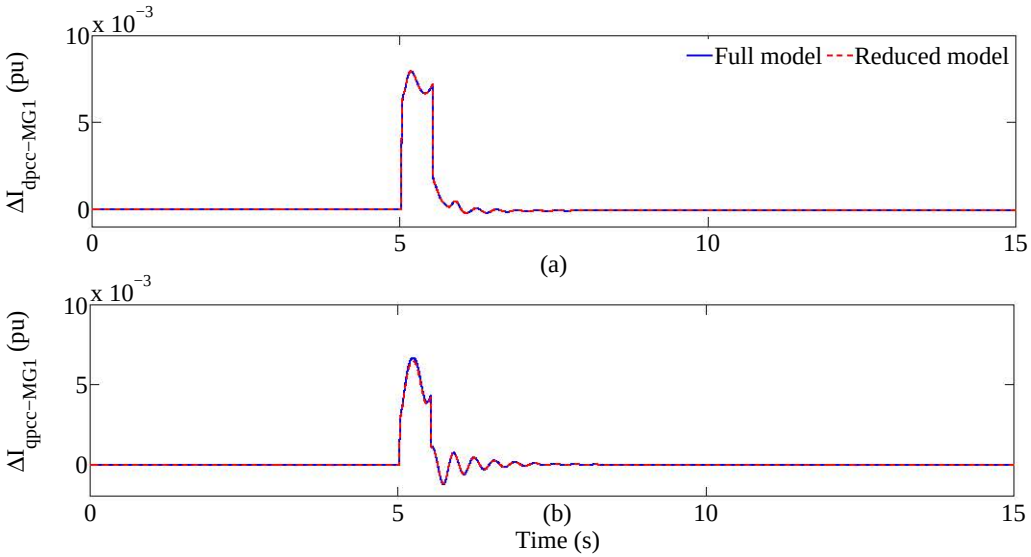

Figure 5.18: Deviations of (a) d-axis current, and (b) q-axis current through PCC of MG 1 caused by a system fault in the external grid

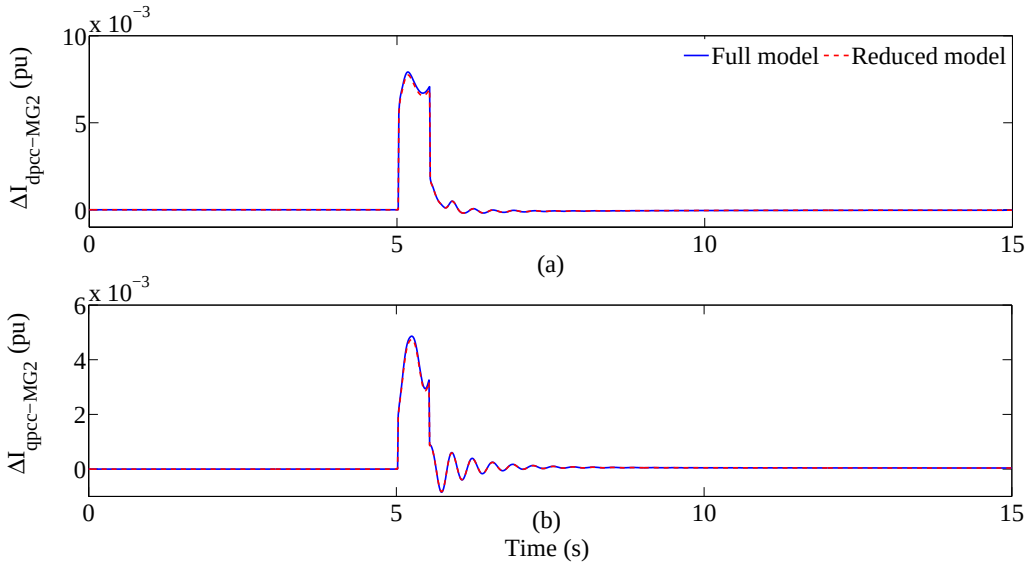

Figure 5.19: Deviations of (a) d-axis current, and (b) q-axis current through PCC of MG 2 caused by a system fault in the external grid

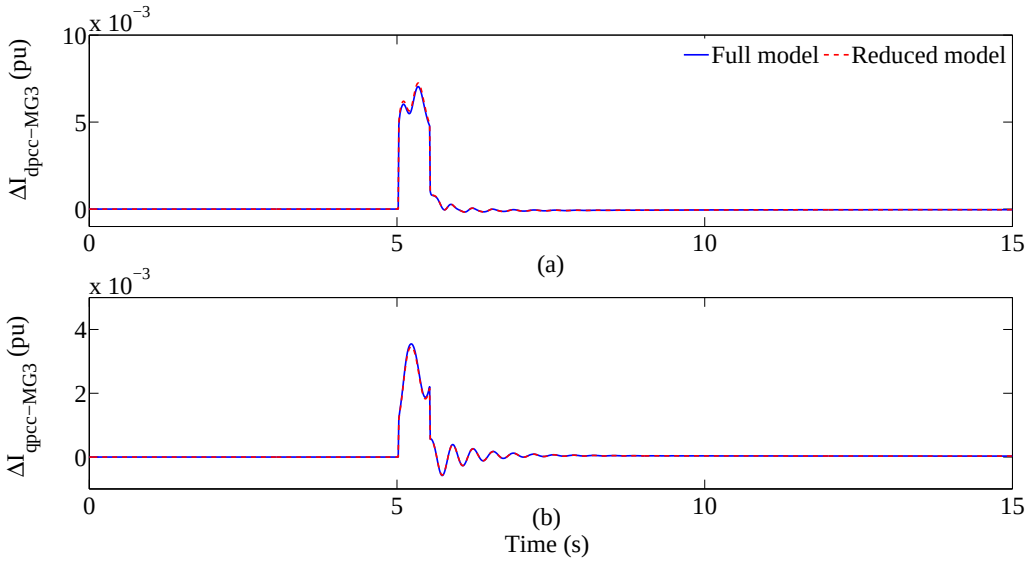

Figure 5.20: Deviations of (a) d-axis current, and (b) q-axis current through PCC of MG 3 caused by a system fault in the external grid

5.5 Discussion

5.5.1 Implementation in Simulation Packages

The dynamic model equivalencing approach for grid connected microgrids presented in this work requires a full eigenvalue analysis of the system. In this approach, insignificant dynamic characteristics when observed from the microgrid PCC are

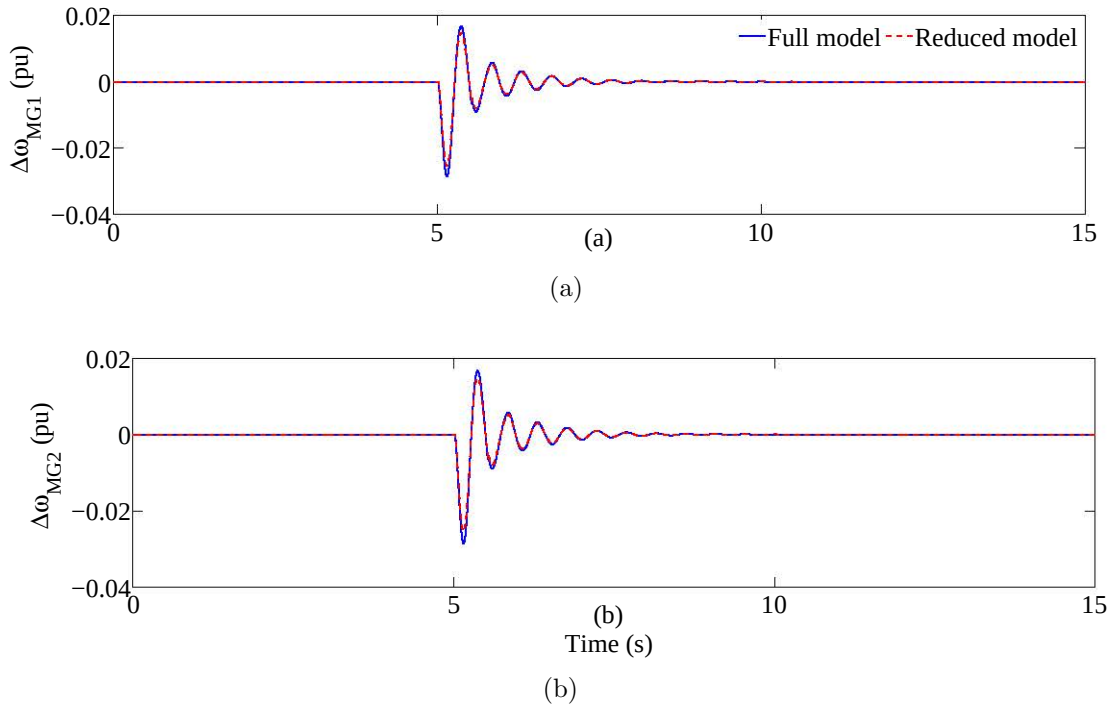

Figure 5.21: Rotor speed deviations of the SGs in (a) MG 1, and (b) MG 2 due to a system fault in the external grid

eliminated from the detailed model. It is difficult to define a common range of system modes to be retained in the equivalent microgrid models due to different types of controllers and dynamic characteristics of DERs and loads. However, once all eigenvalues of the microgrid are available, selection of the dominant modes can be automated by categorising the modes according to their negative real parts. Furthermore, limitations can be incorporated into the algorithm for frequency and damping ratio in selecting the oscillatory modes. After identifying the dominant modes, relevant matrices can be calculated to obtain the equivalent microgrid model as explained in Section 4.3.

As an example, modal analysis can be carried out in DIgSILENT PowerFactory environment, and the eigenvalues, corresponding eigen-vectors and the participation matrix can be exported to MATLAB by interfacing through DIgSILENT engine-mode using Python scripts. After the calculation of the relevant reduced order system matrices in MATLAB, the data can be exported back to the DIgSILENT platform. Alternatively, power system software developers can deploy the method-

ology outlined in this study to develop a separate model reduction module. The equivalent microgrid model can be replaced with a current source having the nominal output current with nominal voltage at the microgrid PCC. According to the deviation of the voltage at the microgrid PCC, deviation of the current flow through the microgrid PCC is calculated using the reduced system matrices. Thus, current output will be a combination of the nominal current and the current perturbation. Graphical representation of such a current source model of a grid connected microgrid is given in Fig. 5.22, where V_{PCC} and I_{PCC} are the steady state voltage and current at the microgrid PCC, and ΔV_{PCC} is the voltage deviation at the microgrid PCC. ΔI_{PCC} is the current deviation through the microgrid PCC which is a function of the dominant state variables and terminal voltages of the dynamic devices within the microgrid. Depending on the capabilities and requirements of different simulation packages, dynamic equivalents of microgrids can be implemented as controlled current sources with nominal output current from the microgrid, where current flow through the microgrid PCC and frequency of the common reference frame are taken as outputs, while voltage at the microgrid PCC is taken as the input to the equivalent model.

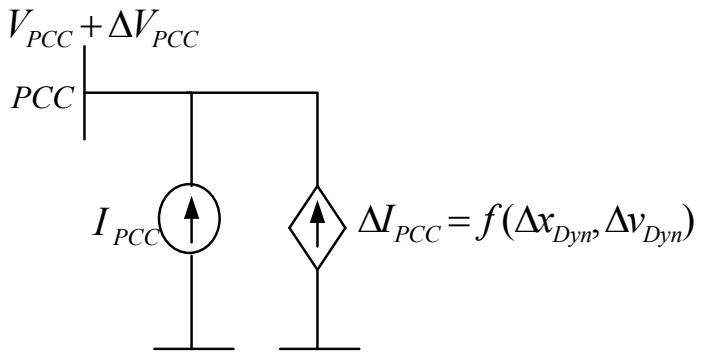

Figure 5.22: Current source model of the grid connected microgrid

5.5.2 Performance of the Proposed Approach and Practical Aspects

Model equivalencing involves a trade off between the model order and the degree to which the characteristics of the original system are reflected in the reduced order

model. In modal methods, if the full order models are to be used in the distribution network dynamic studies, the system matrix (4.1) will be a large square matrix with all system states. However, by using the proposed dynamic model equivalencing approach, the size of the system matrix can be reduced significantly in comparison to a full order model. As demonstrated in the case studies in Section 5.2.1 and Section 5.2.2, 29^{th} order models were reduced to 18^{th} order models. Furthermore, in Section 5.3 and Section 5.4, 54^{th} and 103^{rd} order models were reduced to 28^{th} and 59^{th} order models respectively.

One of the key advantages is the reduction of space/memory required to be allocated for the system matrix in the simulation algorithm. Consequently, execution time of the algorithm will also be reduced. In order to justify the efficiency gained by the model reduction approach, execution times (corresponding to a $10\,s$ simulation time period) required by the MATLAB code to calculate the system output currents using the full and reduced order equivalent models are presented in Table 5.8 for comparison. The proposed model equivalencing approach for grid connected microgrids is perceived to become important in the near future as penetration levels of distributed generation, and subsequently generation markets, propagate further into the distribution system. Full order models of grid connected microgrids can be replaced by the dynamic equivalents for stability studies of large power systems comprising multiple grid connected microgrids. This will simplify the analysis of network performance and operation.

Similar to other model reduction methodologies presented in Section 2.4, the proposed approach also has some drawbacks. If a major change in the microgrid system occurs such as an outage in a distribution line or a generator, the equivalent model is required to be modified by calculating the new system eigenvalues and the corresponding matrices γ_r, $B_r^{'}$, $C^{'}$, and $D^{'}$. Similar to other model reduction methods, a generalised reduced order equivalent model cannot be developed in the proposed approach. There is an inherent limitation of the modal method due to linearisation of the system. Thus, this dynamic equivalencing method can be used

Table 5.8: Comparison of the execution times required for the full model and equivalent models

Microgrid system	Order of system matrix		Execution time (s)	
	Full	Reduced	Full	Reduced
5-Bus system-Power import	29^{th}	18^{th}	0.2437	0.0625
5-Bus system-Power export	29^{th}	18^{th}	0.2392	0.0632
13-Bus system	54^{th}	28^{th}	0.5308	0.1516
Multi-microgrid system	103^{rd}	59^{th}	1.2808	0.6408

for system studies when grid connected microgrids are not directly subjected to large internal disturbances or when the investigated disturbances are not placed too close to the microgrid equivalent model. This microgrid model equivalencing methodology is beneficial for large power systems, where microgrids are not part of the study area of interest. If one or more elements within the microgrids are removed, the equivalent models need to be re-derived. This model eqivalencing approach is not applicable for understanding dynamics during islanded mode of operation of microgrids, as the study area of interest is limited to the microgrid itself. Any type of model equivalencing approach is not suitable for identifying how an individual microgrid component or its control system is affected due to a disturbance within the microgrid or external to the microgrid. However, one advantage of this method over the other model training methods is that, once a dynamic equivalent has been obtained for a grid connected microgrid, numerous faults can be analysed in the study system using the same equivalent, as long as faults are not placed too close to the boundary with the equivalent.

It is difficult to define a common range of system modes to be retained in the equivalent microgrid models due to different types of controllers and dynamic characteristics of DERs and loads. As a solution to this issue, selection of dominant modes can be automated by categorising the modes according to their negative real parts. Cut-off value for the proposed index $\sigma_{i-normalised}$ cannot be generalised and

it will vary depending on the microgrid system. For a given microgrid system, the cut-off value for $\sigma_{i-normalised}$ can be decided by weighting the normalised values.

5.6 Summary

The basic modal method has not been previously applied to grid connected hybrid microgrids as a means of deriving dynamic equivalent models. Thus, Chapter 4 proposed an approach in investigating the applicability of modal analysis as a tool for dynamic model equivalencing of grid connected microgrids with inverter and non-inverter interfaced DERs. In this chapter, the proposed approach was validated considering various practical scenarios.

The main objective of this chapter was to demonstrate the application of the dynamic equivalent methodology explained in Chapter 4. In this chapter, model equivalencing methodology was applied to a five-bus microgrid system comprising two DERs and two types of loads. Several case studies were carried out under different operating conditions of the microgrid system. Furthermore, scalability of the proposed microgrid model equivalencing approach was demonstrated using a larger microgrid model based on the IEEE-13 node distribution test feeder and a multi-microgrid system. It could be observed from the responses of the microgrid system states and the microgrid current outputs obtained from the full order model and reduced order equivalent model were in good agreement. Thus, the proposed dynamic model equivalencing on grid connected microgrids based on basic modal method have captured the important dynamics of the full order microgrid systems.

The process of deriving the dynamic equivalent models of grid connected microgrids can be automated in power system simulation software packages and can be replaced with a current source having the nominal output current with nominal voltage at the microgrid PCC. However, there is an inherent limitation of the modal method due to linearisation of the microgrid system. Thus, this dynamic equivalencing method can be used for system studies when grid connected microgrids are

not directly subjected to large internal disturbances or when the investigated disturbances are not placed too close to the boundary with the microgrid equivalent model. However, one advantage of this method over the other model training methods is that, once a dynamic equivalent has been obtained for a grid connected microgrid, numerous faults can be analysed in the study system using the same equivalent, as long as faults are not placed too close to the boundary with the equivalent. Furthermore, this method has a rigorous mathematical basis and provides a good insight into the various modes of oscillations present in the system. As the relative importance of various system characteristics is highly dependent upon the application, a universal model reduction algorithm cannot be proposed.

Chapter 6

Development of a Capability Diagram for a Grid Connected Microgrid

6.1 Introduction

A grid connected microgrid can be viewed as a single generating entity or a load depending on its power import or export at the grid supply point. Similar to conventional generators, grid connected microgrids have the potential to be able to participate in the energy market in the future in order to achieve technical, financial and environmental benefits. Effective participation in the energy markets requires numerous planning tools and comprehensive understanding of the full capability of such microgrids. Active and reactive power exchange capability of a grid connected microgrid is one of the important features that needs to be known by the distribution network service provider (DNSP) or any other party in order to successfully participate in the future energy market. Hence, the development of an active and reactive power capability diagram of a grid connected microgrid will further facilitate in market operations.

Unlike in a single generator unit with its own machine limitations, active and

reactive power transfer limits of a grid connected microgrid depend on many factors including different and multiple machine capability limits, local load demands, and distribution line capacities. As stated in Chapter 2, no research knowledge exists related to identifying power transfer capability limits of grid connected microgrids with the external grid. Absence of such knowledge is the primary drive for the work presented in this chapter, which presents a systematic approach for deriving a capability diagram for a grid connected microgrid. The diagram represents the active and reactive power exchange capability of the microgrid with the external grid.

The capability diagram can be used as a tool to assist in understanding the full active and reactive power capability of the microgrid, to allow optimum use of distributed energy resources, and to provide coordinated support to the network through ancillary services such as voltage support as required. As stated previously, this graphical tool can be utilised for efficient and effective operation in the markets.

The methodology for developing a capability diagram of a grid connected microgrid is presented in this chapter, and it is not relevant for islanded operation of microgrids, since the market participation of the microgrid is solely focused on supplying power to the external grid.

In order to derive the capability diagram, an optimisation model is developed in Section 6.2 and subsequently, simplified capability diagrams are obtained for two grid connected microgrids.

Deriviation of a detailed and realistic capability diagram considering different load modelling aspects, individual machine limitations is presented in Section 6.3. Impact of different voltage regulation systems and individual distributed generator outages on microgrid power exchange capability is also analysed in this section.

Section 6.4 analyses the effects of plug-in hybrid electric vehicles (PHEVs) and reactive power devices on the microgrid capability diagram.

Section 6.5 presents the applicability of capability diagrams as a graphical tool

in the energy market operation. A discussion on the implementation of microgrid capability diagram is given in Section 6.6 followed by the conclusions in Section 6.7.

6.2 Development of the Microgrid Capability Diagram

6.2.1 Non-linear Optimisation Model

The main objective of this section is to derive a capability diagram for a grid connected microgrid which would represent its active and reactive power transfer capability with the external grid. For this purpose, an optimisation technique was identified to be the most suitable technique, as it would enable the microgrid model to incorporate the boundary conditions. Due to the bidirectional power flow capability at the microgrid grid supply point (GSP), two scenarios were considered in obtaining the four quadrant capability diagram of the grid connected microgrid to represent both power import and export.

One scenario was taken so as to maximise the active power export from the microgrid through the GSP while minimising the active power losses in the microgrid. Reactive power import/export through the GSP was increased iteratively with the optimisation solver invoked at each load flow, and the maximum active power export from the microgrid was recorded at each reactive power value. A similar procedure was implemented in obtaining the maximum active power import at different reactive power levels. Reactive power level was increased until the load flow could not converge. The objective function to maximise the active power export from the microgrid through the GSP while minimising the active power losses in the microgrid is defined as follows:

$$Max(P_{GSP} - \Sigma P_{loss}) \tag{6.1}$$

where, P_{GSP} is the active power through the grid supply point and ΣP_{loss} is the total active power loss in the microgrid.

The objective function given in (6.1) was subjected to the general load flow equalities expressed in (6.2) and (6.3).

$$P_{gi} - P_{li} - P_i = 0 \tag{6.2}$$

$$Q_{gi} - Q_{li} - Q_i = 0 \tag{6.3}$$

where, P_{gi}, Q_{gi} are the active and reactive power outputs from the generator at node i, P_{li}, Q_{li} are the active and reactive power demands of the load at node i, and P_i, Q_i are the active and reactive power flow through node i. P_i, Q_i are defined as follows:

$$P_i = V_i \sum_{i=1}^{n} V_k Y_{ik} cos(\delta_i - \delta_k - \theta_{ik}) \tag{6.4}$$

$$Q_i = V_i \sum_{i=1}^{n} V_k Y_{ik} sin(\delta_i - \delta_k - \theta_{ik}) \tag{6.5}$$

where, θ_{ik} is the phase angle of the line admittance between node i and node k, δ_i is the phase angle of the voltage at node i with respect to the reference node, V_i is the magnitude of the voltage at node i, and Y_{ik} is the $(i,k)^{th}$element in the network admittance matrix.

The capability diagram was derived while maintaining all network voltages and line currents within the acceptable levels. Inequalities which would account for the limits of magnitude and phase angle of nodal voltages are given by (6.6) and (6.7).

$$V_i^{min} \leq V_i \leq V_i^{max} \tag{6.6}$$

$$-\pi \leq \delta_i \leq \pi \tag{6.7}$$

Distribution line capacity limit is given by:

$$I_{ik} \leq I^{max} \tag{6.8}$$

where, I_{ik} is the magnitude of the current flow from node i to node k which is expressed as follows:

$$I_{ik} = \frac{\sqrt{V_i^2 + V_k^2 - 2V_iV_kcos(\delta_i - \delta_k)}}{Z_{ik}} \tag{6.9}$$

where, Z_{ik} is the magnitude of the line impedance between node i and node k.

Power flow between the microgrid and the external grid was limited by the rating of the coupling transformer at the GSP. Thus, the transformer apparent power limit is incorporated using (6.10):

$$\sqrt{(P_{tr}^2 + Q_{tr}^2)} \leq S_{tr} \tag{6.10}$$

where, S_{tr} is the rated apparent power of the transformer.

Furthermore, the maximum and minimum generator power capability limits were incorporated in to the optimisation model by:

$$Q_{gi}^{min} \leq Q_{gi} \leq Q_{gi}^{max} \tag{6.11}$$

$$P_{gi}^{min} \leq P_{gi} \leq P_{gi}^{max} \tag{6.12}$$

Reactive power through the GSP was increased iteratively using Q_{gi} in (6.3), and the optimisation model was solved at each step to obtain the maximum active power flow through the GSP. This procedure was carried out for both power import and export modes in order to develop the complete capability diagram while the objective function was subjected to typical ac power flow constraints expressed in (6.2) - (6.12). Numerical solutions for the non-linear optimisation problem were obtained by using the interior-point algorithm (fmincon) [170] available in the optimisation solver within MATLAB.

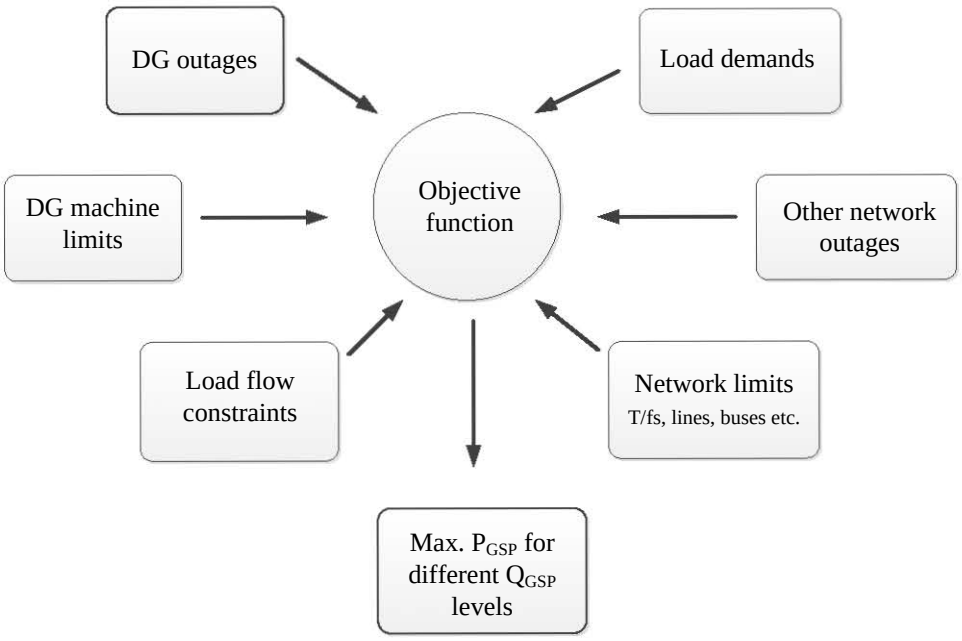

Figure 6.1: Inputs and output of the optimisation model for deriving the microgrid capability diagram

Fig 6.1 presents the graphical representation of the inputs and outputs used for deriving the microgrid capability diagram. DG machine limits, load demands, line thermal ratings, transformer limits, and load flow constraints are taken as the inputs to the optimisation model. At the same time, any outages of the DGs and other network components need to be taken into account in developing the microgrid capability diagram. The input constraints are continuously checked when the objective function is solved iteratively to obtain the maximum active power level for different reactive power levels exchanged through the microgrid GSP.

6.2.2 A Simplified Capability Diagram for Microgrid System - 1

A microgrid system comprising of a 5 MVA synchronous generator (SG) based hydro power plant and a 1.5 MVA DFIG based wind power plant is illustrated in Fig. 6.2. The microgrid is connected to the utility through a 10 MVA, 69 kV/13.8 kV transformer. Load 1 and Load 2 were considered as an industrial customer (4.8 MW peak, 0.85 p.f. lagging) and a commercial customer (1.5 MW peak, 0.85 p.f. lagging) respectively. During this study, the tap positions of the coupling transformers were

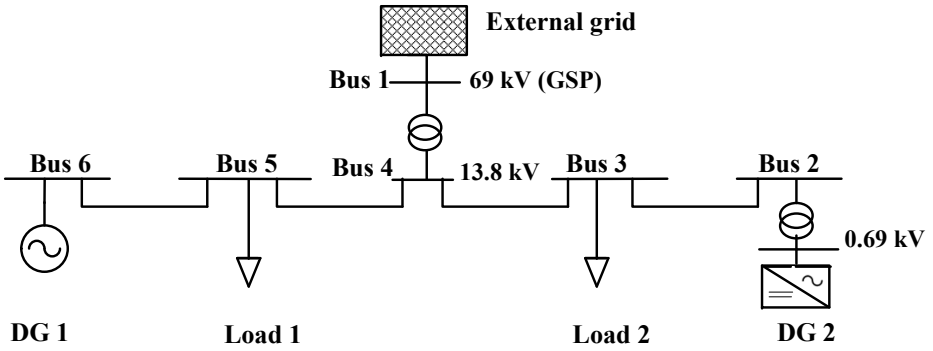

Figure 6.2: Single line diagram of the Microgrid System - 1

assumed to be fixed.

Daily generation and demand profiles on a typical weekday in summer, as illustrated in Fig.6.3 (a) and Fig.6.3 (b) [171] were considered for the derivation of the microgrid capability diagram. Active power demand was normalised based on their rated values. Due to the intermittent nature of wind and time varying load demand patterns, the capability diagram of the microgrid also varies with time. For the purpose of analysis, in this section, the capability diagram was derived for the period when the microgrid has minimum load (1.56 MW) and maximum generation (5.4 MW) (from 2.00 a.m. to 4.00 a.m.). Voltage at the GSP was maintained at $1\angle 0^{\circ}$ pu and bus bar voltage was regulated within $\pm 5\%$ of 1.0 pu. Loads were modelled as constant power loads. These constraint parameters would generally need to be adjusted to suit the particular network requirements. Values for the line capacities, transformer ratings and generator ratings as expressed in (6.8) - (6.12) were also incorporated into the optimisation model which are given in the Appendix B.

Reactive power through the GSP was increased iteratively using Q_{gi} in (6.3), and the optimisation model was executed at each step to obtain the maximum active power flow through the GSP. This procedure was carried out for both power import and export modes in order to develop the complete capability diagram.

Fig. 6.4 illustrates the simplified capability diagram corresponding to the Microgrid System - 1, where the positive values in the capability diagram indicate the surplus power available at the microgrid GSP after fulfilling the local load demand.

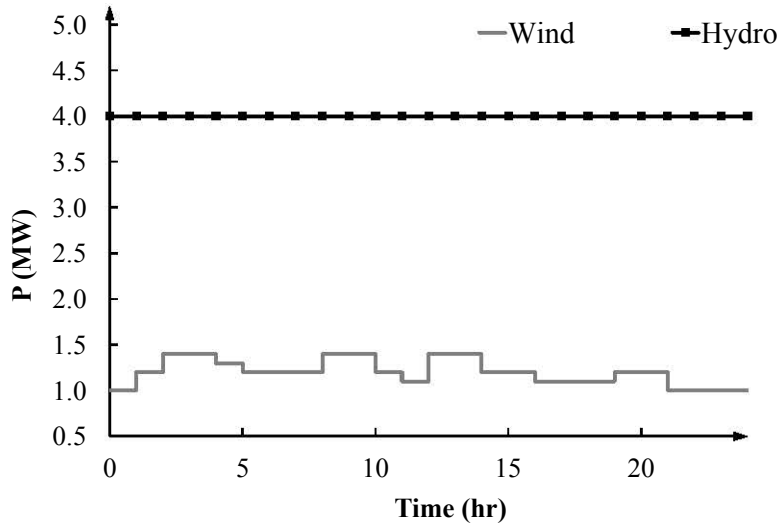

(a)

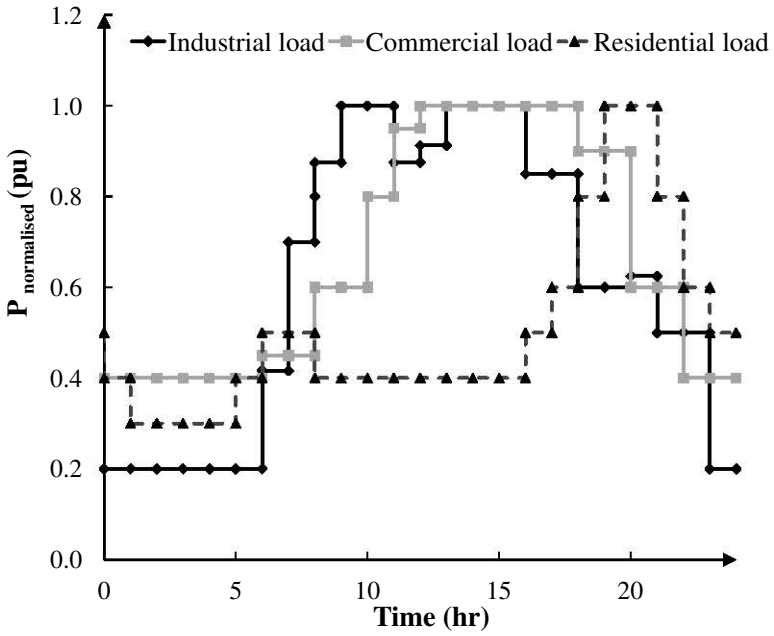

(b)

Figure 6.3: (a) Daily generation profiles of the SG and the DFIG, and (b) Daily load demand profiles for Load 1 and Load 2 during a typical weekday in summer

Similarly, negative values indicate the capability of the microgrid to import power from the external grid in order to satisfy the local load demand. Hence, at any point of the capability diagram, the local load demand was catered for either by the local DGs or by the external grid. It can be observed that during the particular time

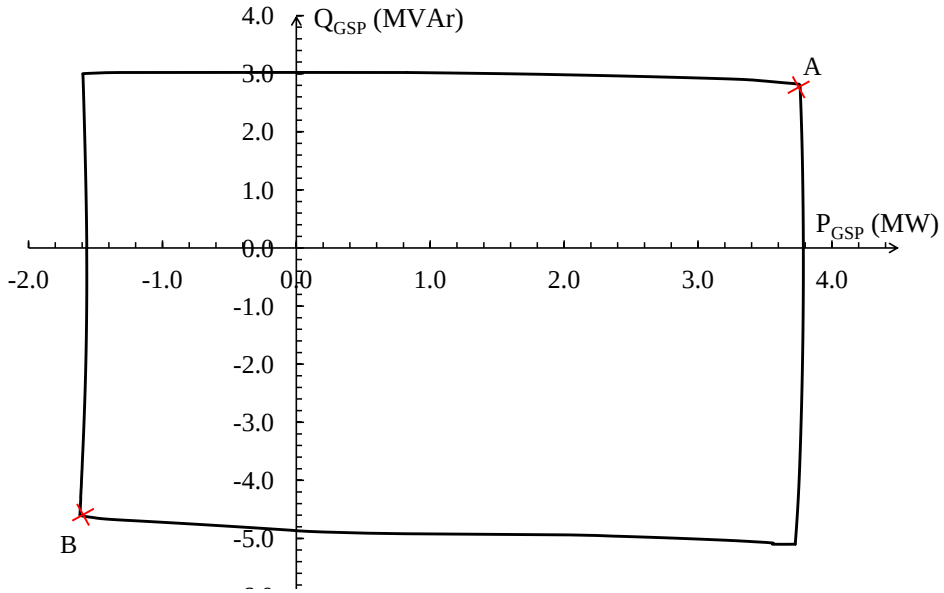

Figure 6.4: Simplified capability diagram for the Microgrid System - 1 from 2.00 a.m. to 4.00 a.m. (minimum load and maximum generation)

interval, the microgrid is capable of exporting a maximum active power of 3.8 MW and reactive power of 3.0 MVAr while supplying the local load demand from the two DGs. Furthermore, the microgrid demonstrates the capability of operating in all four modes of power import/export combinations. The operating points of the capability diagram were verified using load flow solutions of the microgrid model developed in DIgSILENT PowerFactory. Table 6.1 presents the load flow results corresponding to two points A and B on the capability diagram which were obtained employing DIgSILENT PowerFactory. Thus, it is evident that any of the operating points on the capability diagram can be obtained by adjusting the DGs and other network constraints according to the values in the optimisation model.

6.2.3 A Simplified Capability Diagram for Microgrid System - 2

In this section, a more complex and realistic microgrid system is developed based on the IEEE-13 node distribution test feeder [162] comprising of two DFIGs (each 1.5 MW) and a SG (5 MVA). The Microgrid System - 2 illustrated in Fig. 6.5 is connected to the external grid through a 10 MVA, 115 kV/4.16 kV transformer. Generation profiles used in Section 6.2.2 were employed in this study as well, and details

Table 6.1: Load flow results from DIgSILENT PowerFactory

	Point A	Point B
V_1(pu)	1.00	1.00
V_2(pu)	1.030	0.960
V_3(pu)	1.027	0.961
V_4(pu)	1.025	0.963
V_5(pu)	1.032	0.956
V_6(pu)	1.043	0.951
P_{DG1}(MW)	4.000	0.000
Q_{DG1}(MVAr)	2.916	-2.878
P_{DG2}(MW)	1.400	0.000
Q_{DG2}(MVAr)	1.097	-0.430

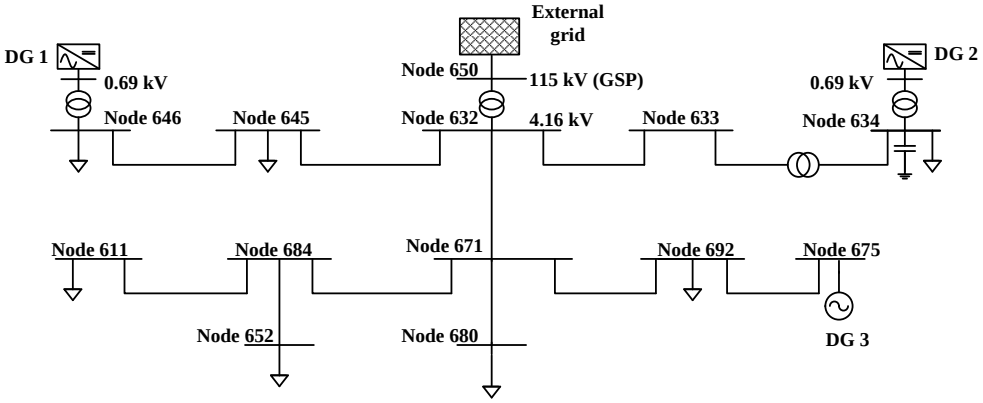

Figure 6.5: Single line diagram of the Microgrid System - 2

of the load models are presented in Table 6.2 [163]. In order to support the network voltage, a fixed capacitor bank rated at 0.5 MVAr was connected to Bus bar 634. Daily load profiles of an industrial load feeder, a commercial load feeder and a residential load feeder are illustrated in Fig. 6.3 (b). Loads were modelled as constant power loads, and for the time interval of interest, the demands were taken from the load profiles and incorporated into the optimisation model. Parameters of the microgrid model are given in Appendix B.

Fig. 6.6 illustrates the simplified capability diagram for the Microgrid System - 2. Similar to the Microgrid System - 1, this microgrid also demonstrated the capability of operating in all four modes of power import/export combinations. However, the capability to export both active and reactive power to the external grid by Microgrid System - 2 is less in comparison to Microgrid System - 1, as illustrated in

Table 6.2: Details of loads in Microgrid System - 2 (α and β are the load model exponents)

Load bus bar	Load class	$P_{\circ}(MW)$	p.f.	α	β
611	Residential	0.3	0.90	1.2	2.9
634	Residential	0.6	0.90	1.2	2.9
645	Commercial	0.5	0.85	0.99	3.5
646	Industrial	0.5	0.85	0.18	6.0
652	Industrial	0.2	0.85	0.18	6.0
680	Commercial	0.5	0.85	0.99	3.5
692	Industrial	0.8	0.85	0.18	6.0

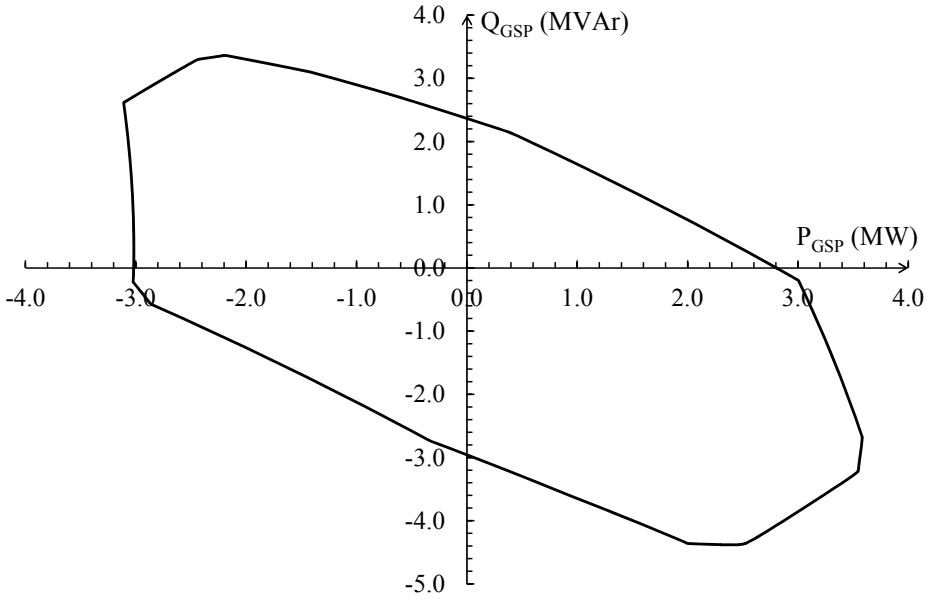

Figure 6.6: Simplified capability diagram for the Microgrid System - 2 at 1.00 pm (day peak)

Fig. 6.6 and Fig. 6.4. It is evident that the shape and size of the microgrid capability diagram varies with microgrid generation and loading conditions, as different constraints/limits will be reached in the optimisation model under each load flow condition.

6.3 Detailed Capability Diagram and Case Studies

The methodology developed in Section 6.2 is further improved in this section by incorporating individual capability limits of the DGs and voltage dependency of loads. Furthermore, case studies were carried out to analyse the impact of DG

outages, voltage regulation, and variation in local loading conditions on microgrid power exchange capability.

6.3.1 Impact of Individual DG Capability Limits

This section presents the impact of neglecting the individual generator limitations on the microgrid capability diagram.

Doubly-Fed Induction Generator (DFIG)

As illustrated in Fig. 6.7, active and reactive power capability of a DFIG is mainly determined by the rotor current limit, stator current limit and the wind turbine rating [123,124]. The rotor current limitation of a DFIG is defined by a circle in the P-Q plane with the center and radius expressed by (6.13) and (6.14) respectively.

$$C_{ir} = -\mid V_s \mid^2 \left(\frac{1}{Z_s + Z_m}\right)^* \tag{6.13}$$

$$r_{ir} = \mid I_r \mid\mid V_s \mid \left|\frac{Z_m}{Z_s + Z_m}\right| \tag{6.14}$$

where, Z_m - magnetising impedance, Z_s - stator impedance $(R_s + jX_s)$, V_s - stator voltage, and I_r - rotor current.

In order to include the rotor current limits in the optimisation model, total apparent power is expressed as follows:

$$\left[\frac{P_{tot} - Re(C_{ir})}{(1-s)}\right]^2 + [Q_{tot} - Im(C_{ir})]^2 = [r_{ir}]^2 \tag{6.15}$$

where, P_{tot} - total active power output from the DFIG, Q_{tot}- total reactive power output from the DFIG, and s - slip.

The stator current limitation is defined by the allowable stator winding heating expressed in terms of the maximum stator current. This limit corresponds to a circle centered at the origin of the P-Q plane with a radius as follows:

$$C_{is} = 0 \tag{6.16}$$

$$r_{is} = \mid I_s \mid\mid V_s \mid \tag{6.17}$$

where, I_s - stator current. Similar to (6.15), an expression is obtained for the apparent power with stator current limitations as follows:

$$\left[\frac{P_{tot}}{(1-s)}\right]^2 + [Q_{tot})]^2 = [r_{is}]^2 \tag{6.18}$$

Mechanical limit of the wind turbine is represented by a straight line as follows:

$$P_{max} = P_{turb} \tag{6.19}$$

For different values of slip, limits of the corresponding capability diagram are obtained using (6.15), (6.18) and (6.19), and expressed as equality and inequality constraints in order to incorporate into the optimisation model.

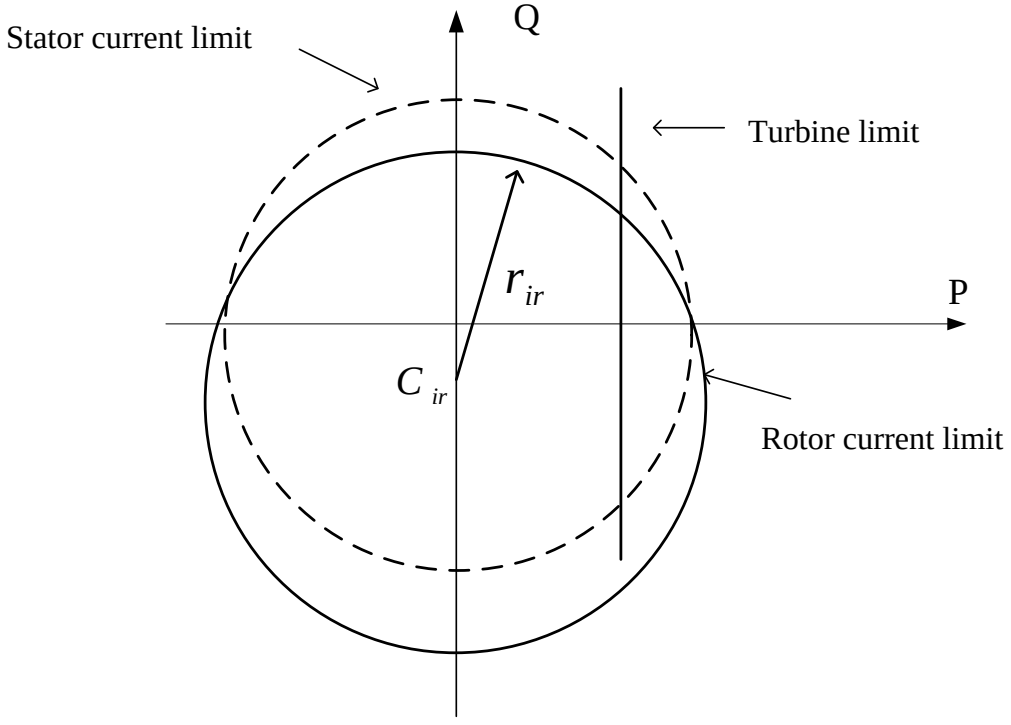

Figure 6.7: Capability diagram of a DFIG

Synchronous Generator (SG)

Synchronous generators driven by small hydro and thermal turbines can be found in distribution networks. The capability diagram defines the generator permissible operating region for a given terminal voltage. As illustrated in Fig. 6.8, the power output capability of a SG based hydro power plant is limited by the stator current limit, rotor current limit, load angle and the hydro-turbine rating [163].

The armature current limitation of the SG is given by a circle in the P-Q plane with the center at the origin and radius equal to the apparent power rating.

$$P_{tot}^2 + Q_{tot}^2 = S_{tot}^2 \tag{6.20}$$

Field current limitation is also expressed as a circle with the center at $\left(0, -\frac{E_t^2}{X_s}\right)$ and radius equal to $\frac{X_{ad}}{X_s} E_t i_{fd}$, where E_t - generator terminal voltage, X_s - generator stator reactance, X_{ad} - generator stator leakage reactance, i_{fd} - field current.

The corresponding equation for the apparent power with field excitation limit in the P-Q plane is as follows:

$$P_{tot}^2 + \left(Q_{tot} + \frac{E_t^2}{X_s}\right)^2 = \left(\frac{X_{ad}}{X_s} E_t i_{fd}\right)^2 \tag{6.21}$$

Mechanical limit of the hydro-turbine is taken as a straight line as follows:

$$P_{max} = P_{turb} \tag{6.22}$$

The load angle limitation is expressed by a line with the gradient of the tangent of the maximum load angle δ_{max} as follows:

$$P_{tot} = (tan\delta_{max}) Q_{tot} + \left(\frac{E_t^2}{X_s} tan\delta_{max}\right) \tag{6.23}$$

Thus, the capability limits of a SG are expressed by (6.20) - (6.23), and expressed as equality and inequality constraints in order to incorporate in the optimsation model.

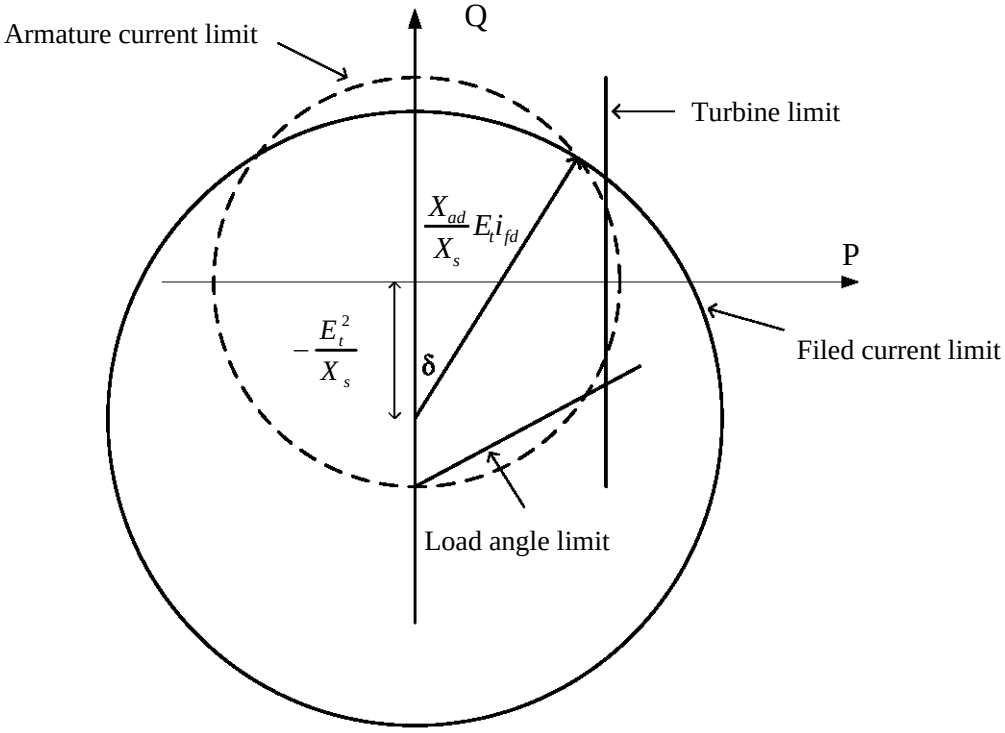

Figure 6.8: Capability diagram of a SG

Ideal Capability Limits for a DG

Disregarding the actual machine capability limits and expressing the active and reactive power capability limits as in (6.11) and (6.12) would result in a simplified rectangular DG capability diagram.

In order to analyse the impact of actual machine capability limits on the microgrid capability diagram, (6.11) and (6.12) in the optimisation model were replaced with (6.15),(6.18) and (6.19) for a DFIG, and by (6.20) - (6.23) for a SG. The rest of the constraints expressed in (6.2) - (6.10) were kept unchanged and the optimisation model was solved iteratively for different loading conditions as explained in Section 6.2.

Fig. 6.9 illustrates the capability diagrams derived for the two microgrid systems described in Section 6.2. In both Fig. 6.9 (a) and Fig. 6.9 (b), it can be observed that considering simplified DG machine capability limitations would yield inaccurate microgrid power exchange capability with the external grid. Hence, incorporation of realistic DG machine limitations into the optimisation model is essential in order

to derive an accurate microgrid active and reactive power capability diagram.

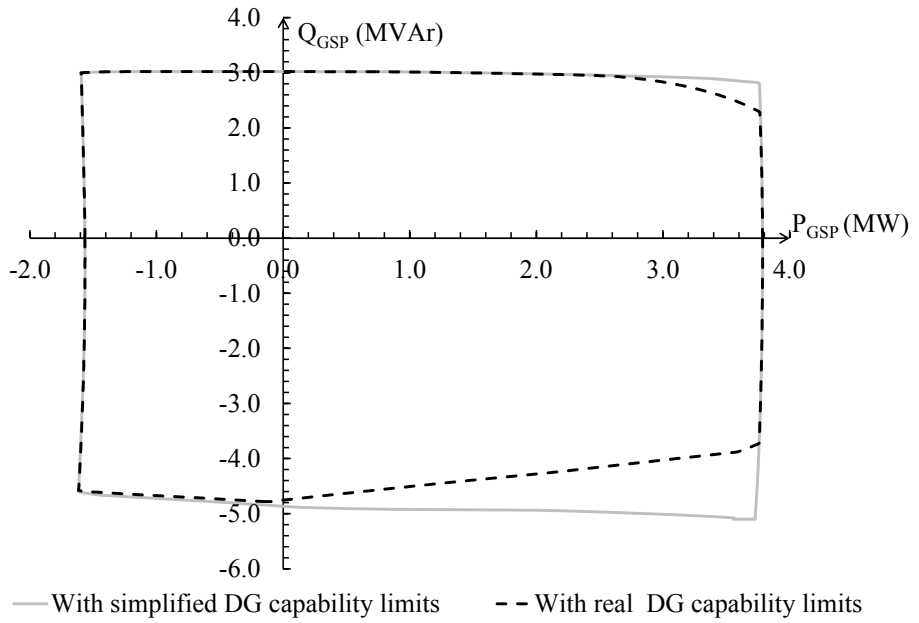

(a)

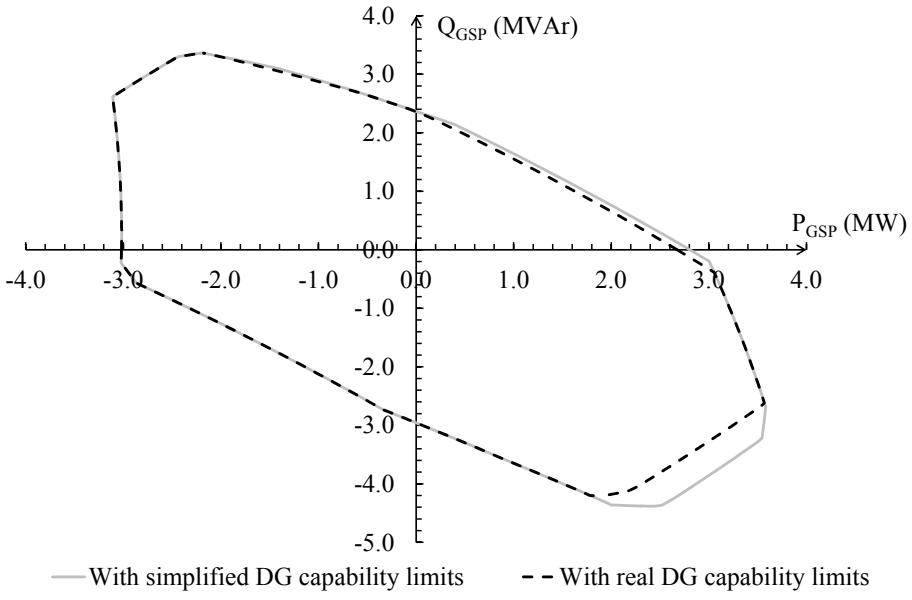

(b)

Figure 6.9: Impact of simplistic and actual DG capability limits on the capability diagram of the (a) Microgrid System - 1 and (b) Microgrid System - 2

6.3.2 Impact of Voltage Dependency of Loads

In previous sections, loads were modelled as constant power loads in the optimisation model. As the active and reactive power demands of loads vary with the load bus

bar voltage, it is important to analyse the impact of voltage dependency of loads on microgrid capability diagram. Hence, voltage dependent load models as expressed in (6.24) were incorporated in the load flow equalities in (6.2) and (6.3) of the optimisation model.

$$P_{li} = P_{oi}\left(\frac{V_i}{V_{oi}}\right)^{\alpha} \qquad Q_{li} = Q_{oi}\left(\frac{V_i}{V_{oi}}\right)^{\beta} \tag{6.24}$$

where, P_{oi}, Q_{oi} are active and reactive power at voltage V_{oi} respectively. Rest of the equations in the optimisation model remained the same as described in Section 6.2.1, with generator limits incorporated as explained in Section 6.3.1. The corresponding factors α and β for the loads in the microgrid models are given in Table 6.2.

Capability diagrams derived for the two microgrid systems are illustrated in Fig. 6.10. For the Microgrid System - 1, it can be observed that the reactive power export capability of the microgrid has been affected to a certain extent by the voltage dependency of loads. Exponent representing reactive power of the load models considered in this scenario are relatively larger than those corresponding to active power exponent, and affects the reactive power limits of the capability diagram in comparison to the active power limits. Compared to the Microgrid System - 1, for the time period considered, power exchange capability of the Microgrid System - 2 has been slightly affected by the voltage dependency of loads.

6.3.3 Variations of the Capability Diagram with Different Load Demands

Due to the intermittent nature of renewable energy generation and different customer behaviour, the power generation and local load demand patterns in a microgrid varies with time. In order to analyse the variation of the microgrid power exchange capability with time, capability diagrams were derived at different periods of the day such that the variation of generation and load demands were captured. In the optimisation model, equations remained the same as in Section 6.2.1 with

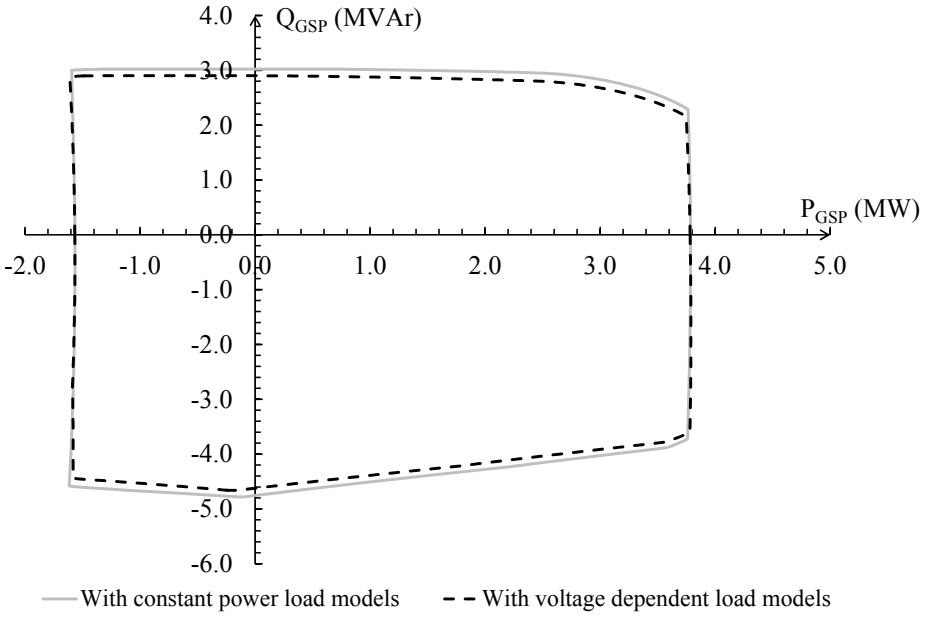

(a)

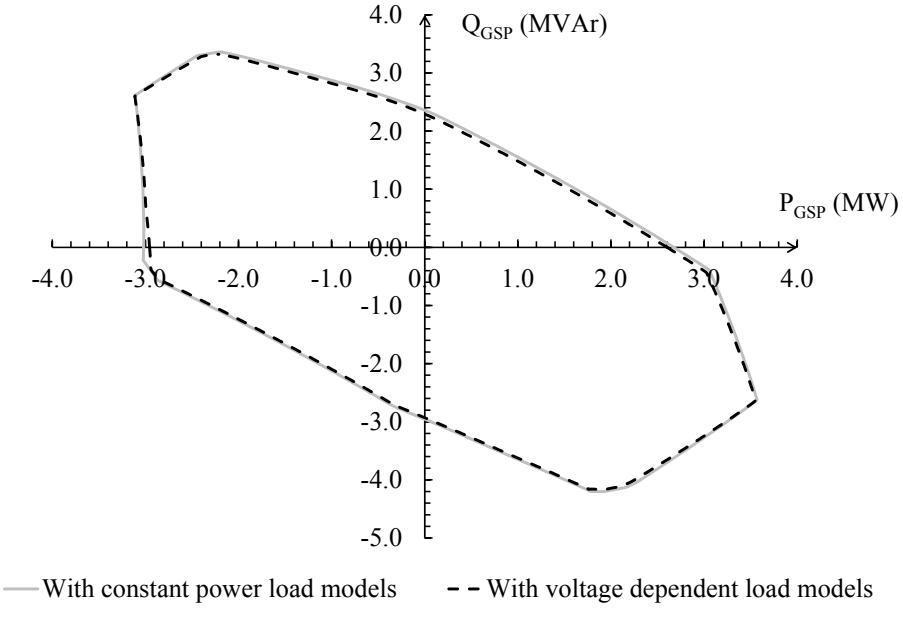

(b)

Figure 6.10: Impact of voltage dependent load modelling on the capability diagram of the (a) Microgrid System - 1 and (b) Microgrid System - 2

generator limits incorporated as explained in Section 6.3.1, and loads modelled as in Section 6.3.2. Capability diagrams derived for the Microgrid System - 1 at 3.00 a.m. (minimum load and maximum generation), at 11.00 a.m. and at 8.00 p.m. are illustrated in Fig. 6.11 (a). As expected, microgrid has a higher capability to export

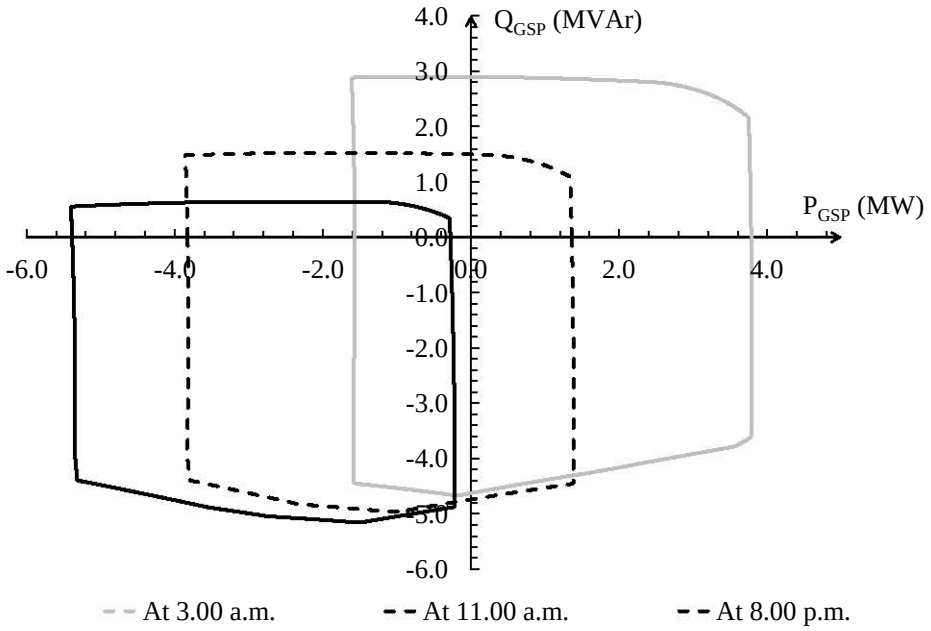

(a)

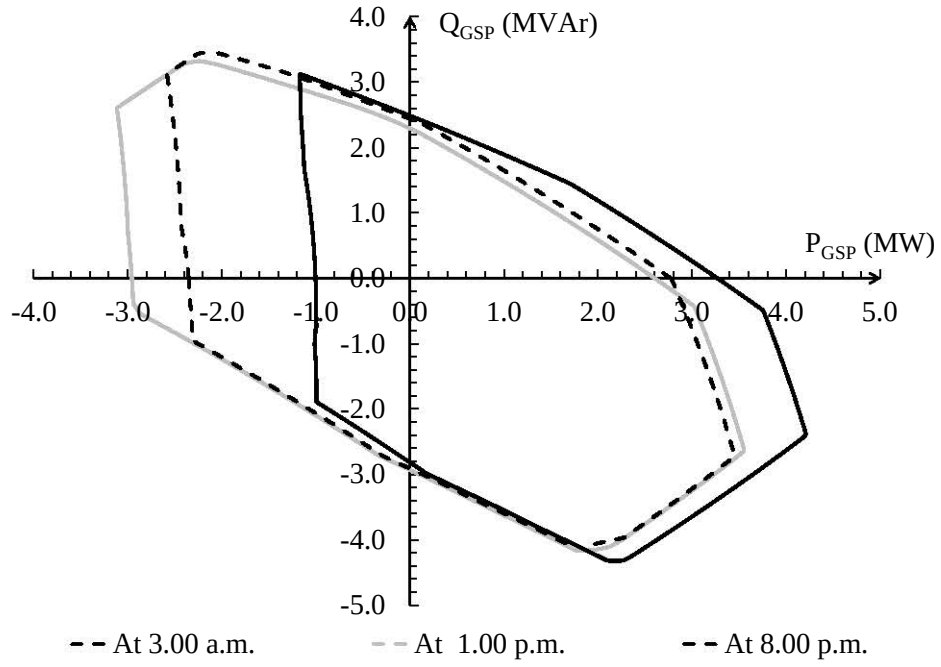

(b)

Figure 6.11: Variations of capability diagram with different loading conditions in (a) Microgrid System - 1 and (b) Microgrid System - 2

power to the upstream network when the difference between the local load demand and the local power generation is high. As an example, at 3.00 a.m., the microgrid has an increased capability to export active and reactive power into the external grid compared to 11.00 a.m. and 8.00 p.m. Furthermore, at 11.00 a.m., the capability

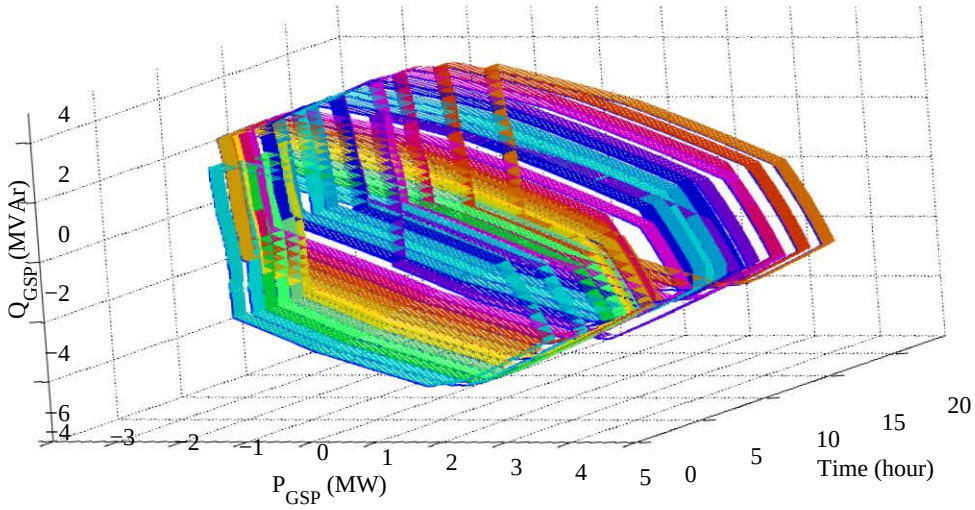

Figure 6.12: Variation of the capability diagram for Microgrid System - 2 over a 24 hour period

diagram is on the left half plane, indicating that the microgrid cannot export any active power to the external grid during that time and requires active power to be imported in order to cater the local load demand.

Fig. 6.11 (b) illustrates the capability diagrams derived for the Microgrid System - 2 at 3.00 a.m. (minimum load and maximum generation), at 1.00 p.m. (maximum load and maximum generation) and at 8.00 p.m. Having the same power generation in the microgrid, capability diagram at 3.00 a.m. (with minimum load) has shifted more into the right half plane compared to the capability diagram at 1.00 p.m. (with maximum loading condition). Fig. 6.12 illustrates the variation of the capability diagram for the Microgrid System - 2 over a 24 hour period.

Comparing the capability diagrams derived for the two microgrid systems in Section 6.2 and Section 6.3, it is evident that the shape and size of the capability diagram vary with microgrid generation and loading conditions, as different constraints/limits need to be met in the optimisation model at each load flow.

6.3.4 Impact of DG Outages on the Capability Diagram

This section analyses the variation of microgrid capability diagram due to DG outages. Variation of the microgrid capability diagram with different DG outages for

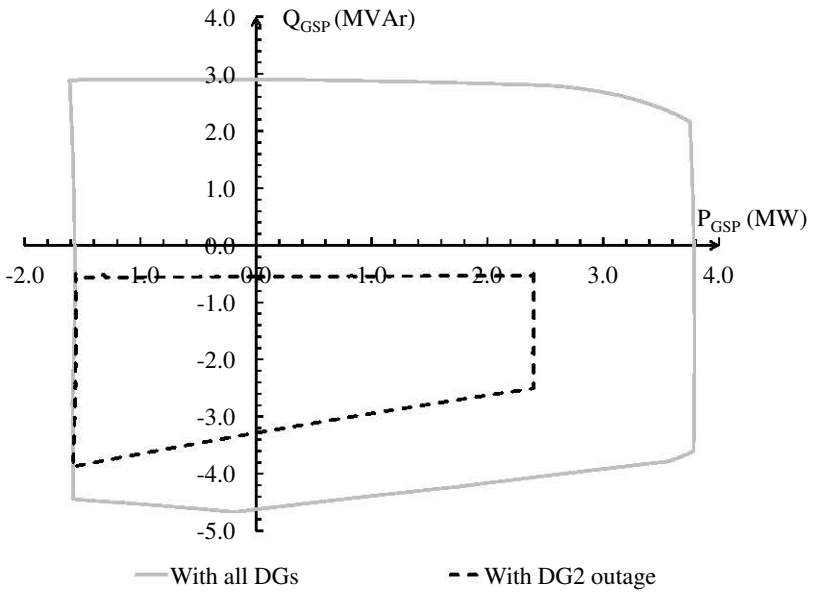

(a)

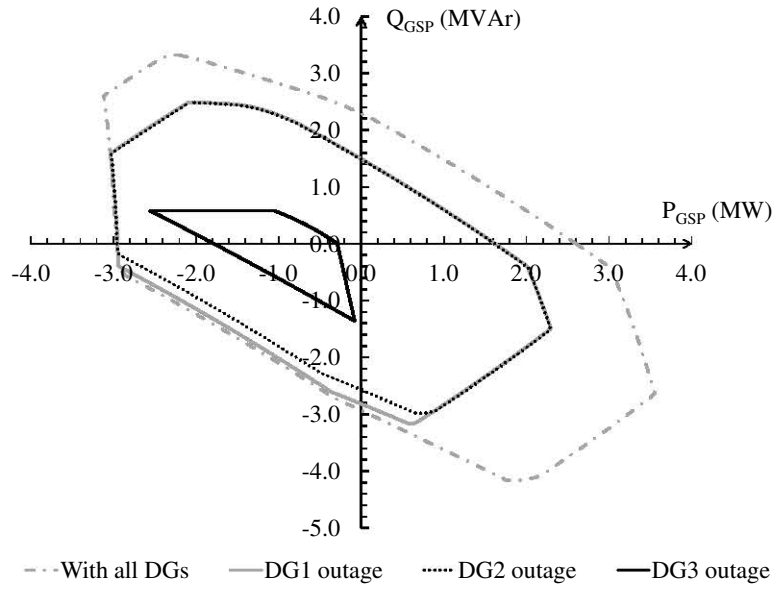

(b)

Figure 6.13: Impact of individual DG outages on the capability diagram of the (a) Microgrid System - 1 and (b) Microgrid System - 2

Microgrid System - 1 and Microgrid System - 2 are illustrated in Fig. 6.13 (a) and Fig. 6.13 (b) respectively. In each scenario, only one DG was disconnected from the

microgrid and capability diagrams were obtained while maintaining the same local load demand. A particular DG outage was represented in the optimisation model by removing the equations corresponding to that generator limits and the generator transformer.

It can be observed from Fig. 6.13 (a) that the outage of the DFIG (DG2) in the Microgrid System - 1 has affected the microgrid reactive power export capability. Having the capability diagram in the bottom half plane in Fig. 6.13 (a) indicates that the reactive power is required to be imported from the external grid for stable operation.

From Fig. 6.13 (b), it can be observed that irrespective of the location, outages of DG1 and DG2 (identical DGs) have similar impacts on the power export capability of Microgrid System - 2. Furthermore, an outage of the largest DG (DG3) will require the particular microgrid to import active power from the external grid as the two DFIGs are insufficient to cater the local load demand. Thus, this type of a graphical tool will be useful for the microgrid controllers to establish an overall idea on the microgrid capability, and to optimally operate the remaining DGs during a major generator outage.

6.3.5 Impact of Voltage Regulation on Microgrid Capability Limits

This section presents the impact of different voltage regulation levels of the microgrid bus bars and the GSP on microgrid power exchange capability limits. For different voltage regulation levels, limits in (6.6) were changed accordingly and the optimisation model was executed as described in Section 6.2.1. As expected, it can be observed from Fig. 6.14 that an increase in the range of acceptable voltage variation at the bus bars within the microgrid is favourable for power export from the microgrid (comparing the capability diagrams Fig. 6.14(a) and Fig. 6.14(b)). Furthermore, it can be observed that for the same microgrid loading conditions, power import and export capability of the microgrid can be increased by allowing the voltage at the GSP to be varied within an acceptable limit, rather than controlling the voltage

at a set point (comparing the capability diagrams Fig. 6.14(a) and Fig. 6.14(c)). In energy market operation, the Microgrid Central Controller (MCC) or the DNSP can refer to the microgrid capability diagram and increase the microgrid capability by issuing suitable control commands to the bus bar voltage regulators.

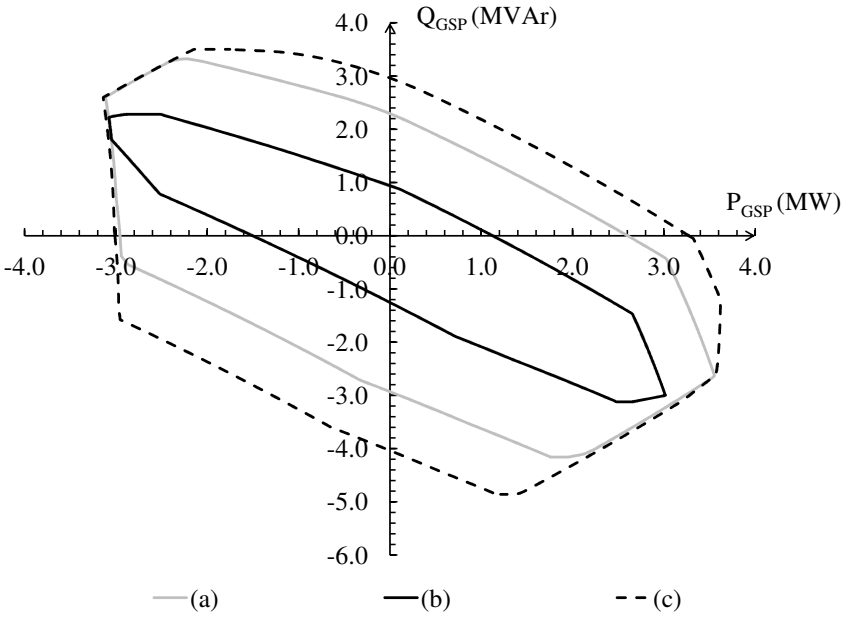

Figure 6.14: Impact of voltage regulation on the capability diagram of Microgrid System - 2 with (a) V_{GSP} = 1pu and microgrid $VR \pm 5\%$, (b) V_{GSP} = 1pu and microgrid $VR \pm 2\%$, and (c) $V_{GSP} = \pm 2\%$ and microgrid $VR \pm 5\%$

Fig. 6.15 illustrates the active power loss corresponding to the capability limits of the Microgrid System - 2 at 8.00 p.m.

6.4 Impacts of PHEVs and Capacitor Banks on the Capability Diagram

PHEVs are becoming popular due to their low emission and efficient mode of transportation compared to fossil fuel based vehicles [172]. PHEVs are connected to the distribution network with other loads for charging and discharging purposes. In the first part of this section, the impact of charging and discharging of PHEVs on

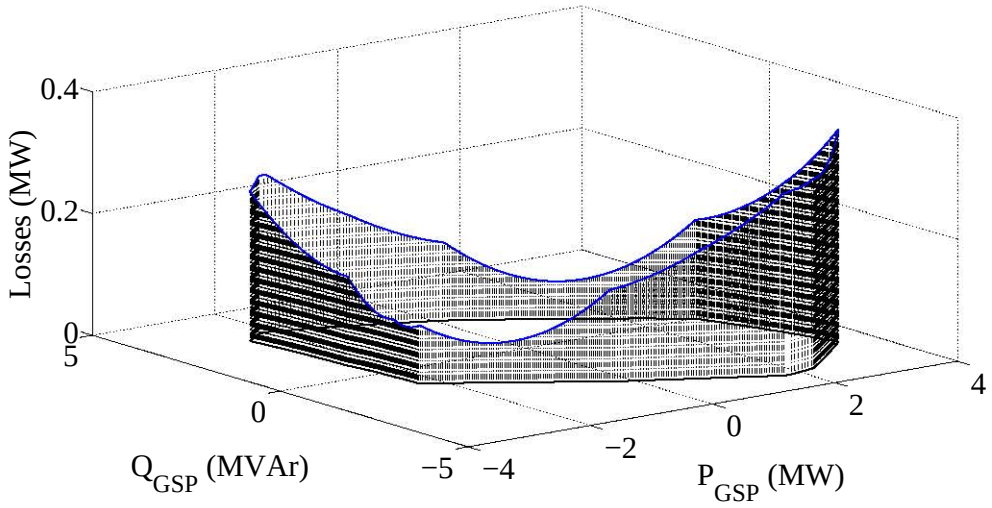

Figure 6.15: Active power losses corresponding to the capability limit of the microgrid system - 2 at 8.00 p.m.

microgrid capability diagram is analysed. For this study, it was assumed that the residential feeders at Bus bar 634 and Bus bar 611 in the Microgrid System - 2 have load profiles as illustrated in Fig. 6.16. The load profiles include the aggregated effect of PHEV charging, where charging occurs mainly during the off-peak hours due to dual tariff [172]. Corresponding capability diagrams were obtained as described in Section 6.3.2, and are illustrated in Fig. 6.17 and Fig. 6.18.

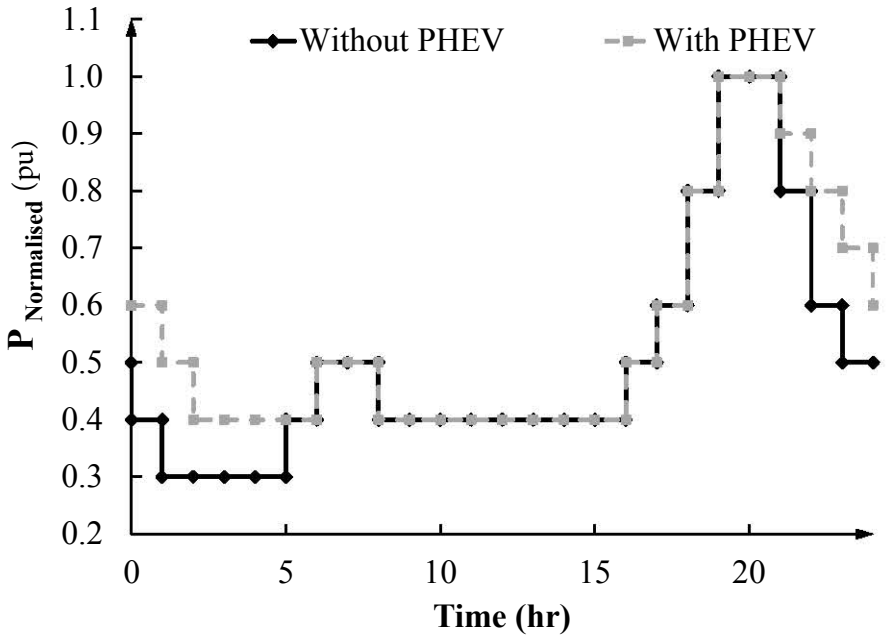

Figure 6.16: Daily load profiles for a residential feeder with and without PHEV during a typical weekday in summer

Fig. 6.17 compares the capability diagrams at 3.00 a.m. with and without PHEV charging at the residential feeders. During the charging process, PHEV could either consume power from the local resources available within the microgrid or import power from the external grid. Charging of PHEV would reduce the power export capability of the microgrid. Apart from residential charging, electric vehicle charging stations can be constructed in commercial and industrial feeders [173].

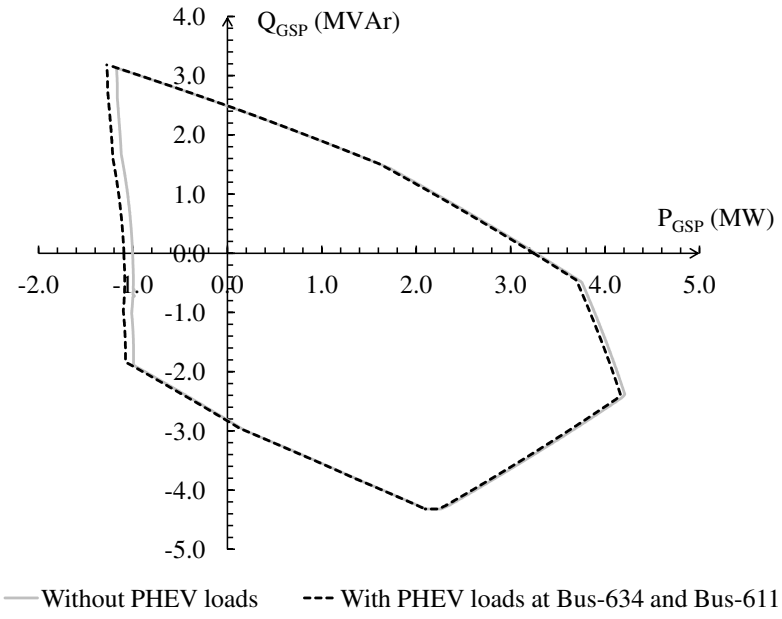

Figure 6.17: Capability diagrams of the Microgrid System - 2 at 3.00 a.m. with and without PHEV charging at residential loads

In the next scenario, it was assumed that PHEV charging stations were located in a commercial feeder (Bus bar 645) and two industrial feeders (Bus bar 652 and Bus bar 692) with a morning peak of 0.1 MW at each station occurring at 9.00 a.m., when PHEV owners charge their vehicles after coming to work or to the city. Fig. 6.18 presents the capability diagrams with fleets of PHEV charging at different stations. It can be observed that the aggregated effect of small scale fleets of charging PHEVs can be represented as simple loads in the microgrid capability diagram.

As a subsequent scenario, Vehicle-to-Grid (V2G) concept was considered where

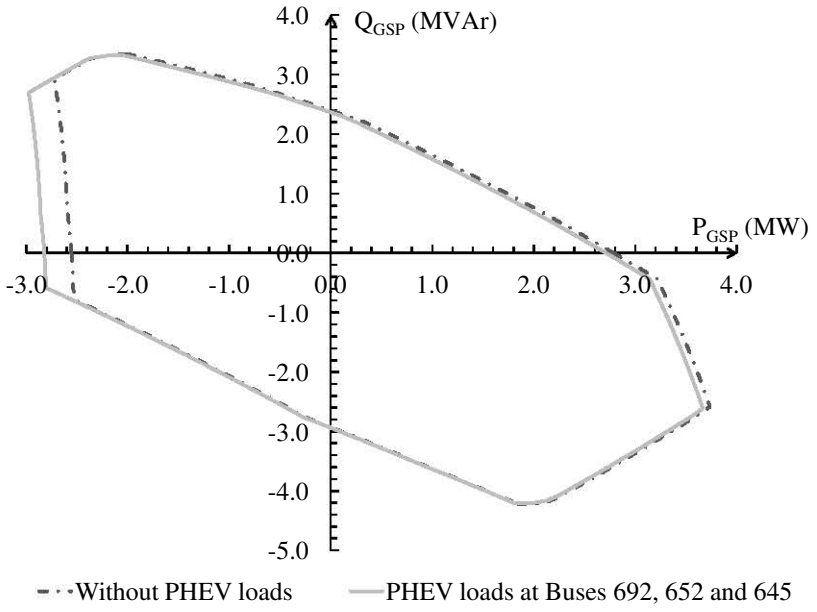

Figure 6.18: Capability diagrams for the Microgrid System - 2 at 9.00 a.m. with PHEV charging stations

fleets of PHEVs discharge in order to supply active power back to the grid for peak shaving [174]. Fleets of PHEVs were assumed to supply 0.1 MW of power for approximately one hour from stations located at Bus bar 645 during the day-peak hour. It can be observed from Fig. 6.19, that V2G can be used to cater the local demand which increases the microgrid power export capability. Storage devices within the microgrid can be utilised to reduce the power import from the external grid. In general, storage devices are utilised to mitigate power mismatch, to smooth out variability in renewable energy generation, to reduce network losses, and to obtain financial benefits in energy markets. When deriving the power import/export capability diagram for a grid connected microgrid, storage devices can be modelled as loads or generators depending on the operation. Energy stored in an individual PHEV is negligible relative to that of the grid. However, fleets of vehicles with a considerable number of PHEVs can be aggregated in order to be considered as a feasible storage option. The aggregator, who is responsible for controlling the

power exchange between the PHEVs and the grid will receive requests for different ancillary services from the microgrid operator and will issue commands to fleets of PHEVs to operate in the V2G mode [175].

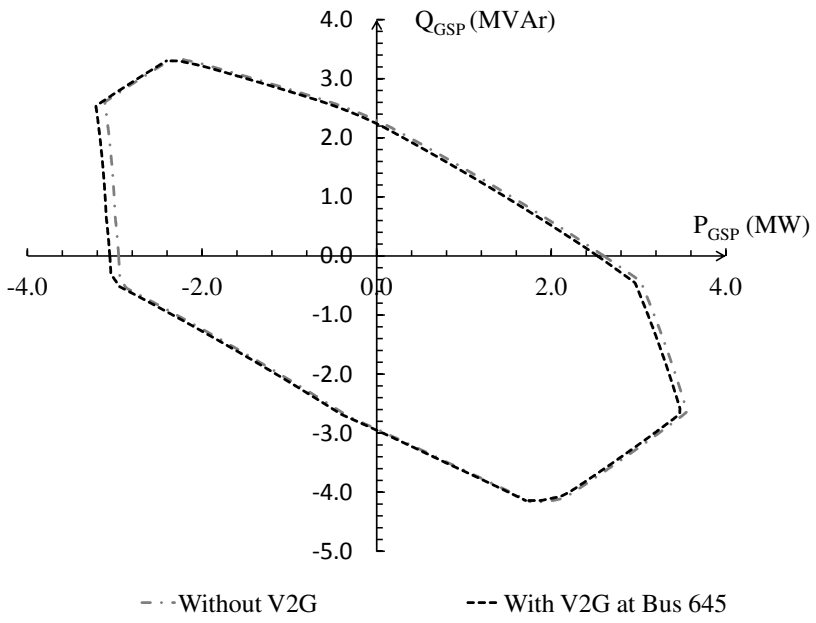

Figure 6.19: Capability diagrams for the Microgrid System - 2 during day-peak with V2G application

Typically, capacitor banks and synchronous condensers are used to support the local voltage by injecting reactive power. In the energy market paradigm, synchronous condensers can contribute to export reactive power from the microgrid to the external grid. However, such operations require careful analysis of financial and technical aspects prior to being incorporated in to the microgrid capability diagram.

6.5 Market Operation and Capability Diagram

Grid connected microgrids can be operated as single entities in the energy market operation. In order to facilitate this, microgrid controllers must have access to tools simplifying the microgrid participation in market operation. Most of the recent research work has concentrated on optimising the internal operation of grid connected

microgrids either by minimising system losses or by minimising the power exchange with the external grid [97, 99, 176–178]. However, as explained in Chapter 2, no research work has suggested the use of a graphical tool for market operation of grid connected microgrids. From various market operation strategies presented in Chapter 2, this section presents two different case studies explaining the use of microgrid capability diagram in market operation as a guideline for future work.

6.5.1 Active Power Exchange with the External Grid

The Microgrid System - 2 described in Section 6.3.2 is considered in these studies, together with the optimisation model developed as described in Section 6.3 considering the limitations of the DGs, local loads, transformers and other network parameters. For the particular microgrid, it is assumed that the microgrid is owned and controlled by the MCC hence, DGs would not bid separately in the energy market. The MCC would send relevant command signals to the DGs and no demand side bidding is considered.

The microgrid operating cost includes the cost of main grid energy transactions (both purchasing and selling), cost of microgrid energy supply, revenue from local consumers, and any curtailment costs. The corresponding active and reactive power capability diagram at 8.00 p.m. is illustrated in Fig. 6.20. Table 6.3 presents the costs associated with the each DG operation and active power buying and selling prices of the external grid.

Table 6.3: Costs associated with the microgrid operation

	Cost ($/kWh)
Average cost of DFIG (DG1, DG2) [179, 180]	0.063
Average cost of small hydro (DG3) [181]	0.055
Active power buying and selling price of the external grid [182]	0.20

The microgrid would sell excess active power from the DGs to the external grid when operating in the positive active power region of the capability diagram. Whereas, in the negative active power region, microgrid would purchase active power

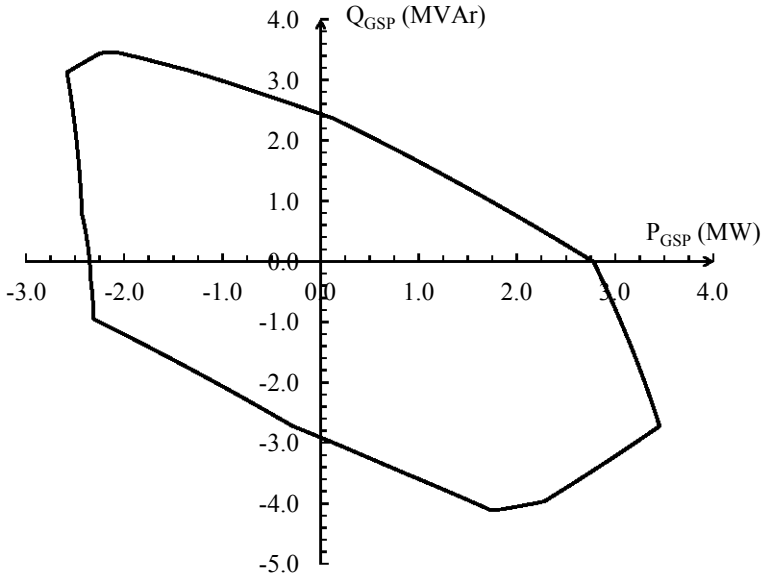

Figure 6.20: Capability diagram for the Microgrid System - 2 at 8.00 p.m.

from the external grid to fulfill the local load demand. For this scenario, it is assumed that no cost is involved with the reactive power exchange between the microgrid and the external grid. Thus, depending on the operation mode, the cost of electricity of the microgrid is calculated using (6.25) and (6.26).

Active power export mode:

$$Electricity\,cost\,(\$/kWh) = \frac{\sum DG\,cost}{\sum P_{DG}} \tag{6.25}$$

Active power import mode:

$$Electricity\,cost\,(\$/kWh) = \frac{Ext.grid\,purchase\,cost + \sum DG\,cost}{P_{ext.grid} + \sum P_{DG}} \tag{6.26}$$

where, $\sum DG\,cost$ is the total cost of DG operation per hour, $\sum P_{DG}$ is the total active power supplied from the DGs, and $P_{ext.grid}$ is the active power imported from the external grid.

Analysing Fig. 6.20 and Fig. 6.21, it is clear that the electricity cost of the microgrid is around \$ 0.06 /kWh during active power export mode. Furthermore, minimum cost of electricity occurs when there is no active power exchange between the

microgrid and the external grid (at $P_{GSP} = 0\,MW$). Cost of electricity reaches the maximum of $\$\,0.20\,$/kWh when the total active power requirement of the microgrid is met by the external grid. Fig. 6.22 illustrates the electricity cost variation of the microgrid corresponding to all the operating points of the capability diagram.

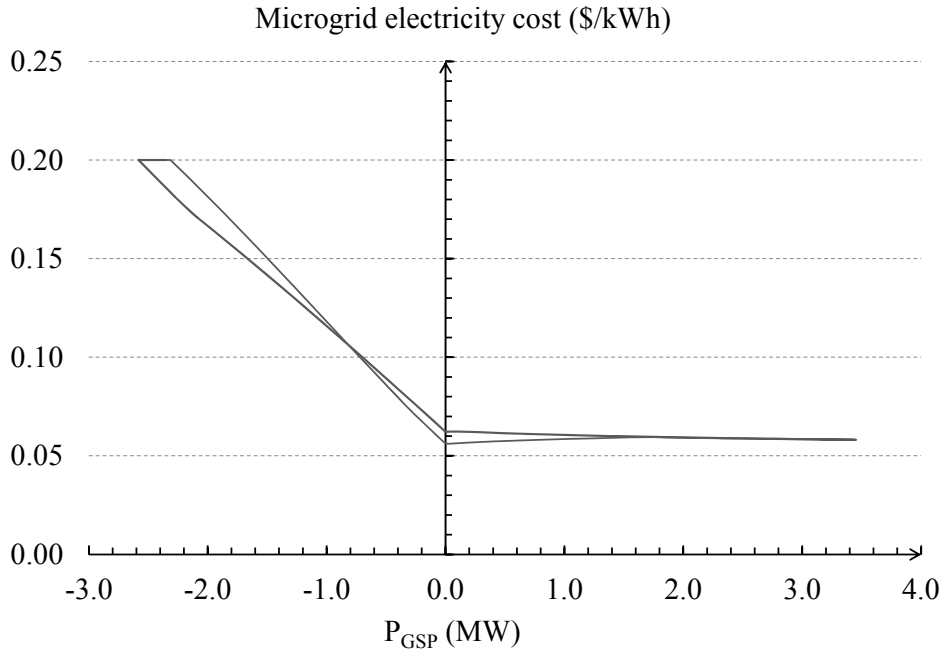

Figure 6.21: Electricity cost of the microgrid corresponding to the operating points of the boundary of the capability diagram

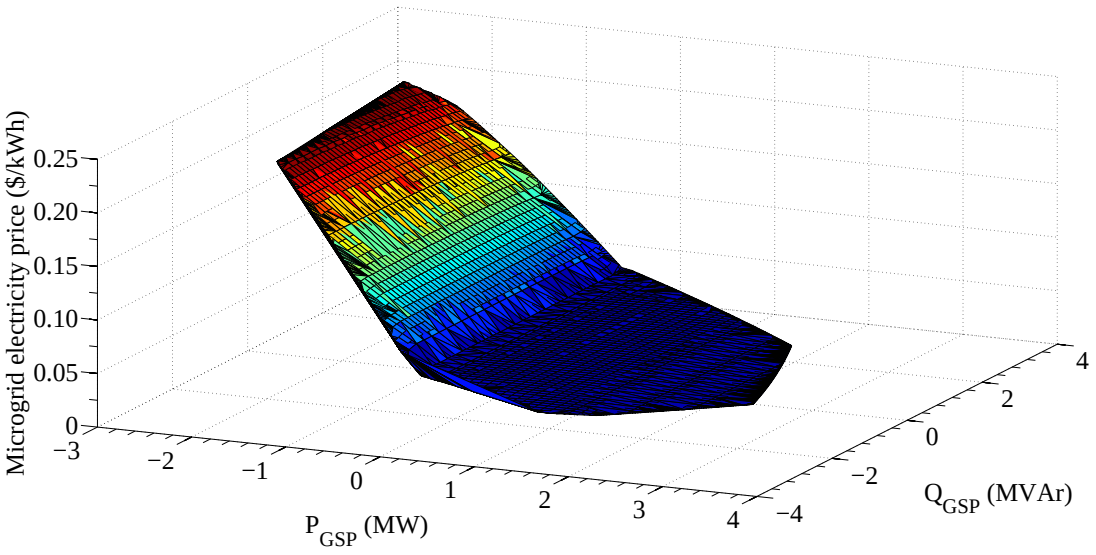

Figure 6.22: Electricity cost variation of the Microgrid System - 2 at 8.00 p.m.

6.5.2 Reactive Power Purchase from the External Grid

The microgrid system described in Section 6.5.1 is considered for this scenario. Apart from the active power market, the MCC would be required to pay the external grid for the reactive power imported into the microgrid. No cost is associated with the reactive power export into the external grid. It is assumed that the MCC purchase reactive power at a rate of $\$\,0.50\,/\mathrm{kVArh}$. Fig. 6.23 illustrates the variation of reactive power cost of the microgrid for reactive power import mode. As expected, it can be observed that the cost of reactive power of the microgrid increases with the increasing reactive power import from the external grid.

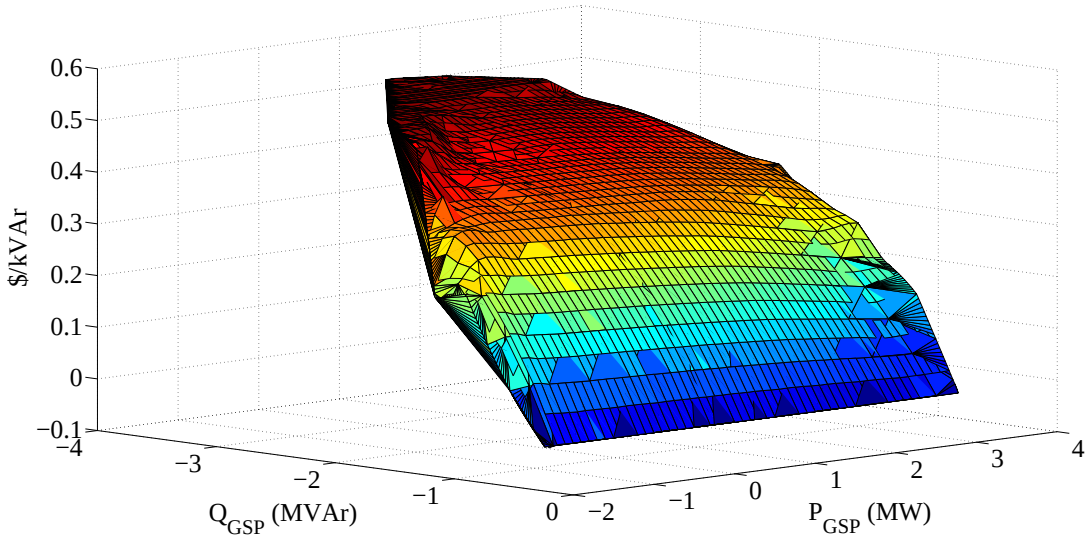

Figure 6.23: Variation of reactive power cost of the microgrid for reactive power import mode

In Section 6.5.1 and Section 6.5.2, only basic aspects of active and reactive power markets were considered. However, depending on the ownership of the microgrid, the market policy in operation can be varied. This would require many other aspects to be considered when assigning cost values for different microgrid operating points. A detailed discussion on this is presented in the following section.

6.6 Discussion

Due to time varying load and generation patterns, the capability diagram of a microgrid will vary with time and it is not practical for the MCC to derive capability diagrams for an entire day. However, MCC can derive the capability diagrams for pre-defined time periods or by using the forecasted generation and demand patterns at critical operation times of the microgrid (i.e. day-peak, night-peak, minimum load, and maximum generation). Furthermore, the capability diagram can be derived online, provided proper communication media exists between the generators, load centres and the MCC.

The proposed methodology and the mathematical model have the flexibility to incorporate any optimisation algorithm and any constraint related to the microgrid for developing capability diagrams. DNSPs and MCCs can run optimisation algorithms to optimise different objective functions subjected to different financial and technical constraints. Regardless of the objective function, if all the technical constraints are kept unchanged, those optimum operating points are located within the microgrid capability diagram.

Through a capability diagram, the maximum possible power can be harnessed from a grid connected microgrid. Furthermore, in a multi-microgrid environment where microgrids trade between themselves, capability diagrams of individual microgrids can be used as a tool to decide the maximum amount of power exchange.

In this chapter, it was assumed that the microgrid was owned by an independent power producer. Hence, the microgrid has the sole responsibility to cater the local load demand either by generating power from local DGs or by importing power from the utility (external grid). In such a situation, the microgrid owner has to bear the expenses related to the electricity generation from DGs and energy purchase from the external grid if any. The main revenue of the microgrid would be income derived from selling energy into the external grid and to the local loads, with latter typically providing larger return on investment.

However, if the local DGs have different owners, the MCC could allow the DGs

to bid in the energy market. In this scenario, apart from the aforementioned costs associated with the energy generation, the MCC would have to bear the expenses related to Lost Opportunity Costs. As an example, a decision to increase reactive power export to the external grid would result in a reduction of active power production from the local DGs. In this situation, MCC would be required to pay lost opportunity cost to the relevant DGs, and buy active power if required from the external grid. The market conditions and the cost of productions determine the value of opportunity cost [183, 184].

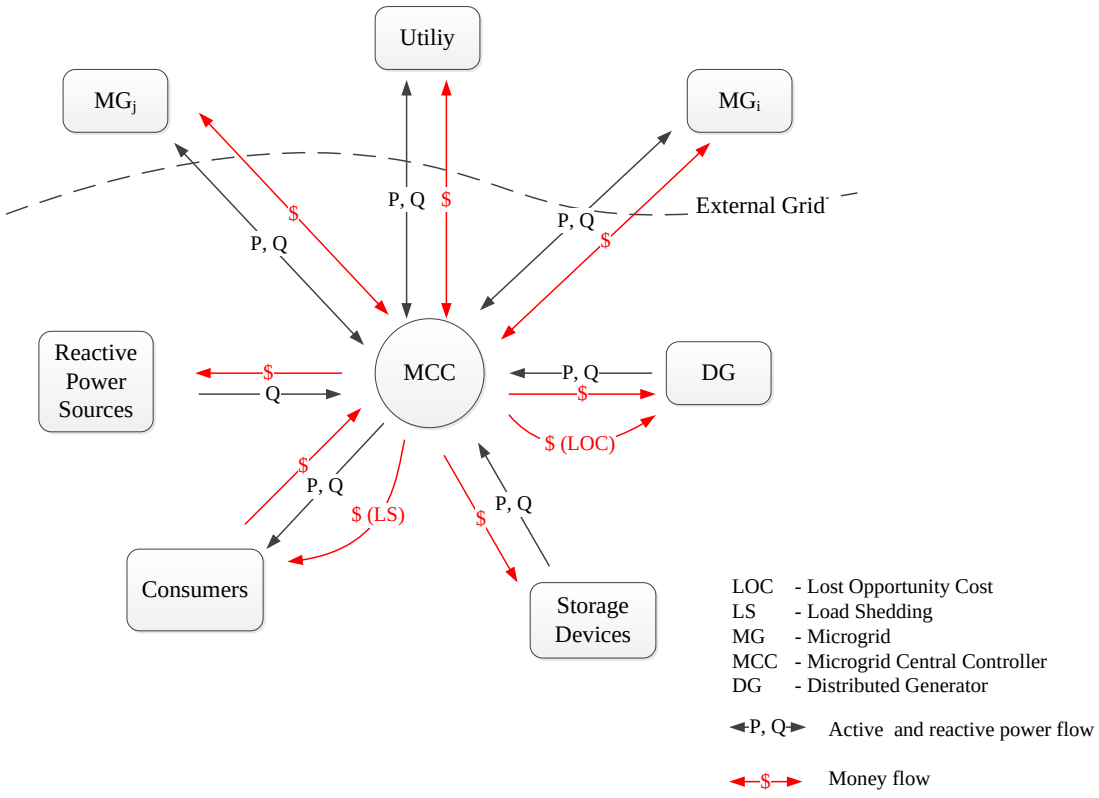

Figure 6.24: Different components associated with the market operation of grid connected microgrids

The price of reactive power is strongly dependent on the location of production. The cost of producing reactive power is much lower than that of active power, because it does not involve fuel costs [185]. However, the capital cost of a reactive compensator, especially generator and synchronous condensers, is remarkably high. Accordingly, the pricing mechanism should include the capital cost associated with these components.

Operation of the microgrid in energy market can be more complex when demand side bidding is considered. The MCC has to optimise the operation of the microgrid by considering the bids from both DGs and the loads. If consumers are willing to shed loads, the MCC will be required to pay a curtailment fee which will contribute to the microgrid operating costs.

Thus, main operating objective of the microgrid will depend on the ownership, network complexity, time of operation, and other market aspects. However, technical feasibility limits a microgrid can be derived regardless of the complexity of the microgrid structure by expanding the methodology presented in this chapter. Furthermore, electricity costs can be assigned to every operating point of the microgrid capability diagram and can be utilised as a tool in market operation with the external grid and when trading between multiple microgrids. Fig. 6.24 illustrates the diagram corresponding to different components associated with the market operation of grid connected microgrids.

6.7 Summary

This chapter presented a new systematic approach for developing an active and reactive power capability diagram corresponding to the GSP of a microgrid, while considering microgrid generation capabilities, local load demands and network constraints. An optimisation model was developed under various network constraints and the solutions were plotted on a P-Q power plane to derive the capability limits for two different microgrid systems. Various features such as different load modelling aspects, individual generator limitations, and effects of plug-in hybrid electric vehicles and reactive power devices were considered in developing the capability diagram.

The optimisation model for the capability diagrams were derived in MATLAB for two different microgrid models, which were validated using DIgSILENT PowerFactory. This graphical representation of the active and reactive power capability at the GSP can be utilised as a new tool to represent the technical feasibility of grid

connected microgrids when trading with the utility and other microgrids. The MCC would be able to use the DERs optimally and to provide ancillary services support to the external network as required.

This chapter introduced the use of microgrid capability diagram as a tool for the market operation of grid connected microgrids. Two case studies were presented in active and reactive power markets where electricity prices were assigned to every operating point of the capability diagram. Such diagrams can be referred to by the MCC in decision making processes.

Chapter 7

Low Voltage Ride Through of Microgrids with Distribution Static Synchronous Compensator (DSTATCOM)

7.1 Introduction

Faults occurring outside a grid connected microgrid can lead to voltage sags at the microgrid point of common coupling (PCC) which would propagate to affect the operation of the distributed energy resources (DERs) and the loads within the microgrid. If the DERs are set to disconnect at relatively shallow voltage sag depth levels, a situation with considerable generation deficit can arise. However, such a scenario can be avoided if the microgrid can regulate the voltage at the PCC and provide dynamic reactive power support to the network during voltage sag events.

Depending on the low voltage ride through (LVRT) behaviour of individual DERs within the microgrid, those DERs can also provide dynamic voltage and reactive power support to the rest of the microgrid. As described in Chapter 2, research outcomes exist related to the individual LVRT behaviour of DERs in compliance

to different grid codes. However, the collective effect of LVRT behaviour of DERs within a microgrid has not been investigated so far.

This chapter takes two approaches in order to investigate the LVRT behaviour of a grid connected microgrid as a single entity. First approach is to improve dynamic voltage support at the microgrid PCC by using a distribution static synchronous compensator (DSTATCOM) at the low voltage side of the microgrid distribution transformer. The second approach is to use the aggregated reactive power capability of DERs within a microgrid to provide voltage and reactive power support to the external grid. During this approach, instead of individual DG capabilities, DSTATCOMs are installed at the DG terminals, and no additional dynamic voltage support (i.e. DSTATCOM) is considered at low voltage side of the microgrid distribution transformer. This chapter is exclusively focussed on the technical assessment of DSTATCOM for microgrids and its advantage for grid connected and islanded modes of operation.

Section 7.2 describes the voltage control mode of a DSTATCOM and selection of the parameters in order to improve dynamic voltage support. The impact of DSTATCOM in a grid connected microgrid under different operating conditions is investigated in Section 7.3. The microgrid is subjected to external and internal faults, and various system parameters are analysed with and without the DSTATCOM operation. DSTATCOMs are installed at DG terminals and at the bus bar with minimum reactive power margin of the microgrid, and the system behaviour is analysed in Section 7.4.

Integration of multiple microgrids into the utility grid will allow the microgrids to provide ancillary services to the utility during normal operation and will enable emergency services to adjacent microgrids during a utility grid outage. Maintaining the microgrids online will avoid sudden loss of active power while avoiding power system collapse. Section 7.5 presents DSTATCOM operation in a multi-microgrid system which is investigated for different faults.

Operation of single microgrids in islanded mode and operation of multiple micro-

grids separated from external grid with DSTATCOMs are presented in Section. 7.6. Section 7.7 presents a case study carried out to investigate grid connected microgrid behaviour with DSTATCOM and induction motor loads followed by the chapter summary in Section 7.8.

7.2 Distribution Static Synchronous Compensator (DSTATCOM)

DSTATCOM is a shunt reactive power compensating device which functions as a controlled shunt reactive admittance and generates ac voltage, which in turn causes a current injection into the system through a shunt transformer. In its most basic form, the DSTATCOM configuration consists of a two-level voltage source inverter (VSI), a dc energy storage device, a coupling transformer connected in shunt with the ac system, and associated control circuits as illustrated in Fig. 7.1 [186].

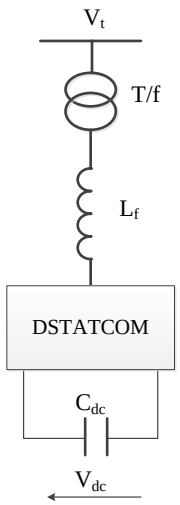

Figure 7.1: General topology of a VSI based DSTATCOM [167]

The VSI converts the dc voltage across the storage device into three-phase ac voltages. These voltages are synchronised with the ac system through the reactance of the coupling transformer. Suitable adjustments of the phase and magnitude of the DSTATCOM output voltage allow effective control of active and reactive power exchange between the DSTATCOM and the ac system. The VSI connected in shunt with the ac system provides a multi-functional topology which can be used for up

to three quite distinct purposes: 1) voltage regulation and compensation of reactive power, 2) correction of power factor, 3) elimination of current harmonics.

Fig. 7.2 illustrates the controller associated with the voltage control mode of the DSTATCOM. In voltage control mode, the difference between the RMS voltage of the terminal and its desired value is used to generate the required voltage magnitude across the filter by exchanging reactive power with the ac network. The droop is usually selected as 5 % to allow small terminal voltage variations while avoiding oscillation [187]. The dc voltage is kept constant through a small active power exchange arrangement with the ac network, which also compensates for the active power losses in the transformer and the inverter.

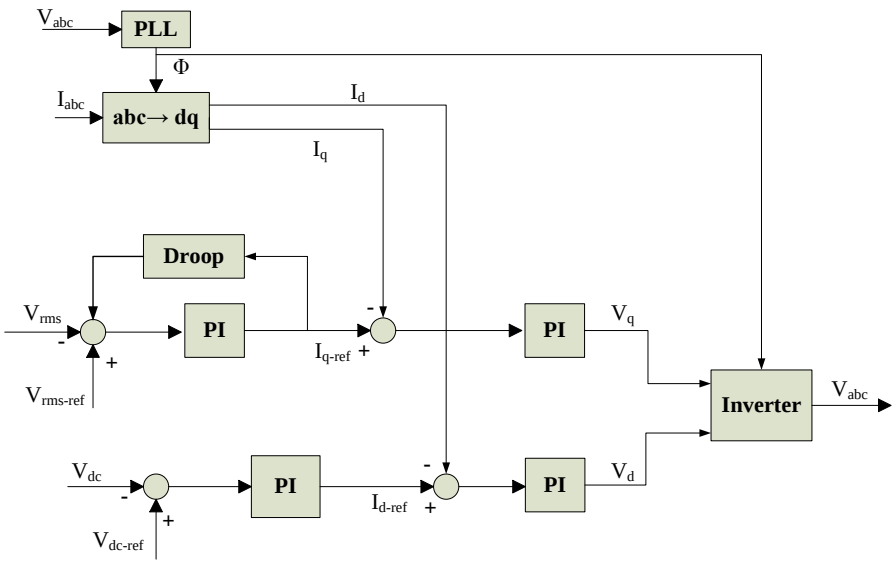

Figure 7.2: DSTATCOM voltage control mode

7.2.1 Design of DSTATCOM Parameters

Reference dc Link Voltage (V_{dcref})

In order to achieve good tracking performance, voltage across the dc storage capacitor is selected to be $1.6V_m$, where V_m is the maximum phase voltage [188].

Storage Capacitance (C_{dc})

Value of the dc capacitor is selected based on the ability to regulate voltage during transients. During transients, the dc capacitor exchanges real power to maintain the load power demand. Assuming the controller starts working after n cycles, nST would be the maximum possible energy that the capacitor can exchange with the load, where S is the maximum load rating, and T is system time period [189]. Hence,

$$\frac{1}{2}C_{dc}(V_{dcref}^2 - V_{dc}^2) = nST \tag{7.1}$$

where, V_{dc} is the magnitude of the maximum allowed voltage deviation from V_{dcref} during transients. Therefore, the dc link capacitor value is selected as follows:

$$C_{dc} = \frac{2nST}{V_{dcref}^2 - V_{dc}^2} \tag{7.2}$$

Interfacing Inductance (L_f)

The inductor is designed to provide good tracking performance at maximum switching frequency. Neglecting filter resistance R_f, interfacing inductance is given by,

$$L_f = \frac{V_{dcref}}{(2h)(2f_{max})} \tag{7.3}$$

where, $2h$ is the ripple in the current and f_{max} is the maximum switching frequency achieved using a hysteresis current controller [189].

7.3 Grid Connected Microgrid in Different Operating Regions with DSTATCOM

In this section, different case studies are carried out to investigate the impact of having a DSTATCOM at the secondary side of the coupling transformer of a grid connected microgrid. Fig. 7.3 illustrates the microgrid system developed for the case studies where DG1 and DG2 represent DFIGs, while DG3 represents a SG based

DG. Both DG1 and DG2 are operated in constant power factor mode while DG3 is operated in voltage control mode.

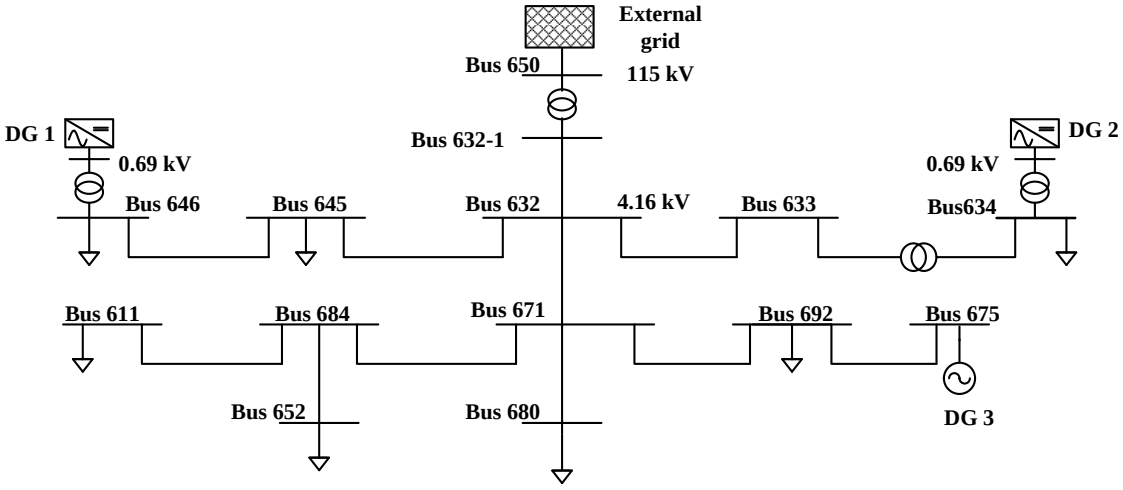

Figure 7.3: Single line diagram of the microgrid system

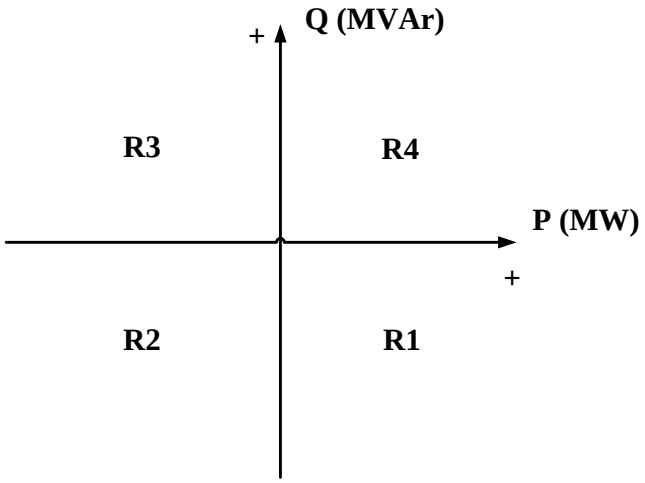

Figure 7.4: Microgrid operating regions for grid connected mode

Fig. 7.4 illustrates the four different microgrid operating regions considered in this section, where positive power values indicate power export from the microgrid. Table 7.1 presents the active and reactive power flow from DGs, the external grid and the total microgrid load demand considered in this section related to the four operating regions.

Table 7.1: Active and reactive power values for different operating regions of the microgrid

	R1		R2		R3		R4	
	P (MW)	Q (MVAr)	P (MW)	Q (MVAr)	P (MW)	Q (MVAr)	P (MW)	Q (MVAr)
DG1	1.200	0	0	0	0.276	0.769	1.100	0.500
DG2	1.200	0	0	0	0.231	0.962	0.900	0
DG3	4.000	-1.840	4.000	0.507	1.527	0.499	1.500	0.687
Ext.Grid	3.575	-3.792	-0.711	-1.603	-0.677	0.617	2.033	0.272
Total load	2.271	1.293	4.552	1.932	2.683	1.563	1.394	0.803

7.3.1 Microgrid Behaviour during an External Fault with DSTATCOM

For the microgrid considered in this study, a 3 MVA DSTATCOM is selected, and the parameters calculated as explained in Section 7.2.1 are presented in Table 7.2.

Table 7.2: Parameters of the DSTATCOM

Parameter	Value	Parameter	Value
C_{dc}	4629 μF	n	0.5
V_{dcref}	6 kV	T	0.02 s
L_f	150 mH	h	1 A
V_{ac}	4.16 kV	f_{max}	10 kHz

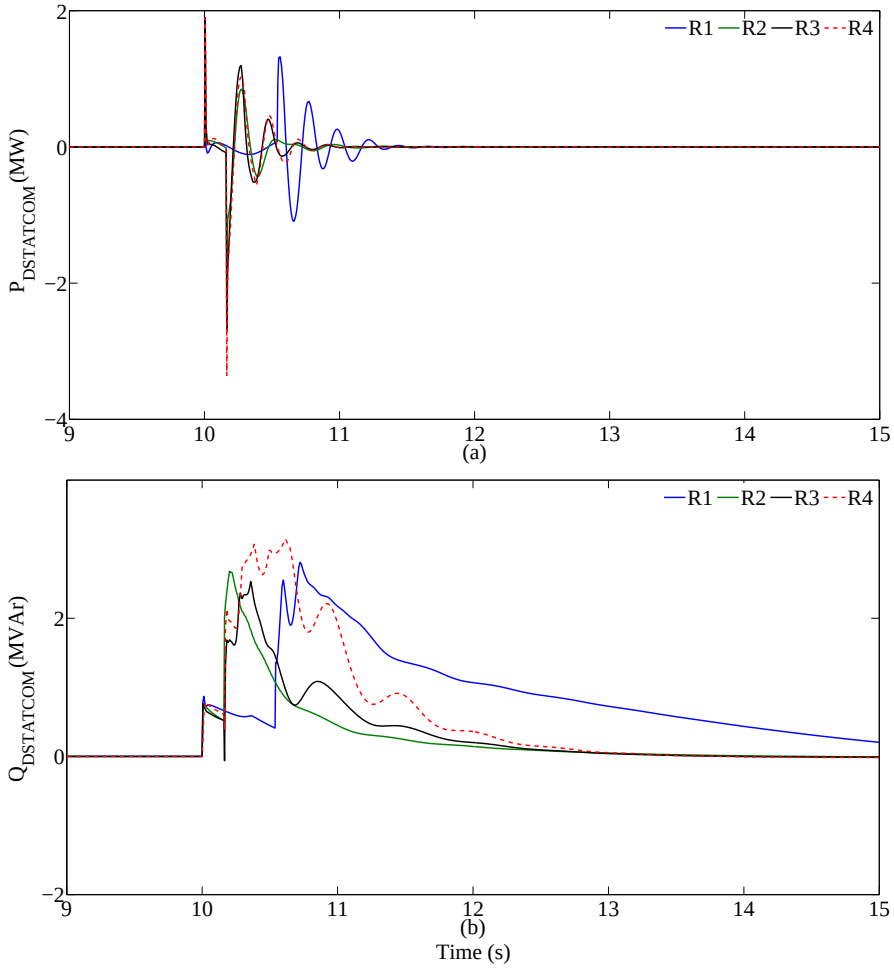

Figure 7.5: Active and reactive power variations of the DSTATCOM in different operating regions of the microgrid (fault duration for R1-538 ms, R2, R3 and R4 - 160 ms)

In order to investigate the impact of the DSTATCOM connected on low voltage

side of the microgrid distribution transformer, a three-phase short-circuit fault was applied to Bus bar 650 at $t = 10\,\text{s}$ and cleared after 160 ms to the microgrid. The study is carried out on all four operating regions of the microgrid.

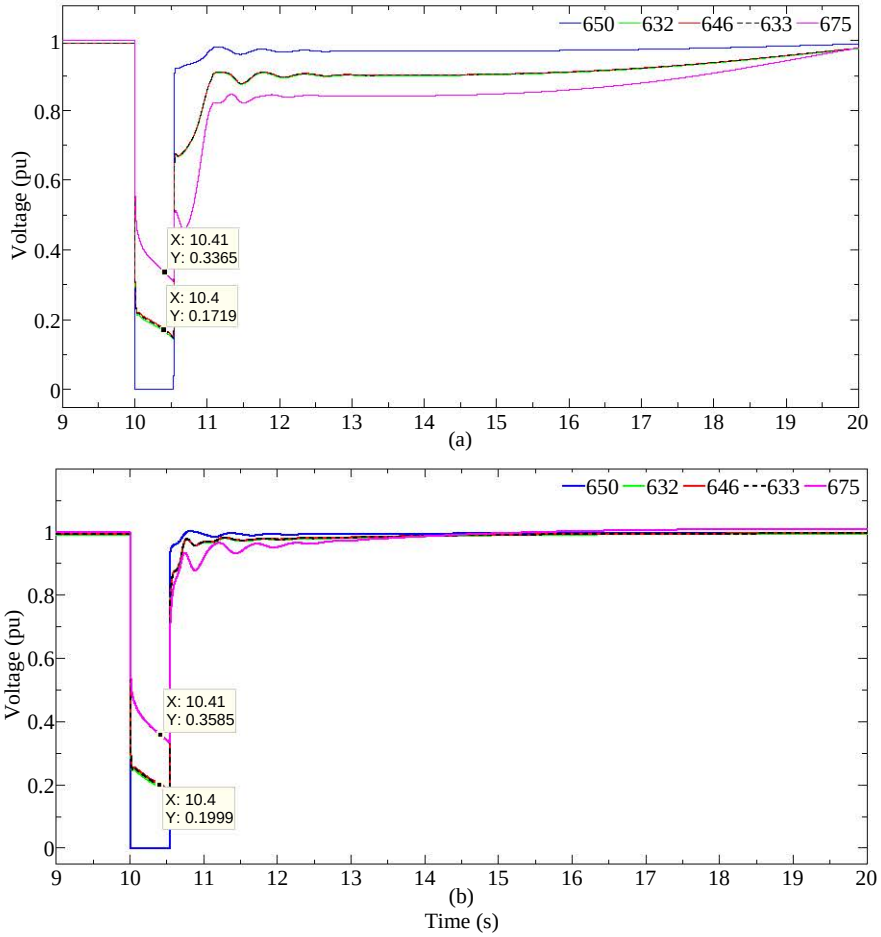

Figure 7.6: Voltage variations at different bus bars in operating region R1 (a) without DSTATCOM and (b) with DSTATCOM (fault duration - 538 ms)

Table 7.3: CCT of the microgrid for different operating regions

Operating region	Without DSTATCOM (ms)	With DSTATCOM (ms)
R1	538	632
R2	298	331
R3	196	218
R4	188	221

Fig. 7.5 (a) and Fig. 7.5 (b) illustrate the active and reactive power variations of the DSTATCOM in the four different microgrid operating regions due to the fault. The DSTATCOM injected reactive power into the network during the fault and after fault clearance in order to maintain the terminal voltage at the pre-fault value. The

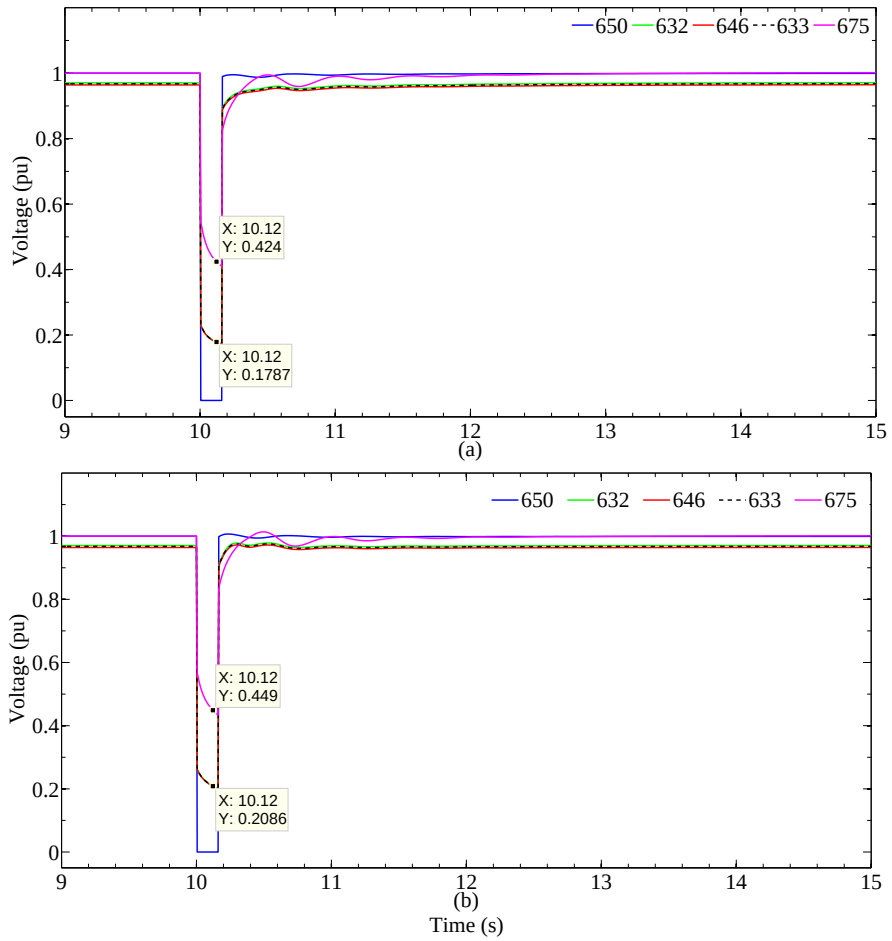

Figure 7.7: Voltage variations at different bus bars in operating region R2 (a) without DSTATCOM and (b) with DSTATCOM (fault duration - 160 ms)

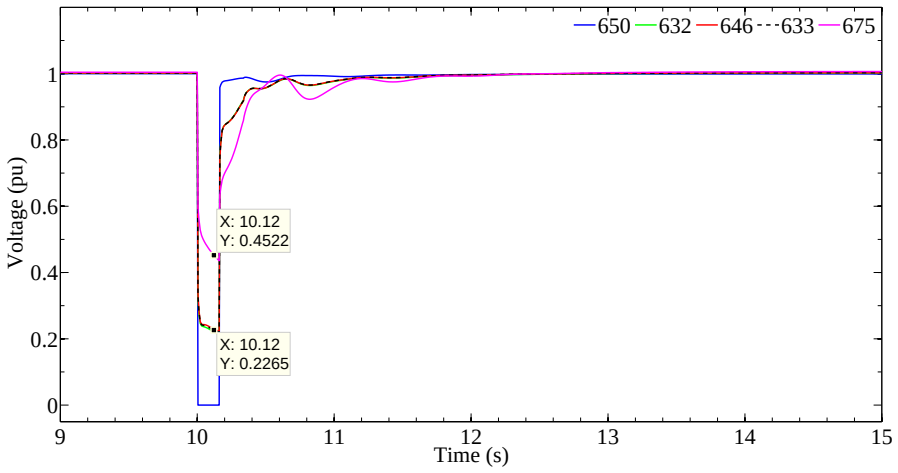

Figure 7.8: Voltage variations at different bus bars in operating region R3 without DSTATCOM (fault duration - 160 ms)

critical clearing time (CCT) of the three-phase short-circuit fault was determined for each operating region of the microgrid with and without the DSTATCOM. The CCT for the microgrid was determined based on the SG pole slip, and any grid code

compliance or the action of protection devices were not taken into consideration. It can be observed from Table 7.3 that the CCT of the microgrid with DSTATCOM is longer compared to the microgrid without the DSTATCOM. Therefore, provision of reactive power support from the DSTATCOM has enabled the microgrid to operate over a longer period during a fault.

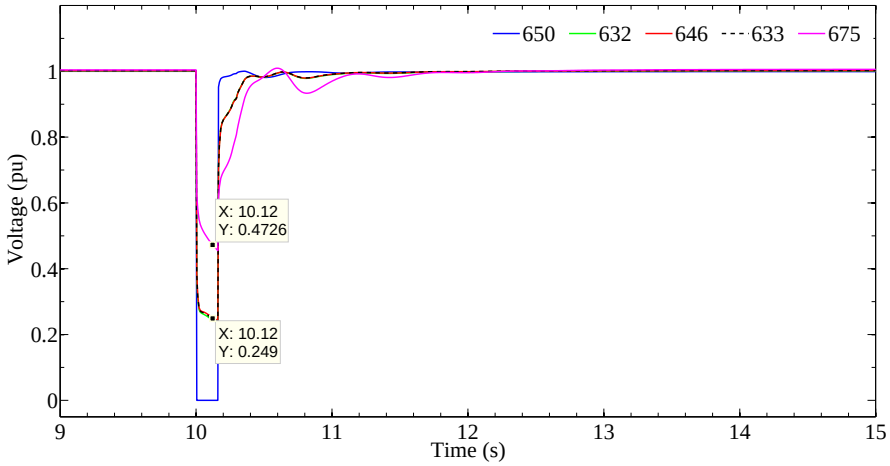

Figure 7.9: Voltage variations at different bus bars in operating region R3 with DSTATCOM (fault duration - 160 ms)

Fig. 7.6 (a) and Fig. 7.6 (b) illustrate the voltage variations of five of the bus bars in the microgrid without and with the DSTATCOM for a fault duration of 538 ms. Comparing those figures, it can be observed that the post fault voltage has improved considerably with the DSTATCOM. Furthermore, depth of the voltage sag has decreased by 0.022 pu during the fault with the DSTATCOM for operating region R1. Fig. 7.7 illustrates the variation of voltage for operating region R2, which indicates approximately a 0.03 pu decrease in the voltage sag during the fault with the DSTATCOM. Similarly, for operating regions R3 and R4, an improvement of the depth of the voltage sag can be noted with the DSTATCOM, as observed from Fig. 7.8 to Fig. 7.10 respectively.

Fig. 7.11 illustrates the reactive power variations of the distribution lines connected to Bus bar 632 with the DSTATCOM. In operating region R1, reactive power has flowed from the distribution transformer to the microgrid during steady state. During the fault, it can be observed that the direction of the reactive power flow has

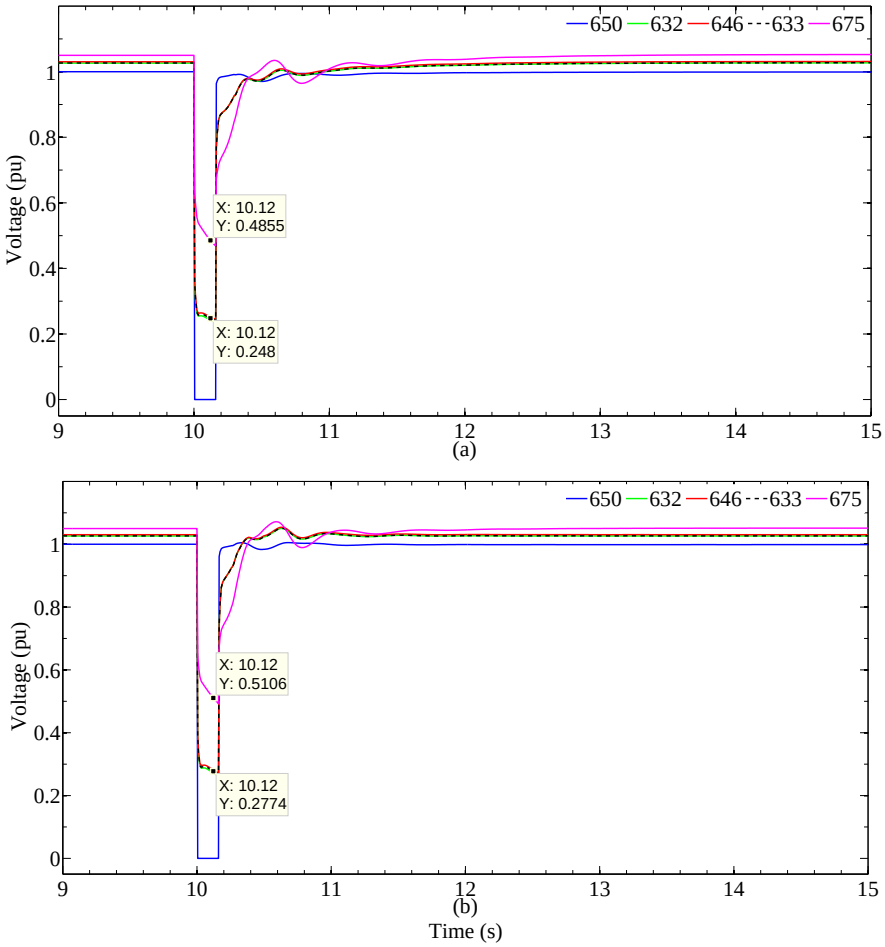

Figure 7.10: Voltage variations at different bus bars in operating region R4 (a) without DSTATCOM and (b) with DSTATCOM (fault duration - 160 ms)

changed from the microgrid to the distribution transformer. With the DSTATCOM, maximum reactive power variation of the microgrid during the fault has increased by 0.8 MVAr. Furthermore, post fault transients are considerably less and system reached the steady state faster with the DSTATCOM in the microgrid. Similar to operating region R1, reactive power has been imported into the microgrid in operating region R2 at steady state. From Fig. 7.12, it can be observed that reactive power contribution from the microgrid has increased during the fault due to the DSTATCOM operation as well as reduction in post fault transients. By examining Fig. 7.13 to Fig. 7.15 corresponding to the operation of regions R1 and R2 of the microgrid, it can be identified that the reactive current contribution from the microgrid into the external grid during the fault has increased due to the reactive power supplied by the DSTATCOM.

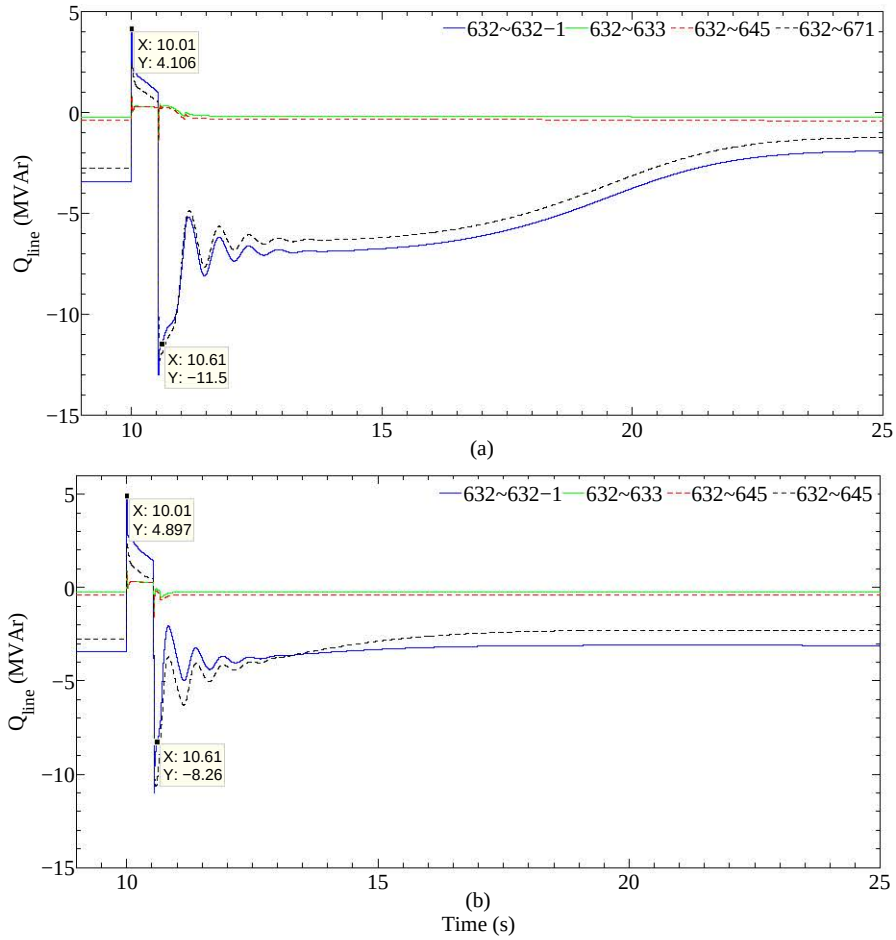

Figure 7.11: Reactive power flow variations in the distribution lines connected to Bus bar 632 (R1) (a) without DSTATCOM operation and (b) with DSTATCOM operation due to an external grid fault

Fig. 7.16 and Fig. 7.17 illustrate the variations of reactive power flow of the distribution lines connected to Bus bar 632 with the DSTATCOM in operating regions R3 and R4 respectively, in which reactive power has been exported to the external grid. Observing those figures, it can be identified that the maximum reactive power flow from the microgrid into the distribution transformer has increased by 1.6 MVAr with the DSTATCOM. Similarly, with the DSTATCOM, approximately 1.0 MVAr of reactive power increase can be observed in operating region R4. With the DSTATCOM, less post fault transients can be observed in the microgrid. By examining Fig. 7.18, Fig. 7.19, and Fig. 7.20 corresponding to the operating regions R3 and R4 of the microgrid, it can be identified that the reactive current contribution from the microgrid into the external grid has increased due to the connection of the DSTAT-

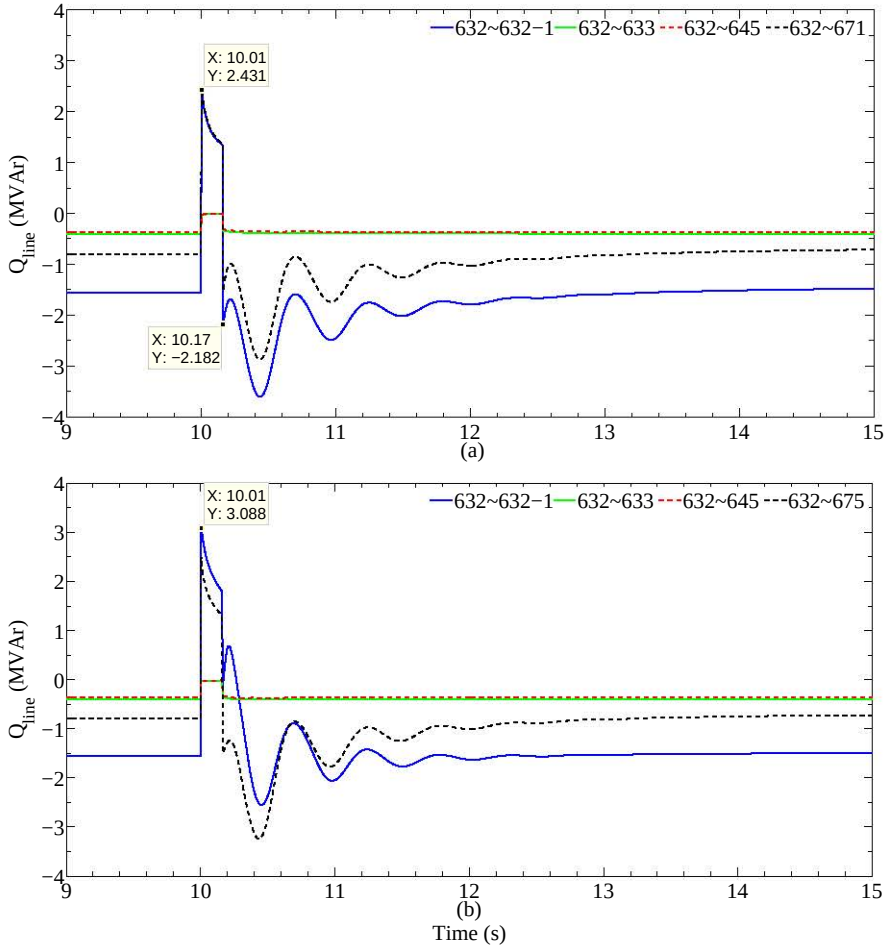

Figure 7.12: Reactive power flow variations in the distribution lines connected to Bus bar 632 (R2) (a) without DSTATCOM operation and (b) with DSTATCOM operation due to an external grid fault

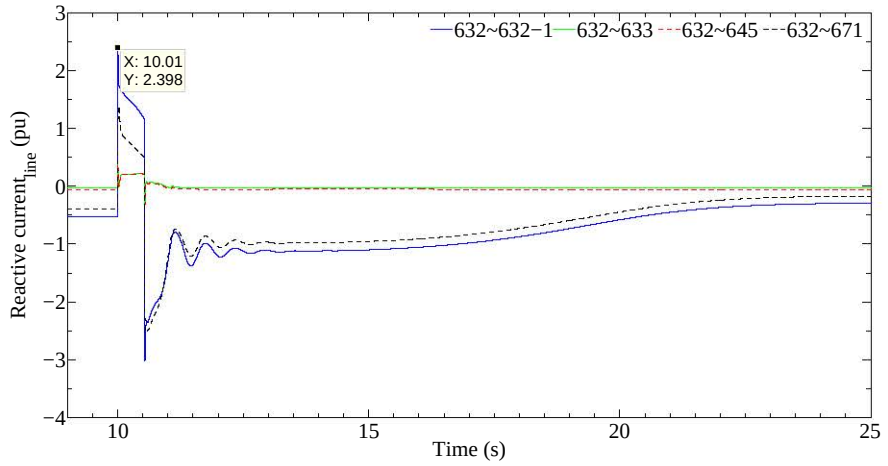

Figure 7.13: Reactive current flow in the distribution lines connected to Bus bar 632 (R1) without DSTATCOM operation due to an external grid fault

COM. Therefore, it is clear that a DSTATCOM can be used to provide additional reactive power during faults in order to improve post fault voltage recovery of the

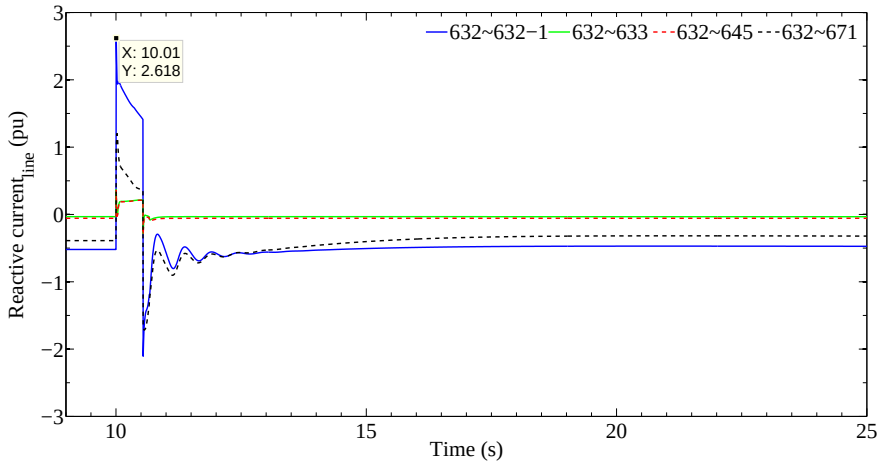

Figure 7.14: Reactive current flow in the distribution lines connected to Bus bar 632 (R1) with DSTATCOM operation due to an external grid fault

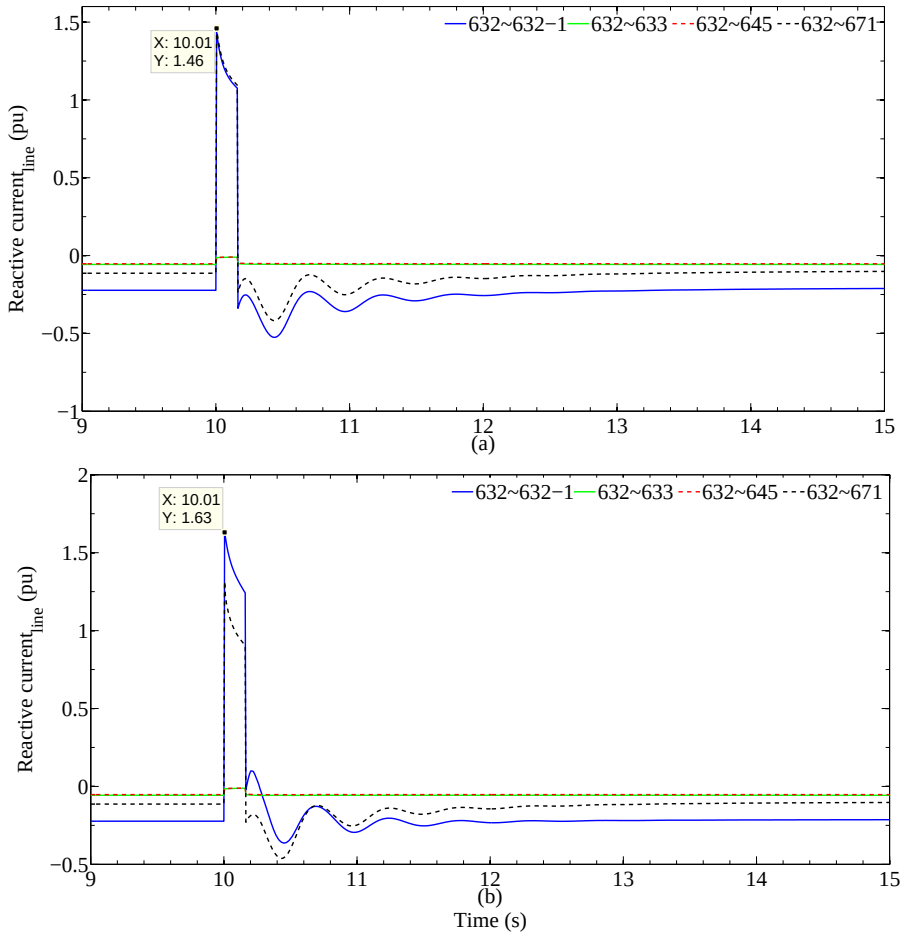

Figure 7.15: Reactive current flow in the distribution lines connected to Bus bar 632 (R2) (a) without DSTATCOM operation and (b) with DSTATCOM operation due to an external grid fault

microgrid.

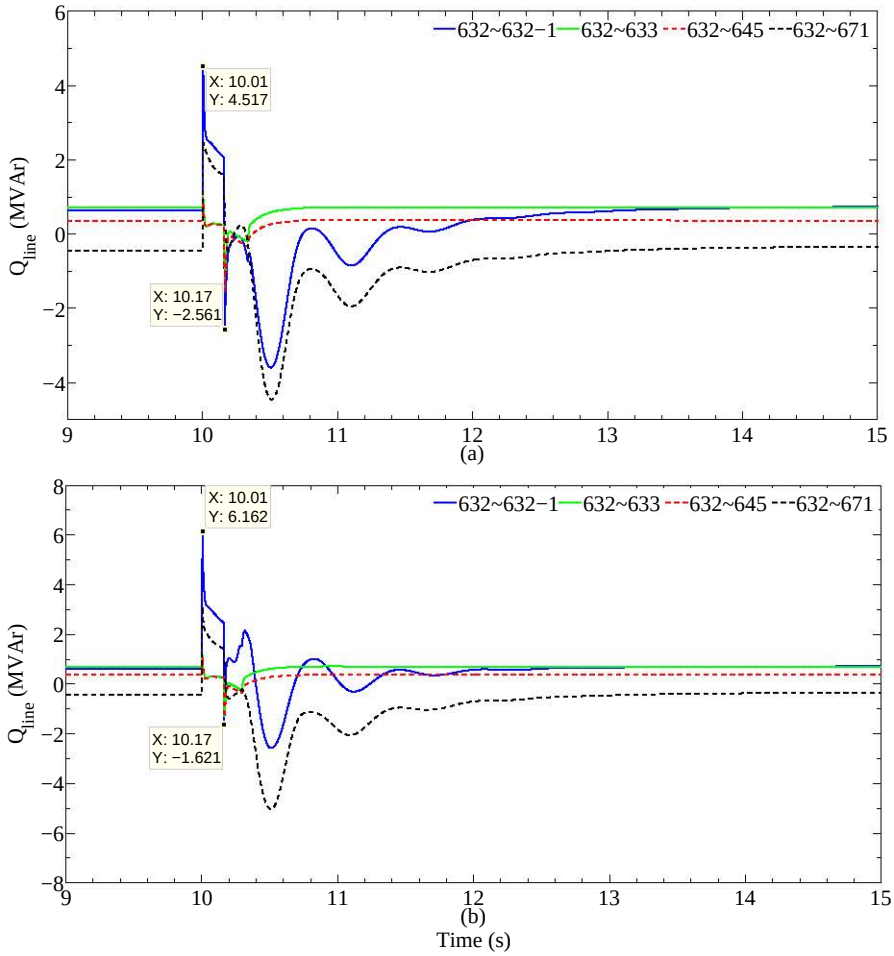

Figure 7.16: Reactive power flow variations in the distribution lines connected to Bus bar 632 (R3) due to an external grid fault

7.3.2 Microgrid Behaviour due to Internal Faults with DSTATCOM

In order to analyse the effect of DSTATCOM due to internal faults, different faults were applied at three different bus bars in the microgrid when operating in region R1. The DSTATCOM was kept connected to Bus bar 632. Three-phase short-circuit faults were applied to Bus bars 611, 633 and 692 through different fault impedances. Fig. 7.21 illustrates the magnitude of the minimum voltage measured at the DSTATCOM terminal during three different faults. It can be observed that during voltage sag, the minimum voltage has improved due to the DSTATCOM operation. Fig. 7.22 illustrates the reactive power injected by the DSTATCOM into the network during microgrid internal faults. Depending on the severity at the DSTATCOM terminal, reactive power support is provided by the DSTATCOM to the microgrid system.

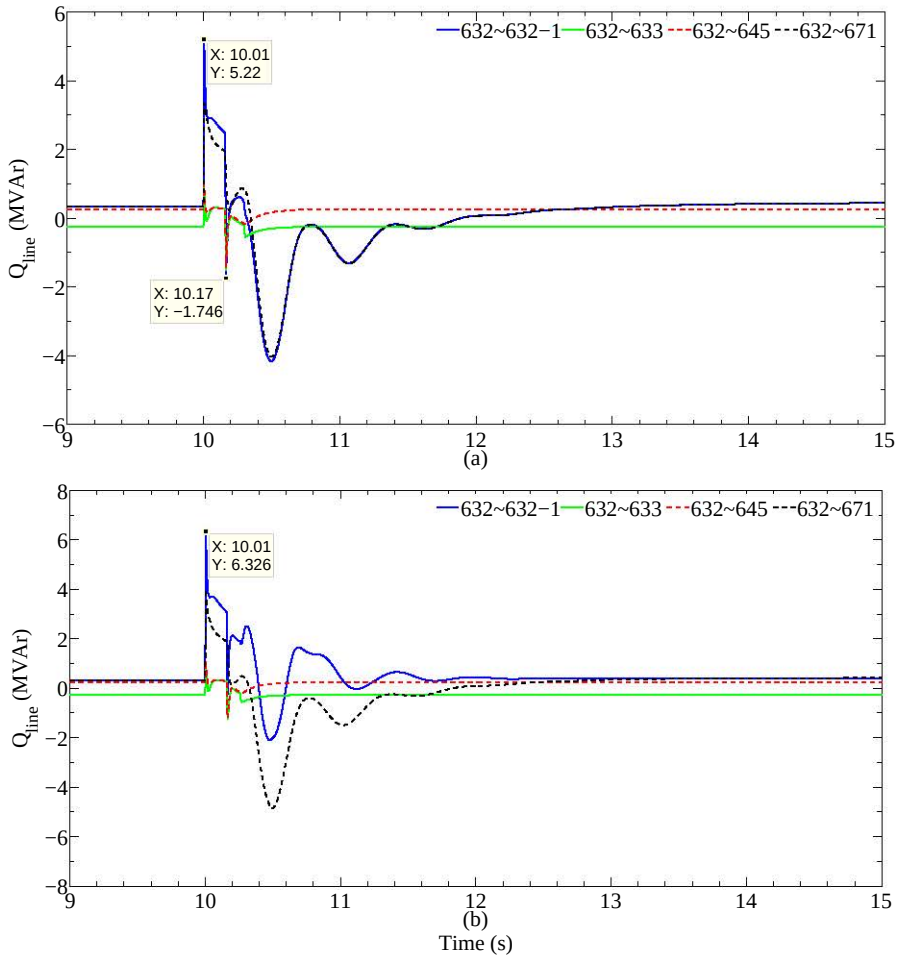

Figure 7.17: Reactive power flow variations in the distribution lines connected to Bus bar 632 (R4) due to an external grid fault

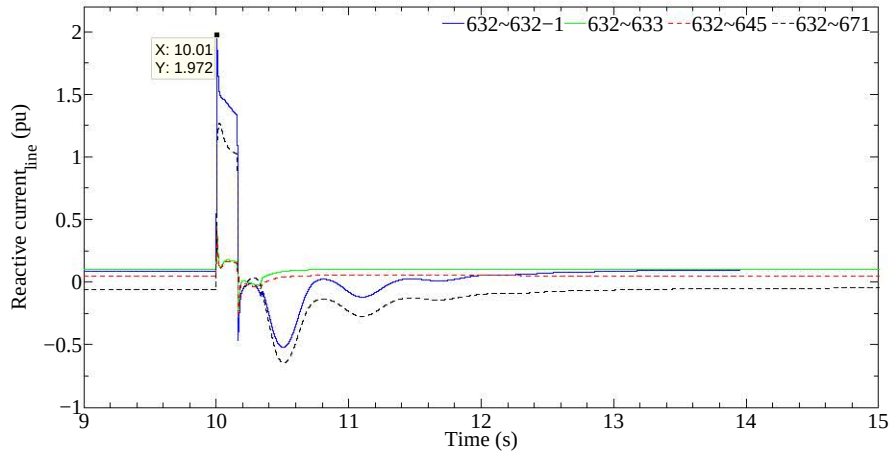

Figure 7.18: Reactive current flow in the distribution lines connected to Bus bar 632 (R3) without DSTATCOM operation due to an external grid fault

7.4 Impact of DSTATCOM Location in the Microgrid

7.4.1 DSTATCOM Connection at DG Terminals

In this section, the DSTATCOM on the secondary side of the distribution transformer was removed from the bus bar in the microgrid system introduced in Sec-

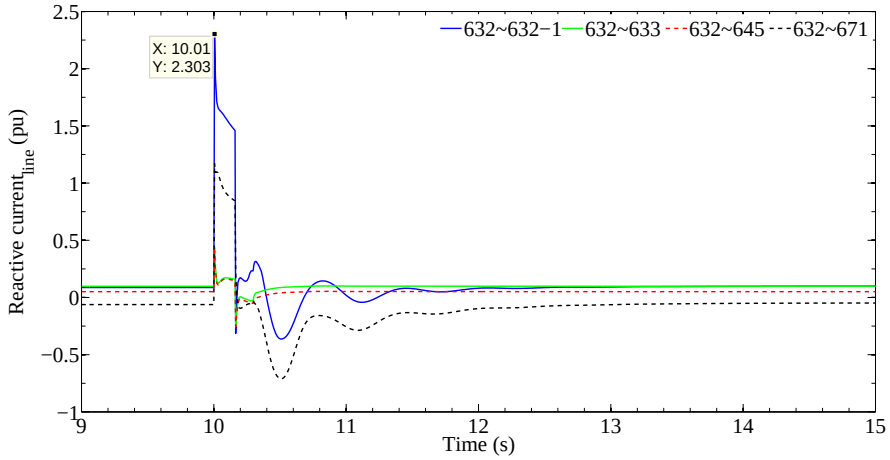

Figure 7.19: Reactive current flow in the distribution lines connected to Bus bar 632 (R3) with DSTATCOM operation due to an external grid fault

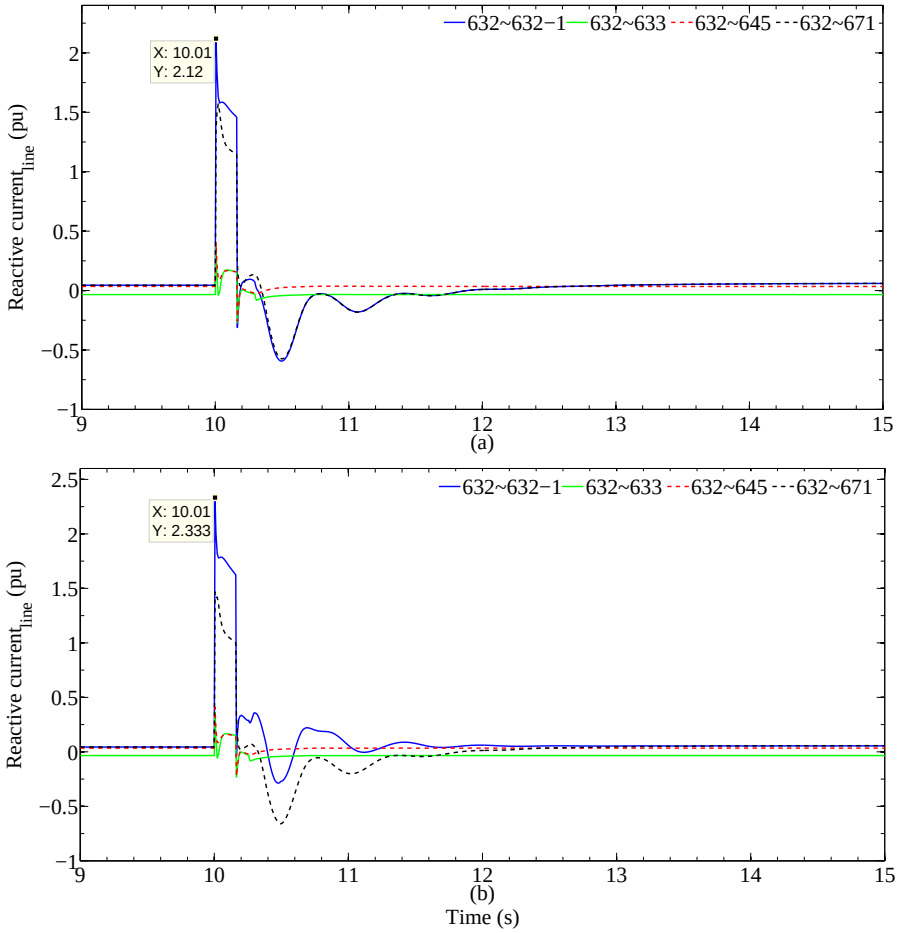

Figure 7.20: Reactive current flow in the distribution lines connected to the DSTATCOM (R4) (a) without DSTATCOM operation and (b) with DSTATCOM operation due to an external grid fault

tion 7.3, and two DSTATCOMs were connected at the two terminals of DG1 and DG2. In order to compare the results with those of Section. 7.3, aggregated gen-

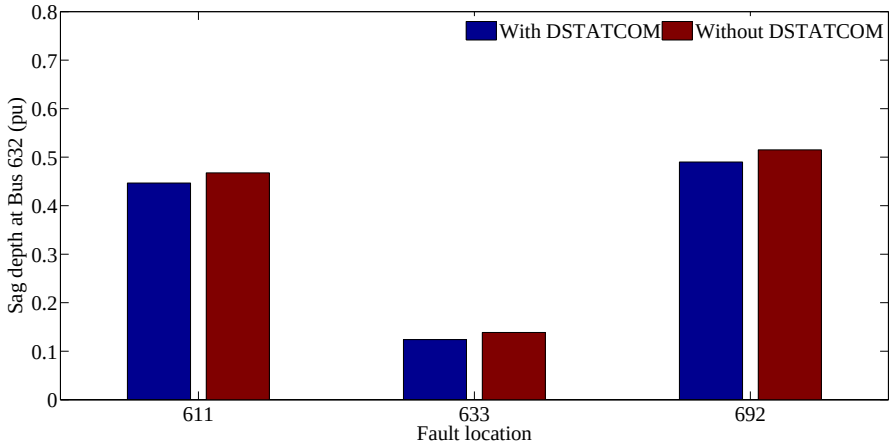

Figure 7.21: Magnitude of the voltage sag depth at Bus bar 632 for different internal faults with and without DSTATCOM

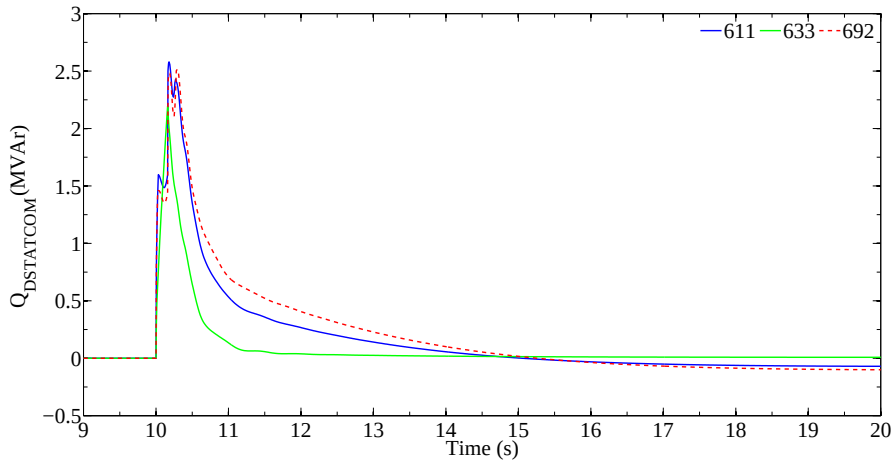

Figure 7.22: Reactive power output of the DSTATCOM for different internal faults in the microgrid

erator capacity was maintained at 3 MVA, hence each DSTATCOM was rated at 1.5 MVA. DG3 was assumed to be disconnected in the microgrid and the different operating conditions considered for this case study are presented in Table 7.4. A three-phase short-circuit fault was applied at Bus bar 650 at $t = 10$ s and cleared after 160 ms.

Fig. 7.23 and Fig. 7.24 illustrate the voltage variations of five bus bars in the microgrid due to the fault. As a result of the fault, terminal voltages of both DG1 and DG2 are zero, and the crowbar protection in both DG1 and DG2 were activated at 10.013 s and deactivated at 10.080 s. However, with the DSTATCOM operation, voltage profile of the microgrid has improved during the fault and the

Table 7.4: Power flow levels of the microgrid

	P (MW)	Q (MVAr)
DG1	0.900	0.0
DG2	0.900	0.0
Ext.grid	0.161	1.101
Total load	1.923	1.042

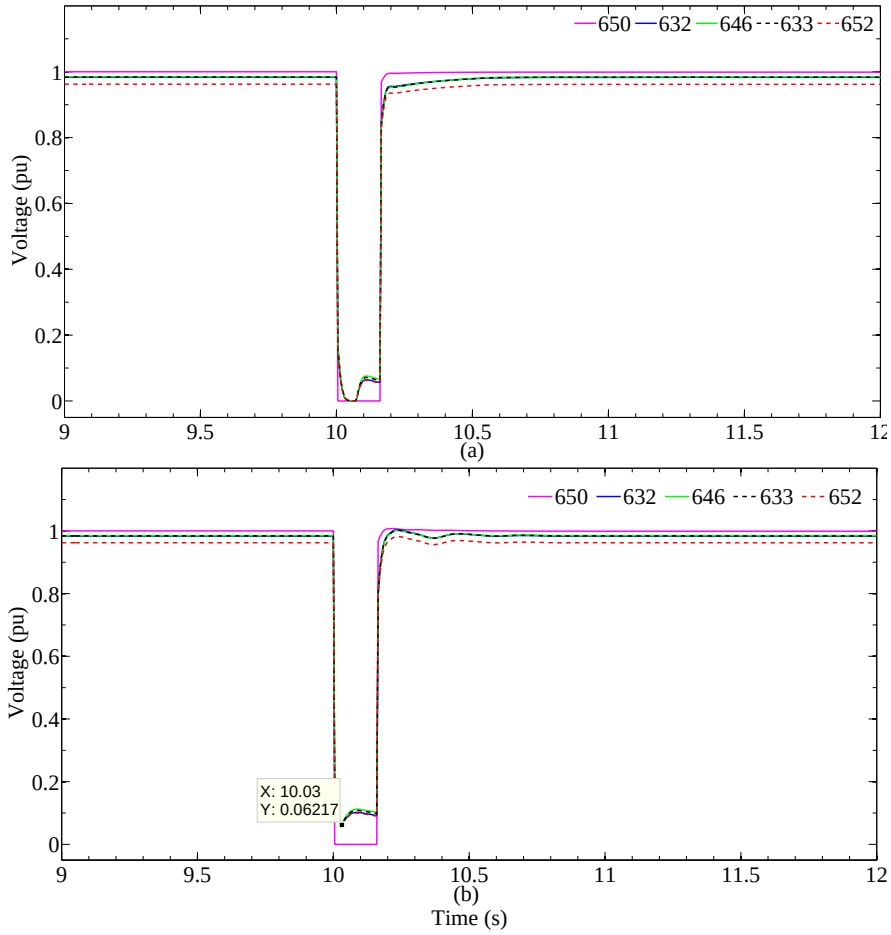

Figure 7.23: Voltage variations (a) without DSTATCOM and (b) with DSTATCOM connected at Bus bar 632 (fault at Bus bar 650)

crowbar protection was not activated as illustrated in Fig. 7.23 (b), and has allowed the DGs to supply power to the microgrid without any interruption. However, it has a less positive effect on the voltage profile compared to the case of having the DSTATCOM on low voltage side of the microgrid distribution transformer.

Fig. 7.25 and Fig. 7.26 present the reactive power flow through the distribution lines connected to Bus bar 632. By examining these figures, it can be observed that having a DSTATCOM on the low voltage side of the microgrid distribution trans-

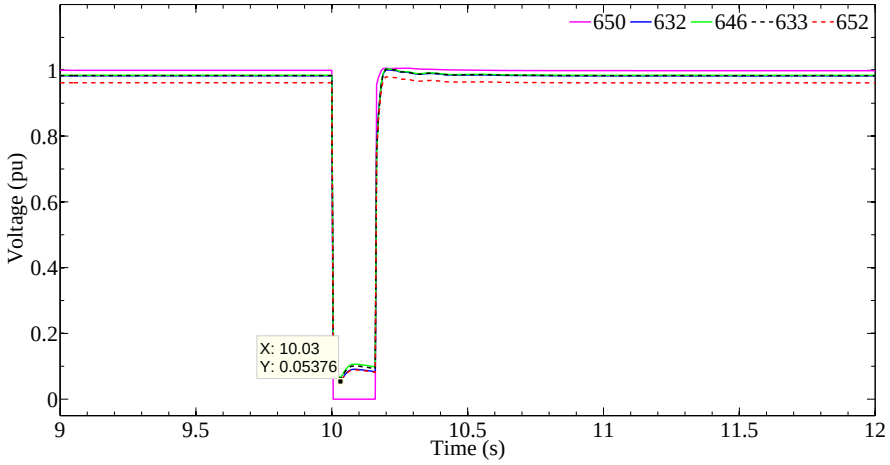

Figure 7.24: Voltage variations with two DSTATCOMs at DG1 and DG2 terminals (fault at Bus bar 650)

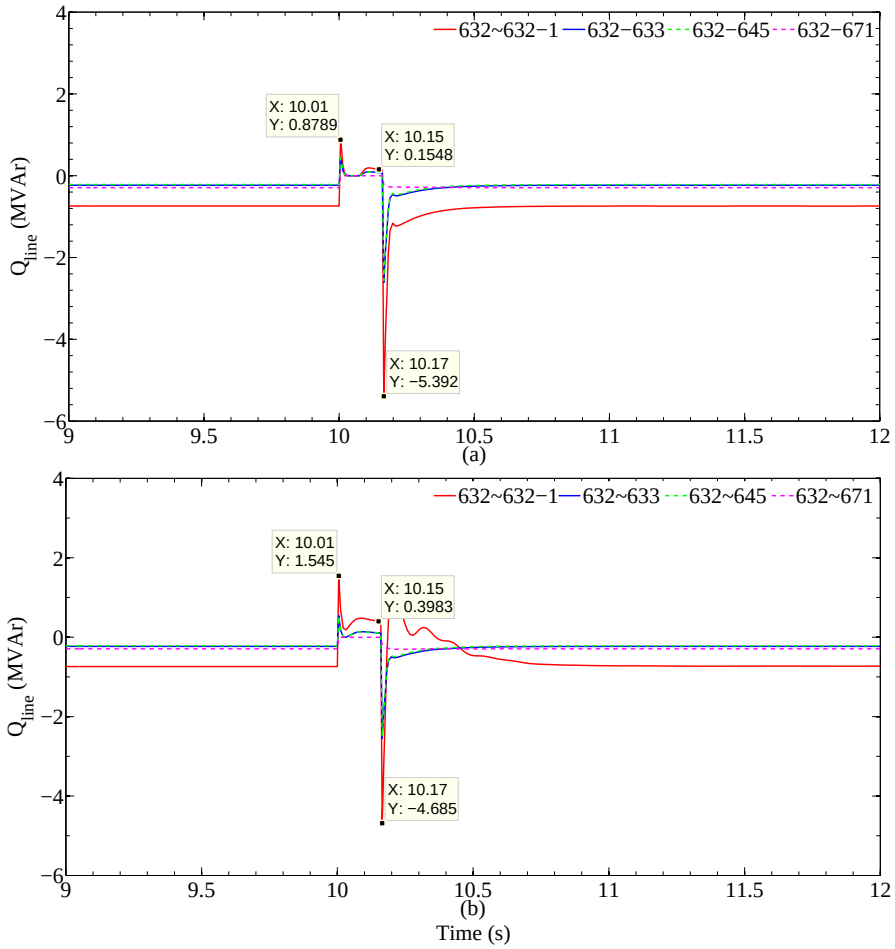

Figure 7.25: Reactive power variations of the distribution lines connected to Bus bar 632, (a) without DSTATCOM and (b) with DSTATCOM connected at Bus bar 632 (fault at Bus bar 650)

former would increase the reactive power flow towards the distribution transformer.

Furthermore, during the post fault transients, reactive power absorption from the

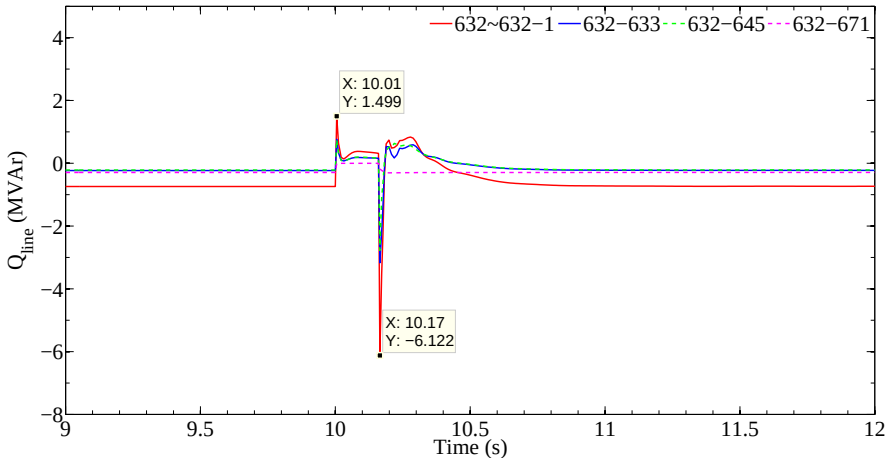

Figure 7.26: Reactive power variations of the distribution lines connected to Bus bar 632 with two DSTATCOMs at DG1 and DG2 terminals (fault at Bus bar 650)

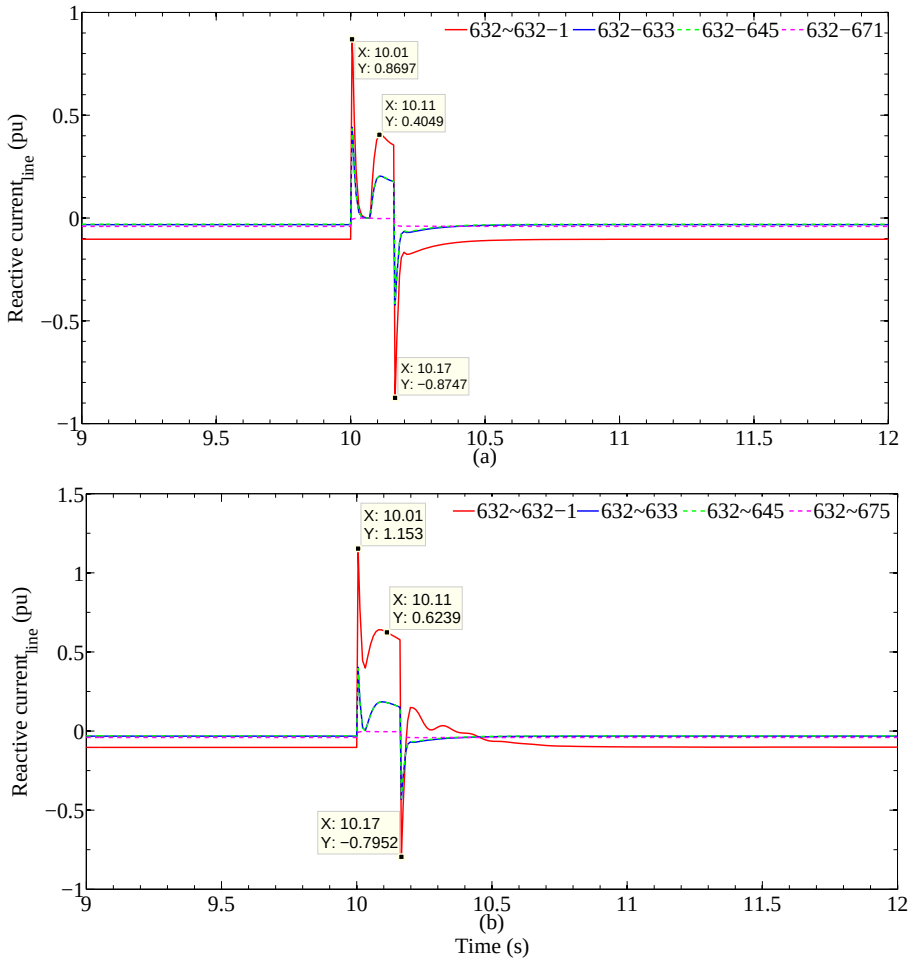

Figure 7.27: Reactive current flow of the distribution lines connected to Bus bar 632 (a) without DSTATCOM and (b) with DSTATCOM connected at Bus bar 632 (fault at Bus bar 650)

microgrid was minimum when the DSTATCOM was installed on the low voltage side of the microgrid distribution transformer.

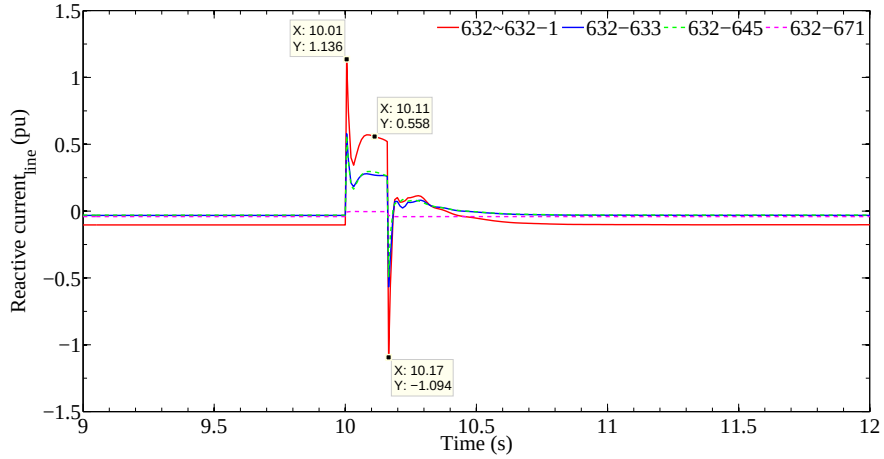

Figure 7.28: Reactive current flow of the distribution lines connected to Bus bar 632 with two DSTATCOMs at DG1 and DG2 terminals (fault at Bus bar 650)

As illustrated in Fig. 7.27, reactive current flow from the microgrid into the external grid has significantly increased due to the operation of the DSTATCOM. Compared to the operation of DSTATCOMs at the DG terminals, a DSTATCOM near the secondary side of the microgrid distribution transformer has better reactive current contribution to the external grid during the fault. Furthermore, by examining Fig. 7.27 and Fig. 7.28, it can be observed that the post fault reactive current flow into the microgrid is high when the DSTATCOMs are connected at DG terminals.

7.4.2 DSTATCOM Connection at the Bus bar with Minimum Reactive Power Margin of the Microgrid

In this section, the DSTATCOM was connected at the bus bar with the minimum reactive power margin of the microgrid in order to investigate the impact of DSTATCOM location on microgrid performance during faults. The same microgrid system described in Section 7.4.1 was used for this case study, and for the purpose of comparison, rating of the DSTATCOM was selected to be 3 MVA. In order to find the bus bar with the minimum reactive power margin in the microgrid, V-Q curve method

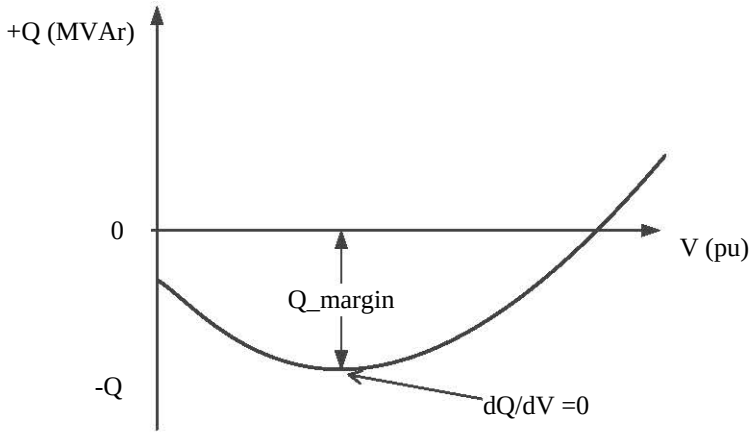

Figure 7.29: V-Q curve and reactive power margin

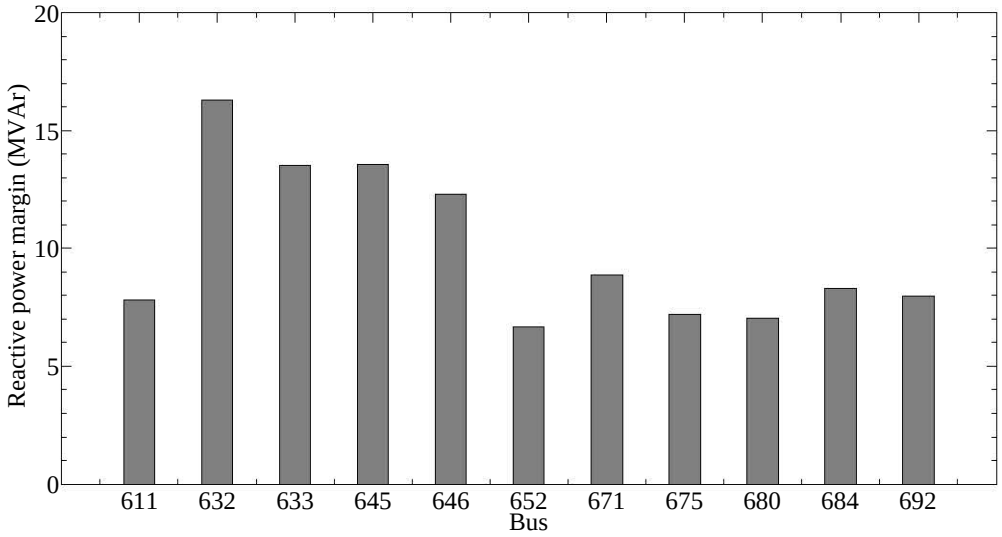

Figure 7.30: Reactive power margins of the bus bars in the microgrid

was used in this section. V-Q curves were used to determine the capability of a bus bar to maintain voltage during normal and abnormal conditions [190]. Minimum of the V-Q curve (where $dQ/dV = 0$) represents the voltage stability limit, where the distance of the operating point at any particular loading to the minimum of the curve gives an indication to the closeness of system collapse [191]. V-Q curves were derived through a series of ac power flow solutions, and the reactive power margin (Q_margin) was measured as the distance between the reactive power level of the V-Q curve at $dQ/dV = 0$ and the voltage axis as illustrated in Fig. 7.29. A positive reactive power margin indicates a deficit of reactive power at the particular bus bar whereas, a negative reactive power margin indicates the amount of reactive

power the bus bar can supply to the system without being unstable.

Fig. 7.30 illustrates the reactive power margins of the bus bars in the microgrid, and Bus bar 652 was identified as the bus bar the minimum reactive power margin.

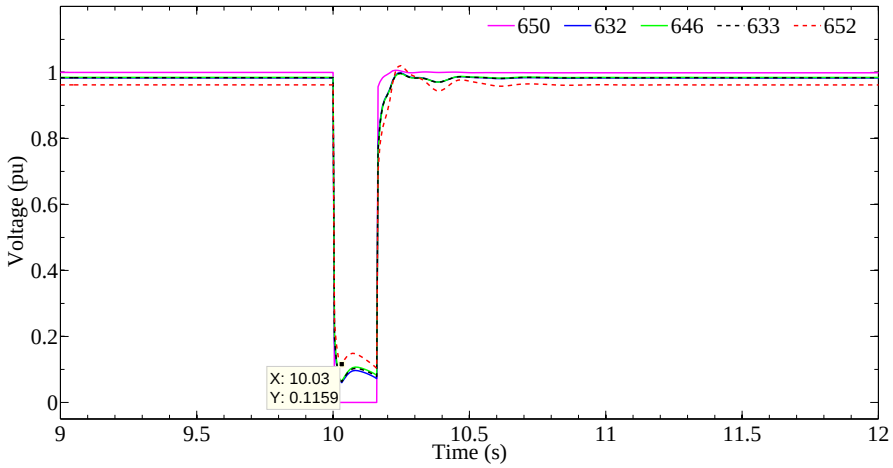

Figure 7.31: Voltage variations with a DSTATCOM at the bus bar with minimum Q-margin (fault at Bus bar 650)

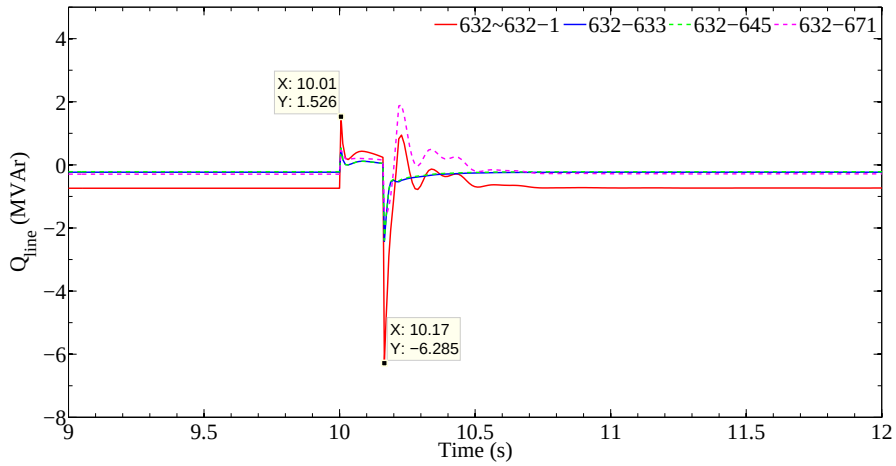

Figure 7.32: Reactive power variations of the distribution lines connected to Bus bar 632 with DSTATCOM connected at the bus bar with minimum Q-margin (fault at Bus bar 650)

The microgrid was subjected to the same three-phase short-circuit fault considered in Section 7.4.1, and Fig. 7.31 presents the voltage variations of the bus bars due to the fault. As expected, it can be observed that the voltage profile of the bus bar connected to the DSTATCOM has improved. Comparing Fig. 7.25 (b) and Fig. 7.27 (b) with Fig. 7.32 and Fig. 7.33, it can be observed that installing a DSTATCOM near the distribution transformer of the microgrid has provided better

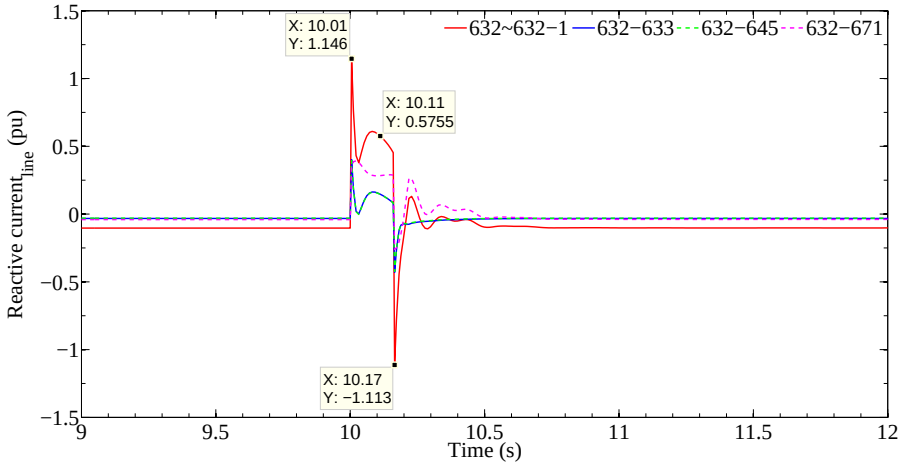

Figure 7.33: Reactive current flow variations of the distribution lines connected to Bus bar 632 with a DSTATCOM connected at the bus with minimum Q-margin (fault at Bus bar 650)

reactive power performance when the microgrid was subjected to faults. When the DSTATCOM was not installed on the low voltage side of the microgrid distribution transformer, the microgrid was unable to utilise the maximum capability of the DSTATCOM to provide support to the external grid.

Fig. 7.34 (a) and Fig. 7.34 (b) illustrate the reactive power output variations of DG1 and DG2 for different DSTATCOM locations. It can be observed that installation of a DSTATCOM in the microgrid has allowed the DGs to provide reactive power into the microgrid continuously without being interrupted by the activation of crowbar protection as explained in Section 7.4.1. Fig. 7.34 (c) illustrates the total reactive power contribution from the DSTATCOMs installed in the microgrid. Reactive power output from the two DSTATCOMs installed at the DG terminals were added together for comparison (as both DSTATCOMs were rated at 1.5 MVA). Analysing the post fault behaviour, it can be observed that when the DSTATCOMs are installed on the low voltage side of the microgrid distribution transformer and at the DG terminals, they provide better reactive power contribution compared to the DSTATCOM at the bus bar with the minimum reactive power margin. Fig. 7.35 summarises the minimum voltage levels experienced by the bus bars in the microgrid during the fault with and without DSTATCOM operation. From a careful analysis, it can be concluded that having the DSTATCOM installed on the low voltage side

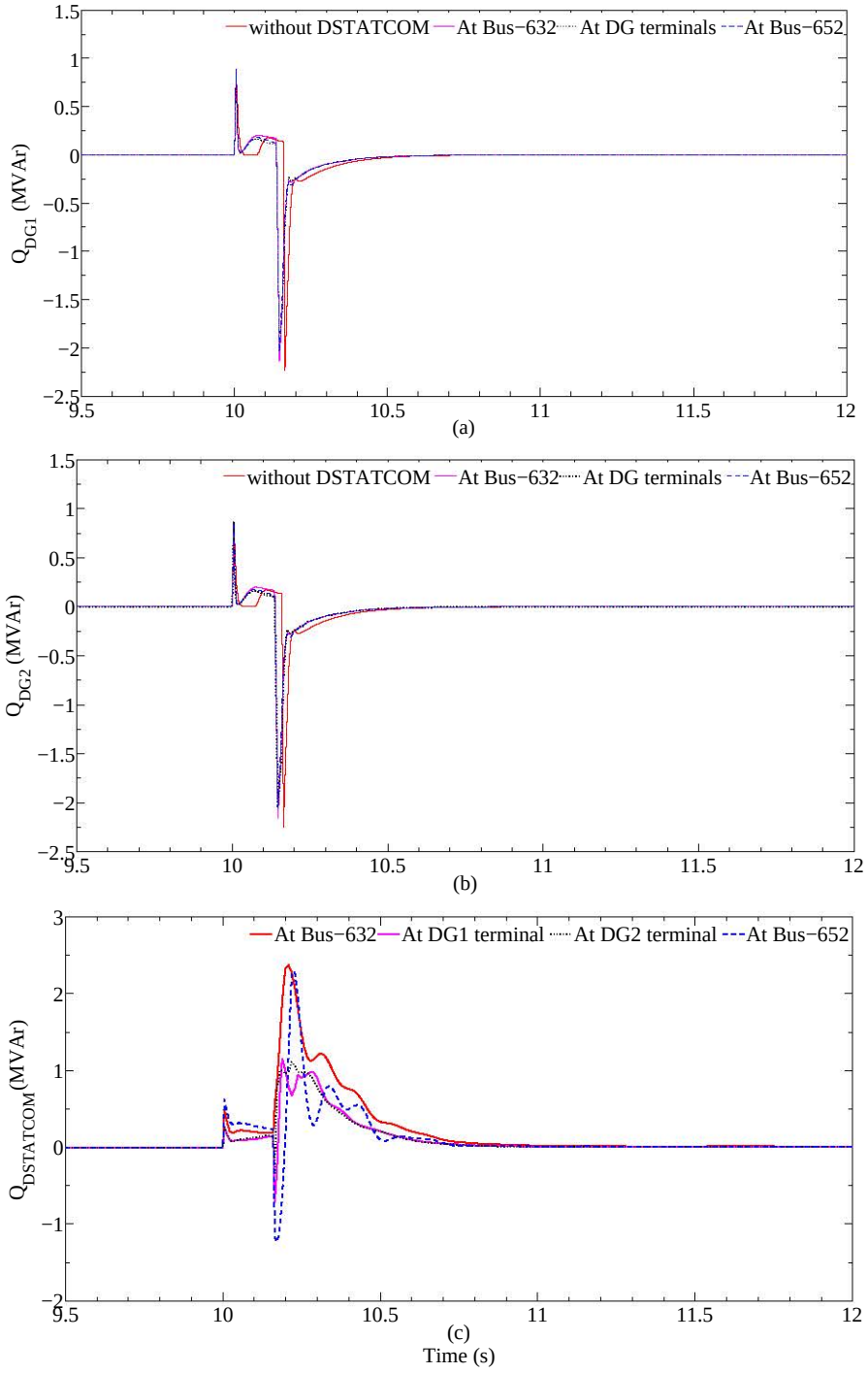

Figure 7.34: Variation of reactive power contribution of (a) DG1, (b) DG2, and (c) DSTATCOM with different DSTATCOM locations (fault at Bus bar 650)

of the microgrid distribution transformer has better impact on all the bus bars of the microgrid compared to the DSTATCOM installed at other locations studied.

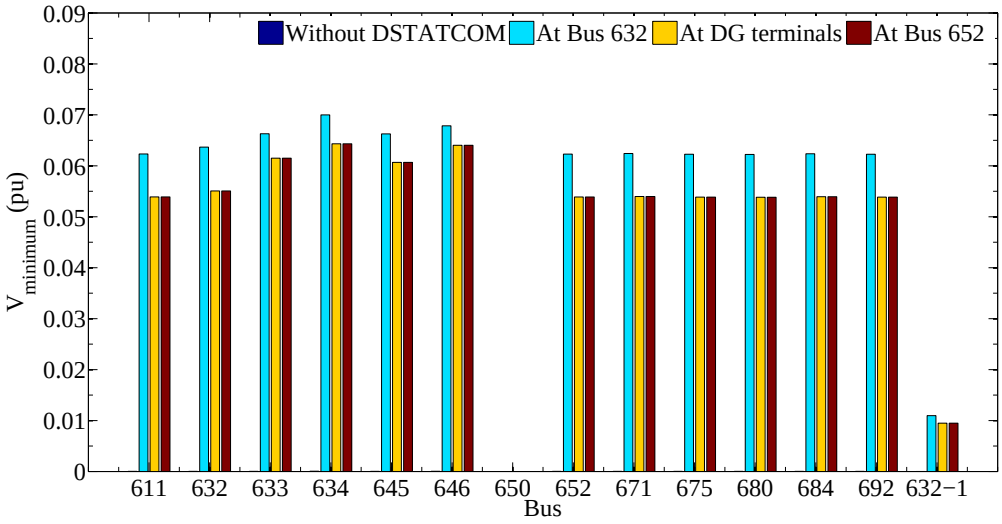

Figure 7.35: Minimum voltage of microgrid bus bars during the fault at Bus bars 650

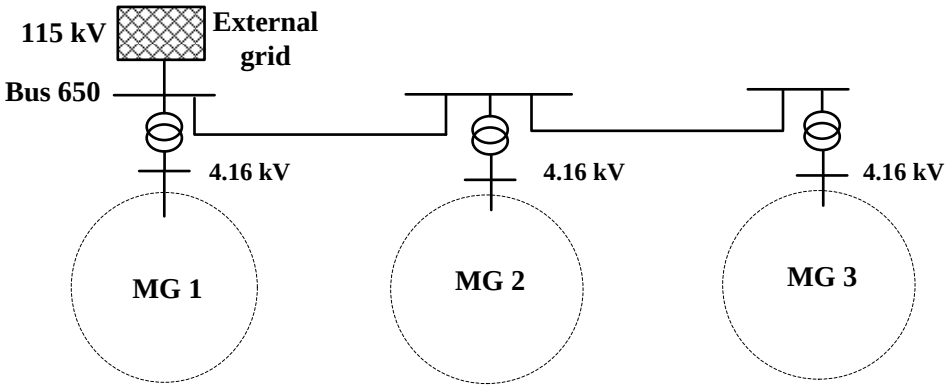

Figure 7.36: Multi-microgrid system

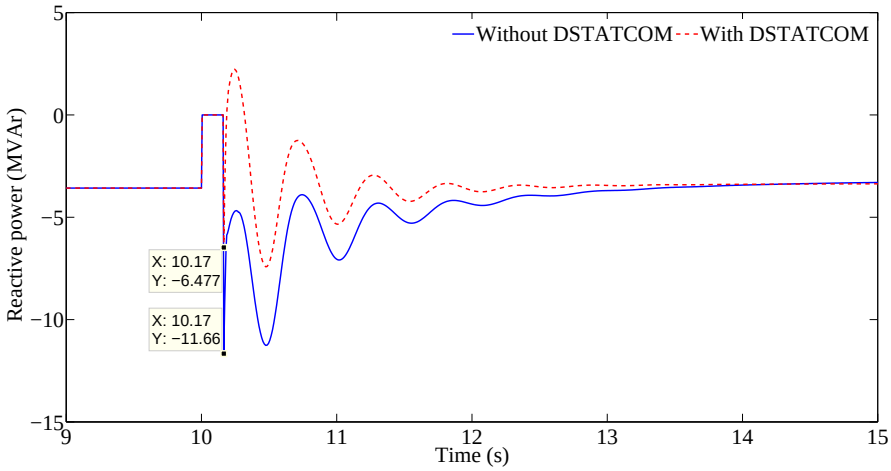

Figure 7.37: Reactive power exchange with the external grid with and without DSTATCOM in each microgrid (fault at Bus bar 650)

Table 7.5: Operating conditions of the microgrids

	MG1		MG2		MG3	
	P (MW)	Q (MVAr)	P (MW)	Q (MVAr)	P (MW)	Q (MVAr)
MG output	3.688	-1.977	0.445	0.381	3.688	-1.976
DG1	1.200	0	0	0	1.200	0
DG2	1.200	0	0.800	0.600	1.200	0
DG3	4.000	-0.123	3.000	1.962	4.000	-0.123
Total load	2.564	1.967	3.275	2.098	2.565	1.968

7.5 DSTATCOM Operation in a Multi-Microgrid System

In this section, operation of a DSTATCOM in a multi-microgrid system which is connected to the utility was analysed. Fig. 7.36 illustrates the multi-microgrid system considered for this study, which consists of three microgrids radially connected to the 115 kV external grid. Case studies were carried out on the microgrid system developed in Section 7.3. Table. 7.5 presents the operating conditions of each microgrid system where MG 1 and MG 3 operated in region R1, while MG 2 operated in region R4.

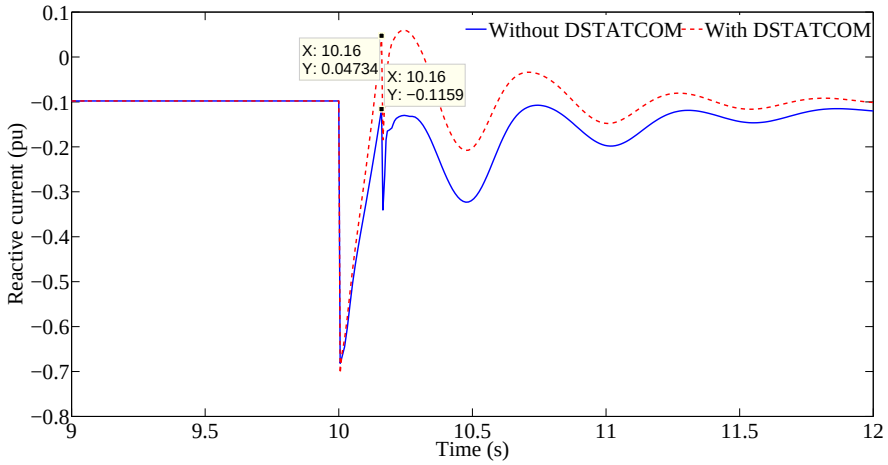

Figure 7.38: Reactive current variation of the external grid due to the fault at Bus bar 650 with and without DSTATCOM

A three-phase short-circuit fault was applied at Bus bar 650 at $t = 10$ s for 150 ms, and the multi-microgrid system behaviour was analysed with and without the DSTATCOM operation. 3 MVA DSTATCOMs were connected to the low voltage side of the microgrid distribution transformers of all three microgrids. Fig. 7.37 illustrates the reactive power exchange with the external grid at Bus bar 650 during

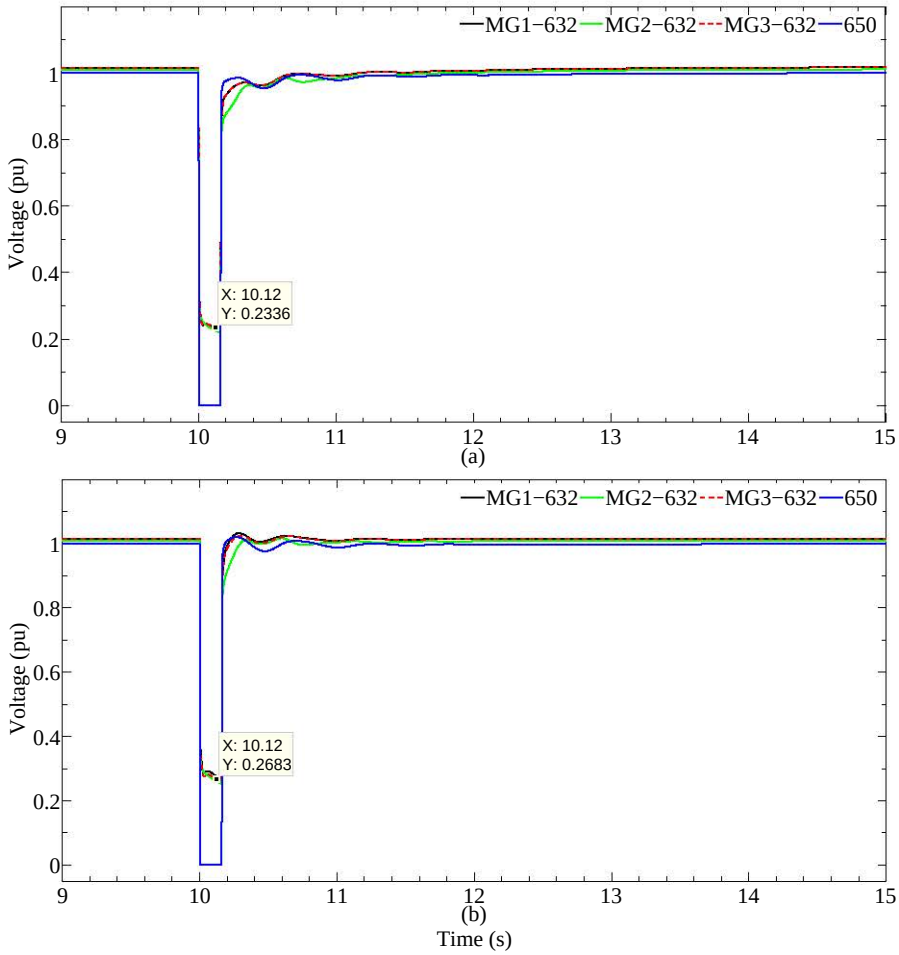

Figure 7.39: Voltage variations of the microgrid bus bars (a) without DSTATCOM and (b) with DSTATCOM (fault at Bus bar 650)

the fault. Prior to the fault, external grid has provided reactive power to the microgrids and after the fault clearance, reactive power absorbed by the microgrid system has considerably reduced with the operation of DSTATCOMs. Furthermore, the multi-microgrid system was able to provide reactive power to the external grid soon after fault clearance, and the system stabilised faster with the DSTATCOM operation. From Fig. 7.38, it can be identified that for the particular operating condition, the multi-microgrid system was able to provide reactive current into the external grid at the instance of fault clearance and after the fault with DSTATCOMs.

Fig. 7.39 (a) and Fig. 7.39 (b) illustrate the voltage variations of the bus bars connected to the DSTATCOM in each microgrid, and the bus bar connected to the external grid (Bus bar 650). It can be observed that with the DSTATCOM, voltage sag at the bus bars have decreased during the fault and the post fault voltage levels have

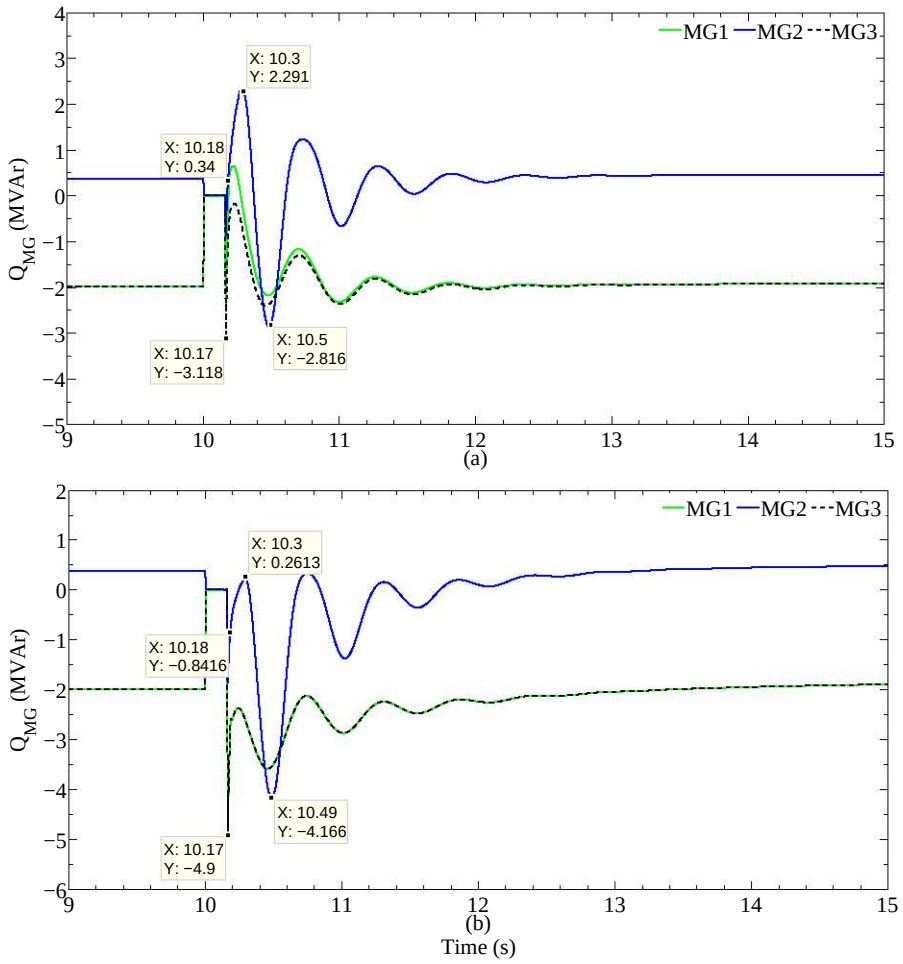

Figure 7.40: Reactive power exchange at the microgrid PCC (a) with and (b) without DSTATCOM (fault at Bus bar 650)

recovered faster. Reactive power exchange through the distribution transformers of each microgrid PCC with and without DSTATCOM are illustrated in Fig. 7.40 (a) and Fig. 7.40 (b) respectively. It can be observed that maximum reactive power import of microgrids after fault clearance transients has reduced considerably with the DSTATCOM. As an example, in MG 1 and MG 3, maximum reactive power import during post fault period has reduced from 4.9 MVAr to 3.118 MVAr. Furthermore, post fault maximum reactive power supply of microgrids has increased. As an example, after the fault clearance, reactive power output from MG 2 has increased considerably from 0.261 MVAr to 2.291 MVAr with the DSTATCOM operation.

As the next scenario, an internal three-phase short-circuit fault was applied at Bus bar 611 at $t = 10$ s for 150 ms in MG 2 and MG 3 separately. Depth of the sag voltage has improved at the DSTATCOM terminal due to the DSTATCOM

operation at each microgrid as presented in Fig. 7.41. Moreover, the DSTATCOM response to faults occurring outside the microgrid depend on the voltage reduction along the feeder. Fig. 7.42 (a) and Fig. 7.42 (b) illustrate the reactive power output variations of the DSTATCOM of each microgrid due to the internal faults at MG 2 and MG 3 respectively.

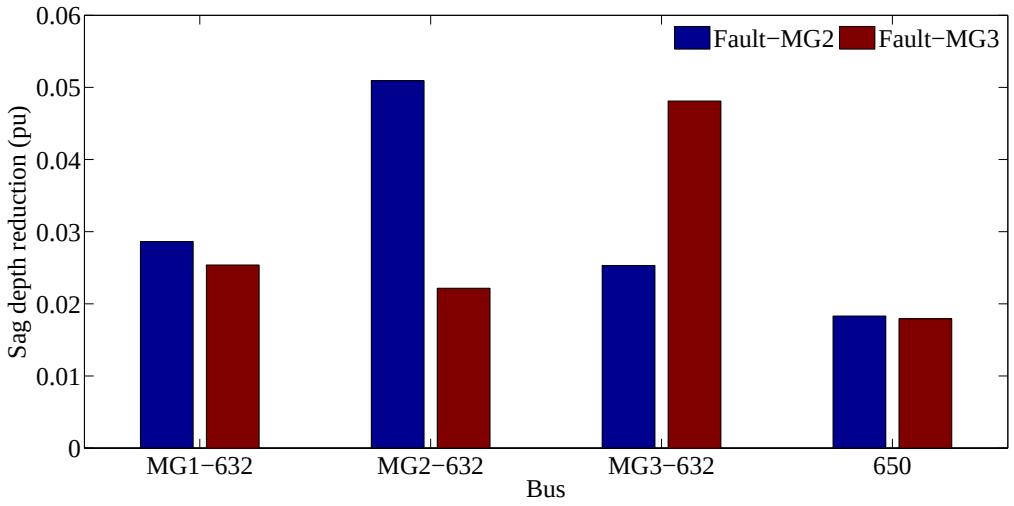

Figure 7.41: Sag voltage reduction at the DSTATCOM terminal in each microgrid and Bus bar 650 subjected to internal faults at different locations

7.6 Islanded Microgrid Operation with DSTATCOM

7.6.1 Single Microgrid System

This section investigates the microgrid performance with DSTATCOMs during islanded mode of operation. The microgrid was disconnected from the external grid by opening the circuit breaker from the secondary side of the distribution transformer. In this scenario, only DG1 and DG3 were supplying power to the local loads, and the steady state active and reactivate power of the islanded microgrid are presented in Table 7.6. A three-phase short-circuit fault was applied to Bus bar 645 at $t = 10\,\mathrm{s}$ and cleared after 150 ms. Behaviour of the microgrid with DSTATCOM operation was investigated by installing 1.5 MVA DSTATCOMs at different locations.

Fig. 7.43 (a) - Fig. 7.43 (c) illustrate the voltage variations of bus bars without DSTATCOM operation, with DSTATCOM installed at DG1 terminal, and with

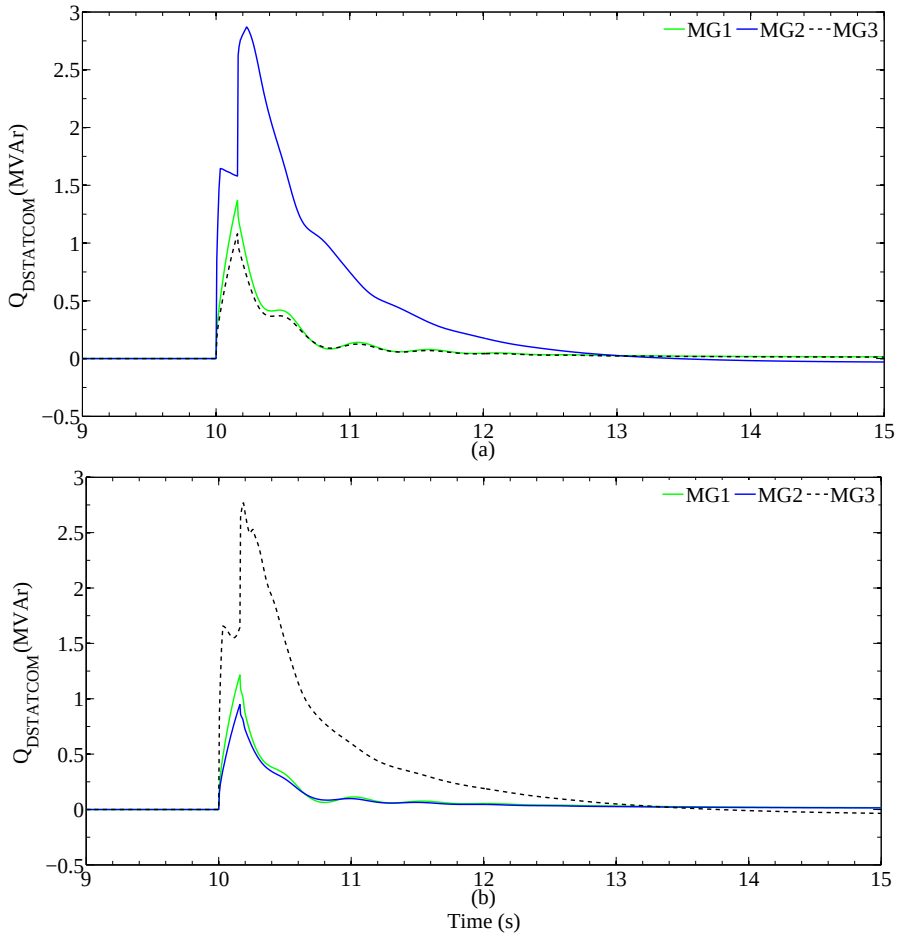

Figure 7.42: Reactive power output variations of the DSTATCOM of each microgrid due to the internal fault (a) at MG 2, and (b) at MG 3

DSTATCOM installed at Bus bar 632. From Section 7.4, it was identified that having the DSTATCOM near low voltage side of the microgrid distribution transformer would benefit both the external grid and the microgrid system in grid connected operation. Hence, Bus bar 632 was selected for this study assuming the possibility of the microgrid transferring from grid connected to islanded mode while having the DSTATCOM installed adjacent to the distribution transformer.

Analysing Fig. 7.43 (a) with Fig. 7.43 (b) and Fig. 7.43 (c), it can be observed that the post fault voltage recovery of the microgrid system has improved with the

Table 7.6: Active and reactive power values of the islanded microgrid system

	P (MW)	Q (MVAr)
DG1	0.900	0.0
DG3	3.520	2.615
Total load	4.330	2.538

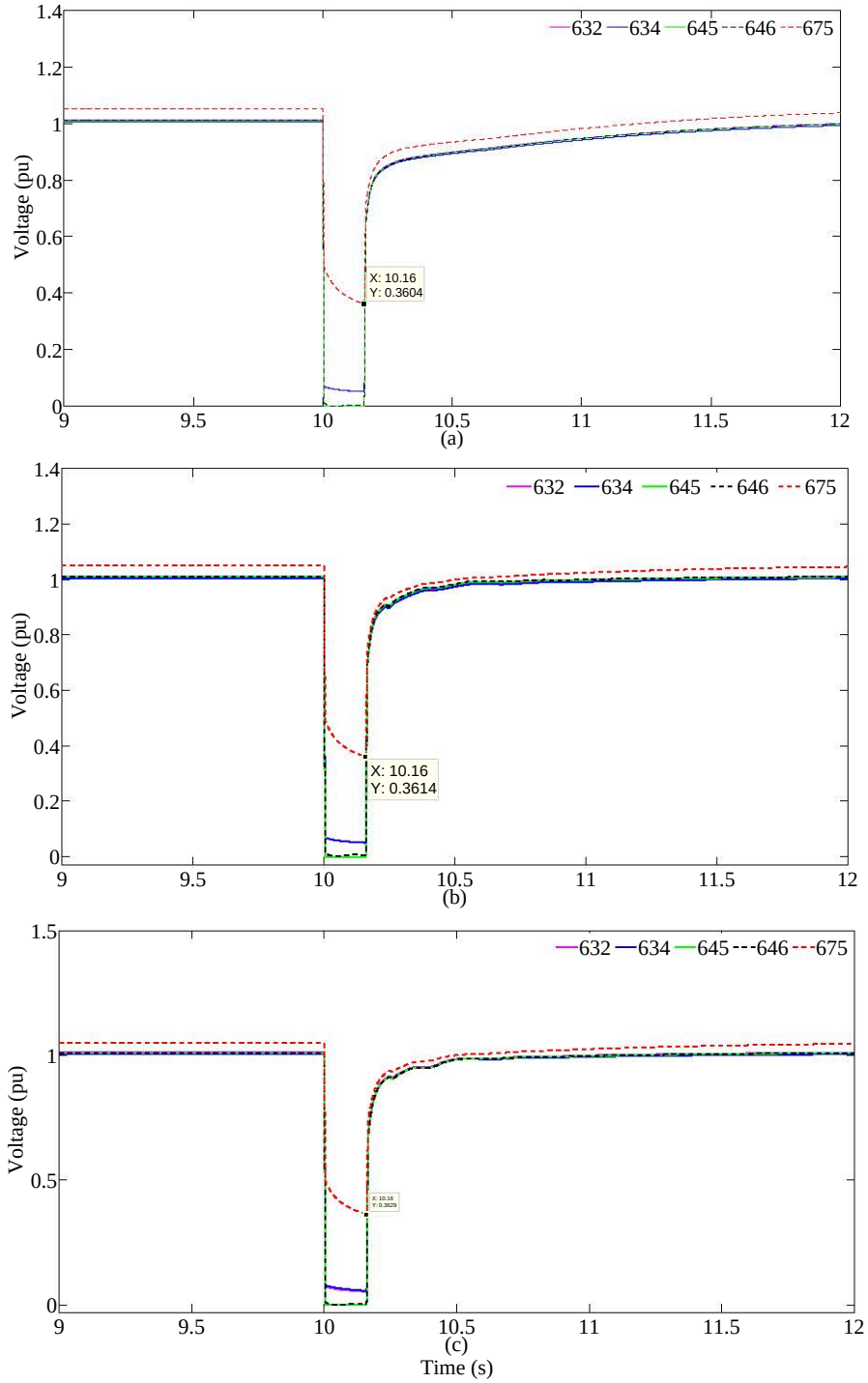

Figure 7.43: Voltage variations due to the internal fault (a) without DSTATCOM, (b) with DSTATCOM at DG1 terminal, (c) with DSTATCOM at Bus bar 632 during islanded mode

DSTATCOM operation. Fig. 7.44 presents a comparison of the voltage at Bus bar 634 with and without DSTATCOM operation. Reactive power variations and reactive current contributions from the DSTATCOM into the microgrid are presented

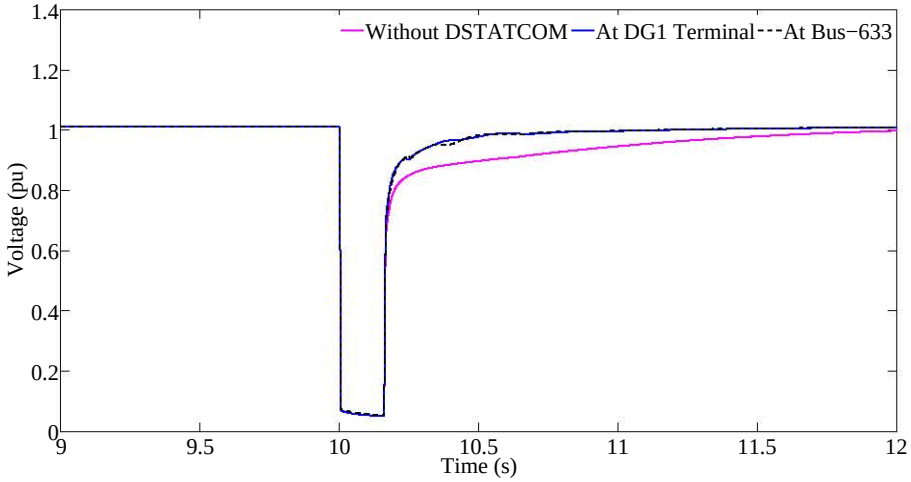

Figure 7.44: Voltage variations due to the internal fault at Bus bar 634 during islanded mode

in Fig. 7.45 and Fig. 7.46 respectively. On both occations, DSTATCOM supply the full reactive power support after fault clearance.

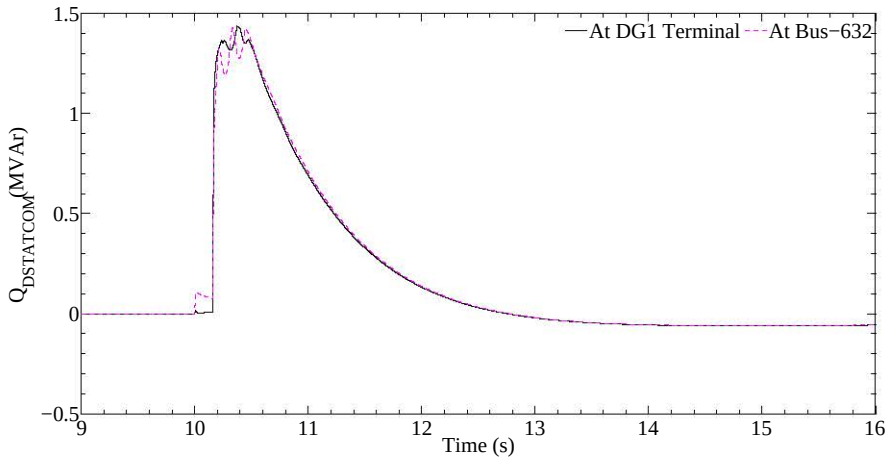

Figure 7.45: Reactive power variations of the DSTATCOMs due to the fault at Bus bar 645 during islanded mode

7.6.2 Multi-Microgrid System

In this section, operation of a DSTATCOM in a multi-microgrid system which is islanded from the external grid is analysed. The multi-microgrid system illustrated in Fig. 7.36 is used for the analysis without the external grid connection. Operating conditions of the DGs of the microgrids and the loading conditions are presented in Table. 7.7, where MG 1 operated in region R3, MG 2 and MG 3 operate in region

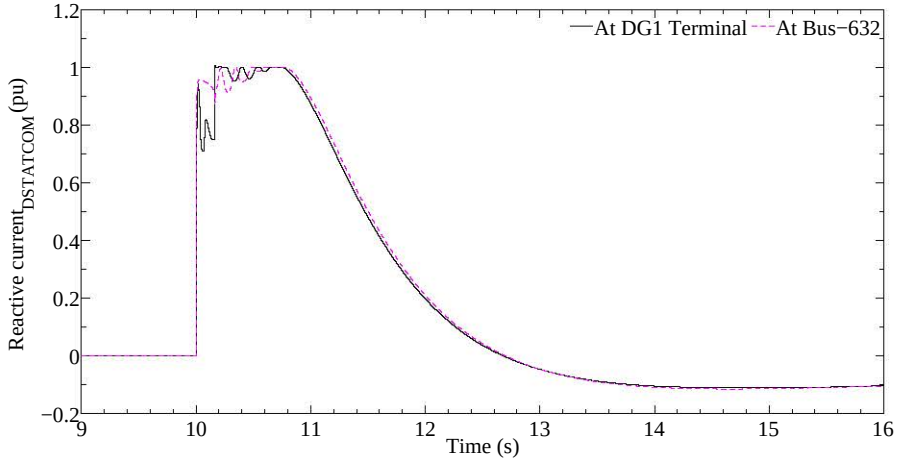

Figure 7.46: Reactive current contribution from DSTATCOM into the microgrid during islanded mode

R1. MG 1 consists of static loads, whereas MG 2 consists of 50 % induction motor loads and MG 3 consists of 30 % of induction motor loads.

Table 7.7: Operating conditions of the multi-microgrid system

	MG1		MG2		MG3	
	P (MW)	Q (MVAr)	P (MW)	Q (MVAr)	P (MW)	Q (MVAr)
MG output	-1.028	0.860	0.501	-0.579	0.527	-0.282
DG1	0.600	0	0	0	0	0
DG2	0	0	1.000	0.600	0	0
DG3	2.972	3.521	4.000	2.171	3.500	1.455
Total load	4.436	2.480	4.344	2.584	2.853	1.600

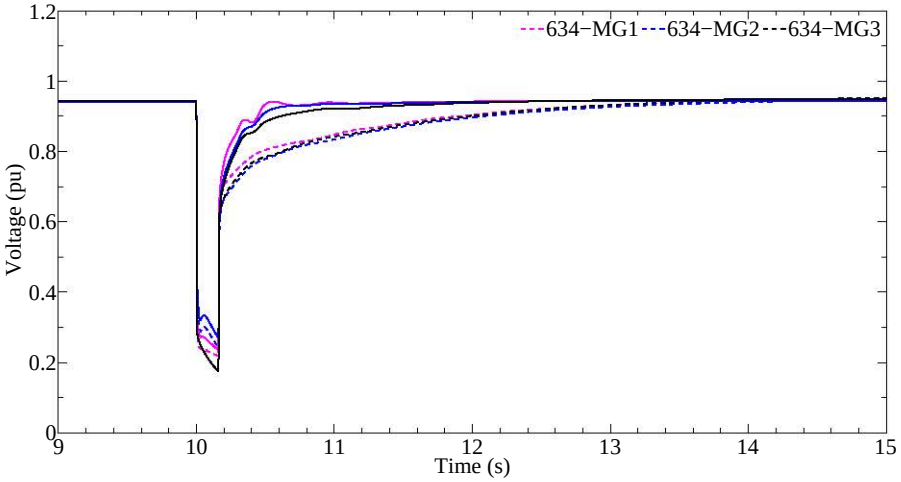

Figure 7.47: Voltage variations at Bus bar 634 due to a fault at Bus bar 650 of MG 1: - - without DSTATCOM, **-** with DSTATCOM

A three-phase short-circuit fault was applied to Bus bar 650 at $t = 10\,\mathrm{s}$ and

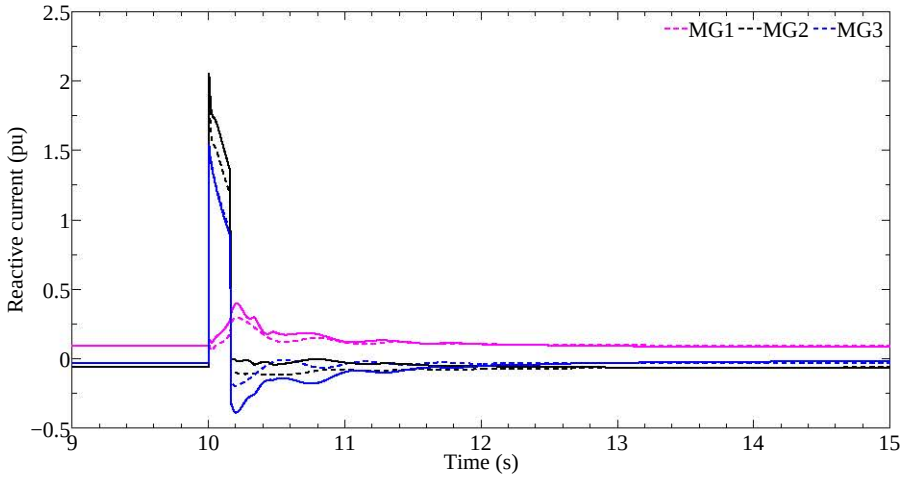

Figure 7.48: Reactive current variations through the distribution transformers of the microgrids due to the fault at Bus bar 650 of MG 1: - - without DSTATCOM, - with DSTATCOM

cleared after 160 ms. DSTATCOMs were considered to be connected on the low voltage side of the microgrid distribution transformer in MG 1 and MG 2 each having a 3 MVA rated capacity. Fig. 7.47 illustrates the voltage variations of Bus bar 643 of each microgrid system due to the fault. It can be observed that the post fault voltage recovery has improved with the presence of the DSTATCOMs in the multi-microgrid system. Furthermore, reactive current contribution from each microgrid into the fault has increased with the DSTATCOM operation as illustrated in Fig. 7.48.

For further analysis, another three-phase short-circuit fault was applied at the terminal of an induction motor load in MG 2 (connected to Bus bar 652 in MG 2) at $t = 10$ s and cleared after 160 ms. Fig. 7.49 (a) illustrates the voltage variations of the bus bars at the high voltage side of the distribution transformer in each microgrid. Fig. 7.49 (b) presents voltage variations of Bus bar 652 of each microgrid system due to the fault. From both figures, it can be identified that the DSTATCOM operation has improved the voltage profile of the microgrids. Fig. 7.50 illustrates the reactive current variations through the distribution transformers of the microgrids due to a fault at Bus bar 652 in MG 2. As a result of the DSTATCOM operation, reactive current absorbed by MG 2 due to the internal fault has decreased, and reactive current output from MG 1 has increased. Operation of DSTATCOMs in MG 1 and

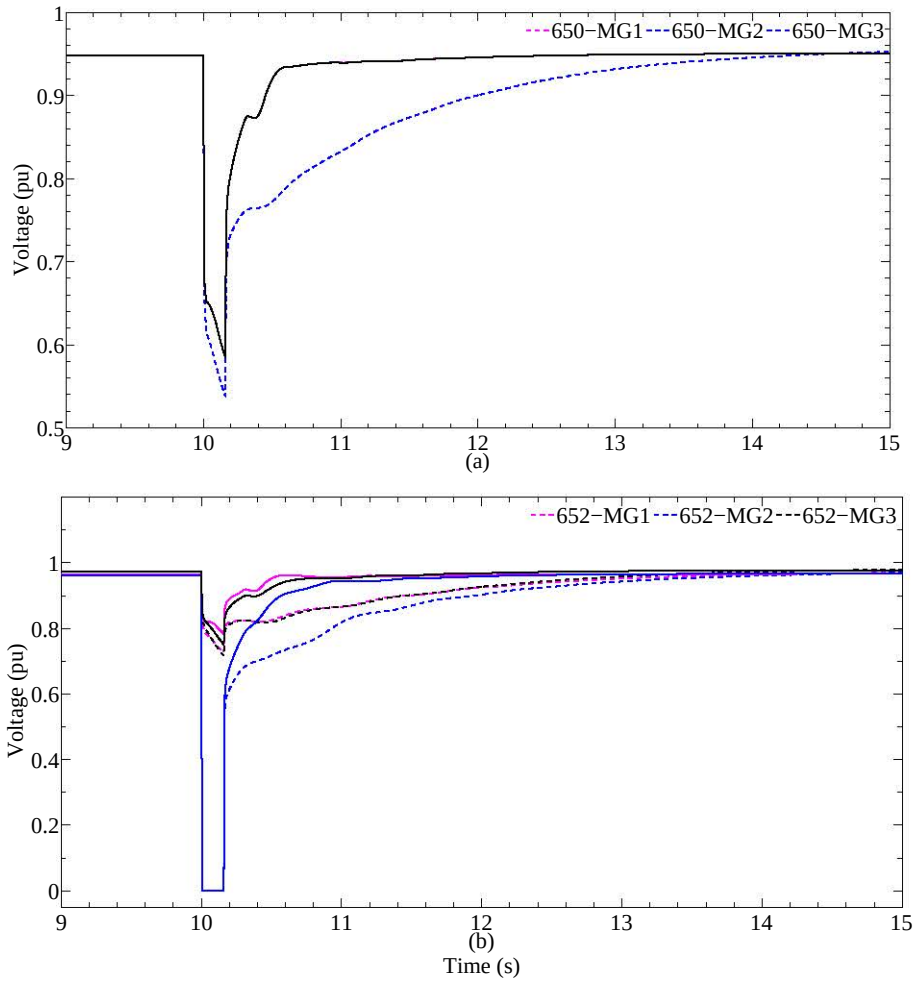

Figure 7.49: Voltage variations of (a) Bus bar 650, and (b) Bus bar 652 in each microgrid due to the fault at Bus bar 652 of MG 2: - - without DSTATCOM, **-** with DSTATCOM

MG 2 has reduced the reactive current flowing out of MG 3 which does not have a DSTATCOM. Hence, by examining all the results, it is clear that the operation of DSTATCOM in islanded microgrid systems improve the system bahaviour caused by faults.

7.7 Impact of Induction Motor Loads and DSTATCOM

In this section, a case study was carried out to investigate grid connected microgrid behaviour with DSTATCOM and induction motor loads. The microgrid system described in Section 7.4.1 was considered for the study and DG3 was assumed to be disconnected resulting the microgrid to operate in region R2. Steady state active

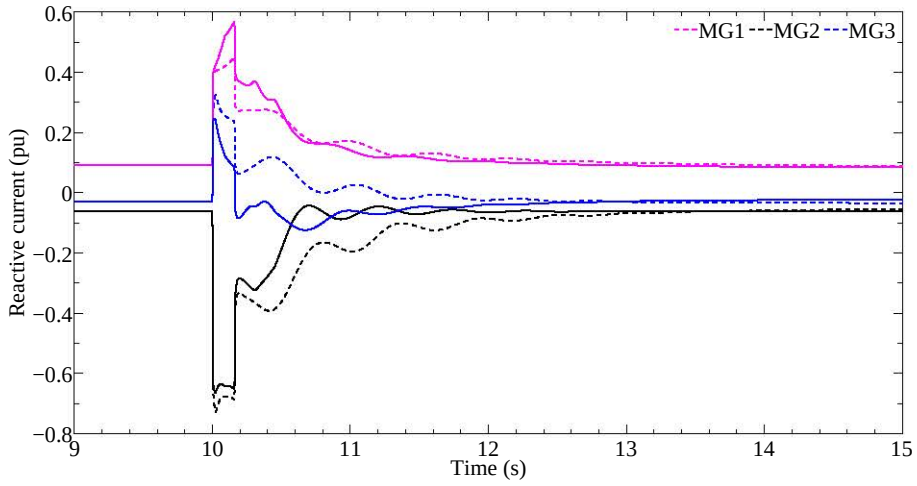

Figure 7.50: Reactive current variations through the distribution transformers of the microgrids due to the fault at Bus bar 652 of MG 2: - - without DSTATCOM, - with DSTATCOM

and reactive power levels considered for this case study are presented in Table 7.8 and a 3 MVA DSTATCOM is connected at Bus bar 632.

Table 7.8: Active and reactive power values in the microgrid

	P (MW)	Q (MVAr)
DG1	0.500	0.0
DG2	0.900	0.0
Total load	2.818	1.582

Fig. 7.51 illustrates the voltage variation of bus bars in the microgrid due to a three-phase short-circuit fault applied at Bus bar 650 for 160 ms. Fig. 7.51 (a) corresponds to the scenario with only static load models, whereas in Fig. 7.51 (b), 40 % of the total microgrid load was replaced with induction motor models. When loads are represented by static loads, the post fault voltage of the microgrid recovered quickly to the pre-fault value with the DSTATCOM. However, even with the DSTATCOM, the voltage has decreased during the fault with induction motor load models, due to induction motor reactive power requirement. Furthermore, post-fault voltage has taken more time to reach the pre-fault voltage profile of the microgrid with induction motor models.

Similarly, a three-phase short-circuit fault was applied inside the microgrid at Bus bar 652 at $t = 10$ s, and cleared after 150 ms. Fig. 7.52 (a) and Fig. 7.52 (b)

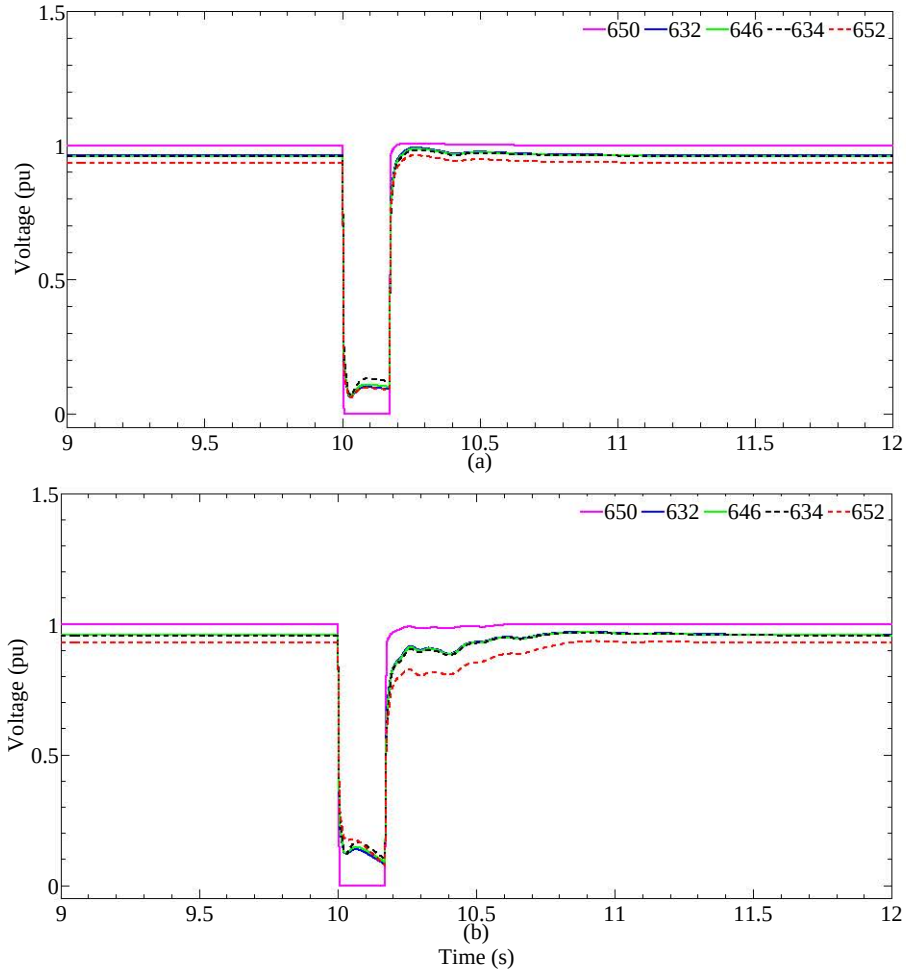

Figure 7.51: Voltage variations of bus bars due to the fault at Bus bar 650 with DSTATCOM for (a) only static loads, and (b) with induction motor loads

illustrate the voltage profile with only static loads and with 40 % induction motor load respectively. Due to the reactive power requirement of the induction motor loads, post-fault voltage recovery of the microgrid can be seen to be slow compared to the microgrid with only static loads even in the presence of DSTATCOM.

Fig. 7.53 (a) and Fig. 7.53 (b) illustrate the reactive power output of the DSTATCOM at Bus bar 632 for the faults at Bus bar 650 and Bus bar 652 respectively. By examining both figures, it can be observed that the DSTATCOM has supplied more reactive power to the system after fault clearance when the microgrid consisted of induction load models. During the fault, amount of reactive power supplied by the DSTATCOM depends on the DSTATCOM terminal voltage.

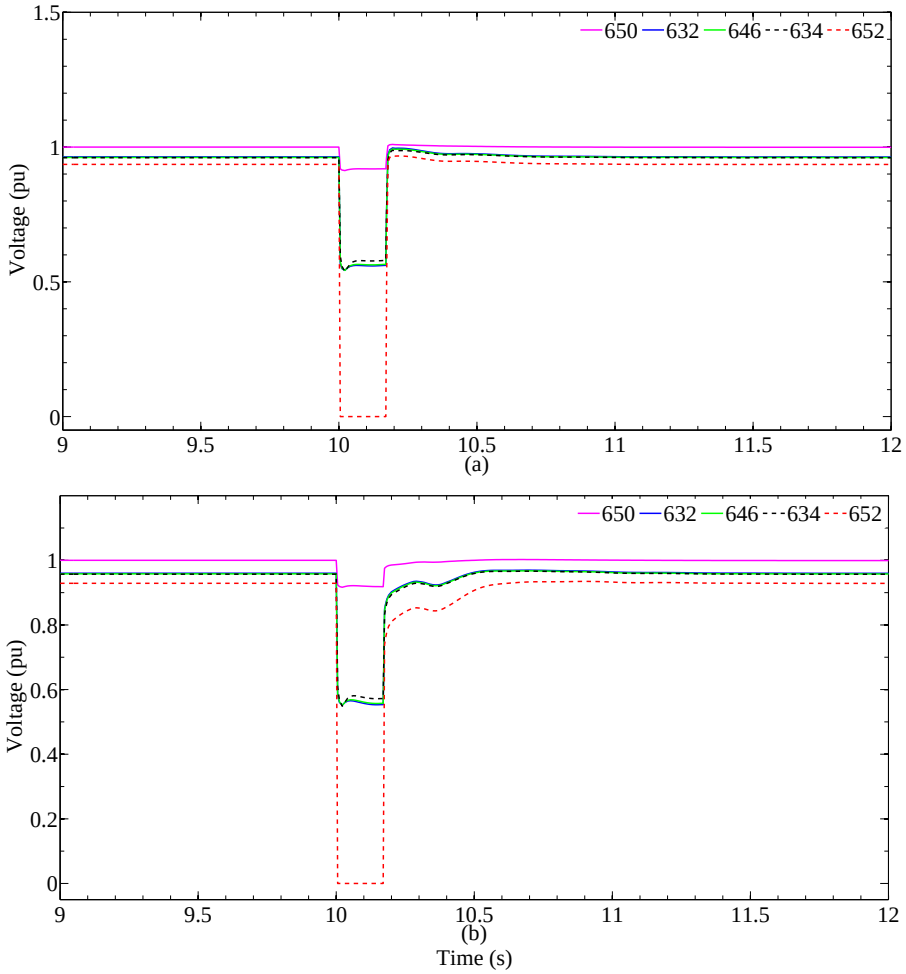

Figure 7.52: Voltage variations at bus bars due to the fault at Bus bar 652 with DSTATCOM for (a) only static loads, and (b) with induction motor loads

7.8 Summary

This chapter presented detailed case studies carried out to investigate DSTATCOM operation in microgrids and the ability to support both microgrid and the external grid during faults. Microgrids operating in four different regions (four quadrants) were subjected to external and internal faults with and without DSTATCOM and the microgrid behaviour was analysed. The reactive power contribution from the microgrid increased during faults due to the DSTATCOM operation and post fault transients have reduced.

Impact of the DSTATCOM location in the microgrid was also analysed by installing the DSTATCOM on the low voltage side of the microgrid distribution transformer, at DG terminals and at the bus bar with minimum reactive power margin

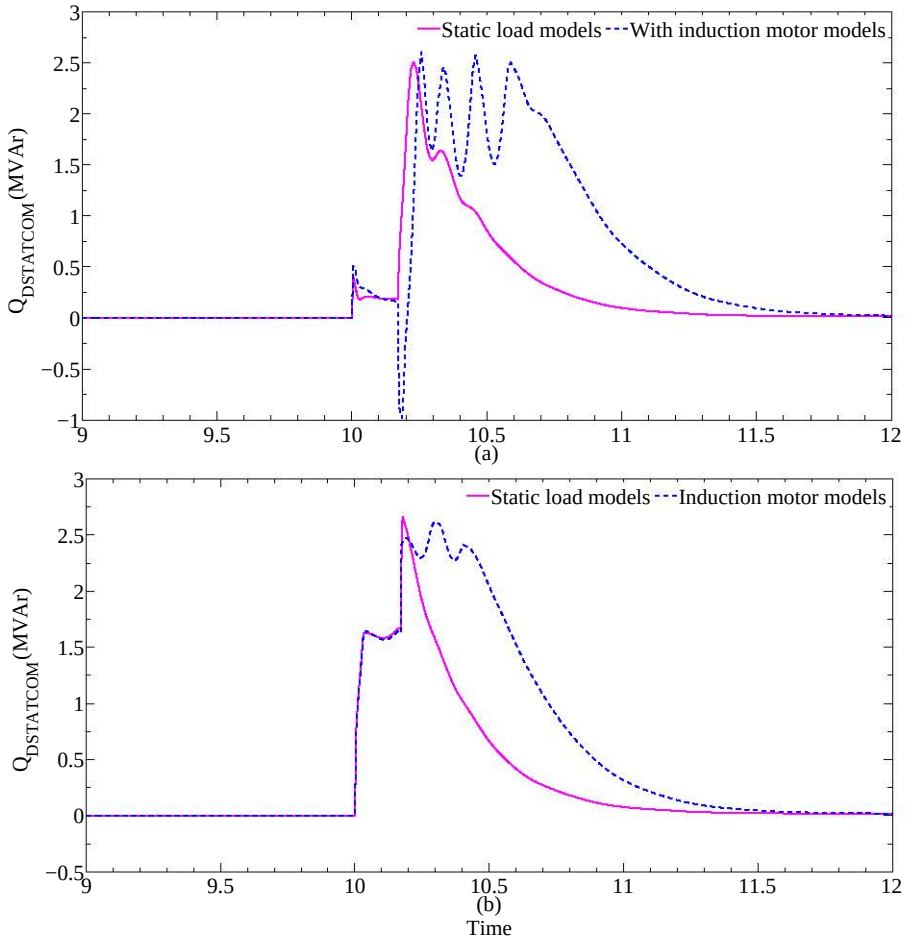

Figure 7.53: Reactive power output of the DSTATCOM for the fault at (a) Bus bar 650, and (b) Bus bar 652

of the microgrid. Variations of the microgrid system parameters during the fault and after fault clearance were analysed to identify the most appropriate location of DfSTATCOM.

Furthermore, DSTATCOMs were installed in a multi-microgrid system and the system was subjected to different faults. Response of DSTATCOMs in single and multi-microgrid systems during islanded operation were also analysed. Installing DSTATCOM on low voltage side of the microgrid distribution transformer provides better performance in both grid connected and islanded modes. During grid connected mode, DSTATCOM will provide better voltage and reactive power support to the external grid as well as improve microgrid voltage profile. Having the DSTATCOM on the low voltage side of the microgrid distribution transformer will be an advantage and will improve the microgrid overall voltage profile, if the microgrid

transfer from grid connected to islanded mode of operation. DSTATCOM operation would reduce the reactive power demand from the external grid arising during faults from microgrids having induction motor loads.

Similar to a DG with reactive power capability, DSTATCOM can be used as a mechanism to provide reactive power support from microgrid to the external grid during low voltage ride through events. However, depending on the capacity of the microgrid, required capacity of the DSTATCOM would change. Thus, it is important to carry out a financial analysis when planning to install DSTATCOM in microgrids. Furthermore, future work would also involve in analysing the placement and sizing of DSTATCOM in microgrid environment under different operating conditions.

Chapter 8

Conclusions and Future Work

8.1 Summary and Conclusions

Increasing penetration level of DERs have transformed distribution networks from passive to active networks and introduced the concept of microgrids. Through a comprehensive literature review carried out in this thesis, some key issues and research gaps were identified related to microgrid modelling and operation. While embarking on the research gaps identified on microgrids, this thesis has examined a number of issues related to the modelling of microgrids, and has investigated different aspects of their operation.

In the first phase of this thesis, the dynamic characteristics associated with microgrids comprising inverter and non-inverter interfaced DERs were investigated. Preliminary studies were carried out on a simulation microgrid model developed comprising a PV system, a DFIG based wind power plant, a mini hydro power plant, and loads. The importance of understanding the dynamic behaviour of microgrids was highlighted through a comparative analysis carried out on the hybrid microgrid. This study revealed that the dynamic characteristics of the microgrid are significantly influenced by the individual characteristics of DERs and their control systems. The study examined the influence of the variations in active power dispatch levels and generator relative sizing on the dynamic characteristics of the microgrid.

It was clearly evident that the DERs with a directly coupled rotor to the network have a signiffcant influence on the post fault oscillations in the microgrid as the inertial response of inverter interfaced DER is either unavailable (e.g. PV system) or decoupled from the network (e.g. DFIG). Microgrids with smaller system rotational inertia have a larger frequency deviation for a given mismatch between load and power generation. Depending on the speed, accuracy and artificial damping provided by the controllers, the inverter interfaced DERs would also have a substantial impact on the microgrid stability. The fast controllers would allow the inverter interfaced DERs to respond to disturbances quickly and reach steady-state after fault clearance. Furthermore, it has been shown that the ROCOF increased with the increasing penetration of inverter-interfaced DERs. It has been noted that during grid connected mode, features of the external grid also have an impact on the microgrid behaviour. It was highlighted that the external grid SCC plays an important role in maintaining an acceptable microgrid voltage profile. Moreover, grid connected microgrids were able to recover faster due to faults when compared to islanded microgrids.

Distribution networks can no longer be represented merely by a static load at the PCC. In particular, dynamics of microgrids during grid connected mode must be taken into account in order to accurately characterise the stability of the network. Unlike traditional SGs and their auxiliary components, effects of grid connected microgrid dynamics on large power systems have yet to be completely characterised. Thus, the second phase of this thesis was focused on aggregated modelling of grid connected microgrids comprising both inverter and non-inverter interfaced DERs.

For stability analysis, the common practice is to separate the power system into a study area of interest and external areas. In general, the study area is represented in a detailed manner while external areas are represented by dynamic equivalents. Thus, the microgrids in the external areas can be represented by linearised single dynamic devices while retaining the important dynamics. It was identified that the basic modal method had not been previously applied to grid connected microgrids

comprising both inverter and non-inverter interfaced DERs as a model equivalencing methodology. Thus, the thesis investigated the applicability of modal analysis as a tool for model equivalencing of grid connected microgrids having inverter and non-inverter interfaced DERs.

Detailed models of an inverter interfaced DERs with power controllers, non-inverter interfaced DERs with governor and excitation controllers, induction motor load and network were developed as a basis for the studies. A new index was defined for identifying the dominant modes which needed to be retained in the reduced order equivalent of the microgrid. Model equivalencing methodology was applied to a five-bus microgrid system comprising two DERs and two types of loads. Several case studies were carried out under different operating conditions of the microgrid system. Furthermore, scalability of the proposed microgrid model equivalencing approach was demonstrated using a larger microgrid model based on the IEEE-13 node distribution test feeder and a multi-microgrid system. It was observed that the responses of the microgrid system states and the microgrid current outputs obtained from the full order model and reduced order equivalent model were in good agreement. Thus, the proposed dynamic model equivalent of the grid connected microgrid based on basic modal method has captured the important dynamics of the full order microgrid systems. However, a limitation of the modal method exists due to the linearisation of the microgrid system. Thus, this dynamic equivalencing method can be used for system studies when grid connected microgrids are not directly subjected to large internal disturbances or when the investigated disturbances are not placed too close to the boundary of the microgrid equivalent model.

The process of deriving the dynamic equivalent models of grid connected microgrids can be automated in power system simulation software packages and can be replaced with a current source having the nominal output current with nominal voltage at the microgrid PCC. However, one advantage of this method over the other model training methods is that, once a dynamic equivalent has been obtained for a grid connected microgrid, numerous faults can be analysed in the study system

using the same equivalent. However, as above, the faults cannot be placed too close to the boundary of the microgrid equivalent model.

Unlike in a single generator unit with its own machine limitations, active and reactive power transfer limits of a grid connected microgrid depend on many factors including different and multiple machine capability limits, local load demands, and distribution line capacities. By conducting a thorough literature survey, it was identified that no research knowledge existed related to identifying power transfer capability limits of grid connected microgrids. Absence of such knowledge was the primary drive for developing a systematic approach for deriving a capability diagram for a grid connected microgrid in the third phase of this thesis.

In order to derive the capability diagram, a non-linear optimisation model was developed considering individual machine limitations, local load demands, distribution line capacities, transformer capacities and network voltage limitations. Using the optimisation model, simplified capability diagrams were obtained for two grid connected microgrid systems. Both capability diagrams represented the active and reactive power exchange capability of the microgrids at the PCC. From the results, it was identified that considering simplified DG machine capability limitations would yield inaccurate microgrid power exchange capability with the external grid. Hence, incorporation of realistic DG machine limitations into the optimisation model is essential in order to derive an accurate microgrid active and reactive power capability diagram. Impact of different voltage regulation systems was analysed and it was noted that an increase in the range of acceptable voltage variation at the buses within the microgrid is favourable for power export from the microgrid. Furthermore, for the same local loading conditions, power import and export capability of the microgrid can be increased by allowing the voltage at the PCC to be varied within an acceptable limit, rather than fixing at a particular voltage level. The shape and size of the capability diagram vary with microgrid generation and loading conditions, as different constraints/limits are met in the optimisation model at each power flow. Impact of individual distributed generator outages on the capability

diagram was also demonstrated using two microgrid systems.

It was noted that charging and discharging pattern of individual PHEVs in microgrids has a negligible impact on the capability diagram as their size is comparably small compared to the DERs. However, the effect of charging and discharging of a fleet of PHEVs can be represented as simple loads or generators in the optimisation model. Applicability of capability diagrams as a tool in the energy market operation was also described. Electricity costs corresponding to all the points of the microgrid capability diagram were derived based on both active and reactive power markets in separate study cases. It was demonstrated that such capability diagrams with economic aspects can be utilisded by the MCC or DNSPs to harness maximum possible power from the microgrids.

In the fourth phase, this thesis investigated the LVRT capability of grid connected microgrids as an ancillary service provider to the utility grid. Two approaches were followed to investigate the LVRT capability of a microgrid as a single entity. In the first approach, dynamic voltage support at the microgrid PCC was improved by using a DSTATCOM at the low voltage side of the distribution transformer of the microgrid. Faults were created at the external grid and the active and reactive power responses from the microgrid PCC were examined. It was observed that irrespective of the active and reactive power flow direction at the microgrid PCC, the microgrid with the DSTATCOM installed provided additional reactive power during and after the fault clearance. Furthermore, the CCT of the microgrid has improved with the operation of DSTATCOM. The collective effect of the reactive power capabilities of the distributed generators in the microgrid was used to provide voltage and reactive power support to the external grid in the second approach. Instead of the inbuilt LVRT capability of DGs, DSTATCOMs were installed at the terminal of the DGs. Improved DG LVRT capability may also achieve similar results.

Furthermore, DSTATCOMs were installed in a multi-microgrid system and the system was subjected to different faults. Response of DSTATCOMs single and multi-microgrid systems in islanded operation were also analysed. It was noted

that by installing a DSTATCOM at low voltage side of the microgrid distribution transformer would provide better performance in both grid connected and islanded modes. During grid connected mode, DSTATCOM would provide better voltage and reactive power support to the external grid as well as improve microgrid voltage profile. Having the DSTATCOM on the low voltage side of the microgrid distribution transformer would improve microgrid overall voltage profile if the microgrid transfer from grid connected to islanded mode of operation. The DSTATCOM would reduce the reactive power demand from the external grid arising during faults in microgrids with induction motor loads. Similar to a DG with LVRT capability, DSTATCOM can be used as a mechanism to provide reactive power support from microgrid to the external grid during faults. However, depending on the capacity of the microgrid, required capacity of the DSTATCOM would change. Thus, it is important to carry out a financial study when planning to install DSTATCOMs within microgrids.

From a careful analysis, it was concluded that having the DSTATCOM installed on the low voltage side of the microgrid distribution transformer has better impact on all the buses of the microgrid compared to the DSTATCOM installed at other locations studied. When the DSTATCOM is not installed on the low voltage side of the microgrid distribution transformer, the microgrid is unable to utilise the maximum capability of the DSTATCOM to provide support to the external grid. During the post fault transients, reactive power absorption from the microgrid is minimum when the DSTATCOM is installed on the low voltage side of the microgrid distribution transformer.

8.2 Recommendations for Future Work

In the future, when microgrids become more commonplace with higher penetration of DERs, the stability and security of the utility grid will be affected significantly. Thus, microgrids need to be designed properly to take care of their dynamic impact on the utility grid such that the overall stability and reliability of the whole system is maintained or significantly improved.

As the dynamic response of inverter interfaced DERs depends on the applied control starategy, future work would be required to study the microgrid behaviour incorporating various control algorithms in different types of DERs. Furthermore, single phase elements (e.g. PV systems and loads) need to be considered with three-phase elements in microgrids, and should conduct time domain simulations using DIgSILENT PowerFactory in order to study the dynamics.

The grid connected microgrid model equivalencing methodology presented in this thesis can be applied for microgrids with any operating mode with any type of control algorithms as long as the control algorithms do not change for the considered time frame. For the time frame of interest, dynamics of the dc side of the inverter interfaced DERs were considered negligible. Once the dc side dynamics are included in the state-space model using ODEs, any change in dc side dynamics would result in a change in the initial values of the microgrid model. Future work will be carried out to investigate the impact of the variation of dc side dynamics on the full order microgrid model and the reduced order microgrid model. Furthermore, future work will include experimental verification of the microgrid equivalencing methodology proposed in this thesis including both inverter and non-inverter interfaced DERs and different types of loads. Depending on the capabilities and requirements of different simulation packages, dynamic equivalents of microgrids can be implemented as controlled current sources with nominal output current from the microgrid as suggested in Chapter 5 of this thesis. This would allow the grid connected microgrid systems to be implemented in simulation packages with reduced size and complexity.

The methodology of deriving capability diagrams of grid connected microgrid systems as presented in Chapter 6 can be derived in real time, provided proper communication media exists between the generators, load centres and the MCC. Furthermore, the proposed methodology and the mathematical model can incorporate other optimisation algorithms for developing capability diagrams. Thus, a comparative analysis can be carried out using different optimisations algorithms on microgrid capability diagrams.

Operation of microgrids in the energy market can be more complex when demand side bidding is considered. The MCC has to optimise the operation of the microgrid by considering the bids from both DGs and loads. If consumers are willing to shed loads, the MCC will be required to pay a curtailment fee which will contribute to the microgrid operating costs. As the work in this thesis focuses on the grid connected mode of operation of microgrids, future work will include business models for microgrids different to the two business models presented in Chapter 6. A more detailed analysis with different market models and the impact on microgrid power import and export capability diagram is identified as future work arising from Chapter 6.

This thesis only investigates the technical assessment of DSTATCOM for microgrids and its advantage for grid connected and islanded modes of operation. As future work, coordination of other voltage control devices operating within the distribution system such as capacitor banks, transformer tapping etc. will be taken into consideration. With LVRT capability, the DSTATCOM can be used as a mechanism to provide reactive power support from microgrid to the external grid during faults. However, depending on the capacity of the microgrid, required capacity of the DSTATCOM would change. Thus, it is important to carry out a financial study when planning to install the DSTATCOM in microgrids. Future work would also be required for analysing the placement and sizing of the DSTATCOM in microgrid environment under different operating conditions. Furthermore, a more detailed economic analysis will be carried out in order to determine if it is cheaper for having distributed LVRT performance expectation from all microgrid components or a simpler DSTATCOM solutionfor the entire microgrid.

References

[1] G. Venkataramanan and C. Marnay. A Larger Role for Microgrids. *Power and Energy Magazine, IEEE*, 6(3):78–82, May 2008.

[2] J. A. Peas Lopes, N. Hatziargyriou, J. Mutale, P. Djapic, and N. Jenkins. Integrating Distributed Generation into Electric Power Systems: A Review of Drivers, Challenges and Opportunities. *Electric Power Systems Research*, 77(9):1189 – 1203, 2007.

[3] F. Katiraei, R. Iravani, N. Hatziargyriou, and A. Dimeas. Microgrids Management. *Power and Energy Magazine, IEEE*, 6(3):54–65, May 2008.

[4] B. Kroposki, R. Lasseter, T. Ise, S. Morozumi, S. Papatlianassiou, and N. Hatziargyriou. Making Microgrids Work. *Power and Energy Magazine, IEEE*, 6(3):40–53, May 2008.

[5] N. W. A. Lidula and A. D. Rajapakse. Microgrids Research: A Review of Experimental Microgrids and Test Systems. *Renewable and Sustainable Energy Reviews*, 15(1):186 – 202, 2011.

[6] N. Hatziargyriou. *Microgrids:Architectures and Control*. Wiley-IEEE Press, 2014.

[7] R. H. Lasseter, J. H. Eto, B. Schenkman, J. Stevens, H. Vollkommer, D. Klapp, E. Linton, H. Hurtado, and J. Roy. CERTS Microgrid Laboratory Test Bed. *IEEE Trans. on Power Delivery*, 26(1):325–332, Jan. 2011.

[8] T. Ackermann, G. Andersson, and L. Sder. Distributed Generation: A Definition. *Electric Power Systems Research*, 57(3):195 – 204, 2001.

[9] J. Driesen and F. Katiraei. Design for Distributed Energy Resources. *Power and Energy Magazine, IEEE*, 6(3):30–40, May 2008.

[10] S. Chowdhury, S. P. Chowdhury, and P. Crossley. *Microgrids and Active Distribution Networks*. The Institution of Engineering and Technology, 2009.

[11] T. L. Vandoorn, J. C. Vasquez, J. De Kooning, J. M. Guerrero, and L. Vandevelde. Microgrids: Hierarchical Control and an Overview of the Control and Reserve Management Strategies. *Industrial Electronics Magazine, IEEE*, 7(4):42–55, Dec. 2013.

[12] R. Masiello and S. Venkata. Microgrids: There May Be One in Your Future. *Power and Energy Magazine, IEEE*, 11(4):14–93, July 2013.

[13] N. Hatziargyriou, H. Asano, R. Iravani, and C. Marnay. Microgrids. *Power and Energy Magazine, IEEE*, 5(4):78–94, July 2007.

[14] C. Abbey, D. Cornforth, N. Hatziargyriou, K. Hirose, A. Kwasinski, E. Kyriakides, G. Platt, L. Reyes, and S. Suryanarayanan. Powering Through the Storm: Microgrids Operation for More Efficient Disaster Recovery. *Power and Energy Magazine, IEEE*, 12(3):67–76, May 2014.

[15] L. Schmitt, J. Kumar, D. Sun, S. Kayal, and S. S. M. Venkata. Ecocity Upon a Hill: Microgrids and the Future of the European City. *Power and Energy Magazine, IEEE*, 11(4):59–70, July 2013.

[16] T. Tanabe, Y. Ueda, T. Funabashi, S. Numata, K. Morino, and E. Shimoda. An Active Network Control Method using Distributed Energy Resources in Microgrids. In *Proc. Power Electronics and Motion Control*, pages 2478–2480, Sept. 2008.

[17] C. K. Sao and P. W. Lehn. Control and Power Management of Converter Fed Microgrids. *IEEE Trans. on Power Systems*, 23(3):1088–1098, Aug. 2008.

[18] A. L. Dimeas and N. D. Hatziargyriou. Operation of a Multiagent System for Microgrid Control. *IEEE Trans. on Power Systems*, 20(3):1447–1455, Aug. 2005.

[19] J. C. Matas J. de Vicua L. G. Guerrero, J. M. Vasquez and Castilla M. Hierarchical Control of Droop - Controlled AC and DC Microgrids-A General

Approach Toward Standardization. *IEEE Trans. on Industrial Electronics*, 58 (1):158–172, 2011.

[20] D. T. Ton, W. M. Wang, and W. T. P. Wang. Smart Grid R & D by the U.S. Department of Energy to Optimize Distribution Grid Operations. In *Power and Energy Society General Meeting, IEEE*, pages 1–5, July 2011.

[21] N. Hatziargyriou, N. Jenkins, and G. Strbac. Microgrids-Large Scale Integration of Microgeneration to Low Voltage Grids. In *Proc. CIGRE*, Aug. 2006.

[22] N. Hatziargyriou. Advanced Architectures and Control Concepts for More Microgrids, http://www.microgrids.eu/documents/esr.pdf, Feb. 2014.

[23] T. Loix. The First Microgrid in the Netherland: Bronsbergen, Feb. 2009.

[24] B. Buchholz, N. Hatziargyriou, I. Furones, and U. Schluecking. Lessons Learned: European Pilot Installations for Distributed Generation - An Overview by the IRED Cluster. In *Proc. CIGRE*, Aug 2006.

[25] M. Barnes, J. Kondoh, H. Asano, J. Oyarzabal, G. Ventakaramanan, R. Lasseter, N. Hatziargyriou, and T. Green. Real-World Microgrids - An Overview. In *Proc. IEEE System of Systems Engineering*, pages 1–8, Apr. 2007.

[26] S. Morozumi, H. Nakama, and N. Inoue. Demonstration Projects for Grid-Connection Issues in Japan. *Elektrotechnik & Informationstechnik*, 125 (3):426–431, Dec. 2008.

[27] K. Hirose, T. Takeda, and S. Muroyama. Study on Field Demonstration of Multiple Power Quality Levels System in Sendai. In *Proc. Telecommunications Energy Conf.*, Sept 2006.

[28] C. Marnay and N. Zhou. Status of Overseas Microgrid Programs: Microgrid Research Activities in the U.S. (English Version), Feb. 2008.

[29] E. Alegria, T. Brown, E. Minear, and R. H. Lasseter. CERTS Microgrid Demonstration with Large-Scale Energy Storage and Renewable Generation. *IEEE Trans. on Smart Grid*, 5(2):937–943, March 2014.

[30] R. Majumder. Some Aspects of Stability in Microgrids. *IEEE Trans. on Power Systems*, 28(3):3243–3252, Aug. 2013.

[31] R. Kamel, A. Chaouachi, and K. Nagasaka. Detailed Analysis of Micro-Grid Stability during Islanding Mode under Different Load Conditions. *Engineering*, 3(5):508–516, 2011.

[32] D. P. Ariyasinghe and D. M. Vilathgamuwa. Stability Analysis of Microgrids with Constant Power Loads. In *Proc. Sustainable Energy Technologies*, pages 279–284, Nov. 2008.

[33] D. M. Vilathgamuwa, X. N. Zhang, S. D. G. Jayasinghe, B. S. Bhangu, C. J. Gajanayake, and K. J. Tseng. Virtual Resistance Based Active Damping Solution for Constant Power Instability in AC Microgrids. In *Proc. Annual Conf. on IEEE Industrial Electronics Society*, pages 3646–3651, Nov. 2011.

[34] H. Karimi, H. Nikkhajoei, and R. Iravani. Control of an Electronically-Coupled Distributed Resource Unit Subsequent to an Islanding Event. *IEEE Trans. on Power Delivery*, 23(1):493–501, Jan. 2008.

[35] F. Katiraei, M. R. Iravani, and P. W. Lehn. Micro-grid Autonomous Operation During and Subsequent to Islanding Process. *IEEE Trans. on Power Delivery*, 20(1):248–257, Jan. 2005.

[36] M. Shahabi, M. R. Haghifam, M. Mohamadian, and S. A. Nabavi-Niaki. Microgrid Dynamic Performance Improvement using a Doubly Fed Induction Wind Generator. *IEEE Trans. on Energy Conversion*, 24(1):137–145, March 2009.

[37] Z. Miao, A. Domijan, and L. Fan. Investigation of Microgrids with Both Inverter Interfaced and Direct AC-Connected Distributed Energy Resources. *IEEE Trans. on Power Delivery*, 26(3):1634–1642, July 2011.

[38] M. Dewadasa, A. Ghosh, and G. Ledwich. Dynamic Response of Distributed Generators in a Hybrid Microgrid. In *Power and Energy Society General Meeting, IEEE*, July 2011.

[39] N. Pogaku, M. Prodanovic, and T. C. Green. Modeling, Analysis and Testing of Autonomous Operation of an Inverter-Based Microgrid. *IEEE Trans. on Power Electronics*, 22(2):613–625, March 2007.

[40] D. J. Lee and Wang. Li. Small-Signal Stability Analysis of an Autonomous Hybrid Renewable Energy Power Generation/Energy Storage System Part I: Time-Domain Simulations. *IEEE Trans. on Energy Conversion*, 23(1):311–320, March 2008.

[41] F. Katiraei and M. R. Iravani. Power Management Strategies for a Microgrid with Multiple Distributed Generation Units. *IEEE Trans. on Power Systems*, 21(4):1821–1831, Nov. 2006.

[42] R. Majumder, A. Ghosh, G. Ledwich, and F. Zare. Control of Parallel Converters for Load Sharing with Seamless Transfer between Grid Connected and Islanded Modes. In *Power and Energy Society General Meeting, IEEE*, July 2008.

[43] J. Machowski, A. Cichy, F. Gubina, and P. Omahen. External Subsystem Equivalent Model for Steady-State and Dynamic Security Assessment. *IEEE Trans. on Power Systems*, 3(4):1456–1463, Nov. 1988.

[44] E. M. De Oliveira, Sebastio and J. F. De Queiroz. Modal Dynamic Equivalent for Electric Power Systems. I. Theory. *IEEE Trans. on Power Systems*, 3(4):1723–1730, Nov. 1988.

[45] J. M. Undrill, J. A. Casazza, E. M. Gulachenski, and L. K. Kirchrnayer. Electromechanical Equivalent for use in Power System Stability Studies. *IEEE Trans. on Power Apparatus and Systems*, PAS-90(5):2060–2071, Sept. 1971.

[46] J. M. Undrill and A. E. Turner. Construction of Power System Electromechanical Equivalents by Modal Analysis. *IEEE Trans. on Power Apparatus and Systems*, PAS-90(5):2049–2059, Sept. 1971.

[47] E. Davison. A Method for Simplifying Linear Dynamic Ssystems. *IEEE Trans. on Autom. Control*, 11(1):93–101, Jan. 1966.

[48] H. Altalib and P. Krause. Dynamic Equivalents by Combination of Reduced Order Models of System Components. *IEEE Trans. on Power App. Syst*, 95:1535–1544, Sept. 1976.

[49] A. Kuppurajulu and S. Elangovan. Simplified Power System Models for Dynamic Stability Studies. *IEEE Trans. on Power Apparatus and Systems*, PAS-90(1):11–23, Jan. 1971.

[50] G. Perez-Arriaga, I. Verghese and F. Schweppe. Selective Modal Analysis with Applications to Electric Power Systems, Part I: Heuristic Introduction,. *IEEE Trans. on Power App. Syst.*, PAS-101(9):3117–3125, Sept. 1982.

[51] I. S. F. Verghese and G.C. Perez-Arriaga. Selective Modal Analysis with Applications to Electric Power Systems, Part II: The Dynamic Stability Problem. *IEEE Trans. on Power App. Syst.*, PAS-101(9):3126– 3134, Sept. 1982.

[52] G. Ramaswamy, G. Verghese, L. Rouco, C. Vialas, and C. DeMarco. Synchrony, Aggregation, and Multi-area Eigenanalysis. *IEEE Trans. on Power Systems*, 12:1986–1993, Nov. 1995.

[53] G. Ramaswamy, C. Evrard, G. Verghese, O. Fillatre, and B. Lesieutre. Extensions, Simplifications, and Tests of Synchronic Modal Equivalencing (SME). *IEEE Trans. on Power Systems*, 12:896–905, May 1997.

[54] J. H. Chow, R. Galarza, P. Accari, and W. W. Price. Inertial and Slow Coherency Aggregation Algorithms for Power System Dynamic Model Reduction. *IEEE Trans. on Power Systems*, 10(2):680–685, May 1995.

[55] A. Ischchenko, X. A. MyrzTang, and W. L. Kling. Dynamic Equivalencing of Distribution Networks with Dispersed Generation. In *Power Engineering Society General Meeting, IEEE*, 2006.

[56] A. Ishchenko, J. M. A. Myrzik, and W. L. Kling. Dynamic Equivalencing of Distribution Networks with Dispersed Generation using Hankel Norm Approximation. *Generation, Transmission & Distribution, IET*, 1:818–825, 2007.

[57] P. V. Kokotovic, R. E. Jr. O'Malley, and P. Sannuti. Singular Perturbations and Order Reduction in Control Theory - An Overview. *Automatica*, 12(2):123 – 132, 1976.

[58] R. M. G. Castro and J. M. Ferreira De Jesus. A Wind Park Reduced-Order Model using Singular Perturbations Theory. *IEEE Trans. on Energy Conversion*, 11(4):735–741, Dec. 1996.

[59] S.K. Joo, C. C. Liu, L. E. Jones, and J.W. Choe. Coherency and Aggregation Techniques Incorporating Rotor and Voltage Dynamics. *IEEE Trans. on Power Systems*, 19(2):1068–1075, May 2004.

[60] A. J. Germond and R. Podmore. Dynamic Aggregation of Generating Unit Models. *IEEE Trans. on Power Apparatus and Systems*, PAS-97(4):1060–1069, July 1978.

[61] R. Podmore. Identification of Coherent Generators for Dynamic Equivalents. *IEEE Trans. Power Apparatus and Systems,*, PAS-97(4):1344–1354, July 1978.

[62] R. Nath, S. S. Lamba, and K. S. Prakasa Rao. Coherency Based System Decomposition into Study and External Areas using Weak Coupling. *IEEE Trans. on Power Apparatus and Systems*, PAS-104(6):1443–1449, June 1985.

[63] J. R. Winkelman, J. H. Chow, B. C. Bowler, B. Avramovic, and P. V. Kokotovic. An Analysis of Interarea Dynamics of Multi-Machine Systems. *IEEE Trans. on Power Apparatus and Systems*, PAS-100(2):754–763, Feb. 1981.

[64] S. T. Y. lee and F. C. Schweppe. Distance Measures and Coherency Recognition for Transient Stability Equivalents. *IEEE Trans. Power Appar. & Syst*, PAS-92:1550–1557, Sept/ Oct 1973.

[65] T. N. Nababhushana, K. T. Veeramanju, and Shivanna. Coherency Identification using Growing Self Organizing Feature Maps [Power System Stability]. In *Proc. Energy Management and Power Delivery Conf.*, pages 113–116 (1), March 1998.

[66] Z. Shuqiang, C. Xianrong, P. Yunjiang, and H. Renmu. A Reduced Order Method for Swing Mode Eigenvalue Calculating Based on Fuzzy Coherency Recognition. In *Proc. Power System Technology Conf.*, pages 1402–1405 (2), Aug. 1998.

[67] M. H. Haque and A. H. M. A. Rahim. An Efficient Method of Identifying Coherent Generators using Taylor Series Expansion. *IEEE Trans. on Power Systems*, 3(3):1112–1118, Aug. 1988.

[68] L. Wang, M. Klein, S. Yirga, and P. Kundur. Dynamic Reduction of Large Power Systems for Stability Studies. *IEEE Trans. on Power Systems*, 12(2):889–895, May 1997.

[69] M. L. Ourari, L. A. Dessaint, and Van-Que Do. Dynamic Equivalent Modeling of Large Power Systems using Structure Preservation Technique. *IEEE Trans. on Power Systems*, 21(3):1284–1295, Aug. 2006.

[70] R. Nath and S. S. Lamba. Development of Coherency-based Time-domain Equivalent Model using Structure Constraints. *Generation, Transmission and Distribution, IEE*, 133(4):165–175, May 1986.

[71] T. L. Le, Q. T. Tran, O. Devaux, O. Chilard, and R. Caire. Reduction and Aggregation for Critical and Emergency Operation of Distribution Network in Presence of Distributed Generators. In *Proc. 20th IntN. Conf. and Exhibition Electricity Distribution - Part 1*, June 2009.

[72] V. Sankaranarayanan, M. Venugopal, S. Elangovan, and N. Dharma Rao. Coherency Identification and Equivalents for Transient Stability Studies. *Electric Power Systems Research*, 6(1):51 – 60, 1983.

[73] S. Geeves. A Modal-Coherency Technique for Deriving Dynamic Equivalents. *IEEE Trans. on Power Systems*, 3(1):44–51, Feb. 1988.

[74] H. Oh. Aggregation of Buses for a Network Reduction. *IEEE Trans. on Power Systems*, 27(2):705–712, May 2012.

[75] J. Machowski, J. W. Bialek, and J. R. Bumby. *POWER SYSTEM DYNAMICS Stability and Control*. John Wiley & Sons, Ltd., 2008.

[76] X. Feng, Z. Lubosny, and J.W. Bialek. Identification based Dynamic Equivalencing. In *Proc. IEEE Lausanne Power Tech.*, pages 267–272, July 2007.

[77] X. Feng, Z. Lubosny, and J. Bialek. Dynamic Equivalencing of Distribution Network with High Penetration of Distributed Generation. In *Proc. Int. Universities Power Engineering Conf.*, pages 467–471 (2), Sept. 2006.

[78] P. N. Papadopoulos, T. A. Papadopoulos, P. Crolla, A. J. Roscoe, G. K. Papagiannis, and G. M. Burt. Black-Box Dynamic Equivalent Model for Microgrids using Measurement Data. *Generation, Transmission Distribution, IET*, 8(5):851–861, May 2014.

[79] J. V. Milanovic and S. Mat Zali. Validation of Equivalent Dynamic Model of Active Distribution Network Cell. *IEEE Trans. on Power Systems*, 28(3):2101–2110, Aug. 2013.

[80] F. O. Resende and J. A. Peas Lopes. Development of Dynamic Equivalents for MicroGrids using System Identification Theory. In *Proc. IEEEPower Tech*, pages 1033–1038, July 2007.

[81] S. M. Zali, N. C. Woolley, and J. V. Milanovic. Development of Equivalent Dynamic Model of Distribution Network using Clustering Procedure. In *Proc. 17th Power Systems Computation Conf.*, 2011.

[82] S. M. Zali and J. V. Milanovic. Generic Model of Active Distribution Network for Large Power System Stability Studies. *IEEE Trans. on Power Systems*, 28(3):3126–3133, Aug. 2013.

[83] A. M. Azmy and I. Erlich. Identification of Dynamic Equivalents for Distribution Power Networks using Recurrent ANNs. In *Proc. IEEE Power Systems Conference and Exposition*, pages 348–353 Vol.1, Oct. 2004.

[84] A. M. Stankovic and A. T. Saric. Transient Power System Analysis with Measurement-based Gray Box and Hybrid Dynamic Equivalents. *IEEE Trans. on Power Systems*, 19(1):455–462, Feb. 2004.

[85] A. M. Stankovic, A. T. Saric, and M. Milosevic. Identification of Nonparametric Dynamic Power System Equivalents with Artificial Neural Networks. *IEEE Trans. on Power Systems*, 18(4):1478–1486, Nov. 2003.

[86] J. M. Ramirez Arredondo and Rodrigo G. V. An Optimal Power System Model Order Reduction Technique. *International Journal of Electrical Power & Energy Systems*, 26(7):493 – 500, 2004.

[87] P. Ju, L. Q. Ni, and F. Wu. Dynamic Equivalents of Power Systems with Online Measurements. Part 1: Theory. *Generation, Transmission and Distribution, IEE*, 151(2):175–178, March 2004.

[88] P. Ju, F. Li, N. G. Yang, X. M. Wu, and N. Q. He. Dynamic Equivalents of Power Systems with Online Measurements Part 2: Applications. *Generation, Transmission and Distribution, IEE*, 151(2):179–182, March 2004.

[89] S. M. Zali and J. V. Milanovic. Dynamic Equivalent Model of Distribution Network Cell using Prony Analysis and Nonlinear Least Square Optimization. In *Proc. IEEE PowerTech*, pages 1–6, June 2009.

[90] Yao-Nan Yu and M. A. El-Sharkawi. Estimation of External Dynamic Equivalents of a Thirteen-Machine System. *IEEE Trans. on Power Apparatus and Systems*, PAS-100(3):1324–1332, March 1981.

[91] M. Poller and S. Achilles. Aggregated Wind Park Models for Analyzing Power System Dynamics. In *Porc. International Workshop on Large Scale Integration of Wind Power and Transmission Networks for Offshore Windfarms.*, 2003.

[92] L. M. Fernndez, C. A. Garca, J. R. Saenz, and F. Jurado. Equivalent Models of Wind Farms by using Aggregated Wind Turbines and Equivalent Winds. *Energy Conversion and Management*, 50(3):691 – 704, 2009.

[93] M. V. A. Nunes, J. A. Peas Lopes, H. H. Zurn, U. H. Bezerra, and R. G. Almeida. Influence of the Variable-Speed Wind Generators in Transient Stability Margin of the Conventional Generators Integrated in Electrical Grids. *IEEE Trans. on Energy Conversion*, 19(4):692–701, Dec. 2004.

[94] V. Akhmatov and H. Knudsen. An Aggregate Model of a Grid-Connected, Large-Scale, Offshore Wind Farm for Power Sstability Investigations-Importance of Windmill Mechanical System. *International Journal of Electrical Power & Energy Systems*, 24(19):709–717, 2002.

[95] A. Tsikalakis and N. Hatziargyriou. Centralized Control for Optimizing Microgrids Operation. *IEEE Trans. on Energy Convers.*, 23:241–248, 2008.

[96] M. Fathi and H. Bevrani. Statistical Cooperative Power Dispatching in Interconnected Microgrids. *IEEE Trans. on Sustainable Energy*, 4(3):586–593, July 2013.

[97] S. A. Arefifar, Y. A. I. Mohamed, and T. H. M. EL-Fouly. Supply-Adequacy-Based Optimal Construction of Microgrids in Smart Distribution Systems. *IEEE Trans. on Smart Grid*, 3(3):1491–1502, Sept. 2012.

[98] A. Gabash and L. Pu. Active-Reactive Optimal Power Flow in Distribution Networks with Embedded Generation and Battery Storage. *IEEE Trans. on Power Systems*, 27(4):2026–2035, Nov. 2012.

[99] L. F. Ochoa, A. Keane, and G. P. Harrison. Minimizing the Reactive Support for Distributed Generation: Enhanced Passive Operation and Smart Distribution Networks. *IEEE Trans. on Power Systems*, 26(4):2134–2142, Nov. 2011.

[100] S. Paudyal, C. A. Canizares, and K. Bhattacharya. Optimal Operation of Distribution Feeders in Smart Grids. *IEEE Trans. on Industrial Electronics*, 58(10):4495–4503, Oct. 2011.

[101] G. Celli, E. Ghiani, S. Mocci, and F. Pilo. A Multiobjective Evolutionary Algorithm for the Sizing and Siting of Distributed Deneration. *IEEE Trans. on Power Systems*, 20(2):750–757, May 2005.

[102] Tiansong Cui, Yanzhi Wang, S. Nazarian, and M. Pedram. An Electricity Trade Model for Microgrid Communities in Smart Grid. In *Proc. of Innovative Smart Grid Technologies Conf.*, pages 1–5, Feb 2014.

[103] Yue Min Ding, Seung Ho Hong, and Xiao Hui Li. A Demand Response Energy Management Scheme for Industrial Facilities in Smart Grid. *IEEE Trans. on Industrial Informatics*, 10(4):2257–2269, Nov 2014.

[104] N. Cicek and H. Delic. Demand Response Management for Smart Grids With Wind Power. *IEEE Trans. on Sustainable Energy*, 6(2):625–634, April 2015.

[105] J.S. Vardakas, N. Zorba, and C.V. Verikoukis. A Survey on Demand Response Programs in Smart Grids: Pricing Methods and Optimization Algorithms. *Communications Surveys Tutorials, IEEE*, 17(1):152–178, Firstquarter 2015.

[106] Peter Cappers, Jason MacDonald, Charles Goldman, and Ookie Ma. An Assessment of Market and Policy Barriers for Demand Response Providing Ancillary Sservices in U.S. Electricity Markets. *Energy Policy*, 62(0):1031 – 1039, 2013.

[107] A.C. Rueda-Medina and A. Padilha-Feltrin. Distributed Generators as Providers of Reactive Power Support; A Market Approach. *IEEE Trans. on Power Systems*, 28(1):490–502, Feb 2013.

[108] V.J. Martinez and H. Rudnick. Active Participation of Demand Through a Secondary Ancillary Services Market in a Smart Grid Environment. *IEEE Trans. on Smart Grid*, 4(4):1996–2005, Dec 2013.

[109] S.D. Manshadi and M.E. Khodayar. A Hierarchical Electricity Market Structure for the Smart Grid Paradigm. *IEEE Trans. on Smart Grid*, PP(99):1–1, 2015.

[110] S.C. Chan, K.M. Tsui, H.C. Wu, Yunhe Hou, Yik-Chung Wu, and F.F. Wu. Load/Price Forecasting and Managing Demand Response for Smart Grids: Methodologies and Challenges. *Signal Processing Magazine, IEEE*, 29(5):68–85, Sept 2012.

[111] R. Raineri, S. Ros, and D. Schiele. Technical and Economic Aspects of Ancillary Services Markets in the Electric Power Industry: An International Comparison. *Energy Policy*, 34(13):1540 – 1555, 2006.

[112] Ali Keyhani, Ashkan Kian, Jose Cruz Jr., and Marwan A. Simaan. Market Monitoring and Control of Ancillary Services. *Decision Support Systems*, 30(3):255 – 267, 2001. Restructuring the electric power business-a marriage of power.

[113] Tarjei Kristiansen. The Nordic Approach to Market-based Provision of Ancillary Services. *Energy Policy*, 35(7):3681 – 3700, 2007.

[114] Joohyun Cho and Andrew N. Kleit. Energy Storage Systems in Energy and Ancillary Markets: A Backwards Induction Approach. *Applied Energy*, 147(0):176 – 183, 2015.

[115] Chiara Lo Prete, Benjamin F. Hobbs, Catherine S. Norman, Sergio Cano-Andrade, Alejandro Fuentes, Michael R. von Spakovsky, and Lamine Mili. Sustainability and Reliability Assessment of Microgrids in a Regional Electricity Market. *Energy*, 41(1):192 – 202, 2012. 23rd International Conference on Efficiency, Cost, Optimization, Simulation and Environmental Impact of Energy Systems, {ECOS} 2010.

[116] Gregory S. Pavlak, Gregor P. Henze, and Vincent J. Cushing. Optimizing Commercial Building Participation in Energy and Ancillary Service Markets. *Energy and Buildings*, 81(0):115 – 126, 2014.

[117] Mrio Helder Gomes and Joo Tom Saraiva. Allocation of Reactive Power Support, Active Loss Balancing and Demand Interruption Ancillary Services in Microgrids. *Electric Power Systems Research*, 80(10):1267 – 1276, 2010.

[118] A.G. Madureira and J.A. Peas Lopes. Ancillary Services Market Framework for Voltage Control in Distribution Networks with Microgrids. *Electric Power Systems Research*, 86(0):1 – 7, 2012.

[119] H. Asano and S. Bando. Economic Evaluation of Microgrids. In *Power and Energy Society General Meeting, IEEE*, pages 1–6, July 2008.

[120] F. Rahimi and A. Ipakchi. Demand Response as a Market Resource Under the Smart Grid Paradigm. *IEEE Trans. on Smart Grid*, 1(1):82–88, June 2010.

[121] IEEE Guide for Operation and Maintenance of Turbine Generators. *IEEE Std 67-2005 (Revision of IEEE Std 67-1990)*, pages 1–69, 2006.

[122] N. E. Nilsson and J. Mercurio. Synchronous Generator Capability Curve Testing and Evaluation. *IEEE Trans. on Power Delivery*, 9(1):414–424, Jan. 1994.

[123] S. Engelhardt, I. Erlich, C. Feltes, J. Kretschmann, and F. Shewarega. Reactive Power Capability of Wind Turbines based on Doubly Fed Induction Generators. *IEEE Trans. on Energy Conversion*, 26(1):364–372, March 2011.

[124] T. Lund, P. E. Sorensen, and J. Eek. Reactive Power Capability of a Wind Turbine with Doubly Fed Induction Generator. *Wind Energy, John/Wiley & Sons Ltd.*, 10:379–394, 2007.

[125] F. Delfino, G. B. Denegri, M. Invernizzi, R. Procopio, and G. Ronda. A P-Q Capability Chart Approach to Characterize Grid Connected PV-Units. In *Proc. Integration of Wide-Scale Renewable Resources Into the Power Delivery System, CIGRE/IEEE PES Joint Symposium*, pages 1–8, July 2009.

[126] A. Losi, M. Russo, P. Verde, and D. Menniti. Capability Chart for Generator-Transformer Units. In *Proc. Mediterranean Electrotechnical Conf.*, volume 3, pages 1580–1583, May 1996.

[127] G. Gargiulo, V. Mangoni, and M. Russo. Capability Charts for Combined Cycle Power Plants. *Generation, Transmission and Distribution, IEE*, 149(4):407–415, July 2002.

[128] J. R. De Silva, C. P. Arnold, and J. Arrillaga. Capability Chart for an HVDC Link. *Generation, Transmission and Distribution, IEE*, 134(3):181–186, May 1987.

[129] S. M. Abdelkader and D. Flynn. Graphical Determination of Network Limits for Wind Power Integration. *Generation, Transmission Distribution, IET*, 3(9):841–849, Sept. 2009.

[130] E. Chiodo, A. Losi, R. Mongelluzzo, and F. Rossi. Capability Chart for Electrical Power Systems. *Generation, Transmission and Distribution, IEE*, 139(1):71–75, Jan. 1992.

[131] P. Cuffe, P. Smith, and A. Keane. Characterisation of the Reactive Power Capability of Diverse Distributed Generators:Toward an Optimisation Approach. In *Power and Energy Society General Meeting, IEEE*, pages 1–5, July 2012.

[132] M. H. J. Bollen. *Understanding Power Quality Problems. Voltage Sags and Interruptions*. Wiley-IEEE Press Series on Power Engineering, 2000.

[133] H. Nikkhajoei and R. H. Lasseter. Microgrid Protection. In *Power Engineering Society General Meeting, IEEE*, pages 1–6, June 2007.

[134] E. J. Estebanez, V. M. Moreno, A. Pigazo, M. Liserre, and A. Dell'Aquila. Performance Evaluation of Active Islanding-Detection Algorithms in Distributed-Generation Photovoltaic Systems: Two Inverters Case. *IEEE Trans. on Industrial Electronics*, 58(4):1185–1193, April 2011.

[135] M. Dewadasa, A. Ghosh, and G. Ledwich. Protection of Microgrids using Differential Relays. In *Proc. 21st Australasian Universities Power Engineering Conf.*, pages 1–6, Sept. 2011.

[136] P. Rodriguez, A. V. Timbus, R. Teodorescu, M. Liserre, and F. Blaabjerg. Flexible Active Power Control of Distributed Power Generation Systems during Grid Faults. *IEEE Trans. on Industrial Electronics*, 54(5):2583–2592, Oct. 2007.

[137] D. M. Vilathgamuwa, P. C. Loh, and Y Li. Protection of Microgrids during Utility Voltage Sags. *IEEE Trans. on Industrial Electronics*, 53(5):1427–1436, Oct. 2006.

[138] Working Gropu B5.34. The Impact of Renewable Energy Sources and Distributed Generation on Substration Protection and Automation. Technical report, CIGRE, Aug 2010.

[139] E.ON Netz GmbH. Grid Code for High and Extra High Voltage. Technical report, Bayreuth, 1 April 2006.

[140] A. H. Kasem, E. F. El-Saadany, H. H. El-Tamaly, and M. A. A. Wahab. An Iimproved Fault Ride-Tthrough Strategy for Doubly Fed Induction Generator-Based Wind Turbines. *IET Renewable Power Generation*, 2(4):201–214, Dec. 2008.

[141] M. M. Kyaw and V. K. Ramachandaramurthy. Fault Ride Through and Voltage Regulation for Grid Connected Wind Turbine. *Renewable Energy*, 36(1):206 – 215, 2011.

[142] M. Molinas, J. A. Suul, and T. Undeland. Low Voltage Ride Through of Wind Farms with Cage Generators: STATCOM versus SVC. *IEEE Trans. on Power Electronics*, 23(3):1104–1117, May 2008.

[143] H. Zou, H. Sun, and J. Zou. Fault Ride-Through Performance of Wind Turbine with Doubly Fed Induction Generator. In *Proc. 2nd IEEE Industrial Electronics and Applications Conf.*, pages 1607–1611, May 2007.

[144] M. R. Rathi and N. Mohan. A Novel Robust Low Voltage and Fault Ride Through for Wind Turbine Application Operating in Weak Grids. In *Proc. Industrial Electronics Conf.*, Nov. 2005.

[145] C. Wessels, F. Gebhardt, and F. W. Fuchs. Fault Ride-Through of a DFIG Wind Turbine using a Dynamic Voltage Restorer during Symmetrical and Asymmetrical Grid Faults. *IEEE Trans. on Power Electronics*, 26(3):807–815, March 2011.

[146] D. Xiang, L. Ran, P. J. Tavner, and S. Yang. Control of a Doubly Fed Induction Generator in a Wind Turbine during Drid Fault Ride-Through. *IEEE Trans. on Energy Conversion*, 21(3):652–662, Sept. 2006.

[147] C. Abbey and G. Joos. Effect of Low Voltage Ride Through (LVRT) Characteristic on Voltage Stability. In *Power Engineering Society General Meeting, IEEE*, pages 1901–1907 (2), June 2005.

[148] M. Tsili and S. Papathanassiou. A Review of Grid Code Technical Requirements for Wind Farms. *Renewable Power Generation, IET*, 3(3):308–332, Sept. 2009.

[149] C. Lee, C. Hsu, and P. Cheng. A Low-Voltage Ride-Through Technique for Grid-Connected Converters of Distributed Energy Resources. *IEEE Trans. on Industry Applications*, 47(4):1821–1832, July 2011.

[150] S. Alepuz, S. Busquets, J. Bordonau, J. Pontt, C. Silva, and J. Rodriguez. Comparison of Control Strategies to meet Low Voltage Ride-Through Requirements in Distributed Power Generation Systems. In *Proc. IEEE International Symposium on Industrial Electronics*, pages 2619–2624, June 2007.

[151] Technical Guideline - Generating Plants Connected to the Medium-Voltage Network. Technical report, (BDEW) Bundesverband der Energieund Wasserwirtschaft e.V., 2008.

[152] M. S. El Moursi, X. Weidong, and J. L. Kirtley. Fault Ride Through Capability for Grid Interfacing Large Scale PV Power Plants. *Generation, Transmission Distribution, IET*, 7(9):1027–1036, Sept. 2013.

[153] A. Marinopoulos, F. Papandrea, M. Reza, S. Norrga, F. Spertino, and R. Napoli. Grid Integration Aspects of Large Solar PV Installations: LVRT Capability and Reactive Power/Voltage Support Requirements. In *Proc. IEEE Trondheim PowerTech*, pages 1–8, June 2011.

[154] H. Kobayashi. Fault Ride Through Requirements and Measures of Distributed PV Systems in Japan. In *Power and Energy Society General Meeting, IEEE*, pages 1–6, July 2012.

[155] C. H. Benz, W.-T. Franke, and F. W. Fuchs. Low Voltage Ride Through Capability of a 5 kw Grid-Tied Solar Inverter. In *Proc. 14th Int. Conf. on Power Electronics and Motion Control*, pages T12–13–T12–20, Sept. 2010.

[156] G. M. S. Islam, A. Al-Durra, S. M. Muyeen, and J. Tamura. Low Voltage Ride Through Capability Enhancement of Grid Connected Large Scale Photovoltaic System. In *Proc. 37th Annual Conf. on IEEE Industrial Electronics Society*, pages 884–889, Nov. 2011.

[157] M. Z. C. Wanik, A. Mohamed, A. F. A. Kadir, and I. Erlich. Low Voltage Ride Through Capability of Fuel Cell Generation System Connected to Low Voltage Network. In *Proc. IEEE 1st Conf. on Clean Energy and Technology*, pages 369–373, June 2011.

[158] Rules and Transitional Periods for Specific Requirements Complementary to the Technical Guideline:Generating Plants Connected to the Medium Voltage Network-Guideline for Generating Plants Connection to and Parallel Operation with the Medium-Voltage Network. Technical report, June 2008.

[159] H. J. Laaksonen. Protection Principles for Future Microgrids. *IEEE Trans. on Power Electronics*, 25(12):2910–2918, Dec. 2010.

[160] H. Yazdanpanahi, W. L. Yun, and X. Wilsun. A New Control Strategy to Mitigate the Impact of Inverter-Based DGs on Protection System. *IEEE Trans. on Smart Grid*, 3(3):1427–1436, Sept. 2012.

[161] G. J. Kish and P. W. Lehn. Microgrid Design Considerations for Next Generation Grid Codes. In *Power and Energy Society General Meeting, IEEE*, pages 1–8, July 2012.

[162] IEEE PES Distribution System Analysis Subcommittee. IEEE-13 Node Test Feeder, 2006.

[163] P. Kundur. *Power System Stability and Control*. McGraw-Hill, 1994.

[164] I. C. Report. Excitation System Models for Power System Stability Studies. *IEEE Trans. on Power Apparatus and Systems*, PAS-100(2):494–509, Feb. 1981.

[165] A. D. Hansen, C. Jauch, P. Sorensen, F. Iov, and F. Blaabjerg. Dynamic Wind Turbine Models in Power System Simulation Tool DIgSILENT. Technical report, Ris report Ris-R-1400(EN), Denmark,, 2004.

[166] K. Ogata. *State Space Analysis of Control Systems*. PRENTICE-HALL, INC., 1976.

[167] C. Schauder and H. Mehta. Vector Analysis and Control of Advanced Static VAr Compensators. *Generation, Transmission and Distribution, IEE*, 140(4):299–306, July 1993.

[168] S. K. Chung. A Phase Tracking System for Three Phase Utility Interface Inverters. *IEEE Trans. on Power Electronics*, 15(3):431–438, May 2000.

[169] U. D. Annakkage, N. K C Nair, Y. Liang, A. M. Gole, V. Dinavahi, B. Gustavsen, T. Noda, H. Ghasemi, A. Monti, M. Matar, R. Iravani, and J. A. Martinez. Dynamic System Equivalents: A Survey of Available Techniques. *IEEE Trans. on Power Delivery*, 27(1):411–420, Jan. 2012.

[170] P. E. Gill, W. Murray, and M. H. Wright. *Practical Optimization*. Academic Press, 1981.

[171] M. Y. Cho and Y. W. Chen. Fixed/Switched Type Shunt Capacitor Planning of Distribution Systems by Considering Customer Load Patterns and Simplified Feeder Model. *Generation, Transmission and Distribution, IEE*, 144(6):533–540, Nov. 1997.

[172] A. Masoum, S. Deilami, P. Moses, M. Masoum, and A. Abu-Siada. Smart Load Management of Plug-in Electric Vehicles in Distribution and Residential Networks withCharging Stations for Peak Shaving and Loss Minimisation Considering Voltage Regulation. *Generation Transmission & Distribution, IEE*, 5:877–888, 2011.

[173] Z. Liu, F. Wen, and G. Ledwich. Optimal Planning of Electric-Vehicle Charging Stations in Distribution Systems. *IEEE Trans. Power Delivery*, 28:102–110, 2013.

[174] M. Yilmaz and P. Krein. Review of the Impact of Vehicle-to-Grid Technologies on Distribution Systems and Utility Interfaces. *IEEE Trans. on Power Electronics*, 28:5673–5689, 2013.

[175] C. Guille and G. Gross. A Conceptual Framework for the Vehicle-to-Grid (V2G) Implementation. *Energy Policy*, 37:4379 – 4390, 2009.

[176] Y. M. Atwa, E. F. El-Saadany, M. M. A. Salama, and R. Seethapathy. Optimal Renewable Resources Mix for Distribution System Energy Loss Minimization. *IEEE Trans. on Power Systems*, 25(1):360–370, Feb. 2010.

[177] S. Nikolova, A. Causevski, and A. Al-Salaymeh. Optimal Operation of Conventional Power Plants in Power System with Integrated Renewable Energy Sources. *Energy Conversion and Management*, 65:697 – 703, 2013. Global Conference on Renewable energy and Energy Efficiency for Desert Regions 2011 2011.

[178] Y. Xu and C . Singh. Adequacy and Economy Analysis of Distribution Systems Integrated with Electric Energy Storage and Renewable Energy Resources. *IEEE Trans. on Power Systems*, 27, 4(4):2332–2341, Nov. 2012.

[179] Gilbert M. Masters. *Renewable and Efficient Electric Power Systems*. John Wiley & Sons, Inc.,, 2004.

[180] Commonwealth of Australia 2006. Uranium Mining, Processing and Nuclear Energy Opportunities for Australia? Technical report, Report to the Prime Minister by the Uranium Mining, Processing and Nuclear Energy Review Taskforce, Dec 2006.

[181] Q. F. Zhang, B. Smith, and W. Zhang. Small Hydropower Cost Reference Model. Technical report, OAK RIDGE National Laboratory, 2012.

[182] Final Report - 2013 Residential Electricity Price Trends. Technical report, Australian Energy Market Commision, Dec. 2013.

[183] J. W. Lamont and J. Fu. Cost Analysis of Reactive Power Support. *IEEE Trans. on Power Systems*, 14(3):890–898, Aug. 1999.

[184] A. D. Papalexopoulos and G. A. Angelidis. Reactive Power Management and Pricing in the California Market. In *Proc. 13th IEEE Melecon Conf.*, volume 2, pages 902–905, May 2006.

[185] G. Chicco and G. Gross. Current Issues in Reactive Power Management: A Critical Overview. In *Power and Energy Society General Meeting, IEEE*, July 2008.

[186] A. Ghosh and G. Ledwich. *Power Quality ENHancement using Custom Power Devices*. Kluwer Academic Publishers, 2002.

[187] W. Freitas, E. Asada, A. Morelato, and W. Xu. Dynamic Improvement of Induction Generators Connected to Distribution Systems using a DSTATCOM. In *Proc. Int. Conf. on Power System Technology*, volume 1, pages 173–177, Oct 2002.

[188] M. K. Mishra and K. Karthikeyan. An Investigation on Design and Switching Dynamics of a Voltage Source Inverter to Compensate Unbalanced and Nonlinear Loads. *IEEE Trans. on Industrial Electronics*, 56(8):2802–2810, Aug. 2009.

[189] C. Kumar and M. K. Mishra. A Modified DSTATCOM Topology with Reduced VSI Rating, DC Link Voltage, and Filter Size. In *Proc. Clean Electrical Power*, pages 325–331, June 2013.

[190] T. V. Cutsem and C. Vournas. *Voltage Stability of Electric Power Systems*. Springer, 1998.

[191] D. O. Dike, S. M. Mahajan, and G. Radman. Development of a Versatile Voltage Stability Index Algorithm. In *Proc. Electrical Power Conf.*, pages 556–561, Oct. 2007.

Appendix A

Network Parameters of the Microgrid Systems

Network parameters of the microgrid system in Chapter 3

Table A.1: Microgrid line lengths

Line	Length (km)
632-632_1	0.6096
632-645	0.1524
632-671	0.6096
645-646	0.0914
632-633	0.1524
684-611	0.0941
684-652	0.2438
684-671	0.0914
692-671	0.1524
675-692	0.1524

Details of the SG, IM and the Network parameters of microgrid system in Chapter 5

- Line lengths and impedances of the microgrid system in Chapter 5 are similar to the values in Chapter 3.

Table A.2: Parameters of the SGs

Parameter	5 MVA,13.8 kV	1.5 MVA,13.8 kV
X_d	1.700 pu	0.990 pu
$X_d^{'}$	0.245 pu	0.157 pu
$X_d^{"}$	0.185 pu	0.111 pu
X_q	1.640 pu	0.570 pu
$X_q^{"}$	0.295 pu	0.130 pu
H	2.700 s	1.500 s
R	0.0011 pu	0.0001 pu
$T_{do}^{'}$	5.900 s	2.730 s
$T_{do}^{"}$	0.003 s	0.045 s
$T_{qo}^{"}$	0.075 s	0.068 s

Table A.3: Parameters of the AVR

Parameter	Value
K_r	1.0
K_a	200
K_e	2
T_a	0.03 s
T_e	0.266 s
K_f	0.0025
T_f	0.0015 s

Table A.4: Parameters of the hydro turbine-governor model

Parameter	Value
R_t	0.4
R_p	0.04
T_g	0.2 s
T_r	5.0 s
T_w	2.0 s

Table A.5: Parameters of the IM load

Parameter	Value
R_s	0.0193 pu
X_s	0.01 pu
X_m	3.04 pu
X_{rm}	0.01 pu
$\mathrm{T}_o^{"}$	0.014 s

Table A.6: Microgrid static load demands

Load	P (MW)	Q (MVAr)
611	0.3	0.1
632	0.4	0.2
634	0.4	0.3
645	0.5	0.3
646	0.5	0.2
652	0.1	0.05
671	0.1	0.06
675	0.1	0.06
692	1.4	0.84

Appendix B

Network Parameters and Constraints of the Optimisation Model

Line capacities, transformer ratings and generator ratings incorporated into the optimisation model in Chapter 6

- Non-linear and linear inequality constraints of the 5 MVA SG (10 MVA, 13.8 kV base)

$$\begin{aligned} 0 &\leq P \leq 0.4 \\ -0.3 &\leq Q \leq 0.3 \\ P^2 + Q^2 &\leq 0.25 \\ P - 2.81Q &\leq 0.815 \end{aligned}$$

- Non-linear and linear inequality constraints of the 1.5 MVA DFIG (10 MVA, 13.8 kV base)

$$
\begin{aligned}
0 &\leq P \leq 0.14 \\
-0.15 &\leq Q \leq 0.15 \\
\frac{P^2}{0.034} &+ \frac{Q^2}{0.0225} \leq 1 \\
\frac{(P-0.0005)^2}{0.0282} &+ \frac{(Q+0.3)^2}{0.0196} \leq 1
\end{aligned}
$$

- Non-linear and linear inequality constraints of the network

$$
\begin{aligned}
0.95 &\leq V \leq 1.05 \\
0 &\leq I \leq 1
\end{aligned}
$$

Network parameters of the microgrid system in Chapter 6

Table B.1: Microgrid line lengths

Line	Length (km)
632-632_1	0.6096
632-645	0.1524
632-671	0.6096
645-646	0.0914
632-633	0.1524
684-611	0.0941
684-652	0.2438
684-671	0.0914
692-671	0.1524
675-692	0.1524

Table B.2: Microgrid parameters (50 Hz)

O/H Line parameters	(0.3+j0.3) Ω/km
Coupling Transformer	10 MVA, 115 kV/4.16 kV
Capacitor bank C 634	0.5 MVAr
External grid short circuit capacity	1000 MVA